

REPORT DOCUMENTATION PAGE

Form Approved
OMB No. 0704-0188

Public reporting burden for this collection of information is estimated to average 1 hour per response, including the time for reviewing instructions, searching existing data sources, gathering and maintaining the data needed, and completing and reviewing this collection of information. Send comments regarding this burden estimate or any other aspect of this collection of information, including suggestions for reducing this burden to Department of Defense, Washington Headquarters Services, Directorate for Information Operations and Reports (0704-0188), 1215 Jefferson Davis Highway, Suite 1204, Arlington, VA 22202-4302. Respondents should be aware that notwithstanding any other provision of law, no person shall be subject to any penalty for failing to comply with a collection of information if it does not display a currently valid OMB control number. **PLEASE DO NOT RETURN YOUR FORM TO THE ABOVE ADDRESS.**

1. REPORT DATE (DD-MM-YYYY) 09-08-2010		2. REPORT TYPE Final Report		3. DATES COVERED (From - To) Dec 2006-Oct 2009	
4. TITLE AND SUBTITLE Shock and Impact Response of Naval Composite Structures				5a. CONTRACT NUMBER	
				5b. GRANT NUMBER N00014-07-1-0423	
				5c. PROGRAM ELEMENT NUMBER	
6. AUTHOR(S) Hoo Fatt, Michelle, S				5d. PROJECT NUMBER	
				5e. TASK NUMBER	
				5f. WORK UNIT NUMBER	
7. PERFORMING ORGANIZATION NAME(S) AND ADDRESS(ES) The University of Akron 302 Buchtel Common Akron, OH 44325-0001				8. PERFORMING ORGANIZATION REPORT NUMBER	
9. SPONSORING / MONITORING AGENCY NAME(S) AND ADDRESS(ES) Office of Naval Research One Liberty Center Arlington, VA 22203-1995				10. SPONSOR/MONITOR'S ACRONYM(S) ONR-Solid Mechanics Pgm (332)	
				11. SPONSOR/MONITOR'S REPORT NUMBER(S)	
12. DISTRIBUTION / AVAILABILITY STATEMENT Approved for public release; distribution is unlimited.					
13. SUPPLEMENTARY NOTES					
14. ABSTRACT Analytical solutions for the impact and blast response of naval composite structures were developed in this research grant. Finite element analysis using ABAQUS and experimental results found in the open literature were also considered in conjunction with the work. Four problems, in particular, were addressed during the course of this grant period. These were as follows: (1) low velocity impact of a sandwich panel with Coremat™, a high impact resistant core, (2) blast response of a composite sandwich panel with traditional PVC foam cores; (3) high velocity impact and perforation of a composite sandwich panel again with traditional PVC foam cores; and (4) implosion of a laminated composite cylinder under external blast. This report summarizes the analyses and findings associated with these four problems.					
15. SUBJECT TERMS Blast, Impact, Composite Sandwich Panel, Composite Shell, Implosion, Analytical Modeling.					
16. SECURITY CLASSIFICATION OF:			17. LIMITATION OF ABSTRACT UU	18. NUMBER OF PAGES 13	19a. NAME OF RESPONSIBLE PERSON Michelle S. Hoo Fatt
a. REPORT U	b. ABSTRACT U	c. THIS PAGE U			19b. TELEPHONE NUMBER (include area code) (330) 972-6308

PROJECT SUMMARY

Analytical solutions for the impact and blast response of naval composite structures were developed in this research grant. Finite element analysis using ABAQUS and experimental results found in the open literature were also considered in conjunction with the work. Four problems, in particular, were addressed during the course of this grant period. These were as follows: (1) low velocity impact of a sandwich panel with CorematTM, a high impact resistant core, (2) blast response of a composite sandwich panel with traditional PVC foam cores; (3) high velocity impact and perforation of a composite sandwich panel again with traditional PVC foam cores; and (4) implosion of a laminated composite cylinder under external blast. This report summarizes the analyses and findings associated with these four problems.

OBJECTIVES

The objective of this project was to develop analytical models for predicting the deformation and failure of naval composite structures subjected to blast and projectile impact loading. These analytical models are essential for elucidating physical mechanisms that control the survivability of composite structures under blast and impact.

TECHNICAL APPROACH

The Principal Investigator (PI) used analytical modeling with FEA simulations for verification purposes. Some analytical models were developed from experimental results found in the open literature.

MAJOR ACCOMPLISHMENTS

Four problems were addressed during the course of this grant period. These were as follows: (1) low velocity impact of a sandwich panel with Coremat™, a high impact resistant core, (2) blast response of a composite sandwich panel with traditional PVC foam cores; (3) high velocity impact and perforation of a composite sandwich panel, again with traditional PVC foam cores; and (4) implosion of a laminated composite cylinder under external blast. This section summarizes major findings of the above-mentioned problems. Specific details of the analyses can be found in the ONR publications listed at the end of this report.

A. Low-Velocity Impact of Composite Sandwich Panels

In 2007, the PI developed analytical solutions for the quasi-static and low-velocity perforation of sandwich panels with woven roving E-glass/vinyl ester facesheets and Coremat™[1,2]. The analytical model was developed using experimental results from Mines et al. [3] and is an extension of the PI's earlier work on impact of sandwich panels consisting of E-glass/epoxy facesheets with aluminum honeycomb core [4]. Coremat™ is a high density/high energy absorption resin impregnated non-woven polyester with 50% microsphere, and is commonly used in the marine industry because of its high impact resistance [5]. Impregnated Coremat™ has a density of around 610 kgm^{-3} , while the standard foam density for marine craft is 100 kgm^{-3} . It is primarily used in decks and hulls that are susceptible to high impulsive loads. The compressive stress-strain curves shown in Fig. 1 indicate that Coremat™ does not exhibit the typical elastic-perfectly plastic behavior of crushable foams but rather elastic-linear strain hardening (or bi-linear) material behavior. This is because of its high density.

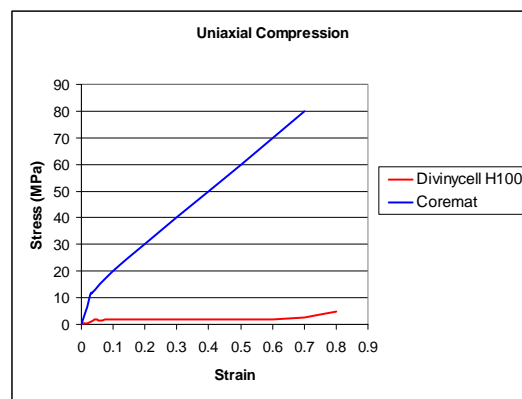


Figure 1 Compressive stress-strain behavior of Coremat and Divinycell H100 foams.

The panel deformation was decomposed into local indentation and global deformation. A multi-stage perforation process involving delamination, debonding, core shear fracture and facesheet fracture was used to predict failure loads. As shown in Fig. 2, analytical predictions of the quasi-static load-

deflection response were within 5% of the test data, and the calculated failure load was about 25% higher than the test data. An equivalent two degree-of-freedom mass-spring-dashpot system was used to find the dynamic response of the composite sandwich panel subjected to a drop-weight impact by a rigid hemispherical-nose projectile. The predicted contact force histories from the equivalent two degree-of-freedom model were within 10% of test data (see Fig. 3).

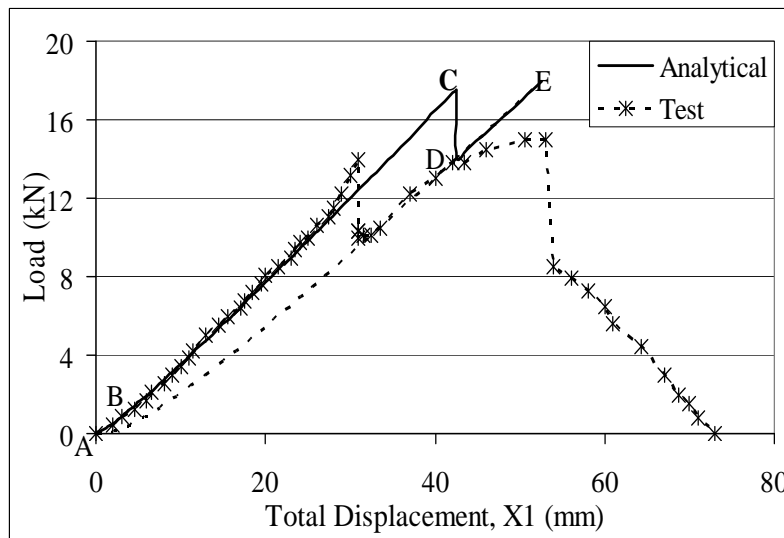


Figure 2 Variation of quasi-static load with indenter displacement.

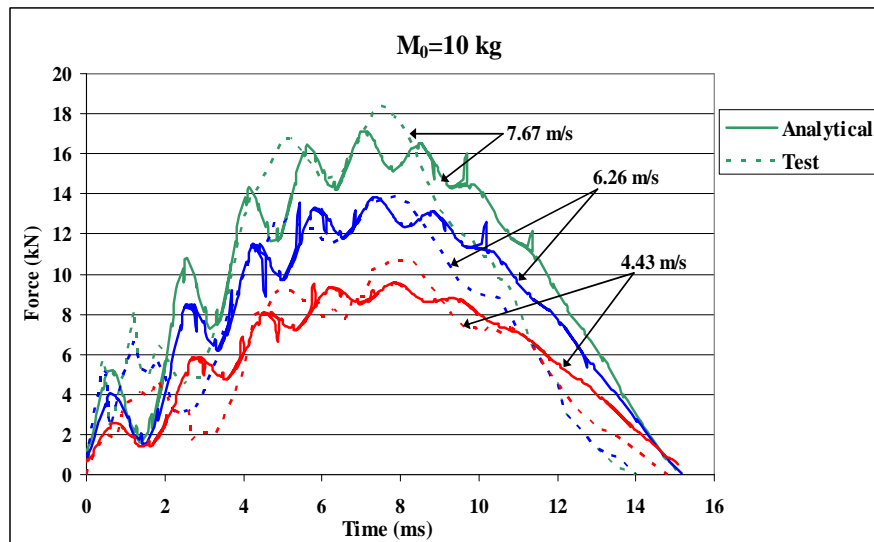


Figure 3 Contact force history with 10 kg mass projectile travelling at various speeds.

The analytical model specifically showed how local core properties can influence the deformation and ultimate failure of a composite sandwich panel. It also provided a simple way to approximately describe the material response of non-traditional, high density and damping foams such as Coremat™. The analytical results indicated that the high core crushing resistance and damping of the Coremat™ limited the amount of local indentation compared to global panel deformation. As a result, the Coremat™ sandwich panel first ruptured in the distal facesheet rather than the impacted facesheet. Such a failure mode may be desirable from a practical standpoint since the outer surface of a composite sandwich vessel undergoing impact from external sources, would remain intact if damage were to just initiate.

B. Blast Response of Sandwich Panels

In 2008, the PI developed a transient, wave propagation model to examine the damage resistance of composite sandwich panels subjected to blast and high velocity projectile impact [6-8]. Analytical solutions were derived for the transient response and damage initiation of a foam-core composite sandwich panel subjected to uniformly-distributed, pressure pulse loading. The panel response was modeled in two consecutive phases: (1) a through-thickness wave propagation phase leading to permanent core crushing deformations (Fig. 4) and (2) a transverse shear wave propagation phase resulting in global panel deflections (Fig. 5).

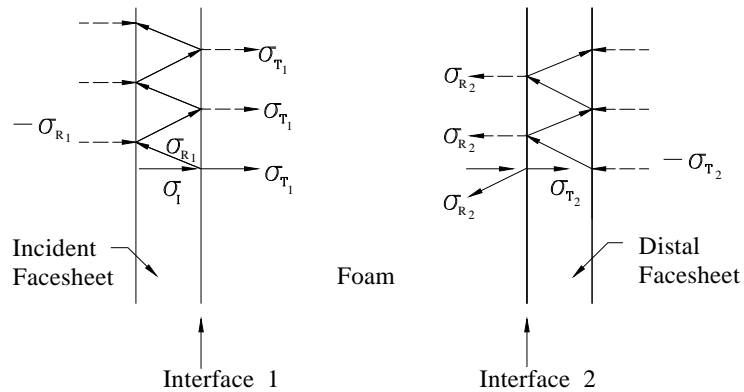


Figure 4 Transmission of stress waves through facesheets and foam in sandwich panel.

Global equilibrium equations of motion were formulated from the system Lagrangian and used to obtain transverse deflection and shear rotations. Finite element analysis (FEA) using ABAQUS Explicit was also done. The predicted transient deformation of the sandwich panel was within 7% of FEA results using ABAQUS Explicit (see Fig. 6). Analytical predictions of the critical impulse for damage initiation also compared fairly well with ABAQUS predictions.

Damage initiation of sandwich panels with 2mm-thick, E glass vinyl ester facesheets and two other cores, namely Divinycell H200 and Klegecell R300 foams, were considered in addition to the Divinycell H100 foam core. As shown in Figure 7, the analytical predictions for the critical impulse to failure compared well to ABAQUS predictions, thereby rendering the analytical model a useful design tool for manufacturing blast resistant composite sandwich panels.

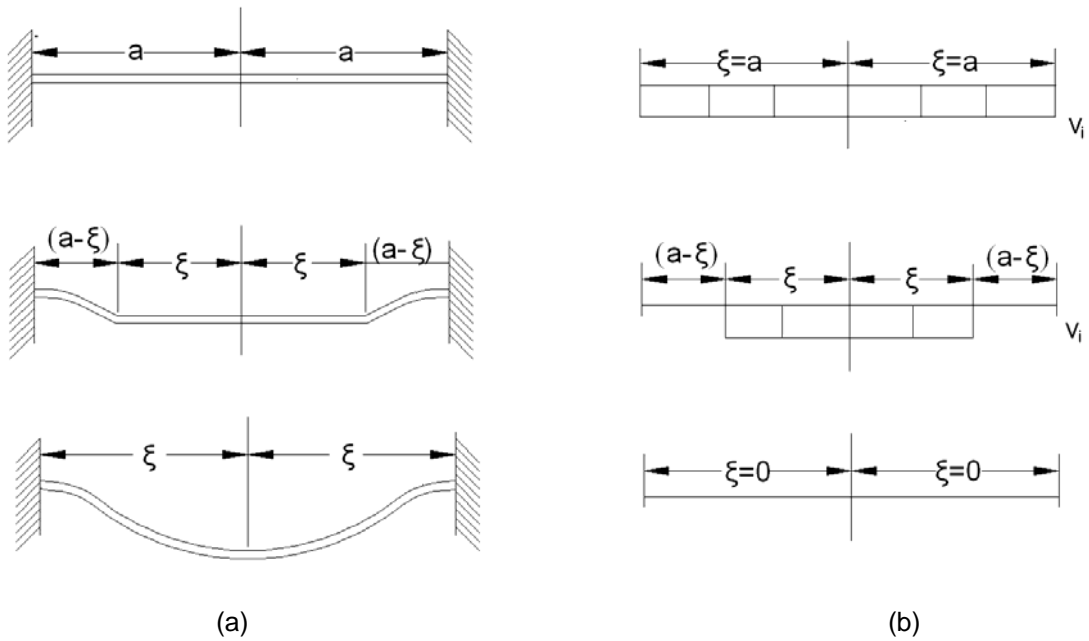


Figure 5 Global panel bending/shear response: (a) Deformation profiles and (b) Velocity fields.

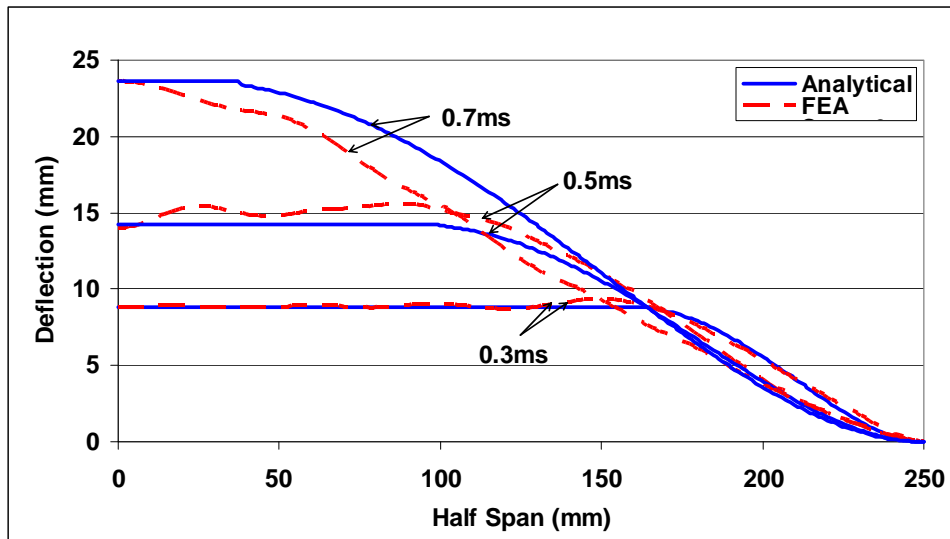


Figure 6 Transient deflection profiles of composite sandwich.

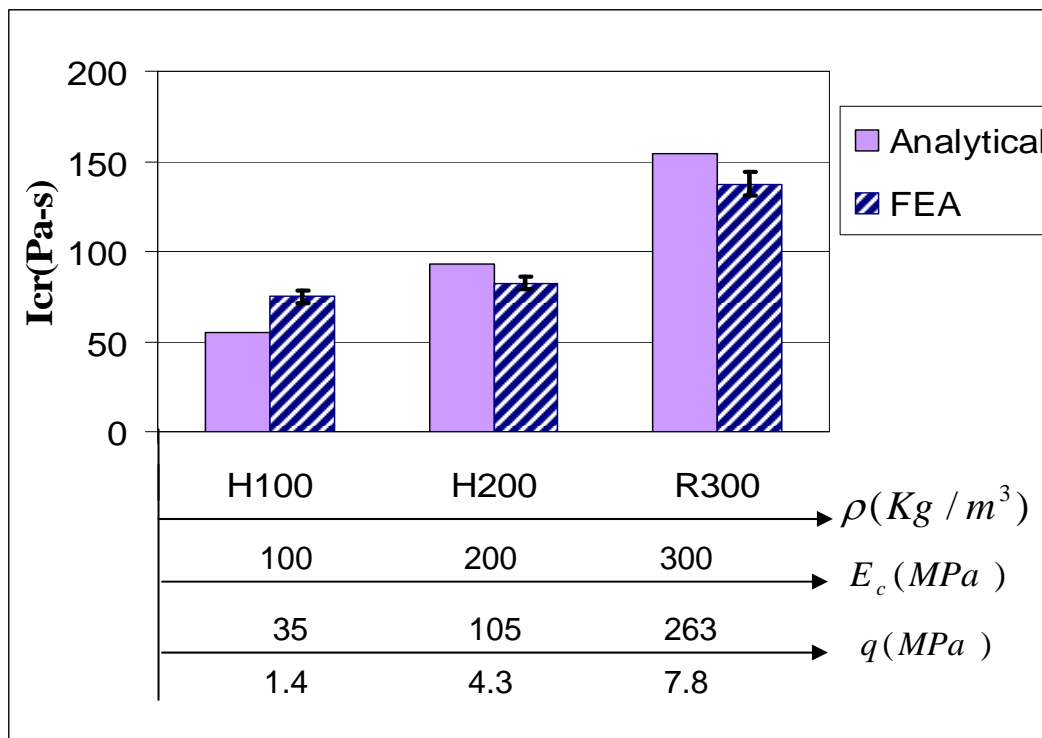


Figure 7 Variation of critical impulse to failure with core material properties.

C. High-Velocity Impact

Also in 2008, analytical solutions for the deformation response of a composite sandwich panel subjected to high velocity impact by a rigid blunt, cylindrical projectile were derived using Lagrangian mechanics [8-10]. Waves travelling through the sandwich core thickness and laterally across the panel were incorporated in a previously developed two degrees-of-freedom model for the sandwich panel. Modelling the sandwich with two degrees of freedom allowed local indentation and core crushing to be coupled with global bending/shear deformations of the sandwich. Unlike most high velocity impact solution, the solution was fully deterministic and involved the use of no empirical equations. Lagrange's equations of motion were written for the projectile and effective mass of the facesheets and core as the shock waves travel through sandwich panel. Simple facesheet and core failure criteria (see Fig. 8) were used to determine when to impose changes in the load-bearing resistance of the sandwich during penetration.

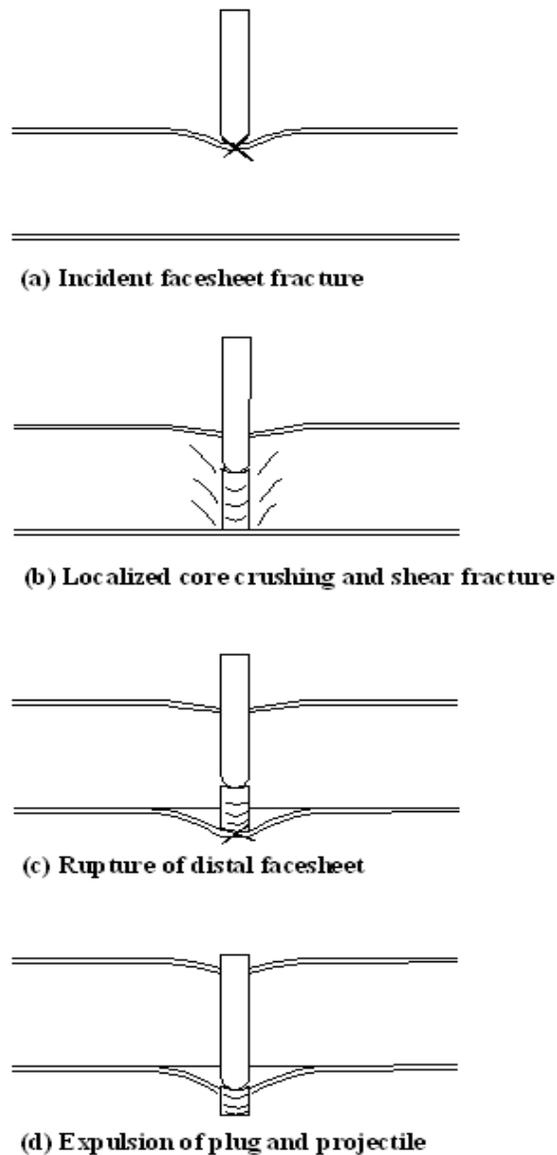


Figure 8 Penetration and perforation of composite sandwich panel: (a) Incident facesheet fracture, (b) Localized core crushing and shear fracture, (c) Rupture of distal facesheet and (d) Expulsion of plug and projectile.

As shown in Figs. 9 (a) and (b), the analytical solution for the local indentation and global deflection under the projectile was found to be within 20% of FEA results. Analytical predictions of the projectile residual velocities were also found to be in good agreement with published experimental data [11]. Figure 10 compares predicted and experimental residual velocities of a steel projectile perforating composite sandwich panels consisting of woven roving E-glass polyester facesheets and PVC H130 foam core.

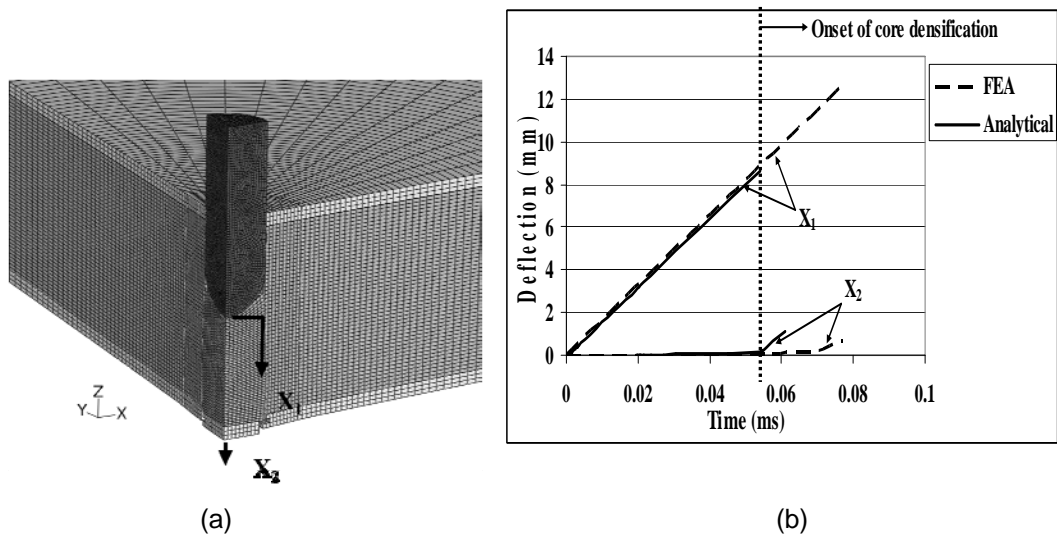


Figure 9 Analytical and FEA results: (a) FEA model and (b) Transient deflections.

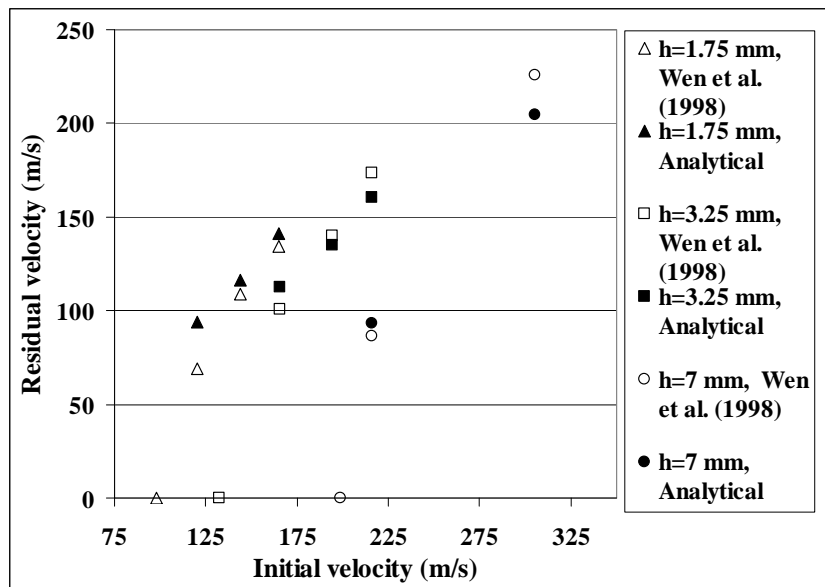


Figure 10 Comparison of the residual velocity between analytical model and test results from Wen et al. [11].

D. Implosion of Composite Cylindrical Shells

In 2009, the PI examined the dynamic stability of a composite cylindrical shell subjected to external shock loading [12,13]. Analytical solutions for the dynamic pulse buckling, vibration and failure laminated composite cylindrical shells subjected to uniform overpressure and asymmetric pressure pulse (side-on explosion), as shown in Fig. 11, were developed.

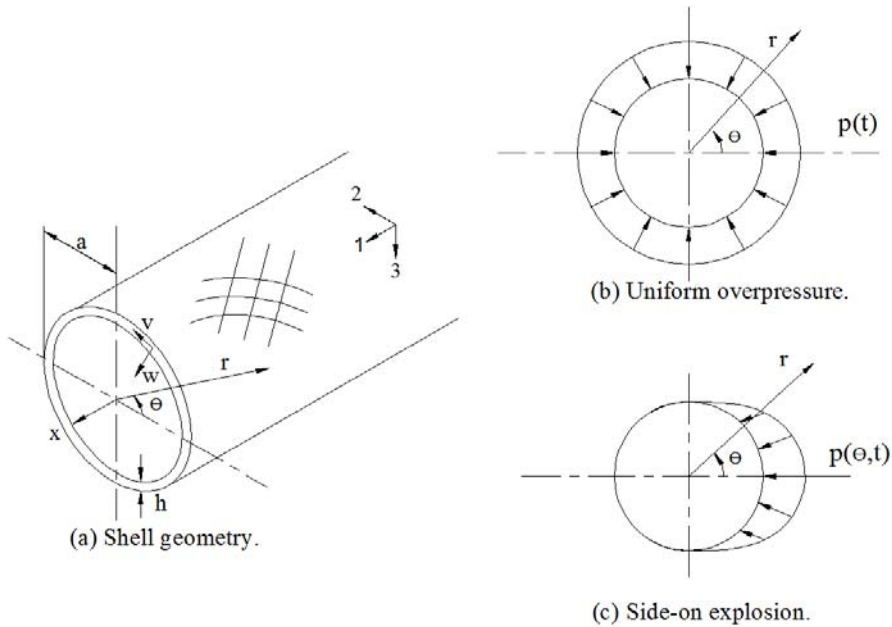


Figure 11
Composite cylinder under

external pressure pulse loading: (a) Shell geometry, (b) Uniform overpressure and (c) Side-on explosion.

The solution for the radial shell deformations was represented by Mathieu differential equations and the dynamic instability of the shells was determined from a Mathieu stability diagram, as depicted in Fig. 12.

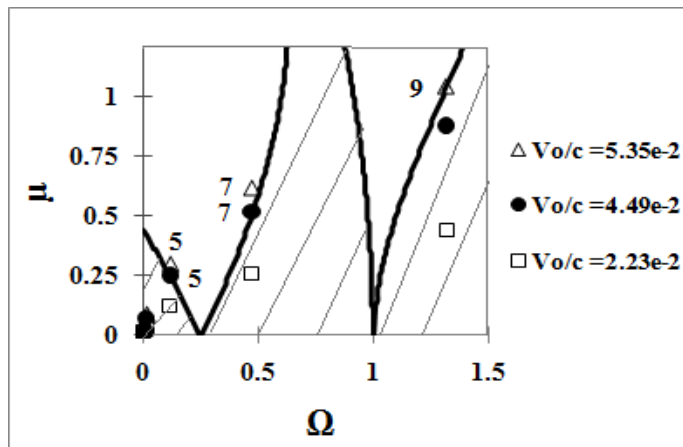


Figure 12
woven E-

Stability diagrams for
Glass/Vinyl Ester shell

with side-on explosion and increasing impulse v_o/c (shaded regions are stable).

It was found that the stability of the shells depended on lay-up, aspect ratio as well as impulse distribution. For a given lay-up, the critical buckling impulse generally decreases as the aspect ratio increases (thinner shells). However, Fig. 13 shows that at a given aspect ratio, the buckling load, I_{cr} , depends on shell lay-up.

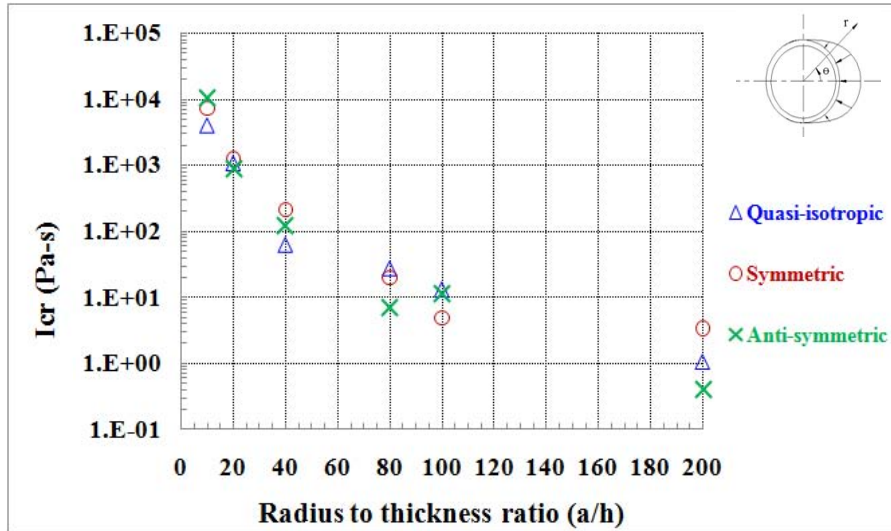


Figure 13 Effect of shell aspect ratio and layup on the critical buckling impulse.

The stable vibration response of woven E-Glass/Vinyl Ester shell with side-on explosion also compared well with finite element solutions using a dynamic, implicit analysis in ABAQUS Standard as shown in Fig. 14.

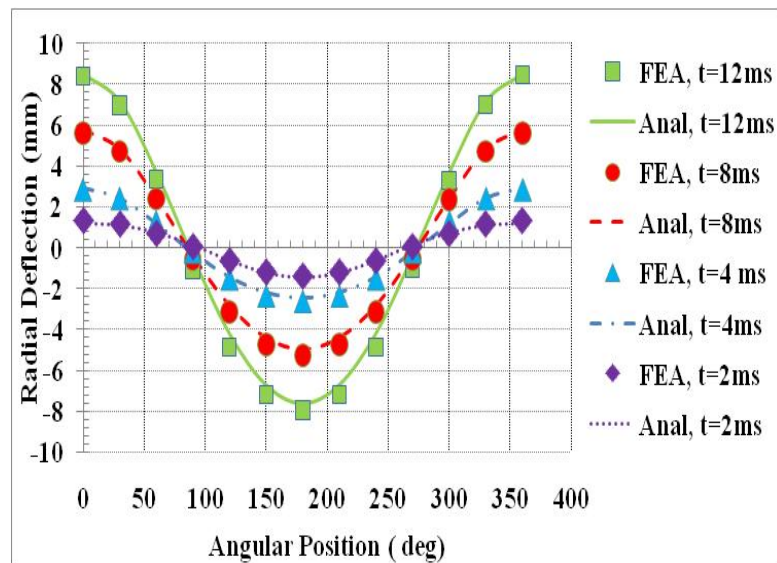


Figure 14 Transient deflections of the orthotropic, woven roving E-Glass/Vinyl Ester shell: $h = 4\text{mm}$, $a = 80\text{mm}$, $p_o = 10\text{MPa}$, $\Delta T = 3.5\ \mu\text{s}$

First-ply failure of the woven E-Glass/Vinyl Ester shell with side-on explosion was predicted using a modified Hashin-Rotem failure criterion. Figure 15 show the variations of shell impulses for fracture and instability with the shell aspect ratio. It was concluded that the thinner shells were more likely to fail by dynamic instability, whereas the thicker shells were more likely to fail by first-ply failure.

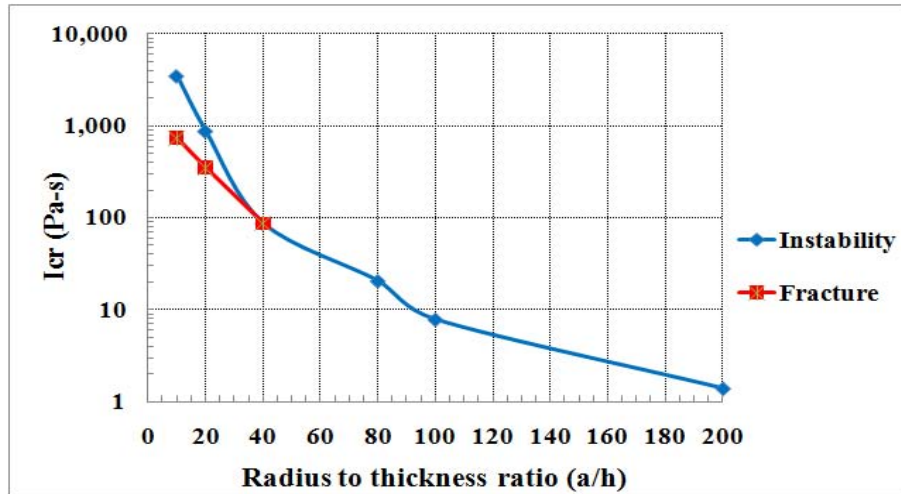


Figure 15 Influence of aspect ratio on the type of failure for woven E-Glass/Vinyl Ester shell with side-on pressure pulse.

IMPACT OF RESEARCH/TRANSITIONS

The analytical solutions provide simple tools for estimating blast and impact response. They are used for setting up experiments and benchmarking more refined FEA. The ONR Publications listed at the end of this report will help the US Navy to design more effective composite structures for military ships, submarines and carriers.

References

1. Hoo Fatt MS, Sirivolu D. Impact Perforation of Sandwich Panels with Coremat®. International Journal of Crashworthiness. 14(1):37-47, 2009.
2. Hoo Fatt MS, Sirivolu D. Impact Perforation of Composite Sandwich Panels. Proceedings of the 16th International Conference on Composite Structures, Kyoto, Japan, July 8-13, 2007.
3. Mines RAW, Worrall CM, Gibson AG. 1998. Low velocity perforation behavior of polymer composite sandwich panels. Int J Impact Engng. 21(10):855-879, 1998.
4. Lin C, Hoo Fatt MS. Perforation of sandwich panels with honeycomb cores by hemispherical-nose projectiles. J Sand Struct Mat. 7(2):113-172, 2005.
5. Lantor Coremat®. Veenendaal, The Netherlands: Lantor BV, 1993.
6. Hoo Fatt MS, Palla L. Analytical Modeling of Composite Sandwich Panels under Blast Loads. Journal of Sandwich Structures and Materials, 11(4):357-380, 2009.
7. Hoo Fatt MS, Palla L. Blast Response of Composite Sandwich Panels. Proceedings of the 8th Int. Conference on Sandwich Structures, Porto, Portugal, May 6-8, 2008.
8. Hoo Fatt MS, Palla L, Sirivolu D. Modeling Blast and High-Velocity Impact of Composite Sandwich Panels. In Major Accomplishments in Composite Materials and Sandwich Structures – An Anthology of ONR Sponsored Research, I.M. Daniel, E.E. Gdoutos and Y.D.S. Rajapakse (editors), Springer, New York, pp. 661-690, 2009.
9. Hoo Fatt MS, Sirivolu D. A Wave Propagation Model for the High Velocity Impact Response of a Composite Sandwich Panel,” International Journal of Impact Engineering, 37(2):117-130, 2010.
10. Hoo Fatt MS, Sirivolu D. High Velocity Impact of a Composite Sandwich Panel” in Structures Under Shock and Impact, the Algarve, Portugal, May 14-17, 2008, and in Structures under Shock and Impact X (edited by N. Jones and C.A. Brebbia), WIT Press, Southampton, UK, 2008, pp. 3-13.

11. Wen HM, Reddy TY, Reid SR, Soden SR. Indentation, penetration and perforation of composite laminates and sandwich panels under quasi-static and projectile loading. *Key Eng Mat* 1998; 141-143(Part 2): 501-552.
12. Hoo Fatt MS, Pothula, SG. Dynamic Pulse Buckling of Composite Shells Subjected to External Blast. *Composites Structures*, 92(7):1716–1727, 2010.
13. Hoo Fatt MS, Pothula SG. Implosion of Composite Shells under Blast. *Proceedings of the 17th International Conference on Composite Materials*, Edinburgh, UK, July 27-31, 2009.

ONR PUBLICATIONS

A. Refereed Journals

1. Hoo Fatt M.S, and Pothula, S.G., "Dynamic Pulse Buckling of Composite Shells Subjected to External Blast," *Composites Structures*, Vol. 92, No. 7, pp. 1716–1727, 2010.
2. Hoo Fatt, M.S. and Sirivolu, D., "A Wave Propagation Model for the High Velocity Impact Response of a Composite Sandwich Panel," *International Journal of Impact Engineering*, Vo. 37, No. 2, pp. 117-130, 2010.
3. Hoo Fatt, M.S. and Palla, L., "Analytical Modeling of Composite Sandwich Panels under Blast Loads," *Journal of Sandwich Structures and Materials*, Vol. 11, No. 4, pp. 357-380, 2009.
4. Hoo Fatt, M.S. and Sirivolu, D., "Impact Perforation of Sandwich Panels with Coremat®," *International Journal of Crashworthiness*, Vol. 14, No. 1, pp. 37-47, 2009.

B. Book Chapters

1. Hoo Fatt, M.S., Palla, L. and Sirivolu, D., "Modeling Blast and High-Velocity Impact of Composite Sandwich Panels," in *Major Accomplishments in Composite Materials and Sandwich Structures – An Anthology of ONR Sponsored Research*, I.M. Daniel, E.E. Gdoutos and Y.D.S. Rajapakse (editors), Springer, New York, pp. 661-690, 2009.

C. Conference Papers

1. Hoo Fatt, M.S. and Pothula, S.G., "Implosion of Composite Shells under Blast" in the Proceedings of the 17th International Conference on Composite Materials, Edinburgh, UK, July 27-31, 2009.
2. Hoo Fatt M.S. and Sirivolu, D., "High Velocity Impact of a Composite Sandwich Panel" presented at the 10th Int. Conference on Structures Under Shock and Impact, the Algarve, Portugal, May 14-17, 2008, and in *Structures under Shock and Impact X* (edited by N. Jones and C.A. Brebbia), WIT Press, Southampton, UK, 2008, pp. 3-13.
3. Hoo Fatt M.S. and Palla, L., "Blast Response of Composite Sandwich Panels" in the Proceedings of the 8th Int. Conference on Sandwich Structures, Porto, Portugal, May 6-8, 2008.
4. Hoo Fatt, M.S. and Sirivolu, D., "Impact Perforation of Composite Sandwich Panels" in the Proceedings of the 16th International Conference on Composite Structures, Kyoto, Japan, July 8-13, 2007.

D. ONR Solid Mechanics Program Review Papers

1. Hoo Fatt, M.S., "Dynamic Stability, Vibrations and Failure of Composite Shells Under External Blast," in the Proceedings of the 2009 ONR Solid Mechanics Program Review, Marine Composites and Sandwich Structures, University of Maryland University College, Adelphi, MD, September 21-23, 2009.
2. Hoo Fatt, M.S., "Analytical Models for Blast and High Velocity Impact of Composite Sandwich Panels," in the Proceedings of the 2008 ONR Solid Mechanics Program Review, Marine Composites and Sandwich Structures, University of Maryland University College, Adelphi, MD, September 17-19, 2008, pp. 211-220.
3. Hoo Fatt, M.S., "Impact and Blast of Composite Sandwich Panels," in the Proceedings of the 2007 ONR Solid Mechanics Program Review, Marine Composites and Sandwich Structures, University of Maryland University College, Adelphi, MD, September 10-12, 2007, pp. 201-209.

Refereed Journals



Dynamic pulse buckling of composite shells subjected to external blast

Michelle S. Hoo Fatt^{*}, Sunil G. Pothula

Department of Mechanical Engineering, The University of Akron, Akron, OH 44325-3903, United States

ARTICLE INFO

Article history:

Available online 21 December 2009

Keywords:

Impulsive loading
Composite shell
Dynamic pulse buckling

ABSTRACT

Dynamic pulse buckling of woven E-Glass/Vinyl Ester and laminated E-Glass/Epoxy cylindrical shells subjected to uniform overpressure and asymmetric pressure pulse (side-on explosion) were examined. The solutions for the radial shell deformations were represented by Mathieu differential equations. The dynamic instability of the shells was determined from a Mathieu stability diagram. It was found that the stability of the shells depended on lay-up, aspect ratio as well as impulse distribution. The stable vibration response of the shells with side-on explosion compared well with finite element solutions using a Dynamic, Implicit analysis in ABAQUS Standard. First-ply failure of the woven E-Glass/Vinyl Ester shell with side-on explosion was predicted using a modified Hashin–Rotem failure criterion. It was shown that the thinner woven E-Glass/Vinyl Ester shells were more likely to fail by dynamic instability, whereas the thicker woven E-Glass/Vinyl Ester shells were more likely to fail by first-ply failure.

© 2009 Elsevier Ltd. All rights reserved.

1. Introduction

Laminated composite cylindrical shells have widespread applications in aerospace and marine industries. In some of these applications, the strength and stability of the composite cylindrical shell may be compromised by external pressure pulse loading, such as one caused by a nearby explosion. There are basically two types of failures that can occur when a laminated composite shell is subjected to external blast: (1) dynamic buckling or instability and (2) stable transient and vibratory response with possible ply-by-ply failure. Most of the papers written on the blast response of composite shells deal with shell vibration response and involve numerical solutions [1–3]. There is very little, if any, in the open literature on the dynamic stability of composite shells exposed to external blast. In addition to this, most of the solutions concerning the dynamic stability of shells involve uniformly-distributed pressure, which is either periodic or suddenly applied and kept constant (step loading). Neither of these dynamic loads describes the pressure pulse loading which results from a blast.

The dynamic stability of a composite shell under periodic loading was investigated by Bolotin [4], who introduced this as a problem involving parametric resonance. Bolotin used Fourier series to derive the vibration response of the shell in terms of Mathieu–Hill equations. He converted simple Mathieu–Hill equations into a standard form of generalized eigenvalue problems to study and compute the dynamic buckling loads of cylindrical shell. Birman and Simites [5] used a similar approach to examine the stability of long cylindrical sandwich shells subjected to uniform lateral

periodic pressure loading. With Sanders shell theory and a plane strain assumption, they investigated the dynamic stability of these vibrations through the solution of linearized equations for perturbed motion. Ganapathi and Balamurugan [6] studied the dynamic instability of composite circular cylindrical shells subjected to combined periodic axial/radial loading. They studied the effect of ply-angle, thickness, aspect ratio on the dynamic stability of the shell. They concluded that for a given shell the value of circumferential wave number plays an important role in predicting the dynamic instability region and the effect of pulsating pressure loads on the dynamic instability zone is significant, even for small load amplitudes. Schokker et al. [7] used the *p*-version finite element analysis and axisymmetric solid elements to compute the buckling and vibration modes of interior ring stiffened composite shell subjected to hydrostatic pressure loading. They found that the dynamic limit load of an imperfect composite cylindrical shell can be significantly lower than the static limit load.

Under blast loading, the external pressure is impulsive and can be non-uniformly distributed, depending on the stand-off distance of explosion source. The specific type of dynamic instability that occurs under impulsive loading is termed dynamic pulse buckling. Bisagani [8] has examined dynamic buckling of a composite shell under an impulsive axial compressive load, but analytical solutions for the composite shell under external, radial impulsive loading have not been given to date. Although the dynamic pulse buckling due to external pressure pulse has not been addressed for composite shells, it has been dealt with substantially for isotropic, metallic shells [9]. One of the earliest papers on the dynamic pulse buckling of an isotropic, elastic shell subjected to nearly uniform radial impulse was written by Goodier and McIvor [10]. This paper and many others involving pulse buckling were compiled cohesively

^{*} Corresponding author. Tel.: +1 330 972 6308; fax: +1 330 972 6027.
E-mail address: hoofatt@uakron.edu (M.S. Hoo Fatt).

Nomenclature

a	shell radius	X_T, Y_T	longitudinal and transverse tensile strength
a_n, b_n	Fourier coefficients of the normalized radial deflection	z	through-thickness coordinate
c_n, d_n	Fourier coefficients of the normalized tangential deflection	α	bending-to-membrane stiffness ratio
A_{ij}	membrane stiffness matrix	α_n, β_n	Fourier coefficients of the initial radial velocity
B_{ij}	coupling stiffness matrix	α_n, β_n	Fourier coefficients of the initial radial velocity
c	circumferential wave speed	$\gamma_{x\theta}$	in-plane shear strain
dS	differential shell surface area	ΔT	pulse duration
D_{ij}	bending stiffness matrix	ε_b	bending strain
E_{ij}	Young's modulus	ε_x	axial strain
G_{ij}	shear modulus	$\varepsilon_{x\theta}$	in-plane shear strain
h	shell thickness	ε_θ	hoop strain
I_{cr}	impulse for instability	$\varepsilon_{\theta m}$	mid-surface hoop strain
l	length of shell	$\zeta = w/a$	normalized radial deflection
L	Lagrangian	θ	circumferential coordinate
n	mode number in Fourier series	κ_x	bending curvature in axial direction
N	number of plies	$\kappa_{x\theta}$	twisting curvature
N_{ij}	membrane resistance	κ_θ	bending curvature in hoop direction
M_{ij}	bending moment resistance	κ_0	curvature in hoop direction at $\theta = 0$
p	pressure pulse	κ_π	curvature in hoop direction at $\theta = \pi$
p_o	pressure pulse amplitude	μ	Mathieu stability parameter
q_n	generalized Lagrangian coordinate	ν_{ij}	Poisson's ratio
Q_{ij}	transformed stiffness matrix	Π	total potential energy
r	radial coordinate	ρ	shell density
S_L, S_T	longitudinal and transverse shear strength	σ_x	axial stress
t	time	σ_θ	circumferential stress
T	kinetic energy	$\tau = ct/a$	normalized time
U	strain energy	$\tau_{x\theta}$	shear stress
v	tangential deflection	φ	deformed circumferential position
v_o	initial velocity amplitude	$\psi = v/a$	normalized circumferential deflection
w	radial deflection	Ω	Mathieu stability parameter
x	axial coordinate	$[\ast] = \partial[\ast]/\partial\tau$	normalized time derivative
X_C, Y_C	longitudinal and transverse compressive strength	$[\ast]' = \partial[\ast]/\partial\theta$	derivative with respect to θ

to explain the phenomenon of dynamic pulse buckling of isotropic, elastic–plastic structures in Ref. [9]. The present paper examines dynamic pulse buckling of a laminated composite shell subjected to impulsive pressure loads. In particular, the influence of shell anisotropy and pressure pulse asymmetry, such as one caused by a side-on explosion, are examined.

2. Problem formulation

Consider a long and thin, laminated composite cylinder of radius a and thickness h , subjected to impulsive pressure loading as shown in Figs. 1a–c. The composite shell may be subjected to uniformly-distributed impulsive pressure loads

$$p(t) = p_o \left[1 - \frac{t}{\Delta T} \right] \quad (1)$$

or an asymmetric impulsive pressure loads, such as one caused by a side-on explosions.

$$p(\theta, t) = \begin{cases} p_o \cos^2 \theta \left[1 - \frac{t}{\Delta T} \right], & |\theta| \leq \pi/2 \\ 0, & |\theta| > \pi/2 \end{cases} \quad (2)$$

where p_o is the peak pressure, ΔT is the pulse duration and t is time.

3. Shell kinematics

The analysis is limited to shells that are thin, $a/h > 10$, and long, $l/a > 20$, where l is the length of the shell. The later assumption

combined with the fact that the pressure load do not vary along the shell longitudinal axis allows us to consider the cylinder as a ring deforming under plane strain conditions. Following the plane strain assumptions $\varepsilon_x = 0$, $\varepsilon_{x\theta} = 0$, $\kappa_x = 0$, and $\kappa_{x\theta} = 0$. The hoop strain ε_θ in the shell is

$$\varepsilon_\theta = z\kappa_\theta \quad (3)$$

where $\varepsilon_{\theta m}$ is the mid-surface strain, κ_θ is the change in curvature of the shell and is z the radial coordinate in shell measured from the mid-surface of the shell. The mid-surface hoop strain of the shell is found by considering the differential arc length before and after deformation shown in Fig. 2. Points on the mid-surface of the cylindrical shell have polar coordinates a, θ . After the deformation, points have polar coordinates r, φ in the deformed configuration. The cylindrical shell has radial displacement $w(\theta, t)$ and angular displacement $\psi(\theta, t)$ where

$$w = a - r \quad (4)$$

and

$$\frac{v}{a} = \phi - \theta \quad (5)$$

The mid-surface strain is the change in length of the element divided by its undeformed length $ad\theta$:

$$\varepsilon_{\theta m} = \frac{1}{ad\theta} \left\{ \left[\left(\frac{dr}{d\theta} d\theta \right)^2 + \left(r \frac{d\phi}{d\theta} d\theta \right)^2 \right]^{\frac{1}{2}} - ad\theta \right\} \quad (6)$$

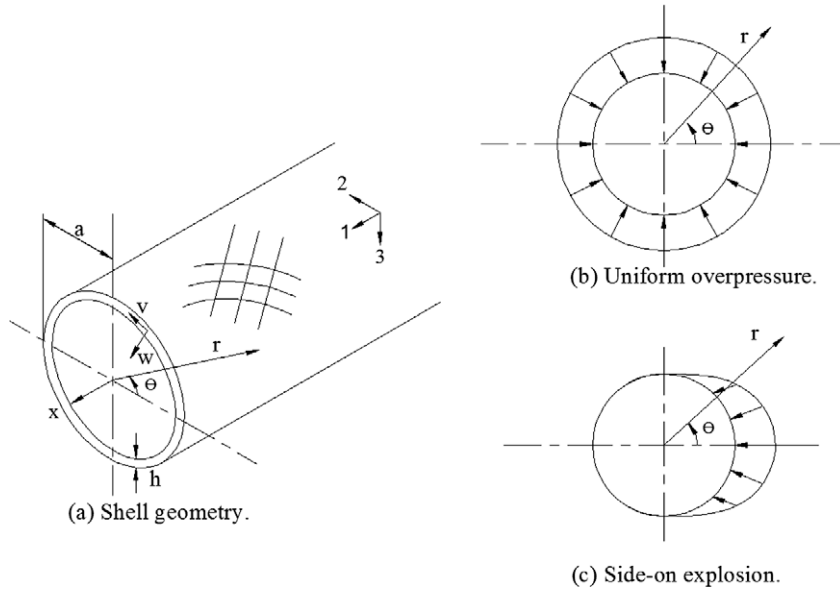


Fig. 1. Composite cylinder under external pressure pulse loading: (a) shell geometry, (b) uniform overpressure, and (c) side-on explosion.

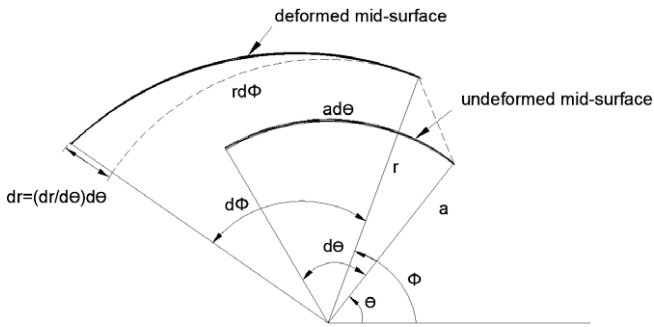


Fig. 2. Shell kinematics.

Differentiating Eqs. (4) and (5) give

$$\frac{dw}{d\theta} = -\frac{dr}{d\theta} \quad (7)$$

$$\frac{d\phi}{d\theta} = 1 + \frac{1}{a} \frac{dv}{d\theta} \quad (8)$$

Substituting Eqs. (7) and (8) into Eqs. (6) gives

$$\varepsilon_{\theta m} = \frac{1}{a} \left[\left(\frac{\partial w}{\partial \theta} \right)^2 + (a-w)^2 \left(1 + \left(\frac{1}{a} \frac{\partial v}{\partial \theta} \right)^2 \right) \right]^{\frac{1}{2}} - 1 \quad (9)$$

The change in shell curvature is

$$\kappa_{\theta} = \frac{1}{a^2} \left(\frac{\partial^2 w}{\partial \theta^2} + w \right) \quad (10)$$

4. Equations of motion

It is convenient to derive the equations of motion for the shell using the Lagrangian method. In this method, the Lagrangian is $L = T - \Pi$, where T is the kinetic energy and Π is the total potential energy of the shell. The kinetic energy of the shell is given by

$$T = \frac{1}{2} \rho h \int_0^{2\pi} \left[\left(\frac{\partial w}{\partial t} \right)^2 + \left(\frac{\partial v}{\partial t} \right)^2 \right] a d\theta \quad (11)$$

The total potential energy of the shell is the sum of the strain energy U and potential of the work done by external forces. For an impulsively loaded shell, the total potential energy of the shell consists only of strain energy because energy is transferred from the pressure pulse as an initial velocity or impulse. There are no loads acting on the shell during deformation and $\Pi = U$.

4.1. Strain energy of a laminated shell

The elastic strain energy of a laminated composite shell is given by

$$U = \frac{1}{2} \int_S (N_x \varepsilon_{xm} + N_{\theta} \varepsilon_{\theta m} + N_{x\theta} \varepsilon_{x\theta} + M_x \kappa_x + M_{\theta} \kappa_{\theta} + M_{x\theta} \kappa_{x\theta}) dS \quad (12)$$

where $dS = a d\theta dx$ is the differential shell surface area and the membrane resistance ($N_x, N_{\theta}, N_{x\theta}$) and bending moment resistance ($M_x, M_{\theta}, M_{x\theta}$) are given in terms of mid-surface strains ($\varepsilon_{xm}, \varepsilon_{\theta m}, \varepsilon_{x\theta m}$) and curvature ($\kappa_x, \kappa_{\theta}, \kappa_{x\theta}$) by the following:

$$\begin{Bmatrix} N_x \\ N_{\theta} \\ N_{x\theta} \\ M_x \\ M_{\theta} \\ M_{x\theta} \end{Bmatrix} = \begin{bmatrix} A_{11} & A_{12} & A_{16} & B_{11} & B_{12} & B_{16} \\ A_{12} & A_{22} & A_{26} & B_{12} & B_{22} & B_{26} \\ A_{16} & A_{26} & A_{66} & B_{16} & B_{26} & B_{66} \\ B_{11} & B_{12} & B_{16} & D_{11} & D_{12} & D_{16} \\ B_{12} & B_{22} & B_{26} & D_{12} & D_{22} & D_{26} \\ B_{16} & B_{26} & B_{66} & D_{16} & D_{26} & D_{66} \end{bmatrix} \begin{Bmatrix} \varepsilon_{xm} \\ \varepsilon_{\theta m} \\ \varepsilon_{x\theta m} \\ \kappa_x \\ \kappa_{\theta} \\ \kappa_{x\theta} \end{Bmatrix} \quad (13)$$

where $A_{ij} = \sum_{k=1}^N (\bar{Q}_{ij})_k (z_k - z_{k-1})$ is the membrane stiffness, $B_{ij} = \frac{1}{2} \sum_{k=1}^N (\bar{Q}_{ij})_k (z_k^2 - z_{k-1}^2)$ is the coupling stiffness, $D_{ij} = \frac{1}{3} \sum_{k=1}^N (\bar{Q}_{ij})_k (z_k^3 - z_{k-1}^3)$ is the bending stiffness, \bar{Q}_{ij} is the reduced stiffness matrix, and N is the total number of plies (the subscripts ij refer to the composite material directions 1, 2, 6). Following the plane strain assumption, the elastic strain energy of the long, composite shell reduces to

$$U = \frac{1}{2} \int_0^{2\pi} (A_{22} \varepsilon_{\theta m}^2 + B_{12} \varepsilon_{\theta m} \kappa_{\theta} + B_{22} \varepsilon_{\theta m} \kappa_{\theta} + D_{22} \kappa_{\theta}^2) a d\theta \quad (14)$$

A special class of laminated composite shells for which $B_{12} = 0$ and $B_{22} = 0$, is examined in this paper. These include shells that are orthotropic, mid-plane symmetric as well as those consisting of

anti-symmetric angle-ply laminates. For these types of laminated composite shells, the elastic strain energy becomes

$$U = \frac{1}{2} \int_0^{2\pi} (A_{22}\epsilon_{\theta m}^2 + D_{22}\kappa_{\theta}^2) a d\theta \quad (15)$$

However, the theory is not restricted to only these classes of shells. Other laminated shells which do not fall into the above-mentioned category may still have $B_{12} = 0$ and $B_{22} = 0$. An example of this is a balanced quasi-isotropic shell with a shell lay-up of $[60^\circ/0^\circ/-60^\circ]$.

4.2. Initial velocity

The initial velocity imparted to the shell from the impulsive pressure is found from conservation of momentum

$$\rho h \frac{dw}{dt}(\theta, 0) = \int_0^{\Delta T} p(\theta, t) dt \quad (16)$$

Substituting the pressure pulse defined in Eqs. (1) and (2) into Eq. (16) gives

$$\frac{dw}{dt}(\theta, 0) = v_o \quad (17)$$

for the uniformly distributed load and

$$\frac{dw}{dt}(\theta, 0) = v_o \cos^2 \theta \quad (18)$$

for the side-on pressure pulse, where $v_o = \frac{p_o \Delta T}{2\rho h}$ is the amplitude of the distributed velocity field.

4.3. Normalized variables

Define a normalized radial deflection $\zeta = \frac{w}{a}$, tangential deflection $\psi = \frac{v}{a}$ and time $\tau = \frac{ct}{a}$, where $c = \sqrt{\frac{A_{22}}{\rho h}}$ is the wave speed in the circumferential direction.

The kinetic and potential energy in terms of the above normalized variables are

$$T = \frac{1}{2} A_{22} a \int_0^{2\pi} (\dot{\zeta}^2 + \dot{\psi}^2) d\theta \quad (19)$$

where $[\dot{\cdot}] = \partial[\cdot]/\partial\tau$ and

$$U = \frac{1}{2} A_{22} a \int_0^{2\pi} [(\psi' - \zeta)^2 + (\psi' - \zeta)(\zeta'^2 - 2\zeta\psi') + \alpha^2(\zeta'' + \zeta)^2] d\theta \quad (20)$$

where $\alpha^2 = D_{22}/(a^2 A_{22})$ and $[\cdot]' = \partial[\cdot]/\partial\theta$.

The normalized initial velocity are

$$\dot{\zeta}(\theta, 0) = \frac{v_o}{c} \quad (21)$$

for the uniformly pressure loaded shell and

$$\dot{\zeta}(\theta, 0) = \frac{v_o}{c} \cos^2 \theta \quad (22)$$

for the shell with side-on pressure loading.

5. Fourier series solution

Assume Fourier series representation of normalized radial and tangential displacement

$$\zeta = a_0(\tau) + \sum_{n=1}^{\infty} [a_n(\tau) \cos n\theta + b_n(\tau) \sin n\theta] \quad (23)$$

and

$$\psi = \sum_{n=1}^{\infty} [c_n(\tau) \cos n\theta + d_n(\tau) \sin n\theta] \quad (24)$$

where n is the mode number. The term at $n=0$ or $a_0(\tau)$ is the breathing mode whereby the shell goes in and out of hoop compression. The term at $n=1$ denotes rigid-body motion, while the terms for $n \geq 2$ are bending modes.

Inextensional deformations of thin rings and shells originated from Lord Rayleigh [11], when he showed that displacement due to the extension of mid-surface are negligibly small in comparison with displacements due to bending. Goodier and McIvor [10] later demonstrated that the amplitude of the extensional modes were indeed negligible compared to the amplitude of the bending modes in studying the stability of an isotropic elastic shell subjected to uniform radial impulse. Following the inextensionality condition, $\psi' = \zeta - a_0$. This condition implies that $c_n = -b_n/n$ and $d_n = a_n/n$.

Substituting Eqs. (23) and (24) into Eqs. (19) and (20) and using inextensionality condition give

$$T = \pi A_{22} a \left[a_0^2 + \frac{1}{2} \sum_{n=1}^{\infty} \left(\frac{n^2 + 1}{n^2} \right) (\dot{a}_n^2 + \dot{b}_n^2) \right] \quad (25)$$

for the kinetic energy

$$U = \pi A_{22} a \left\{ a_0^2 (1 + \alpha^2) + \frac{1}{2} \sum_{n=1}^{\infty} [\alpha^2 (n^2 - 1)^2 - (n^2 - 2)a_0] (a_n^2 + b_n^2) \right\} \quad (26)$$

for the strain energy. Note that the integration in Eqs. (19) and (20) are simplified because ζ and ψ are orthogonal over the integration limits. Since deflections are small, terms of order higher than a_n^2 and b_n^2 have been neglected. Lagrange's equations of motion for the shell is given by

$$\frac{d}{d\tau} \left(\frac{\partial T}{\partial \dot{q}} \right) + \frac{\partial U}{\partial q} = 0 \quad (27)$$

where the generalized Lagrangian coordinate q_n represents a_n and b_n .

Substituting Eqs. (25) and (26) into Eq. (27) gives the solution for the breathing mode ($n=0$)

$$\ddot{a}_0 + a_0(1 + \alpha^2) - \frac{1}{4} \sum_{n=1}^{\infty} (n^2 - 2)(a_n^2 + b_n^2) = 0 \quad (28)$$

and for modes of $n \geq 1$

$$\ddot{a}_n + \frac{n^2}{n^2 + 1} [(n^2 - 1)^2 \alpha^2 - (n^2 - 2)a_0] a_n = 0 \quad (29)$$

and

$$\ddot{b}_n + \frac{n^2}{n^2 + 1} [(n^2 - 1)^2 \alpha^2 - (n^2 - 2)a_0] b_n = 0 \quad (30)$$

The breathing mode is in general coupled with the rigid-body motion and bending modes. The above equations of motion are solved with initial conditions:

$$\zeta(\theta, 0) = 0 \quad \text{and} \quad \dot{\zeta}(\theta, 0) = \alpha_0 + \sum_{n=1}^{\infty} [\alpha_n \cos n\theta + \beta_n \sin n\theta] \quad (31)$$

where $\dot{a}_0(0) = \alpha_0$, $\dot{a}_n(0) = \alpha_n$, $\dot{b}_n(0) = \beta_n$, $a_0(0) = 0$, $a_n(0) = 0$, and $b_n(0) = 0$.

When deflections are small, a_n^2 and b_n^2 are negligible compared to a_n and b_n .

In addition, $\alpha^2 \ll 1$ because it is on the order of $(h/a)^2$. Eqs. (28)–(30) then reduce to

$$\ddot{a}_0 + a_0 = 0 \quad (32)$$

$$\ddot{a}_n + (\Omega_n - \mu_n \sin \tau) a_n = 0, \quad n \geq 1 \quad (33)$$

$$\ddot{b}_n + (\Omega_n - \mu_n \sin \tau) b_n = 0, \quad n \geq 1 \quad (34)$$

where $\Omega_n = \frac{\alpha^2 n^2 (n^2 - 1)^2}{(n^2 + 1)}$ and $\mu_n = \frac{n^2 (n^2 - 2)}{(n^2 + 1)} \alpha_0$.

The differential equations described in Eqs. (33) and (34) are Mathieu equations. The interested reader may find applications of Mathieu equations in dynamic stability analysis and nonlinear vibrations of several other mechanical systems discussed in Refs. [4,12], respectively.

An n th mode solution may become unstable for certain values of μ_n and Ω_n in Eqs. (33) and (34). Stability of these linear differential equations with periodic coefficients is analyzed using Floquet theory [13]. A MATLAB program was written to determine the values of μ_n and Ω_n that would give stable and unstable modal solutions, and the results are plotted in Fig. 3. Here values of μ_n and Ω_n that give stable solutions of a_n and b_n lie in the shaded regions, while values of μ_n and Ω_n that give unstable solutions of them lie in the un-shaded regions. The Mathieu stability diagram is used to examine dynamic stability of the shell with uniform and side-on pressure pulse loadings in the next section.

5.1. Uniform pressure

Under uniform pressure load, there can be no rigid-body motion of the shell. Hence, the terms involving $n = 1$ do not exist and the solution for the shell is given in terms of its Fourier series

$$\zeta = a_0(\tau) + \sum_{n=2}^{\infty} [a_n(\tau) \cos n\theta + b_n(\tau) \sin n\theta] \tag{35}$$

The initial velocity condition becomes

$$\dot{\zeta}(\theta, 0) = \alpha_0 + \sum_{n=2}^{\infty} [\alpha_n \cos n\theta + \beta_n \sin n\theta] \tag{36}$$

For the uniform velocity, $\alpha_0 = \frac{v_0}{c}$. The coefficients α_n and β_n will be non-zero because of shell imperfections, which are not considered at this time.

5.2. Side-on pressure

For the side-on distributed pressure pulse described by Eq. (2), the shell deforms and moves with rigid-body motion ($n = 1$ term is not neglected) and only the cosine terms of the Fourier series are retained because of load symmetry, i.e., $b_n = 0$:

$$\zeta = a_0(\tau) + \sum_{n=1}^{\infty} a_n(\tau) \cos n\theta \tag{37}$$

The centroid of the shell will have a non-zero velocity in a fixed plane and motion will be referred to a plane travelling with it. The initial velocity of the shell is then written as

$$\dot{\zeta}(\theta, 0) = \alpha_0 + \frac{1}{2} \alpha_1 \cos \theta + \sum_{n=2}^{\infty} \alpha_n \cos n\theta \tag{38}$$

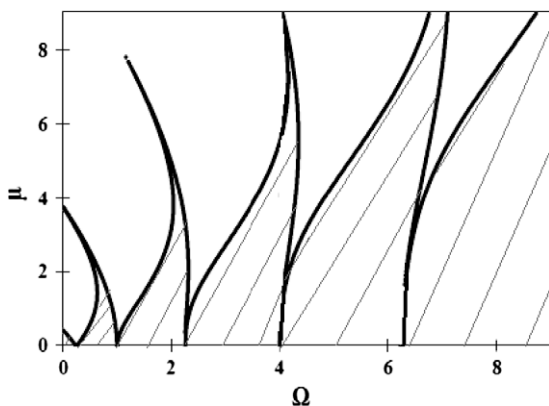


Fig. 3. Mathieu stability diagram (stable regions are shaded).

The Fourier coefficients for the initial velocity in Eq. (22) gives $\alpha_0 = \frac{1}{4} \frac{v_0}{c}$ and

$$\alpha_n = \frac{1}{2\pi} \left\{ \frac{2}{n} \sin\left(\frac{n\pi}{2}\right) + \frac{1}{(n+2)} \sin\left(\frac{\pi(n+2)}{2}\right) + \frac{1}{(n-2)} \sin\left(\frac{\pi(n-2)}{2}\right) \right\} \frac{v_0}{c}, \quad n \geq 1 \tag{39}$$

With the exception of the $n = 2$ term, all even terms vanish in Eq. (39). Once again the stability of the solution depends on the values of μ_n and Ω_n . If these lie in the stable regions of the Mathieu stability diagram, the shell undergoes deformation with each mode shape. For a brittle, laminated composite shell, the shell may also fail due to excessive deformation even if does not undergo dynamic pulse buckling.

6. Dynamic stability

The stability of the composite shell when it is subjected to a uniform overpressure and side-on explosion is examined in the next sections. Four laminated shell geometries are chosen: (1) an orthotropic shell made of woven roving E-Glass/Vinyl Ester and three E-Glass/Epoxy shells with (2) a symmetric, layup ($[60^\circ/-45^\circ]_s$), (3) an anti-symmetric layup ($75^\circ/-15^\circ/15^\circ/-75^\circ$) and (4) a quasi-isotropic layup ($60^\circ/0^\circ/-60^\circ$). Each of the cylinders has a total shell thickness $h = 4$ mm and a shell radius $a = 80$ mm (or an aspect ratio of $a/h = 20$), unless specified otherwise. Material properties for the woven roving E-Glass/Vinyl Ester [14] and uni-directional E-Glass/Epoxy [15] are given in Table 1.

6.1. Uniform overpressure

First consider the stability of the woven roving E-Glass/Vinyl Ester, orthotropic shell. With the geometric and material properties specified above, $\alpha^2 = D_{22}/(E_{22}a^2) = 2.08e^{-4}$ for the orthotropic shell. This value is used to generate coordinates of μ_n and Ω_n for three different normalized velocity v_0/c on the Mathieu stability diagram shown in Figs. 4a and b. For any given value of v_0/c , μ_n increases roughly parabolically with Ω_n but the higher modes are less likely to fall in the unstable (un-shaded) regions. However, the instability also depends on Ω_n . The region in which modes will most likely become unstable lie near $\Omega = 0.25$. For this particular orthotropic shell, Mode 6 would be the first unstable mode since

Table 1 Material properties of 0/90 woven roving E-glass/Vinyl Ester and uni-directional E-Glass/Epoxy.

Material	0/90 Woven roving E-Glass/Vinyl Ester	Uni-directional E-Glass/Epoxy
Density (kg/m ³)	1391.3	2050
E ₁₁ (GPa)	17	48
E ₂₂ (GPa)	17	12
E ₃₃ (GPa)	7.48	12
ν_{12}	0.13	0.19
ν_{23}	0.28	0.26
ν_{13}	0.28	0.19
ν_{31}	0.12	0.05
G ₁₂ = G ₂₁ (GPa)	4.0	6
G ₂₃ = G ₃₂ (GPa)	1.73	5
G ₁₃ = G ₃₁ (GPa)	1.73	6
X _T (MPa)	270	1020
X _C (MPa)	200	490
Y _T (MPa)	270	8
Y _C (MPa)	200	78
Z _T (MPa)	23.22	8
Z _C (MPa)	343.5	78
S _c (MPa)	40	23
S _T (MPa)	31.6	66

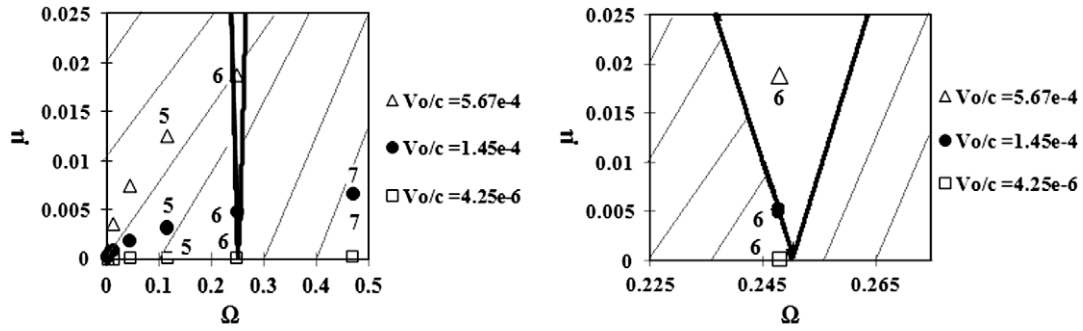


Fig. 4. Stability diagrams for woven E-Glass/Vinyl Ester shell with uniform overpressure and increasing v_o/c : (a) first seven modes and (b) region near $\Omega = 0.25$.

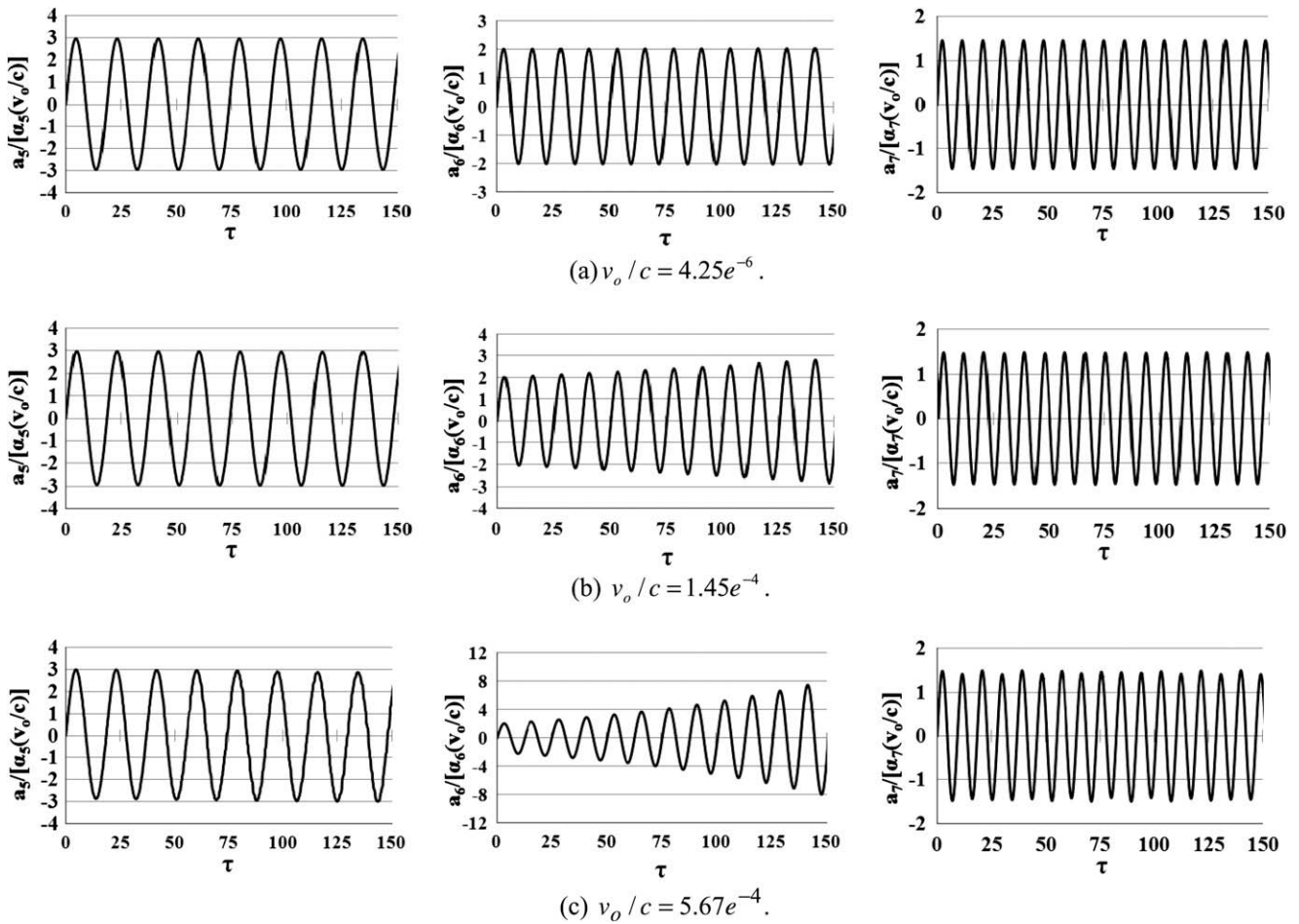


Fig. 5. Response of Modes 5–7 for woven E-Glass/Vinyl Ester shell with uniform overpressure: (a) $v_o/c = 4.25e^{-6}$, (b) $v_o/c = 1.45e^{-4}$ and (c) $v_o/c = 5.67e^{-4}$.

$\Omega_6 = 0.2478$. As one increases v_o/c , points on the Mathieu stability diagram shift upwards until the point at $\Omega_6 = 0.2478$ just becomes unstable. This is clearly shown by the solid circle in Fig. 4b. Thus Mode 6 just becomes unstable at a critical impulse velocity of $v_o/c = 1.45e^{-4}$. The response of Mode 6 and its adjacent modes, Modes 5 and 7, are shown in Fig. 5b for $v_o/c = 1.45e^{-4}$. As one can see, Modes 5 and 7 exhibit stable oscillations, but the amplitude of oscillations of Mode 6 increases without bound. Mode 6 will always be unstable if the impulse velocity is greater than this critical value, as observed when $v_o/c = 5.67e^{-4}$. The response of Modes 5, 6 and 7 for the three values of v_o/c are shown in Figs. 5a and c for contrast. If the impulse velocity is less than this critical value, sta-

ble oscillations are observed and the shell undergoes elastic vibrations.

6.1.1. Effect of layup

The stability diagrams for the symmetric, anti-symmetric and quasi-isotropic E-Glass/Epoxy shells with $h = 4$ mm and a shell radius $a = 80$ mm are given in Fig. 6. Even though all these shells have the same geometry and are made from the same uni-directional E-Glass/Epoxy ply, the different layups result in different α^2 and c values as shown in Table 2. Mode 6 is still the critical mode for instability but its proximity to $\Omega = 0.25$ depends on α^2 . According to Fig. 6, the anti-symmetric layup gives the highest critical v_o/c .

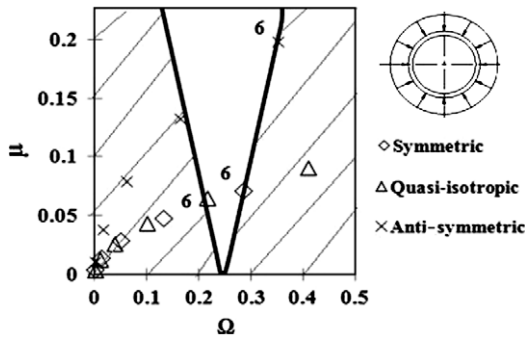


Fig. 6. Stability diagrams for E-Glass/Epoxy shells with various layups and uniform overpressure.

Table 2
Critical buckling impulse for composite shells with uniform overpressure.

	c (m/s)	α^2	I_{cr} (Pa s)	Unstable modes
Orthotropic E-Glass/Vinyl Ester	3525	$2.08e^{-4}$	3.5	6
Symmetric E-Glass/Epoxy ([60°/−45°] _s)	3723	$2.39e^{-4}$	65.3	6
Anti-symmetric E-Glass/Epoxy (75°/−15°/15°/−75°)	3763	$2.95e^{-3}$	189.0	6
Quasi-isotropic E-Glass/Epoxy (60°/0°/−60°)	4321	$1.82e^{-4}$	69.6	6

However the critical impulse for each shell I_{cr} also depends on the circumferential wave speed, c which changes with shell layup. The critical impulse for the shell is calculated from the formula $I_{cr} =$

$p_0 \Delta T / 2 = \rho h v_0$, and is listed in Table 2 for the three E-Glass/Epoxy shells together with the woven E-Glass/Vinyl Ester shell. The anti-symmetric E-Glass/Epoxy shell still has the highest buckling resistance of all three layups.

6.1.2. Effect of aspect ratio

Points on the Mathieu stability diagram shift to the left as α^2 decreases and to the right as α^2 increases. Since the shell becomes thinner as α^2 decreases, thinner shells are more likely to become unstable as the higher modes shift leftwards into the unstable region of Mathieu stability diagram. Figs. 7a and b show how aspect ratio affects the stability of the woven E-Glass/Vinyl Ester shell. The unstable mode is listed for each aspect ratio in Figs. 7a and b. The shells with $a/h = 10, 20$ and 40 become unstable at modes 6, 6, and 8, respectively. The thinner shells with $a/h = 80, 100$, and 200 have become unstable at higher modes of 11, 13 and 18, respectively.

In general, the critical impulse increases with lower aspect ratios (thicker shells). Thicker shells have greater bending resistance and should buckle at higher loads. However, the complicated nature of Mathieu stability diagram results in exceptions to this rule. For the orthotropic E-Glass/Vinyl Ester shell, the critical impulse velocity is minimum when $a/h = 20$ because Ω_6 is very close to $\Omega = 0.25$. The critical impulse velocity for the shell with $a/h = 40$ is higher than for the shell with $a/h = 20$ even though it is thinner. The variation of the critical impulse I_{cr} with shell aspect ratio is shown in Fig. 8 for the E-Glass/Epoxy shell with the three different layups. The anti-symmetric layup has a very visible minimum I_{cr} at $a/h = 10$. The symmetric and quasi-isotropic layups also appear to have I_{cr} that are below the general trend at $a/h = 40$ and $a/h = 80$, respectively.

6.2. Side-on pressure

The Fourier coefficients for even modes greater than 2 are zero with the side-on pressure described by Eq. (2), and this will affect

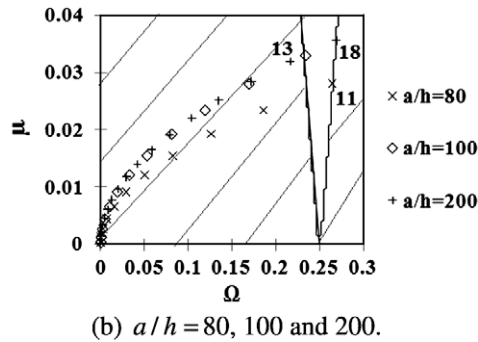
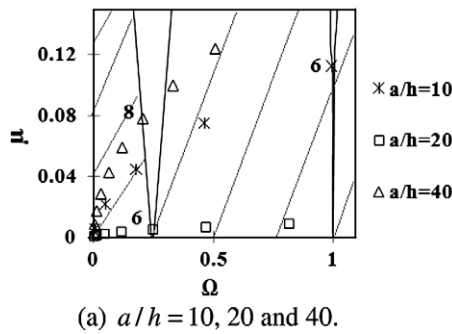


Fig. 7. Stability diagrams for woven E-Glass/Vinyl Ester shell with various aspect ratio and uniform overpressure: (a) $a/h = 10, 20, 40$ and (b) $a/h = 80, 100, 200$.

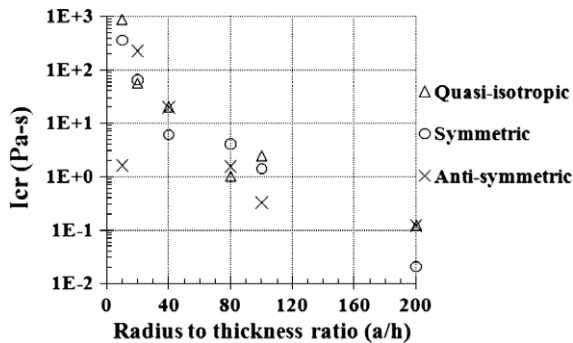


Fig. 8. Critical buckling impulse v_0 . Aspect ratio for E-Glass/Epoxy shells with various layups and uniform overpressure.

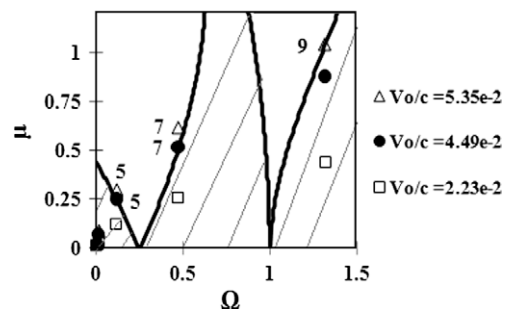


Fig. 9. Stability diagrams for woven E-Glass/Vinyl Ester shell with side-on pressure pulse and increasing v_0/c .

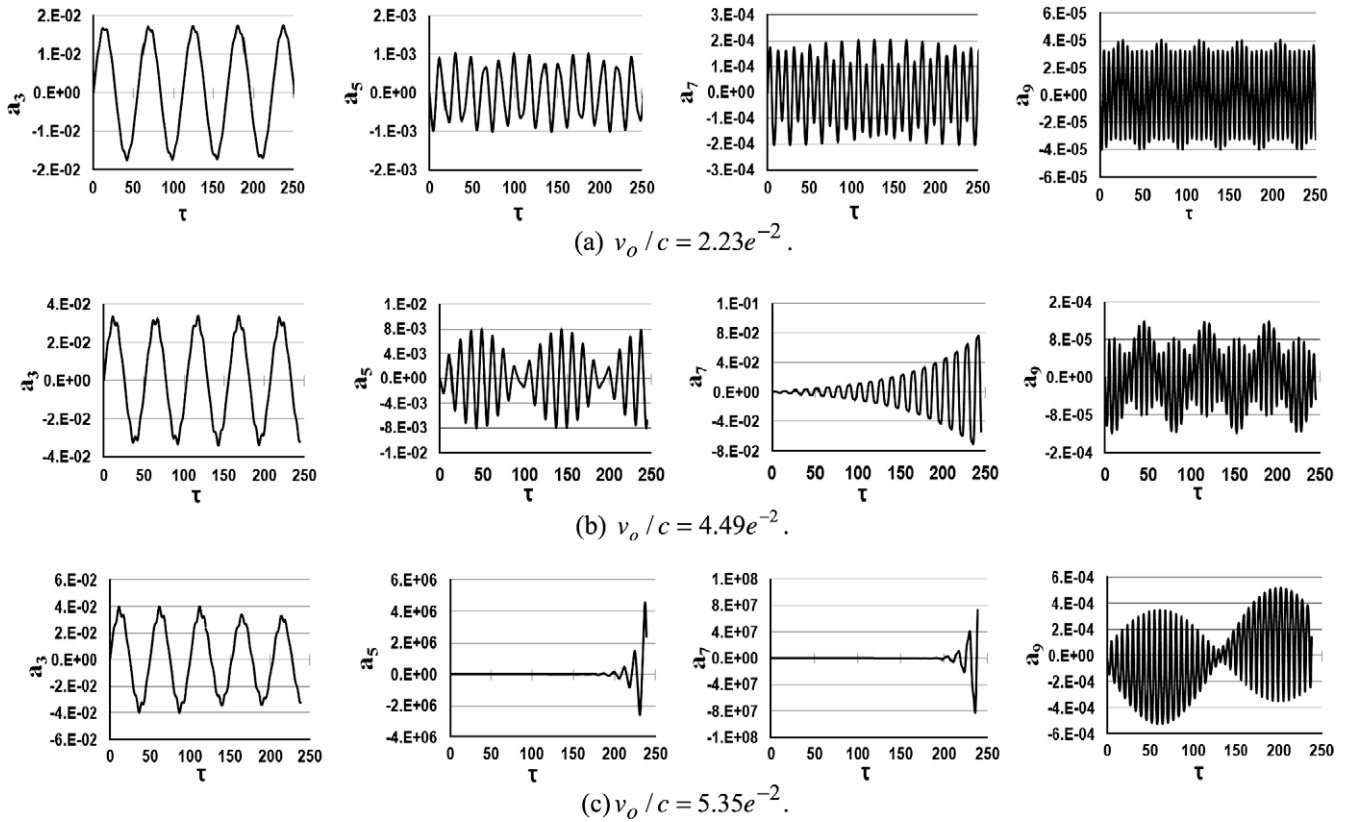


Fig. 10. Response of Modes 3, 5, 7, and 9 for woven E-Glass/Vinyl Ester shell with side-on pressure pulse: (a) $v_o/c = 2.23e^{-2}$, (b) $v_o/c = 4.49e^{-2}$ and (c) $v_o/c = 5.35e^{-2}$.

stability of the shell since some Ω_n values do not exist. For instance, in the woven E-Glass/Vinyl Ester, orthotropic shell, the fifth and seventh mode both just become unstable when $v_o/c = 4.49e^{-2}$ as shown in Fig. 9. Figs. 10a–c show the response for the Modes 3, 5, 7, and 9 with impulse velocities below and above this threshold value. When $v_o/c = 2.23e^{-2}$, all modes are stable. At $v_o/c = 4.49e^{-2}$, Mode 7 is unstable and Mode 5 shows a beating phenomenon and is on the verge of unstable oscillations. At $v_o/c = 5.35e^{-2}$, Modes 5 and 7 are unstable while Mode 9 begins to show the same beating phenomenon as Mode 5 did at $v_o/c = 4.49e^{-2}$. As seen in Fig. 9, that Mode 9 lies on the Mathieu stability boundary when $v_o/c = 5.35e^{-2}$. The critical impulse for buckling instability for this shell corresponds to $v_o/c = 4.49e^{-2}$ or $I_{cr} = 882$ Pa s, which is much higher than the critical impulse for the same shell under uniform overpressure. Thus pressure pulse distribution can affect the buckling resistance of the shell.

6.2.1. Effect of layup

The stability diagram for the various layups of E-glass/Epoxy shells are given in Fig. 11, which also indicates which modes are unstable. Note that the unstable modes are not the same for each shell. Table 3 summarized the critical impulse and unstable modes for each shell. Here it is shown that the symmetric E-Glass/Epoxy has the highest buckling strength for the case of side-on pressure. This is in contrast to the anti-symmetric layup for the case of uniform overpressure.

6.2.2. Effect of aspect ratio

The variation of I_{cr} with aspect ratio for all the various layups for the E-Glass/Epoxy shell are shown in Fig. 12. As in the case of uniform overpressure, the critical buckling impulse is a complicated function of shell aspect ratio and layup. In general, the critical buckling impulse decreases as the aspect ratio increases (thinner shells). However, anomalies to this rule because of the complicated nature of the Mathieu stability diagram. For instance, in the case of the anti-symmetric layup, the critical buckling impulse of the shell with an aspect ratio of 80 is lower than that for

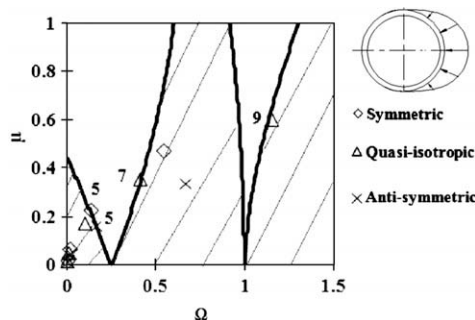


Fig. 11. Stability diagrams for E-Glass/Epoxy shells with various layups and side-on pressure pulse.

Table 3
Critical buckling impulse for composite shells with side-on pressure pulse.

	c (m/s)	α^2	I_{cr} (Pa s)	Unstable modes
Orthotropic E-Glass/Vinyl Ester	3525	$2.08e^{-4}$	882	5,7
Symmetric E-Glass/Epoxy ([60°/−45°] _s)	3723	$2.39e^{-4}$	1247	5
Anti-symmetric E-Glass/Epoxy (75°/−15°/15°/−75°)	3763	$2.95e^{-4}$	902	5
Quasi-isotropic E-Glass/Epoxy (60°/0°/−60°)	4321	$1.82e^{-4}$	1090	7,9

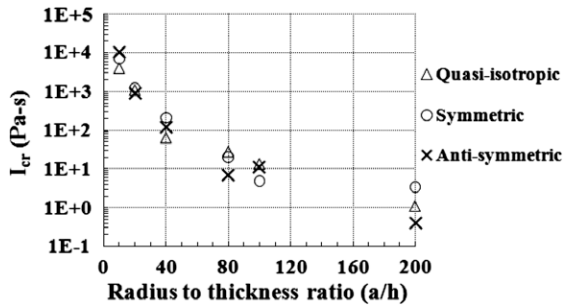


Fig. 12. Critical buckling impulse ν . Aspect ratio for E-Glass/Epoxy shells with various layups and side-on pressure pulse.

aspect ratio of 100, even though it is a thicker shell. Another point of interest is that at a given aspect ratio, I_{cr} depends on shell lay-up but the dependency varies from one aspect ratio to another. For instance, at an aspect ratio of 100, the anti-symmetric shell has the highest buckling resistance, but at an aspect ratio of 200, it has the lowest.

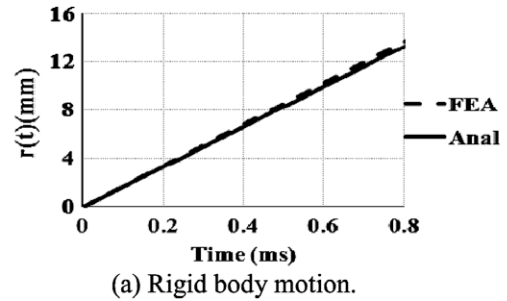
7. Shell vibrations and failure

Stable shell vibrations result if the impulse is below the critical buckling value. The behavior of the woven E-Glass/Vinyl Ester shell (radius $a = 80$ mm and thickness $h = 4$ mm) subjected to the side-on pressure pulse is examined in this section. The radial shell deflections are represented by the Fourier series expression in Eq. (37). An impulse with $p_0 = 250$ MPa and $\Delta T = 3.5 \mu s$ is chosen so that μ_n and Ω_n occur in the stable region of the Mathieu stability diagram (this shell buckles when $p_0 = 504$ MPa and $\Delta T = 3.5 \mu s$). The rigid-body motion and radial deformation history at $\theta = 0^\circ, 90^\circ$ and 180° are shown in Figs. 13a and b. The peak radial deformation was found to occur at approximately 0.77 ms, which is a quarter period of the shell response. The transient shell deformation profiles are shown for this case in Fig. 14. These analytical solutions are compared to finite element predictions using ABAQUS Standard, which are discussed in the next section.

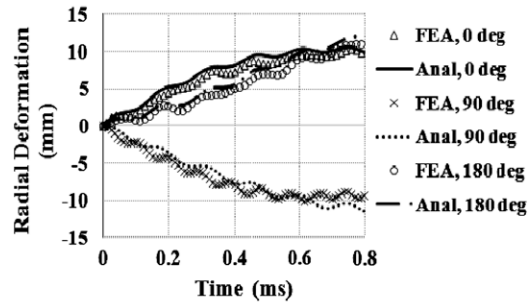
7.1. Finite element analysis

The numerical implementation involved Dynamic, Implicit analysis with ABAQUS Standard. Dynamic, Explicit analysis, although less computationally expensive, could not be used for this type of problem because of numerical damping used to stabilize the explicit algorithm in ABAQUS Explicit. The direct-integration method provided for Dynamic, Implicit analysis in ABAQUS Standard is the Hilber–Hughes Taylor operator, which is an extension of the trapezoidal rule. Automatic time increment with specified half-step residual was used. A parametric study was done to determine the appropriate size of the half-step residual that would yield accurate results. No numerical damping was specified in the problem.

The FEA model of the cylinder in plane strain is the two-dimensional ring shown in Fig. 15. Continuum plane strain elements with full integration (CPE4) were chosen in order to account for three-dimensional shell material properties as well as any variation in ply orientation or layup. A total of elements 6000 were used; there were four elements through the shell thickness (see Fig. 15). The composite material properties were specified in a local cylindrical coordinate (RTZ) according to the ABAQUS User Manual, Version 6.7 [16]. Specific details of the FEA, including special considerations for entering material orientation, can be found in Pothula [17].



(a) Rigid body motion.



(b) Deformation at $\theta = 0, 90$ and 180 degrees.

Fig. 13. Transient response of woven E-Glass/Vinyl Ester shell with side-on pressure pulse; $p_0 = 250$ MPa, $\Delta T = 3.5 \mu s$: (a) rigid-body motion, $r(t)$ and (b) radial deformation at $\theta = 0^\circ, 90^\circ$ and 180° .

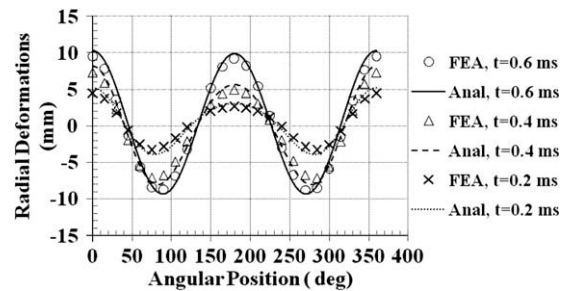


Fig. 14. Transient radial deformation profiles of the woven E-Glass/Vinyl Ester shell with side-on pressure pulse; $p_0 = 250$ MPa, $\Delta T = 3.5 \mu s$.

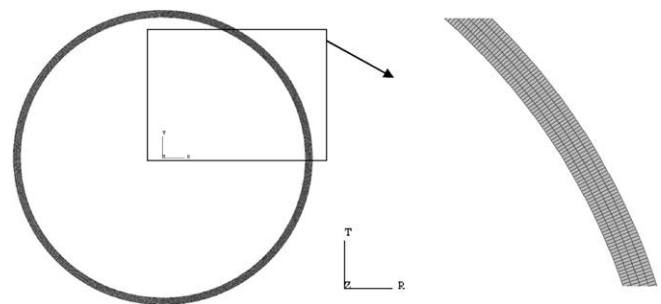


Fig. 15. Finite element model of cylinder in plane strain.

The side-on pressure pulse with $p_0 = 250$ MPa and $\Delta T = 3.5 \mu s$ was applied to the orthotropic, woven E-Glass/Vinyl ester shell discussed in the previous section. Comparisons of the radial deformation at $\theta = 0^\circ, 90^\circ$ and 180° from analytical and FEA results are shown in Fig. 13. The difference between the analytical and FEA results is 7%. The analytical and FEA predictions of the radial shell deformation for the pressure pulse at 250 MPa also compared very well to each other, as shown in Fig. 14.

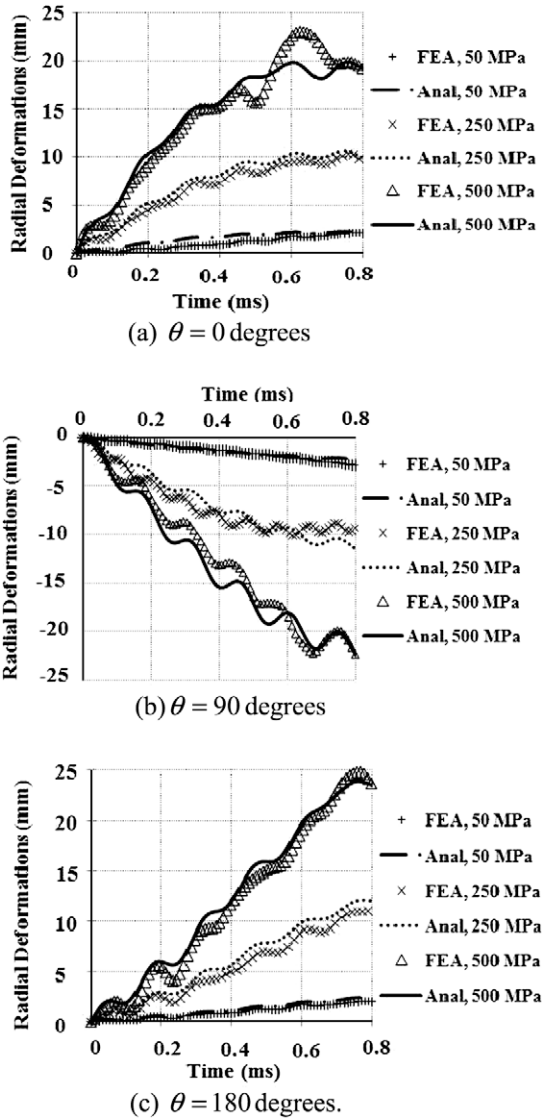


Fig. 16. Radial shell deformations for orthotropic E-Glass/Vinyl Ester shell under various side-on pressure pulse at (a) $\theta = 0^\circ$, (b) $\theta = 90^\circ$ and (c) $\theta = 180^\circ$.

In an effort to justify the assumption of small a_n , the deformation response of the shell over a range of pressure pulse amplitudes up to the point of dynamic instability was simulated with ABAQUS Standard. Figs. 16a–c show a comparison of analytical and FEA predictions of the radial deformation history at $\theta = 0^\circ$, 90° and 180° , respectively, when the pressure pulse amplitude is 50 MPa, 250 MPa, and 500 MPa. The two compare very well in all cases except when the pressure pulse amplitude approaches the buckling pressure amplitude of 504 MPa. At 0° , the FEA solution at 500 MPa begins to show unstable response when the pressure pulse amplitude is near the critical buckling pressure amplitude. Nevertheless, the good agreement between the analytical and FEA results validates the assumption that a_n is small.

Good agreement between the analytical and FEA solutions for the E-Glass/Epoxy shells with different layups was also found. Figs. 17a–c give a comparison of the transient deflection profiles for the three different layups of E-Glass/Epoxy shells. Here the shell geometry and load were kept the same as for the orthotropic woven E-Glass/Vinyl Ester shell. Each of the four layers, which made up the laminated composite shell, was given individual ply properties in a local cylindrical coordinate system for the symmetric and anti-symmetric layups. Only three layers were used in the

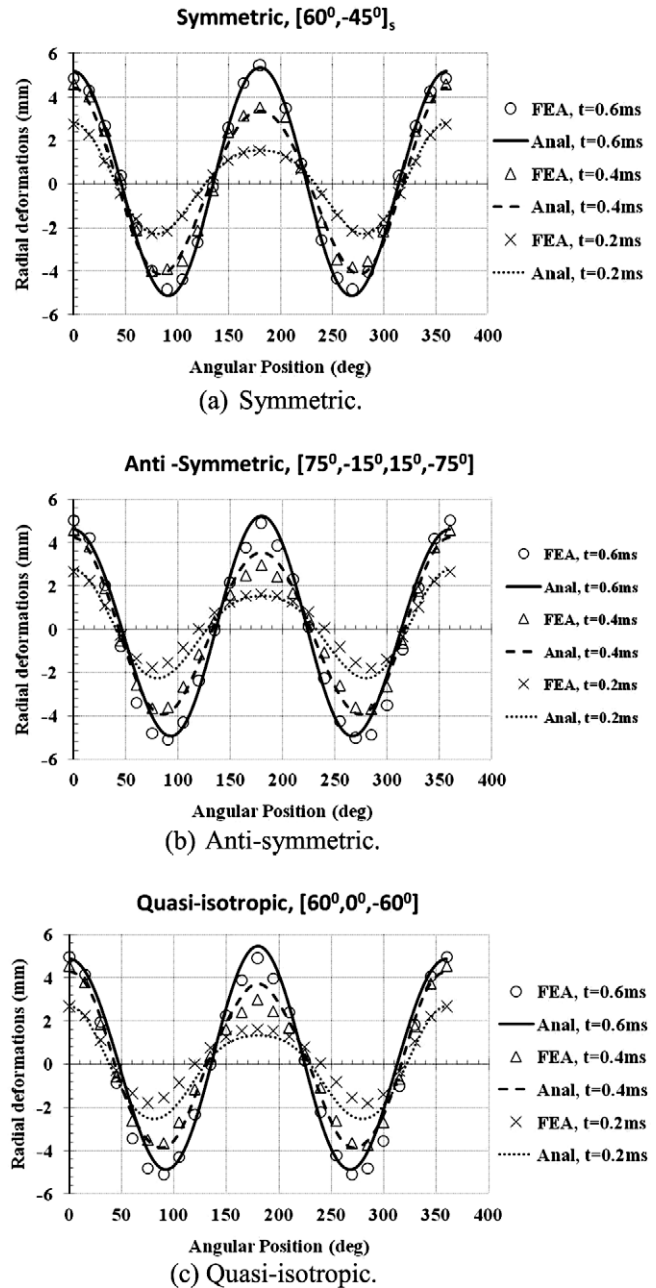


Fig. 17. Transient radial deformation profiles of E-Glass/Epoxy shells with side-on pressure pulse; $p_0 = 250$ MPa, $\Delta T = 3.5 \mu s$: (a) symmetric, (b) anti-symmetric and (c) quasi-isotropic.

case of the quasi-isotropic layup. Overall the E-Glass/Epoxy shells with different layups are stiffer than the orthotropic woven E-Glass/Vinyl Ester shell. There was very little variation in the deflection for the different layups of the E-Glass/Epoxy, even though there were noticeable differences in the critical buckling impulses among these shells in Table 3. This is because the dynamic buckling mode is 5 or higher for these shells, and the fifth modal contribution to the shell radial deflection is very small compared to the lower modes in the vibration analysis.

7.2. Shell fracture

A brittle composite shell may actually fail due to delamination and local tensile or compressive failure of individual plies instead of dynamic instability. To examine local ply failure, one can

calculate strains and use laminate shell theory and failure criteria to determine first-ply failure. Shell fracture of the woven E-Glass/Vinyl Ester shell is examined in this section.

The bending strains in the cylinder are given by

$$\varepsilon_b = Z\kappa_\theta \quad (40)$$

where from Eq. (10) the curvature is given by

$$\kappa_\theta = \frac{1}{a} \left[a_0 - \sum_{n=2}^{\infty} a_n (n^2 - 1) \cos n\theta \right] \quad (41)$$

The above curvature varies with time t and angular position θ . They have maximum magnitude at $\theta = 0, \pi$. Denote the curvature at $\theta = 0$

$$\kappa_0 = \frac{1}{a} \left[a_0 - \sum_{n=2}^{\infty} a_n (n^2 - 1) \right] \quad (42)$$

and the curvature at $\theta = \pi$ as

$$\kappa_\pi = \frac{1}{a} \left[a_0 - 3a_2 + \sum_{n=3}^{\infty} a_n (n^2 - 1) \right] \quad (43)$$

A modified Hashin–Rotem [18] is used to examine lamina failure of the woven roving E-Glass/Vinyl Ester. According to the modified Hashin–Rotem failure criteria, the failure of the composite occurs when

$$\frac{|\sigma_x|}{X_T} = 1 \quad \text{if } \sigma_x > 0 \quad \text{or} \quad \frac{|\sigma_x|}{X_C} = 1 \quad \text{if } \sigma_x < 0 \quad (44)$$

$$\frac{|\sigma_\theta|}{X_T} = 1 \quad \text{if } \sigma_\theta > 0 \quad \text{or} \quad \frac{|\sigma_\theta|}{X_C} = 1 \quad \text{if } \sigma_\theta < 0 \quad (45)$$

$$\frac{|\tau_{x\theta}|}{S_L} = 1 \quad (46)$$

For an orthotropic shell, the relationship between the principal stress and strains are given by

$$\begin{Bmatrix} \sigma_x \\ \sigma_\theta \\ \tau_{x\theta} \end{Bmatrix} = \begin{bmatrix} \bar{Q}_{11} & \bar{Q}_{12} & 0 \\ \bar{Q}_{12} & \bar{Q}_{22} & 0 \\ 0 & 0 & \bar{Q}_{66} \end{bmatrix} \begin{Bmatrix} \varepsilon_x \\ \varepsilon_\theta \\ \gamma_{x\theta} \end{Bmatrix} \quad (47)$$

where $\bar{Q}_{11} = E_{11}/(1 - \nu_{12}\nu_{21})$, $\bar{Q}_{22} = E_{22}/(1 - \nu_{12}\nu_{21})$, $\bar{Q}_{21} = \nu_{12}E_{22}/(1 - \nu_{12}\nu_{21})$, and $\bar{Q}_{66} = G_{12}$.

In the plane strain problem, the stresses in the shell are reduced to

$$\sigma_x \equiv \bar{Q}_{12}\varepsilon_\theta \quad (48)$$

$$\sigma_\theta = \bar{Q}_{22}\varepsilon_\theta \quad (49)$$

Since $\bar{Q}_{22} > \bar{Q}_{12}$, $\sigma_\theta > \sigma_x$ and failure of the shell will occur in tangential direction. For the orthotropic shell the maximum tangential stress would occur at the outer plies where the bending strains are maximum, i.e., at $z = \pm h/2$. Thus evaluating ε_θ at $z = \pm h/2$ from Eq. (40) and substituting the results into Eq. (49) and then Eq. (45) give

$$\frac{\bar{Q}_{22}h\kappa_\theta}{2X_T} = 1 \quad \text{if } \sigma_\theta > 0 \quad (50)$$

and

$$\frac{\bar{Q}_{22}h\kappa_\theta}{2X_C} = 1 \quad \text{if } \sigma_\theta < 0 \quad (51)$$

The value of the curvature at which failure occurs is thus given by

$$\kappa_f = \frac{2}{h\bar{Q}_{22}} \min(X_T, X_C) \quad (52)$$

The above expression describes the maximum allowable shell curvature based on a Hashin–Rotem composite failure criterion. From Table 1, one finds that $X_C < X_T$ for woven roving E-Glass/Vinyl Ester.

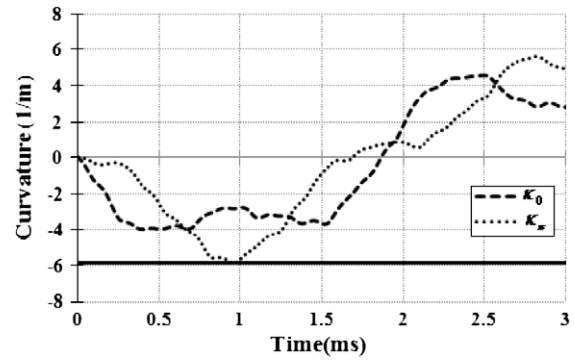


Fig. 18. Transient curvature in woven E-Glass/Vinyl Ester shell ($a = 80$ mm, $h = 4$ mm) with side-on pressure pulse; $p_0 = 200$ MPa, $\Delta T = 3.5$ μ s.

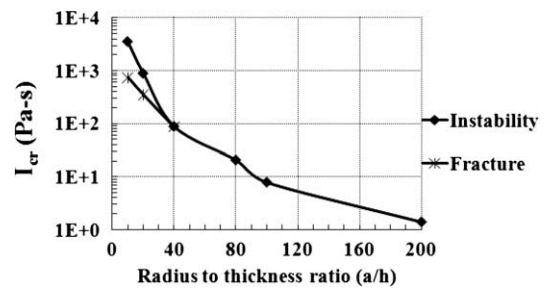


Fig. 19. Influence of aspect ratio on the type of failure for woven E-Glass/Vinyl Ester shell with side-on pressure pulse.

Thus compressive failure is more likely to occur in the woven E-Glass/Vinyl Ester shell. For the 4-mm thick shell, the curvature at which failure occurs is $\kappa_f = 5.8$ m^{-1} . The pressure pulse amplitude that would cause compressive failure on the outer plies of the 4-mm thick woven E-Glass/Vinyl Ester shell is found by setting either Eqs. (42) or (43) equal to 5.8 m^{-1} .

Figs. 18 shows the transient response of κ_0 and κ_π for the orthotropic shell with radius $a = 80$ mm and thickness $h = 4$ mm, subjected to side-on pressure pulse amplitude of 200 MPa. The κ_π first reaches the curvature for failure value. Note that the 200 MPa pressure pulse amplitude that would just cause shell rupture must be found iteratively or by trial-and-error because the curvature is represented as a Fourier series. The pressure pulse amplitude or impulse cannot be solved explicitly. Consideration of failure for the different layups of E-Glass/Epoxy shells would be more difficult since one must determine which ply would undergo first-ply failure in addition to iterating for the critical curvature at failure.

Since the 4-mm thick woven E-Glass/Vinyl Ester shell ruptures below the critical buckling pressure pulse amplitude of 504 MPa, the more likely mode of failure for this shell is compressive failure of the outer ply rather than buckling. First-ply failure was carried out for other shell thicknesses or aspect ratios, and the results are shown in Fig. 19. It was found that the thicker E-Glass/Vinyl Ester shells were more likely to fail by first-ply failure, while the thinner E-Glass/Vinyl Ester shells were more likely to buckle.

8. Concluding remarks

The dynamic stability of laminated composite shells when they are subjected to uniformly distributed overpressure and asymmetric pressure pulse (side-on explosion) was examined. The shell response was described by a set of Matheiu differential equations.

The critical buckling impulse was found to depend on the shell lay-up, aspect ratio and impulse distribution. In general, the critical buckling impulse decreases as the aspect ratio increases (thinner shells). However, certain composite shell layups do not follow this pattern because of the complicated nature of the Mathieu stability diagram.

The analytical solution for the stable shell vibrations was validated using a Dynamic, Implicit finite element analysis in ABAQUS Standard. Radial shell deformations were found to be in good agreement, within 7%, of those from FEA. It was also shown that first-ply shell failure can occur at an impulse below the critical buckling impulse for certain aspect ratios of the woven E-Glass/Vinyl Ester shell. A parametric study revealed that the thicker woven E-Glass/Vinyl Ester shells were more likely to fail by first-ply failure, whereas the thinner shells were more likely to fail by dynamic instability. One should therefore be cautious in assuming the mode of failure of a composite shell but instead consider all possibilities.

The composite shells analyzed in this paper were assumed to be ideal with no imperfections (shell eccentricity or out-of-roundness) and no damping. Both imperfection and damping would modify the results. Future research is on the way to incorporate the effects of shell imperfections and damping in the model.

Acknowledgement

The authors would like to acknowledge financial support from Dr. Yapa Rajapakse at the Office of Naval Research under Grant N00014-07-1-0423.

References

- [1] Turkmen HS. Structural response of laminated composite shells subjected to blast loading: comparison of experimental and theoretical methods. *J Sound Vib* 2002;249(4):663–78.
- [2] Prusty BG, Satsangi SK. Finite element transient dynamic analysis of laminated stiffened shells. *J Sound Vib* 2001;248(2):215–33.
- [3] Lee Y-S, Lee K-D. On the dynamic response of laminated circular cylindrical shells under impulse loads. *Comput Struct* 1997;63(1):149–57.
- [4] Bolotin VV. The dynamic stability of elastic systems. San Francisco (CA): Holden-Day; 1964.
- [5] Birman V, Simites GJ. Dynamic stability of long cylindrical sandwich shells and panels subjected to periodic in loading. *J Compos Mater* 2002;38(7):591–612.
- [6] Ganapathi M, Balamurugan V. Dynamic instability analysis of a laminated composite cylindrical shell. *Comput Struct* 1998;69(2):181–9.
- [7] Schokker A, Sridharran S, Kasagi A. Dynamic buckling of composite shells. *Comput Struct* 1996;59(1):43–53.
- [8] Bisagni C. Dynamic buckling of fiber composite shells under impulsive axial compression. *Thin Wall Struct* 2005;43(3):499–514.
- [9] Lindberg HE, Florence AL. Dynamic pulse buckling. Dordrecht: Martinus Nijhoff Publishers; 1987.
- [10] Goodier JN, McIvor IK. The elastic cylindrical shell under nearly uniform radial impulse. *J Appl Mech* 1964;31:259–66.
- [11] Lord Rayleigh. Theory of sound. New York (NY): Dover Publications; 1945.
- [12] Nayfeh AH, Mook DT. Nonlinear oscillations. New York: John Wiley & Sons; 1979.
- [13] Hale JK. Ordinary differential equations. 2nd ed. Malabar (FL): Kreiger Publishing Company; 1980.
- [14] Hoo Fatt MS, Palla L. Analytical modeling of composite sandwich panels under blast loads. *J Sandwich Struct Mater* 2009;11(4):357–80.
- [15] Lapp CK. Design allowables substantiation. In: Peters ST, editor. Handbook of composites. London: Chapman & Hall; 1998. p. 758–77.
- [16] ABAQUS, Inc. ABAQUS user manual. version 6.7. Dassault Systèmes; 2007.
- [17] Pothula SG. Dynamic response of composite cylindrical shells under external impulsive loads. MS thesis. University of Akron; 2009. OhioLINK ETD. <<http://etd.ohiolink.edu/view.cgi?acc%5Fnum=akron1248097987>>.
- [18] Daniel IM. Failure of composite materials. *Strain* 2007;43(1):4–12.



A wave propagation model for the high velocity impact response of a composite sandwich panel

Michelle S. Hoo Fatt*, Dushyanth Sirivolu

Department of Mechanical Engineering, The University of Akron, Akron, OH 44325-3903, USA

ARTICLE INFO

Article history:

Received 15 December 2008

Received in revised form

10 March 2009

Accepted 15 September 2009

Available online 22 September 2009

Keywords:

High velocity impact

Composite sandwich panels

Analytical model

ABSTRACT

A solution methodology to predict the residual velocity of a hemispherical-nose cylindrical projectile impacting a composite sandwich panel at high velocity is presented. The term high velocity impact is used to describe impact scenarios where the projectile perforates the panel and exits with a residual velocity. The solution is derived from a wave propagation model involving deformation and failure of facesheets, through-thickness propagation of shock waves in the core, and through-thickness core shear failure. Equations of motion for the projectile and effective masses of the facesheets and core as the shock waves travel through sandwich panel are derived using Lagrangian mechanics. The analytical approach is mechanistic involving no detail account of progressive damage due to delamination and debonding but changes in the load-bearing resistance of the sandwich panel due to failure and complete loss of resistance from the facesheets and core during projectile penetration. The predicted transient deflection and velocity of the projectile and sandwich panel compared fairly well with results from finite element analysis. Analytical predictions of the projectile residual velocities were also found to be in good agreement with experimental data.

© 2009 Elsevier Ltd. All rights reserved.

1. Introduction

Lightweight composite sandwich panels, consisting of fiber-reinforced polymer facesheets and polymeric foam core, are becoming more widely used in military vehicles because they offer greater load-bearing capabilities per unit weight and easier maintenance. In some instances, these composite sandwich panels may be subjected to high velocity impact by bullets and flying debris from a nearby explosion. The objective of this paper is to develop an analytical model for quantifying the deformation and failure of a polymer composite sandwich panel subjected to high velocity projectile impact. The term high velocity impact is used to describe impact scenarios whereby the projectile perforates the panel and exits with residual velocity. Knowledge of the residual projectile velocity is important for the protection of people and equipment behind the panel, especially if the sandwich panel is used for armor or as a sacrificial protective layer.

Projectile impact studies on polymer composite sandwich panels have been mainly concentrated in the low velocity impact regime because of its association with barely visible impact damage

[1–3] and finding the panel's ballistic limit, a term used to describe the projectile impact velocity that would just cause perforation. This paper is concerned with projectile impacts that produce visible damage, including facesheet indentation and fracture of facesheets and core. Some recent survey articles on visible impact damage of composite structures are given in Refs. [4,5]. At the ballistic limit, the kinetic energy of the projectile is consumed completely in panel deformation and damages associated with the projectile penetration process. The ballistic limit represents a panel's ability to resist projectile perforation because it provides a quantitative measure of the maximum amount of kinetic energy the panel can absorb before it is perforated by the projectile. There are very few papers which deal with the issue of high velocity impact of composite sandwich panels, i.e., situations when the projectile impact speed is in excess of the ballistic limit. High velocity impact is dominated by inertial forces, wave propagation and changes in material stiffness, strength and fracture energy due to high strain rate.

Fig. 1(a–c) show three distinct types of impact regimes for monolithic panels. In low velocity impact, the panel span (shown with radius a) and boundary conditions affect the amount of energy that is absorbed before perforation (see Fig. 1(a)). In high velocity impact, the panel span and boundary conditions are irrelevant in the impact analysis because perforation occurs during wave propagation and before stress waves can reach the panel boundaries. As

* Corresponding author. Tel.: +1 330 972 6308; fax: +1 330 972 6027.

E-mail address: hoofatt@uakron.edu (M.S. Hoo Fatt).

Nomenclature			
a	plate radius	t_o	wave travel time through incident facesheet
C	lateral wave propagation speed	t_I	time of Phase I
C_d	dilatational wave speed in core	U_I	local strain energy of facesheet indentation
C_e	uniaxial stress elastic wave speed in core	U_g	global bending/shear strain energy of sandwich
C_f	through-thickness wave speed in facesheet	U	strain energy potential
C_p	plastic wave speed in core	V_o	initial projectile velocity
C_t	through-thickness wave propagation speed	V_1	projectile velocity after impact
D_p	plastic work dissipated in core crushing	V_2	back facesheet velocity under projectile
\bar{D}	equivalent bending stiffness of laminate	w	facesheet deflection
D_{ij}	bending stiffness of facesheet	x,y	in-plane rectangular coordinates of sandwich panel
E_c	core compressive Young's modulus	X_1	deflection of impacted facesheet
E_{ij}	Young's modulus	X_2	deflection of back facesheet
h	facesheet thickness	X_c	laminate longitudinal compressive strength
h_e	depth of elastic zone in core	X_f	in-plane fiber failure stress
h_p	depth of plastic zone in core	X_T	laminate longitudinal tensile strength
H	core thickness	Y_c	laminate through-thickness compressive strength
L	Lagrangian	Y_T	laminate through-thickness tensile strength
L_c	core linear momentum	Z_f	laminate through-thickness strength
L_f	facesheet linear momentum	z	through-thickness coordinate
L_p	length of projectile	δ	local indentation
L_{pl}	length of plastic zone	Δ	global sandwich deflection
m_c	effective mass of core	ε	strain
m_f	effective mass of incident facesheet	ε_D	densification strain
m_{bf}	effective mass of back facesheet	ε_x	strain in the x-direction
m_p	mass of core plug	ε_y	strain in the y-direction
M_o	projectile mass	γ_{xy}	in-plane shear strain
P_c	equivalent core resistance	λ, μ	Lame's elastic constant
P_{cr}	critical core resistance at shear failure	ν_{ij}	Poisson's ratio
P_{bf}	back facesheet bending resistance	Π	potential energy
P_l	local resistance of incident facesheet and core	ρ_c	density of core
q	core plateau stress	ρ_D	density of core after densification
\bar{Q}_{ij}	reduced stiffness matrix	ρ_f	density of facesheet
r, θ	in-plane radial and circumferential coordinates	σ	stress
r_p	projectile radius	σ_D	plastic stress at densification strain
S_L	laminate longitudinal shear strength	σ_{ij}	stress tensor
S_T	laminate through-thickness shear strength	τ_{cr}	through-thickness shear strength of core
t	time	ξ	extent of local indentation
T	kinetic energy	ξ_1	extent of deformation in incident facesheet
T_c	core kinetic energy	ξ_2	radius of debonded back facesheet
T_f	facesheet kinetic energy	Ξ	extent of global deflection

indicated in Fig. 1(b), the panel deformation is localized to a region (radius ξ) determined by the propagation speed of lateral waves C. Some of the initial kinetic energy of the projectile is consumed in panel deformation and fracture. The remaining initial kinetic energy of the projectile results in residual velocities of the projectile and debris after panel perforation. With increasing projectile speed, the extent of panel deformation ξ decreases because of panel perforation. Olsson [6] proposed an impactor-plate mass criterion to distinguish low velocity impact from small-mass, wave controlled impact. This criterion can be used to address the panel deformation response but does not address perforation or failure of the composite panel. If the impact velocity is very high, perforation of the panel may occur without any panel deformation. This situation is termed ballistic impact and as shown in Fig. 1(c), is dominated by the propagation of through-thickness waves. The through-thickness wave speed C_t and plate thickness h are important parameters in ballistic impact studies.

Although a similar distinction of impact regimes can be made for sandwich panels with crushable cores, the penetration and perforation of the sandwich panel is not as simple as for the

monolithic panel. Deformation and perforation of the incident facesheet can occur without actual perforation of the entire sandwich. The core of the sandwich panel not only offers crushing resistance below the incident facesheet but a nesting zone for the projectile after it perforates the incident facesheet. In keeping with the classification shown in Fig. 1(a–c), high velocity impact of a sandwich panel would occur when the projectile has completely perforated the panel and exits with non-zero residual velocity. In order for this to happen, the projectile must perforate multiple layers of facesheet and core materials.

One of the earliest and most comprehensive studies on high velocity projectile impact and perforation of E-glass woven roving facesheet and foam core sandwich panels is by Wen et al. [7]. The study included static, low velocity and high velocity impact of facesheets and sandwich configurations with blunt, hemispherical and cylindrical-conical nose projectiles of various diameters. Different failure modes, dependent on the projectile nose-shape, were highlighted in Ref. [7]. In all cases the impact energy absorption was greater than that during static indentation because of inertial forces and possible changes in material properties at high

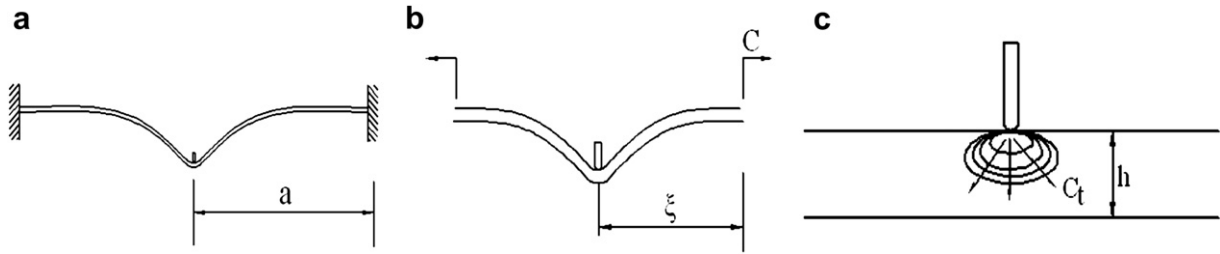


Fig. 1. Classification of impact regimes: (a) Low velocity, (b) High velocity and (c) Ballistic impact.

strain rate. Empirical formulae were used to determine the penetration and perforation energies of the sandwich panel during projectile impact.

Skvortsov et al. [8] developed a semi-analytical model to determine the relative energy absorption of composite sandwich panels subjected to high velocity impact. They assumed the total energy absorbed by the panel consisted of kinetic energy, global deformation energy and damage energy, and they derived an expression for the sum of the kinetic and deformation energy in terms of the damage energy. A closed-form expression for the combined kinetic and global deformation energy of the panel was obtained by considering bending and shear deformations of an axisymmetric, centrally loaded plate. The damage energy was then estimated from experiments. The predicted panel kinetic and deformation energy in terms of this damage energy was found to be close to the experimental values and errors were attributed to the strain rate effects, plastic behavior and hardening phenomena, which were not considered in the analysis.

Velmurugan et al. [9] studied the projectile impact on composite sandwich panels in the range of 30–100 m/s. The sandwich panels in their study were not the typical sandwich panels in the conventional sense. They had a core height comparable to the facesheet thickness. The core thus acted as a bonding agent between the facesheets. An energy balance was used to determine the ballistic limit, residual velocity and energy absorption of three different sandwich panels. In developing the analytical solution, they assumed the sandwich panel acted as a single plate since the foam layer was thin and comparable to facesheet thickness. Failure mechanisms were also assumed uniform through the panel thickness.

None of the above-mentioned studies provides a fully deterministic approach for predicting the deformation and damage of the composite sandwich panel. The solutions provided by Wen et al. [7] and Skvortsov et al. [8] are either empirical or semi-empirical, and the solution provided by Velmurugan et al. [9] addressed a laminated plate rather than a sandwich plate. In this paper, we attempt to derive analytical solutions for projectile impact and perforation of a sandwich panel with fiber-reinforced laminated facesheets and foam core. A mechanistic approach is taken to estimate the impact response and the residual velocity of the projectile as it perforates the sandwich panel at high impact speeds. First, a wave propagation model will be established to calculate transient deformations and evaluate key parameters for damage initiation and ultimate failure of facesheet and core materials. Simple composite failure criteria will be applied for the fracture and perforation of the facesheets and core. The loss of load-bearing capacity of the individual facesheets and core is considered and during each failure mechanisms is used to determine the transient response of the projectile and panel during penetration. High velocity impact and perforation of the composite sandwich panel will also be simulated with ABAQUS Explicit. The numerical predictions will be used to gage the accuracy of the analytical model. Finally the analytical solutions will be compared to high velocity projectile impact test data from Wen et al. [7].

2. Problem formulation

Consider the composite sandwich panel as shown in Fig. 2. The facesheets are orthotropic plates of thickness h , and the core is a crushable polymeric foam of thickness H . The hemispherical-nose cylindrical projectile has a radius r_p , a mass M_0 and a velocity V_0 . The projectile radius is assumed small compared to the core thickness, $r_p < H$, although the length of the projectile L_p may be on the order of the core thickness. The projectile is assumed rigid compared to the sandwich panel.

At the early stages of impact, compressive stress waves are generated under the projectile. These stress waves must travel through the incident facesheet, core and back facesheet before global through-thickness shear and bending waves can be transmitted laterally in the sandwich panel. Thus there are two phases associated with the impact of the composite sandwich panel: Phase I involves the propagation through-thickness waves and Phase II involves the propagation of lateral wave.

During Phase I, the problem becomes one of local indentation only, i.e., the incident facesheet deflects under the projectile and the core crushes as if the back facesheet of the sandwich panel were rigidly supported, as shown in Fig. 3(a). Local indentation under the projectile is denoted δ and the lateral extent of deformation is denoted ξ . Once the through-thickness compressive stress waves have reached the lower side of the sandwich panel, global panel bending/shear deformation can initiate. These global bending/shear deformations are shown independently of the local indentation in Fig. 3(b). The global deflection under the projectile is denoted Δ and the lateral extent of global deformation is denoted Ξ . Simultaneous local indentation and global deformation (see Fig. 3(c)) actually

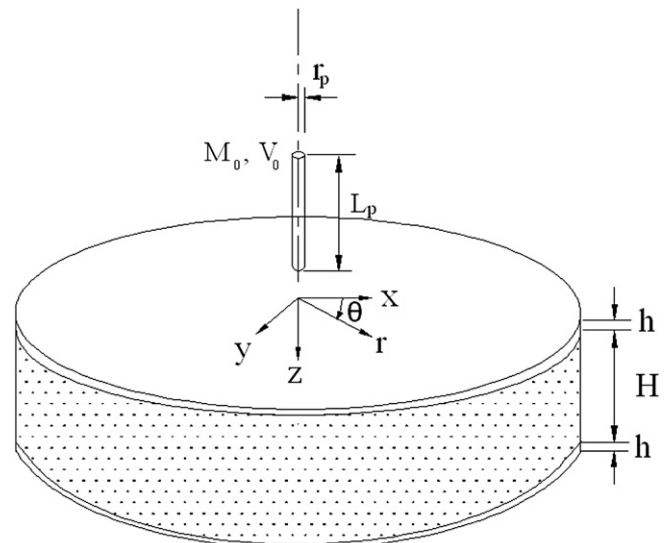


Fig. 2. Projectile impact of composite sandwich panel.

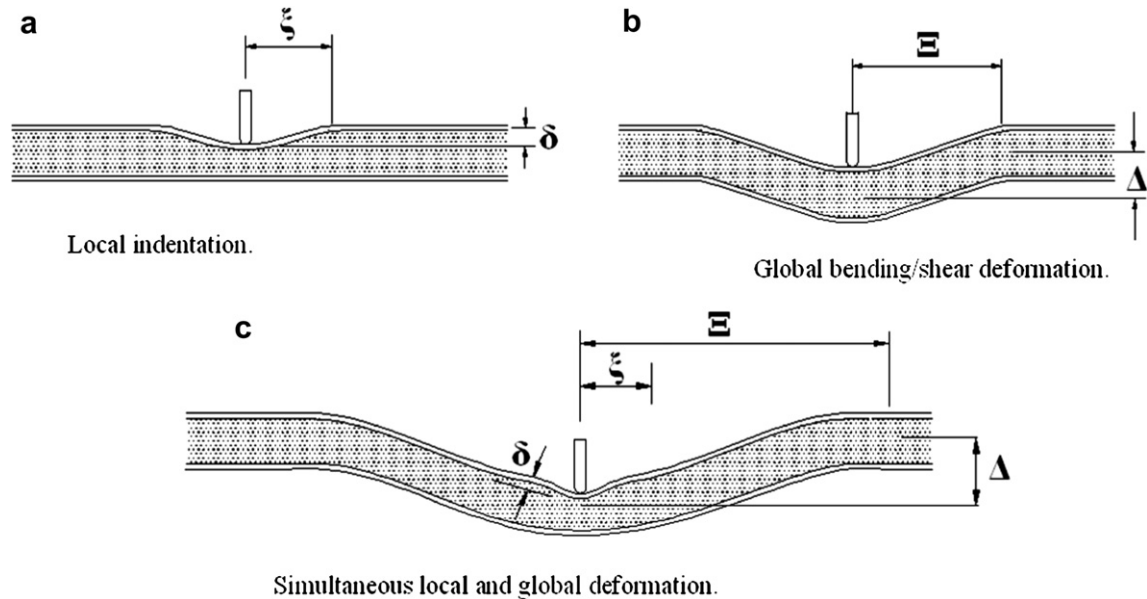


Fig. 3. Local and global sandwich deformations: (a) Local indentation, (b) Global bending/shear deformation and (c) Simultaneous local and global deformation.

occurs until the core can no longer crush because of material densification or failure has occurred. A wave propagation model for the impact response of an E-glass vinylester-Divynicell H100 foam sandwich panel under projectile impact was presented by Hoo Fatt and Sirivolu [10] based on Fig. 3(a–c). This impact model did not include damage or failure of the facesheets and core, which are likely to occur under high velocity impact. The present paper addresses failure and is an extension of this earlier work.

If the initial projectile velocity is above the ballistic limit of the panel, global bending/shear deformation will not take place because localized failure of the incident facesheet and core shear failure under the projectile during Phase I prevent the type of deformation shown in Fig. 3(b) and (c). Fig. 4(a–d) show the sequence of failure events that take place during projectile penetration and perforation when the impact velocity exceeds the ballistic limit. First, the incident facesheet ruptures under the projectile as a consequence of high in-plane stresses (Fig. 4(a)). Elastic and plastic compressive stress waves propagate within the core directly under the projectile. The core then undergoes through-thickness shear fracture and localized core compression under the projectile, as shown in Fig. 4(b). The core under the projectile becomes a plug. Debonding of the back facesheet begins as a consequence of load transmitted by the projectile and plug. Eventually the back facesheet ruptures when the in-plane stresses in the back facesheet exceed critical values and the plug and projectile are expelled from the sandwich panel (Fig. 4(c) and (d)).

Damages to the composite sandwich panel involve the interaction of several complicated mechanisms that occur over multiple length scales ranging from the microscale of individual fibers to the macro-scale of the complete sandwich panel. The damages manifest themselves in delaminations in the facesheets, debonding between the facesheet and core, core shear fracture and fracture of the facesheets. The above failure mechanisms may be the result of accumulated damage and are characterized by progressive degradation of material stiffness, which eventually lead to material failure [11]. Physically based composite failure criteria, such as Hashin's composite failure criteria for unidirectional fiber-reinforced laminates [12], can be used to indicate damage initiation of a particular failure mode, but the actual failure of the material is determined from damage evolution laws [13–15]. These damage

evolution laws are extremely complex and are usually developed for specific composite configurations and under specific load applications. In addition to this, crack propagation in the facesheets is usually brittle or unstable leading to a sudden loss in panel stiffness or impact load resistance. Fracture mechanics is often used to calculate the critical contact loads associated with delamination and debonding [16].

We propose to use simple failure criteria for mechanisms that would cause significant changes in the load resistance of the sandwich. These mechanisms are associated with failure of the incident facesheet, core shear failure, and failure of the back facesheet. Previous work on static indentation and low velocity impact of sandwich panels with hemispherical-nose projectiles has shown that the load resistance curves up to facesheet failure remain relatively unchanged by delamination and debonding, which are known to occur during penetration of these panels [17,18]. This is in contrast to composite laminates, where localized intra and inter-laminar matrix cracking, fiber breaking, and delamination under the projectile may have a more prominent effects on degrading the laminate bending and membrane stiffness [19]. The transient deformation and failure of the sandwich panel under high velocity impact are examined in Phases I and II in the following sections. Phase I is an initial phase, involving the propagation of through-thickness stress waves. Phase I ends and Phase II begins when the stress wavefront first reaches the back surface of the sandwich. During Phase I, the impact load resistance may be reduced by the failure of the incident facesheet and core shear fracture. Phase I is thus broken into sub-phases Ia and Ib in order to describe the panel behavior before and after failure, respectively. Likewise Phase II is broken into sub-phases IIa and IIb to describe panel response before and after back facesheet failure, respectively.

3. Phase I: Through-thickness wave propagation

Compressive stress waves must pass through the full thickness of the sandwich, i.e., two facesheets and core, before any response can be characterized as global sandwich deformation. The through-thickness wave travel time depends on the wave speed in the facesheet and core.

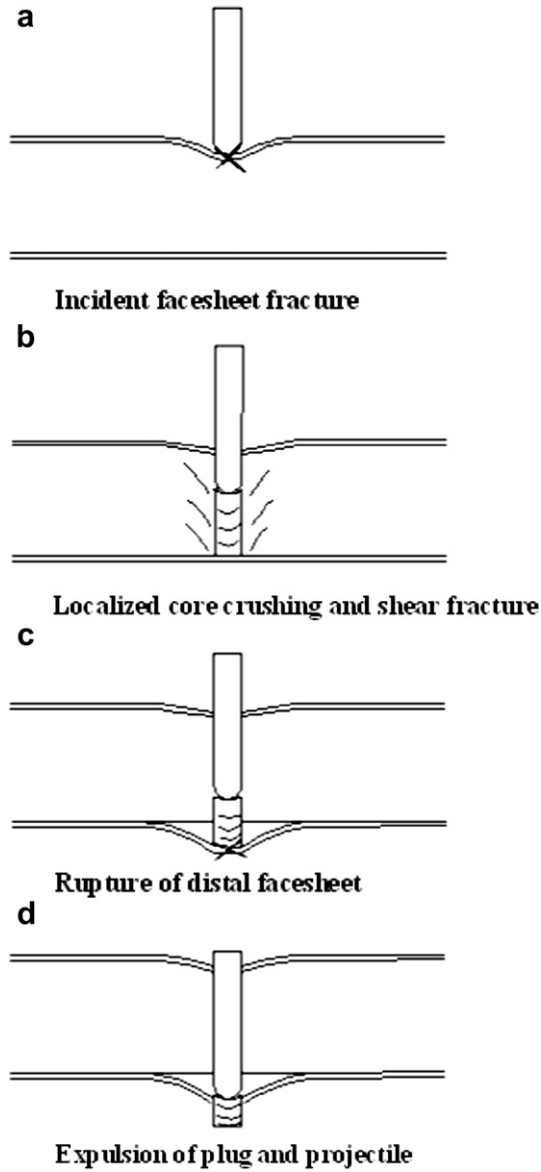


Fig. 4. Penetration and perforation of composite sandwich panel: (a) Incident facesheet fracture, (b) Localized core crushing and shear fracture, (c) Rupture of back facesheet and (d) Expulsion of plug and projectile.

3.1. Through-thickness wave speed

The wave travel time through the entire thickness of the core is given by

$$t_l = \frac{2h}{C_f} + \frac{H}{C_d} \tag{1}$$

where C_f is the wave speed in the through-thickness direction of the facesheet and C_d is the dilatational wave speed in the core. The through-thickness wave speed in an orthotropic plate is given by

$$C_f = \sqrt{\frac{E_{33}(1 - \nu_{12}\nu_{21})}{\rho_f(1 - \nu_{12}\nu_{21} - \nu_{23}\nu_{32} - \nu_{13}\nu_{31} - 2\nu_{21}\nu_{32}\nu_{13})}} \tag{2}$$

where E_{ij} , ν_{ij} and ρ_f are the elastic modulus, Poisson's ratio and density of the orthotropic facesheet, respectively [20]. The wave speed in the foam is determined by the amount of core crushing.

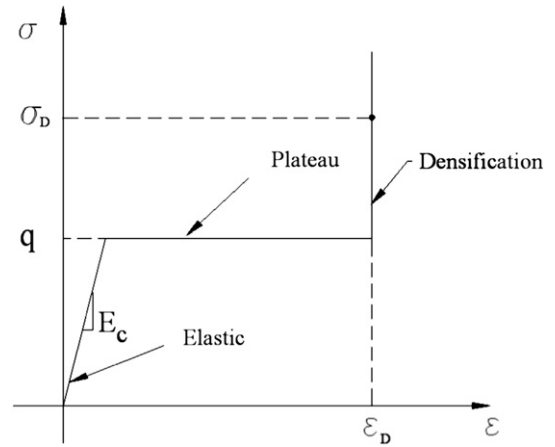


Fig. 5. Idealised compressive stress-strain curve of polymeric foam.

A polymeric foam core is elastic-plastic with a compressive stress-strain characteristic as shown in Fig. 5 [21]. The foam is linear elastic with a compressive modulus of E_c until yielding at a flow stress, q . Rapid compaction of cells causes the density to change during the plateau region until full densification has occurred at ϵ_D . The stress rises to a maximum plastic stress, σ_D , at the densification strain. Both elastic and plastic waves could therefore be generated in the foam.

The uniaxial elastic wave speed in the foam is given by $C_e = \sqrt{E_c/\rho_c}$ and the plastic wave speed is given by $C_p = \sqrt{\sigma_D - q/(\rho_c \epsilon_D)}$ [22], where ρ_c is the foam density. The elastic wave speed is generally faster than the plastic wave speed so that the through-thickness wave travel time calculated in Eq. (1) is controlled by the corresponding elastic dilatational speed. This is given in terms of Lamé's constant, λ and μ , as follows:

$$C_d = \sqrt{\frac{(\lambda + 2\mu)}{\rho_c}} \tag{3}$$

where $\lambda = E_c \nu_c / [(1 + \nu_c)(1 - 2\nu_c)]$, $\mu = E_c / [2(1 + \nu_c)]$ and ν_c is Poisson's ratio of the foam.

3.2. Phase Ia: local indentation

Local indentation is found by considering the projectile presses onto the incident facesheet resting on a foam foundation. A single degree-of-freedom model for the projectile and affected part of the sandwich panel is considered as shown in Fig. 6(a). The projectile and effective facesheet and core masses are represented by M_o , m_f and m_c , respectively. During through-thickness wave propagation the effective facesheet and core mass increase in time are functions of the local indentation δ and lateral extent of local indentation ξ_1 . The local indentation resistance from incident facesheet bending/membrane resistance as well as core plastic crushing resistance is indicated by $P_l(\delta, \xi_1)$. The equation of motion governing the dynamics of the projectile and effective facesheet mass can be written considering the system Lagrangian. The Lagrangian L for a system is defined as $L = T - \Pi$, where T and Π are the kinetic energy and potential energy of the system, respectively.

3.2.1. Kinetic energy

The kinetic energy of the system is given by

$$T = \frac{1}{2}M_o V_1^2 + \frac{1}{2}m_f V_1^2 + \frac{1}{2}m_c V_1^2 \tag{4}$$

where V_1 is the velocity under the projectile at any time, m_f is the

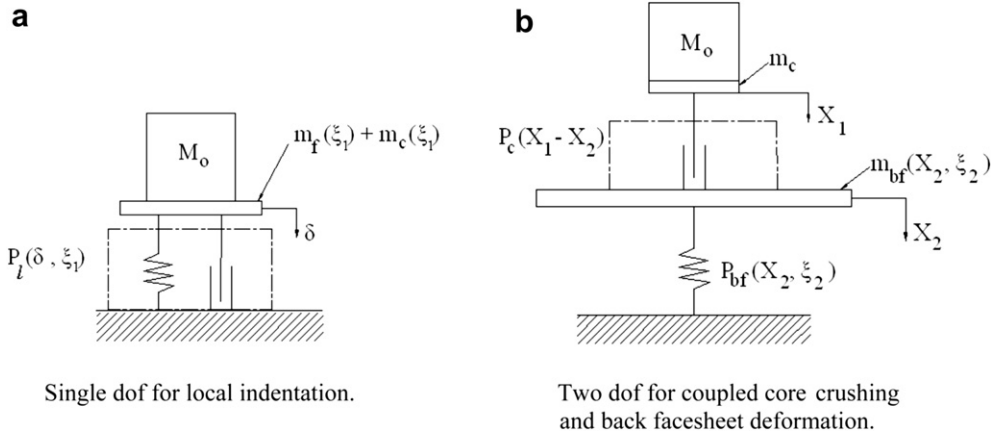


Fig. 6. Lumped parameter models: (a) Single dof for local indentation and (b) Two dof for coupled core crushing and back facesheet deformation.

effective mass of the facesheet and m_c is the effective mass of core. The last two terms in Eq. (4) increase over time as waves propagate laterally across the panel and through the thickness of the panel. The effective mass of the facesheet is found by assuming that the projectile induces the following linear velocity field in the facesheet:

$$\dot{w} = V_1 \left[1 - \frac{r}{\xi_1} \right] \quad (5)$$

The spread of the deformation zone ξ_1 in the above equation varies with time, i.e., the velocity field has a moving boundary and the effective facesheet mass grows as the velocity field spreads away from the impact site. The total kinetic energy of the facesheet is derived in Appendix A as

$$T_f = \frac{\pi \rho_f h}{12} \xi_1^2 V_1^2 \quad (6)$$

Thus the effective facesheet mass m_f is given as

$$m_f = \frac{\pi \rho_f h}{6} \xi_1^2 \quad (7)$$

The effective mass of core is more complicated to evaluate because core particle velocities are governed by elastic and plastic response. Elastic and plastic regions in the foam are shown in Fig. 7. Under the projectile, the elastic wave front has advanced a distance $C_d t$, while the plastic wave front has advanced a distance L_{pl} . As the deformation spreads laterally, the distances from the incident facesheet to the elastic and plastic wave fronts decrease in an approximately linear fashion. The volume of plastic and elastic foam is described by a truncated cone and a cone, respectively.

The particle velocity in the plastic zone is controlled by the projectile impact speed and the velocity field of incident facesheet, which is described in Eq. (5). Under the projectile the particle velocity is V_1 and the plastic wave speed is given by $C_p = V_1/\varepsilon_D$ [22]. The particle velocity in the elastic zone depends on the magnitude of the elastic stress $V = \sigma/\rho_c C_d$. Thus the maximum particle velocity in the elastic zone is $V_e = q/\rho_c C_d$. It is assumed that the elastic particle velocity decreases linearly through the thickness of the foam. The variation of the particle velocities through the foam thickness under the projectile and half-way across the local deformation zone is shown in Fig. 7.

The kinetic energy in the elastic portion of foam may be neglected when V_e is small compared to V_1 . The kinetic energy of the foam is derived in Appendix B from the above-mentioned particle velocity distribution in the plastic region as

$$T_c = \frac{\pi \rho_c L_{pl}}{20(1 - \varepsilon_D)} \xi_1^2 V_1^2 \quad (8)$$

The effective mass of the core is therefore

$$m_c = \frac{\pi \rho_c L_{pl}}{10(1 - \varepsilon_D)} \xi_1^2 \quad (9)$$

3.2.2. Potential energy

The total potential energy of the system, Π , consists of the elastic strain energy of the facesheet, U_l , and the plastic work dissipated in crushing the core, D_p :

$$\Pi = U_l + D_p \quad (10)$$

Assuming in-plane deformations are negligibly small compared to through-thickness deflections, w , the elastic strain energy due to bending in an orthotropic facesheet is

$$U_l = \frac{1}{2} \int_S \left[D_{11} \left(\frac{\partial^2 w}{\partial x^2} \right)^2 + 2D_{12} \frac{\partial^2 w}{\partial x^2} \frac{\partial^2 w}{\partial y^2} + D_{22} \left(\frac{\partial^2 w}{\partial y^2} \right)^2 + 4D_{66} \left(\frac{\partial^2 w}{\partial x \partial y} \right)^2 \right] dS \quad (11)$$

where D_{ij} is the bending stiffness of the facesheet and S is the surface area associated with indentation.

The through-thickness deflection of the facesheet is assumed to take on the same shape as the deflection profile of an isotropic, clamped circular plate under point load [23]:

$$w(r) = \delta \left[2 \left(\frac{r}{\xi_1} \right)^2 \log \left(\frac{r}{\xi_1} \right) + 1 - \left(\frac{r}{\xi_1} \right)^2 \right] \quad (12)$$

where $r^2 = x^2 + y^2$. Sirivolu [24] has shown that the above deflection profile agrees very well with finite element predictions of the transient facesheet deflection in a composite sandwich panel. To evaluate the integral expression in Eq. (11) in polar coordinates, set $dS = r dr d\theta$ and derivatives with respect to x and y as $\partial/\partial x = \cos \theta (\partial/\partial r) - (\sin \theta/r) (\partial/\partial \theta)$ and $\partial/\partial y = \sin \theta (\partial/\partial r) + (\cos \theta/r) (\partial/\partial \theta)$, respectively. The strain energy due to facesheet bending is

$$U_l = \bar{D} \frac{\delta^2}{\xi_1^2} \quad (13)$$

where $\bar{D} = \pi[3(D_{11} + D_{22}) + 2(D_{12} + 2D_{66})]$.

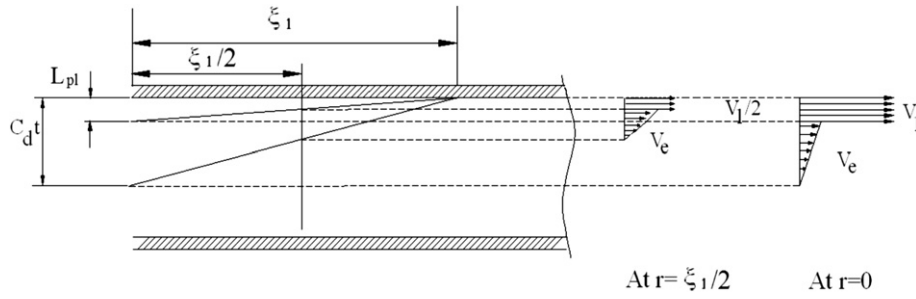


Fig. 7. Propagation of elastic and plastic waves in the core and the distribution of particle velocities during Phase I.

The core absorbs both elastic strain energy and plastic work in Phase I. The plastic work dissipated in the core plastic region shown in Fig. 7 is

$$D_p = 2\pi \int_0^{\xi_1} q \epsilon_D L_{pl} \left(1 - \frac{r}{\xi_1}\right) r dr \quad (14)$$

$$= \frac{\pi q \epsilon_D L_{pl} \xi_1^2}{3}$$

The length of the plastic zone is related to the indentation and densification strain by $L_{pl} = \delta/\epsilon_D$. Therefore, the plastic work is

$$D_p = \frac{\pi q \delta \xi_1^2}{3} \quad (15)$$

The plastic work dissipated in core crushing, although dissipative, is considered part of the potential energy of the system because the impact loading is monotonic in this phase. Thus the potential energy of the system is

$$\Pi = \bar{D} \frac{\delta^2}{\xi_1^2} + \frac{\pi q \delta \xi_1^2}{3} \quad (16)$$

3.2.3. Equation of motion

Lagrange's equation of motion for the projectile and effective facesheet mass is

$$\frac{\partial}{\partial t} \left(\frac{\partial L}{\partial V_1} \right) - \frac{\partial L}{\partial \delta} = 0 \quad (17)$$

where $L = T - \Pi$ and $V_1 = d\delta/dt$. Substituting T and Π into Eq. (17) gives

$$\left(M_o + m_f + m_c \right) \frac{d^2 \delta}{dt^2} + \left(\frac{dm_f}{dt} + \frac{dm_c}{dt} \right) \frac{d\delta}{dt} + \frac{2\bar{D}\delta}{\xi_1^2} + \frac{\pi q \xi_1^2}{3} = 0 \quad (18)$$

Substituting Eqs. (7) and (9) into Eq. (18) gives

$$\left(M_o + \frac{\pi \rho_f h \xi_1^2}{6} + \frac{\pi \rho_c L_{pl} \xi_1^2}{10(1-\epsilon_D)} \right) \frac{d^2 \delta}{dt^2} + 2\xi_1 \frac{d\xi_1}{dt} \left(\frac{\pi \rho_f h}{6} + \frac{\pi \rho_c L_{pl}}{10(1-\epsilon_D)} \right) \frac{d\delta}{dt} + \frac{2\bar{D}\delta}{\xi_1^2} + \frac{\pi q \xi_1^2}{3} + \frac{\pi \rho_c \xi_1^2 C_p V_1}{10(1-\epsilon_D)} = 0 \quad (19)$$

where $C_p = dL_{pl}/dt$. The densification strain can be written in terms of the local indentation and the length of the plastic zone $\epsilon_D = \delta/L_{pl}$. Thus using that $L_{pl} = \delta/\epsilon_D$ and $C_p = V_1/\epsilon_D$, one gets

$$\left(M_o + \frac{\pi \rho_f h \xi_1^2}{6} + \frac{\pi \rho_c \delta \xi_1^2}{10(1-\epsilon_D)\epsilon_D} \right) \frac{d^2 \delta}{dt^2} + 2\xi_1 \frac{d\xi_1}{dt} \times \left(\frac{\pi \rho_f h}{6} + \frac{\pi \rho_c \delta}{10(1-\epsilon_D)\epsilon_D} \right) \frac{d\delta}{dt} + \frac{\pi q \xi_1^2}{3} + \frac{\pi \rho_c \xi_1^2 V_1^2}{10(1-\epsilon_D)\epsilon_D} = 0 \quad (20)$$

The last term in Eq. (20) represents the hydrodynamic inertial resistance of the core. Conservation of linear momentum relates the projectile V_1 with ξ_1 :

$$M_o V_o = M_o V_1 + \frac{\pi \rho_f h \xi_1^2}{3} V_1 + \frac{\pi \rho_c \delta \xi_1^2}{6\epsilon_D(1-\epsilon_D)} V_1 \quad (21)$$

Thus,

$$\xi_1^2 = \frac{M_o(V_o - V_1)}{\left[\frac{\pi \rho_f h}{3} + \frac{\pi \rho_c \delta}{6(1-\epsilon_D)\epsilon_D} \right] V_1} \quad (22)$$

Equation (20) becomes a nonlinear second order differential equation in δ when Eq. (22) is differentiated with respect to time in order to eliminate the term $2\xi_1 d\xi_1/dt$. The initial conditions for Eq. (20) are applied after an instantaneous transfer of momentum at $t = h/C_f$. The projectile momentum is transferred to a deformation zone $\xi = r_p/2$. Thus $\delta(t_o) = 0$ and $\frac{d\delta}{dt}(t_o) = M_o V_o / (M_o + \frac{\pi \rho_f h}{3} (\frac{r_p}{2})^2)$, where $t_o = h/C_f$ is the time it takes for a compressive stress wave to travel through the facesheet.

3.3. Incident facesheet failure

Failure of the incident facesheet is said to take place when the projectile has completely penetrated the facesheet. The failure process starts with a very thin crack directly under the hemispherical-nose projectile. For instance, in orthotropic woven E-glass polyester facesheets thin cracks run parallel to the 0 and 90 degree fiber directions, thereby forming four petals that are bent back as the projectile fully penetrates the incident facesheet [7]. The projectile contact force is resisted by both the bending resistance of the cracked plate and the core crushing resistance. Complete penetration of the facesheet occurs when these petals suddenly bend back enough so that the facesheet can no longer offer resistance to the contact force of the projectile.

Rather than considering crack initiation, propagation and the sudden loss of support triggered by petal bending, we take a more simplified approach to predict the incident facesheet failure. In order for petaling to take place, failure of the incident facesheet must take place over a central area equivalent to the projectile's cross-sectional area πr_p^2 . A simple failure criteria for the incident facesheet is to apply composite failure criteria so that the facesheet fails within this region, i.e., for $r < r_p$.

3.3.1. Modified Hashin-Rotem composite failure criteria

In the modified Hashin-Rotem composite failure theory for textiles [25], the following damage mechanisms are considered:

Fiber tension

$$\left(\frac{\sigma_{11}}{X_T}\right)^2 = 1 \quad \text{and} \quad \left(\frac{\sigma_{22}}{Y_T}\right)^2 = 1 \tag{23}$$

Fiber compression

$$\left(\frac{\sigma_{11}}{X_C}\right)^2 = 1 \quad \text{and} \quad \left(\frac{\sigma_{22}}{Y_C}\right)^2 = 1 \tag{24}$$

Interfiber failure on plane 1

$$\left(\frac{\sigma_{31}}{S_T}\right)^2 + \left(\frac{\sigma_{12}}{S_L}\right)^2 = 1 \tag{25}$$

Interfiber failure on plane 2

$$\left(\frac{\sigma_{23}}{S_T}\right)^2 + \left(\frac{\sigma_{12}}{S_L}\right)^2 = 1 \tag{26}$$

Interfiber failure on plane 3

$$\left(\frac{\sigma_{33}}{Z_f}\right)^2 + \left(\frac{\sigma_{23}}{S_T}\right)^2 + \left(\frac{\sigma_{31}}{S_T}\right)^2 = 1 \tag{27}$$

where X_T and Y_T are the longitudinal and through-thickness tensile strengths, X_C and Y_C are the longitudinal and through-thickness compressive strengths, S_L is the longitudinal shear strength, S_T is the through-thickness shear strength, and Z_f is the through-thickness strength (for projectile impact Z_f would be the through-thickness strength in compression). The above criteria may be simplified if one assume that the thin orthotropic facesheets are in a state of plane stress: $\sigma_{33} = \sigma_{13} = \sigma_{23} = 0$. Only fiber tension, fiber compression, and interfiber failure on either planes 1 and 2 are active. Furthermore, for fabric composites with equal warp and fill directions, $\sigma_{11} = \sigma_{22}$, $X_T = Y_T$ and $X_C = Y_C$, and the same fiber tension and compression criteria apply in both principal directions.

3.3.2. Applying the modified Hashin-Rotem composite failure criteria

With fibers in 0 and 90 degrees parallel to the x- and y-axes, one gets the following relationship between principal stresses and strains:

$$\begin{Bmatrix} \sigma_{11} \\ \sigma_{22} \\ \sigma_{12} \end{Bmatrix} = \begin{bmatrix} \bar{Q}_{11} & \bar{Q}_{12} & 0 \\ \bar{Q}_{12} & \bar{Q}_{11} & 0 \\ 0 & 0 & \bar{Q}_{66} \end{bmatrix} \begin{Bmatrix} \epsilon_x \\ \epsilon_y \\ \gamma_{xy} \end{Bmatrix} \tag{28}$$

where \bar{Q}_{ij} is the transformed stiffness matrix. The in-plane normal and shear bending strains in rectangular coordinates are evaluated in transformed polar coordinates as follows:

$$\epsilon_x = z \frac{\partial^2 w}{\partial x^2} = z \frac{4\delta}{\xi_1^2} \left[\log\left(\frac{r}{\xi_1}\right) + \cos^2\theta \right] \tag{29}$$

$$\epsilon_y = z \frac{\partial^2 w}{\partial y^2} = z \frac{4\delta}{\xi_1^2} \left[\log\left(\frac{r}{\xi_1}\right) + \sin^2\theta \right] \tag{30}$$

$$\gamma_{xy} = 2z \frac{\partial^2 w}{\partial x \partial y} = 2z \frac{4\delta}{\xi_1^2} \cos\theta \sin\theta \log\left(\frac{r}{\xi_1}\right) \tag{31}$$

Note that the above expressions for the in-plane strains are undefined at $r=0$ and only valid when $0 < r < \xi_1$ because the

deformation field described in Eq. (12) is for point loading. The principal stresses calculated from Eq. (28) are also expressed in polar coordinates as

$$\begin{aligned} \sigma_{11} &= \sigma_{22} \\ &= z \frac{4\delta}{\xi_1^2} \left[(\bar{Q}_{11} + \bar{Q}_{12}) \log\left(\frac{r}{\xi_1}\right) + (\bar{Q}_{11} \cos^2\theta + \bar{Q}_{12} \sin^2\theta) \right] \end{aligned} \tag{32}$$

$$\sigma_{12} = z \bar{Q}_{66} \frac{8\delta}{\xi_1^2} \cos\theta \sin\theta \log\left(\frac{r}{\xi_1}\right) \tag{33}$$

The magnitude of principal bending stresses are greatest at the top or bottom of the facesheet, $z = \pm h/2$, thereby giving maximum tensile or compressive stresses. Thus the modified Hashin-Rotem's failure parameter for in-plane fiber failure is given as

$$\frac{4\delta^2 h^2}{\xi_1^4 X_f^2} \left[(\bar{Q}_{11} + \bar{Q}_{12}) \log\left(\frac{r}{\xi_1}\right) + (\bar{Q}_{11} \cos^2\theta + \bar{Q}_{12} \sin^2\theta) \right]^2 = 1 \tag{34}$$

where $X_f = \min(X_C, X_T)$. The modified Hashin-Rotem's failure parameter for interfiber failure is also given by

$$\frac{4\delta^2 h^2}{\xi_1^4 S_L^2} \left[2\bar{Q}_{66} \sin\theta \cos\theta \log\left(\frac{r}{\xi_1}\right) \right]^2 = 1 \tag{35}$$

Equation (34) has a maximum value at $\theta = 0^\circ$. Therefore, a condition for in-plane fiber failure of the incident facesheet at radial distance r is

$$\frac{4\delta^2 h^2}{\xi_1^4 X_f^2} \left[(\bar{Q}_{11} + \bar{Q}_{12}) \log\left(\frac{r}{\xi_1}\right) + \bar{Q}_{11} \right]^2 = 1 \tag{36}$$

Equation (35) has a maximum value at $\theta = 45^\circ$. Therefore, a condition for interfiber failure of the incident facesheet at radial distance r is

$$\frac{4\delta^2 h^2}{\xi_1^4 S_L^2} \left[\bar{Q}_{66} \log\left(\frac{r}{\xi_1}\right) \right]^2 = 1 \tag{37}$$

The above expressions are used to determine facesheet failure by setting $r = r_p$.

3.4. Core shear failure

Localized core shear failure can take place under high projectile impact forces. The critical impact force is given by

$$P_{cr} = 2\pi r_p (C_e t - \delta) \tau_{cr} \tag{38}$$

where τ_{cr} is the through-thickness shear strength of the core. After facesheet failure, the load transmitted to the core is

$$P_c = \pi r_p^2 \left(q + \frac{\rho_c V_1^2}{\epsilon_D} \right) \tag{39}$$

Therefore, a criterion for core shear fracture is

$$V_1 = \sqrt{\frac{\epsilon_D}{\rho_c} \left(\frac{2(C_e t - \delta) \tau_{cr} - q r_p}{r_p} \right)} \tag{40}$$

3.5. Phase Ib: equation of motion after incident facesheet rupture and core shear failure

After facesheet and core shear failure, the projectile penetrates into the sandwich. The projectile's contact force is resisted by the core crushing resistance as well as friction between the interface of the projectile and core and friction between the interface of core and core where it has sheared. These frictional forces are very difficult to measure because they are indistinguishable from the through-thickness shear fracture strength of the core during material testing. Frictional force resistance will be ignored in the subsequent analysis. It is assumed that inertial forces and core crushing resistance dominate the load resistance of the sandwich panel during penetration.

The kinetic energy of the system once the incident facesheet has failed and core has sheared is given by

$$T = \frac{1}{2}M_oV_1^2 + \frac{1}{2}m_cV_1^2 \quad (41)$$

where m_c is the mass of core in the plastic zone. The affected core is a cylindrical region of radius r_p below the projectile. Plastic stress waves advance a distance L_{pl} so that the effective mass of the core is

$$m_c = \frac{\pi r_p^2 \rho_c L_{pl}}{(1 - \varepsilon_D)} \quad (42)$$

The potential energy of system is governed primarily by plastic work dissipation in the core,

$$\Pi = \pi r_p^2 q \delta \quad (43)$$

Lagrange's equation of motion for the projectile and effective facesheet mass is

$$\frac{\partial}{\partial t} \left(\frac{\partial L}{\partial V_1} \right) - \frac{\partial L}{\partial \delta} = 0 \quad (44)$$

where $L = T - \Pi$ and $V_1 = d\delta/dt$. Substituting T and Π into Eq. (44) gives

$$\left(M_o + \frac{\pi r_p^2 \rho_c L_{pl}}{(1 - \varepsilon_D)} \right) \frac{d^2 \delta}{dt^2} + \frac{\pi r_p^2 \rho_c C_p}{(1 - \varepsilon_D)} V_1 + \pi r_p^2 q = 0 \quad (45)$$

Using that $L_{pl} = \delta/\varepsilon_D$ and $C_p = V_1/\varepsilon_D$, one gets

$$\left(M_o + \frac{\pi r_p^2 \rho_c \delta}{(1 - \varepsilon_D)\varepsilon_D} \right) \frac{d^2 \delta}{dt^2} + \frac{\pi r_p^2 \rho_c}{(1 - \varepsilon_D)\varepsilon_D} V_1^2 + \pi r_p^2 q = 0 \quad (46)$$

Equation (46) becomes a nonlinear second order differential equation in δ . The initial displacement and velocity follow from the final conditions of Phase Ia.

4. Phase II: local core crushing and back facesheet deformation

Phase II begins when the compressive elastic stress waves in the foam are completely transmitted through the back facesheet. The back facesheet debonds and deforms relative to the core under the compressive shock wave. The two degree-of-freedom model shown in Fig. 6(b) is used to describe the response in this stage: X_1 denotes the motion of the projectile mass M_o and the effective mass of the core m_c and X_2 denotes the motion of the effective mass of the back facesheet m_{bf} under the projectile. As indicated in Fig. 6 (b), the effective masses of the core and the back facesheet depend on relative deformation $X_1 - X_2$, the back facesheet deflection X_2 and lateral extent of debonding in the back facesheet ξ_2 . The core plastic

crushing resistance is indicated by $P_c(X_1 - X_2)$, while the back facesheet bending resistance is given by $P_{bf}(X_2, \xi_2)$. Eventually the effective mass of the core densifies completely when the plastic wave front in the core reaches the back facesheet. When this happens, $X_1 = X_2$ and the two degrees-of-freedom become a one degree of freedom. Equations of motion are derived separately for both these cases below.

4.1. Phase IIa: deformation before core plug formation

The velocity and deformation profiles for the back facesheet is similar to that given for the incident facesheet in Eqs. (5) and (12), respectively. The kinetic energy is given by

$$T = \frac{1}{2}M_oV_1^2 + \frac{1}{2}m_cV_1^2 + \frac{1}{2}m_{bf}V_2^2 \quad (47)$$

where $V_1 = dX_1/dt$, $V_2 = dX_2/dt$, $m_c = \pi r_p^2 \rho_c L_{pl}/(1 - \varepsilon_D)$, $m_{bf} = \pi \rho_f h \xi_2^2/6$ and ξ_2 is the extent of the debonded zone. The potential energy of system is due to core crushing and back facesheet bending

$$\Pi = \pi r_p^2 q (X_1 - X_2) + \frac{2\bar{D}}{\xi_2^2} X_2^2 \quad (48)$$

Applying Lagrange's equations of motion gives

$$\left(M_o + \frac{\pi r_p^2 \rho_c L_{pl}}{(1 - \varepsilon_D)} \right) \frac{d^2 X_1}{dt^2} + \frac{\pi r_p^2 \rho_c C_p}{(1 - \varepsilon_D)} V_1 + \pi r_p^2 q = 0 \quad (49)$$

$$\frac{\pi \rho_f h \xi_2^2}{6} \frac{d^2 X_2}{dt^2} + \frac{\pi \rho_f h}{6} V_2 \left(2\xi_2 \frac{d\xi_2}{dt} \right) + \frac{2\bar{D}}{\xi_2^2} X_2 - \pi r_p^2 q = 0 \quad (50)$$

Conservation of linear momentum gives

$$\left(M_o + \frac{\pi r_p^2 \rho_c \delta_{lo}}{(1 - \varepsilon_D)\varepsilon_D} \right) V_{lo} = \left(M_o + \frac{\pi r_p^2 \rho_c (X_1 - X_2)}{(1 - \varepsilon_D)\varepsilon_D} \right) V_1 + \frac{\pi \rho_f h}{3} \xi_2^2 V_2 \quad (51)$$

where δ_{lo} and V_{lo} are the projectile's displacement and velocity at the end of Phase Ib. The radius of the debonded zone may be evaluated from Eq. (51),

$$\xi_2^2 = \frac{3}{\pi \rho_f h V_2} \left[\left(M_o + \frac{\pi r_p^2 \rho_c \delta_{lo}}{(1 - \varepsilon_D)\varepsilon_D} \right) V_{lo} - \left(M_o + \frac{\pi r_p^2 \rho_c (X_1 - X_2)}{(1 - \varepsilon_D)\varepsilon_D} \right) V_1 \right] \quad (52)$$

Equation (52) is differentiated with respect to time and used to eliminate $2\xi_2 d\xi_2/dt$ in Eq. (50). Using that $L_{pl} = (X_1 - X_2)/\varepsilon_D$ and $C_p = V_1/\varepsilon_D$, one gets the following equations of motion:

$$\left(M_o + \frac{\pi r_p^2 \rho_c (X_1 - X_2)}{(1 - \varepsilon_D)\varepsilon_D} \right) \frac{d^2 X_1}{dt^2} + \frac{\pi r_p^2 \rho_c}{(1 - \varepsilon_D)\varepsilon_D} V_1^2 + \pi r_p^2 q = 0 \quad (53)$$

and

$$\frac{\pi r_p^2 \rho_c}{2(1 - \varepsilon_D)\varepsilon_D} V_1 V_2 + \frac{2\bar{D}}{\xi_2^2} X_2 - \frac{\pi r_p^2 q}{2} = 0 \quad (54)$$

The above equations of motion are no longer valid when plastic shock waves in the foam reach the back facesheet because the foam densifies into a rigid plug. A condition for when the plastic shock waves in the core reach the back facesheet is

Table 1
Facesheet and foam material properties.

	Woven Roving E-Glass/Polyester	Divinycell H130
Density (kg/m ³)	1,650	130
Thickness (mm)	1.75, 3.25, 7	25
E ₁₁ (+) (GPa)	24	–
E ₂₂ (+) (GPa)	24	–
E ₃₃ (+) (GPa)	10.56	–
E ₁₁ (–) (GPa)	–	0.175
E ₂₂ (–) (GPa)	–	0.175
E ₃₃ (–) (GPa)	–	0.175
v ₁₂ = v ₂₁	0.15 ^a	0.32 ^e
v ₁₃ = v ₂₃	0.28 ^b	0.32 ^e
v ₃₁ = v ₃₂	0.12	0.32 ^e
G ₁₂ = G ₂₁ (GPa)	4.0 ^c	0.050
G ₂₃ = G ₃₂ (GPa)	1.8	0.050
G ₁₃ = G ₃₁ (GPa)	1.8	0.050
q (MPa)	–	2.5
ε _D	–	0.45
σ _{1f} (+) (MPa)	345	–
σ _{1f} (–) (MPa)	255.2 ^c	–
σ _{2f} (+) (MPa)	345	–
σ _{2f} (–) (MPa)	255.2 ^c	–
σ _{3f} (+) (MPa)	36.08 ^d	–
σ _{3f} (–) (MPa)	669.17 ^d	–
τ _{12f} (+) = τ _{21f} (+) (MPa)	51.1	2
τ _{13f} (+) = τ _{31f} (+) (MPa)	45	2
τ _{23f} (+) = τ _{32f} (+) (MPa)	45	2

^a Ref. [26].

^b Ref. [27].

^c Ref. [28].

^d Ref. [29].

^e Ref. [30].

$$H - (X_1 - X_2) = L_{pl} = \frac{X_1 - X_2}{\varepsilon_D} \quad (55)$$

The left-hand side of Eq. (55) is the current height of the core during penetration, while the right-hand side is the current length of the plastic zone.

4.2. Phase IIb: deformation after core plug densification

There is no relative motion between the projectile/plug and back facesheet after the plastic shock wave reach the back facesheet. The kinetic energy of the system is given by

$$T = \frac{1}{2}(M_o + m_p)V_2^2 + \frac{1}{2}m_{bf}V_2^2 \quad (56)$$

where $m_p = \pi r_p^2 \rho_c H$, $m_{bf} = \pi \rho_f h \xi_2^2 / 6$ and ξ_2 is the extent of the debonded zone.

The potential energy of system is only due to back facesheet bending

$$\Pi = \frac{\bar{D}}{\xi_2^2} X_2^2 \quad (57)$$

Following Lagrange's equation of motion,

$$\left(M_o + m_p + \frac{\pi \rho_f h \xi_2^2}{6} \right) \frac{d^2 X_2}{dt^2} + \frac{\pi \rho_f h}{6} V_2 \left(2 \xi_2 \frac{d \xi_2}{dt} \right) + \frac{2 \bar{D}}{\xi_2^2} X_2 = 0 \quad (58)$$

Conservation of linear momentum gives

$$(M_o + m_p)V_{1IIa} + \frac{\pi \rho_f h}{3} \xi_{IIa}^2 V_{2IIa} = \left(M_o + m_p + \frac{\pi \rho_f h}{3} \xi_2^2 \right) V_2 \quad (59)$$

where V_{1IIa} and V_{2IIa} are the final velocities of the projectile and back facesheet, respectively, and ξ_{IIa} is the debond radius at the end of Phase IIa. The debond radius is given by

$$\xi_2^2 = \frac{3}{\pi \rho_f h V_2} \left[(M_o + m_p)V_{1IIa} + \frac{\pi \rho_f h}{3} \xi_{IIa}^2 V_{2IIa} - (M_o + m_p)V_2 \right] \quad (60)$$

Differentiating Eq. (60) with respect to time in order to eliminate $2 \xi_2 d \xi_2 / dt$ in Eq. (58) gives

$$\frac{1}{2}(M_o + m_p) \frac{d^2 X_2}{dt^2} + \frac{2 \bar{D}}{\xi_2^2} X_2 = 0 \quad (61)$$

The initial displacement for X_2 follows from the final value of in Phase IIa, but the initial velocity, V_{2IIb} , results from an instantaneous transfer of momentum:

$$\left(M_o + m_p + \frac{\pi \rho_f h}{3} \xi_{IIa}^2 \right) V_{2IIb} = (M_o + m_p)V_{1IIa} + \frac{\pi \rho_f h}{3} \xi_{IIa}^2 V_{2IIa} \quad (62)$$

Therefore,

$$V_{2IIb} = \frac{\left[(M_o + m_p)V_{1IIa} + \frac{\pi \rho_f h}{3} \xi_{IIa}^2 V_{2IIa} \right]}{\left(M_o + m_p + \frac{\pi \rho_f h}{3} \xi_{IIa}^2 \right)} \quad (63)$$

4.3. Back facesheet failure

The modified Hashin-Rotem criteria for textile composites are again used to determine back facesheet failure. Failure criteria for in-plane fiber and interfiber failure follow from Section 3.3. The in-plane fiber failure of the back facesheet is

$$\frac{4X_2^2 h^2}{\xi_2^4 X_f^2} \left[(\bar{Q}_{11} + \bar{Q}_{12}) \log \left(\frac{r_p}{\xi_2} \right) + \bar{Q}_{11} \right]^2 = 1 \quad (64)$$

Similarly, interfiber failure of the back facesheet is given by

$$\frac{4X_2^2 h^2}{\xi_2^4} \frac{1}{S_l^2} \left[\bar{Q}_{66} \log \left(\frac{r_p}{\xi_2} \right) \right]^2 = 1 \quad (65)$$

5. Comparison with FEA

As an example, consider one of the high velocity projectile impact tests of a fully clamped sandwich panel made of woven roving E-glass polyester facesheets and PVC H130 foam core with a hemispherical-nose projectile taken from Wen et al. [7]. The sandwich panel had a radius of 150 mm, facesheet thickness of 1.75 mm, and core thickness of 25 mm. Material properties for the woven roving E-glass polyester and the PVC H130 foam are given in Table 1. Most of these properties were given in Ref. [7], but some were also taken from references listed in the footnote of Table 1. The sandwich panel undergoes high velocity impact by a steel cylindrical rod of radius 5.25 mm, mass 18 g, and velocity 165 m/s.

The projectile impact problem was modeled using ABAQUS Explicit and continuum C3D8R elements for both the facesheets and the foam. The FEA quarter model for the projectile and sandwich panel is shown in Fig. 8. The facesheets and core were

modeled with 3 and 50 elements through the thickness, respectively, in order to capture through-thickness wave propagation. The PVC H130 foam was modeled as crushable foam with isotropic hardening. Additional foam properties, such as the plastic hardening curve were derived from the compressive stress-strain curve for Divinycell H130 foam in Ref. [7]. A VUMAT user-material subroutine was written to describe orthotropic facesheet material properties and to implement the modified Hashin-Rotem's composite failure criteria for the woven roving E-glass polyester. When the Hashin-Rotem's composite failure criteria were met, elements were eroded or deleted so that the projectile could pass through the facesheets. This simplified criterion for element erosion is less accurate and very conservative when compared to the progressive damage criteria discussed earlier in Section 2. However, it is consistent with the failure criteria used in developing the analytical model and adequate for comparison purposes.

In the interest of computational efficiency, a few simplifications were taken to model damage and perforation of the composite sandwich panel in the FEA. These included the following:

1. The facesheets were homogenized with the stiffness and strength characteristics of the woven roving E-glass polyester. In real life, the facesheet is a laminate consisting of individual plies that may delaminate upon impact.
2. Bonding between facesheets and core was described by a penalty contact interaction law whereby debonding would occur when the inter-laminar shear stress was exceeded. Sliding friction would also occur after debonding. A coefficient of friction equal to 0.75 was assigned between facesheet and core.
3. A fracture surface over which through-thickness shear fracture of the core would occur was pre-defined. The condition for through-thickness shear fracture was described by a penalty contact interaction law whereby fracture would occur when the shear strength of the core was exceeded. A coefficient of friction equal to 0.75 was assigned between core and core.

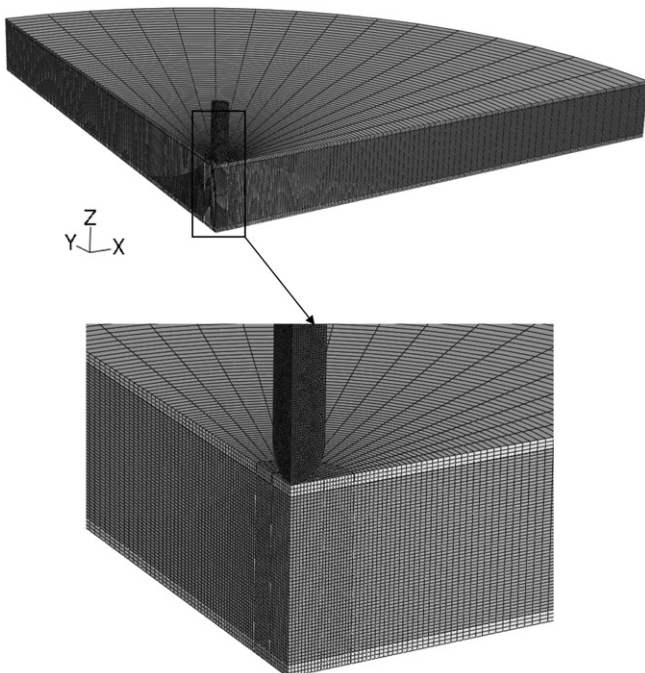


Fig. 8. Finite element mesh of projectile impacting sandwich panel (quarter model).

The fully perforated sandwich panel in the FEA is shown in Fig. 9 using the above simplifications. Note that the projectile is still embedded in the core after the back facesheet elements have been eroded and there is no other penetration resistance except for core friction. The projectile exits the panel fully with a residual velocity. The analytical solutions for the facesheet deflection under the projectile X_1 and the back facesheet deflections under the projectile X_2 are compared to FEA results in Fig. 10(a). The corresponding velocities of the incident and back facesheets are also given in Fig. 10(b). The predicted results from the analytical model compared relatively well with FEA only up to core plug densification. The time when this occurs is indicated in Fig. 10(a) and (b). This is because core densification at the densification strain for H130 foam could not be predicted with the plasticity constitutive equation for the foam in the FEA. The plastic hardening curve for the foam in the FEA extended far beyond the densification strain reported in Ref. [7], and there is still relative motion between X_1 and X_2 in the FEA because of this. In our analytical model, velocity V_2 would be equivalent to the projectile residual velocity because the core densified and the projectile and core both move as a rigid body. However, since the core does not densify in the FEA solution, the V_2 from FEA is not the same as the projectile velocity. The residual velocity from the FEA is found from the projectile after it exits the sandwich panel.

The analytical solution for the residual velocity of the projectile was calculated to be 142.9 m/s, while that found from the FEA was 161.1 m/s. The main reason for the discrepancy between the analytical solution and the FEA is due to the element erosion in the ABAQUS user-subroutine for the facesheet failure. Too many elements were being eroded and removed in the FEA. As may be seen in Fig. 9, all of the elements under and surrounding the projectile were eroded in the incident facesheet before it was fully penetrated and all of the elements at the edge of the projectile were eroded in the back facesheets when it was fully penetrated. When elements are eroded or deleted, they do not contribute to the strain energy or the kinetic energy of the plate. Removing elements under the projectile reduced the amount of strain energy and kinetic energy that could be absorbed in the facesheets. As a result, the FEA over-predicted the projectile's residual kinetic energy and velocity. A better approach for modeling projectile penetration and perforation would be to use an extremely fine mesh in the impact zone, the

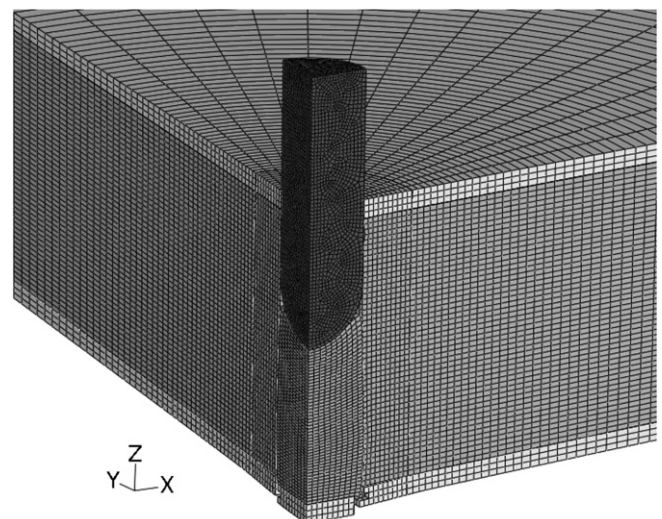


Fig. 9. Perforated sandwich panel after eroding facesheet elements.

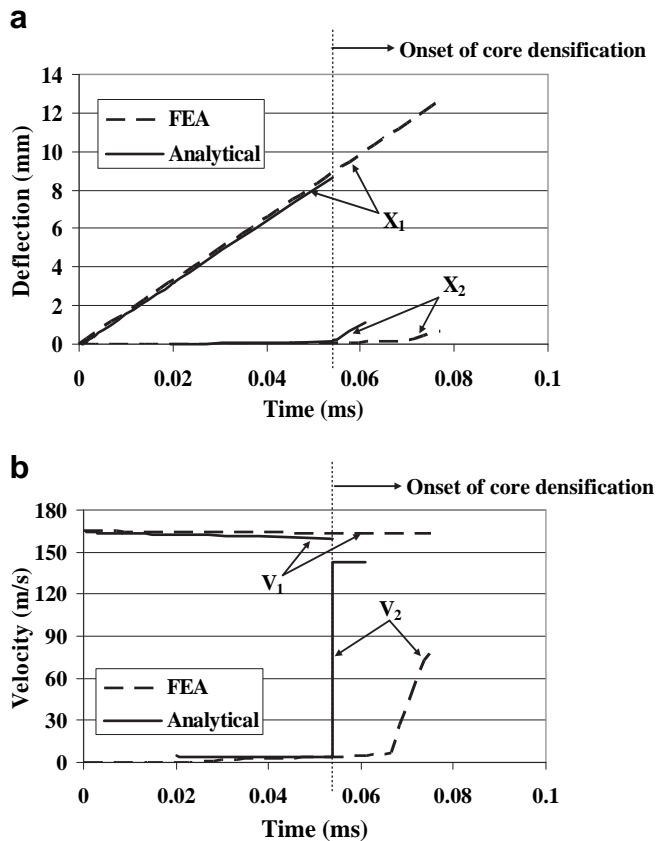


Fig. 10. Comparisons between analytical solution and FEA results: (a) Transient deflection and (b) Transient velocities.

Hashin-Rotem's composite failure criteria for damage initiation, and a progressive damage evolution to specify when to delete elements. All of the above, however, would require computational storage and run time in excess of our current facilities. The purpose of the FEA solution was not to accurately determine the residual velocity of the projectile but to gage how accurate the analytical solution would be in predicting the transient response of the projectile and sandwich panel.

6. Comparison with test data

The residual velocity of the projectile that was reported in this test from Wen et al. [7] was 134.1 m/s. The 1.75 mm-thick facesheets in the test specimen had 3 layers (plies) of woven E-glass polyester. Thus the analytical prediction was only 6.6% higher than the test results without accounting for friction, making any adjustments for high strain rate in material properties, or including accumulated damage and delamination in the facesheets. The frictional force resistance may have been small compared to the inertial forces and load resistances shown in Fig. 6(a) and (b) and used to derive the equations of motion for the incident and back facesheets. The analytical model was used to estimate the strain rates in the facesheets and core. The in-plane strain rates of the facesheets at the projectile radius were estimated to be around 7200 s^{-1} and 1100 s^{-1} for the incident and back facesheets, respectively. The core through-thickness compressive strain rate was about 6400 s^{-1} . At these strain rates, the use of quasi-static material properties may be inappropriate.

High strain rate material properties of the woven roving E-glass polyester were not available, but Harding and Welsh [31]

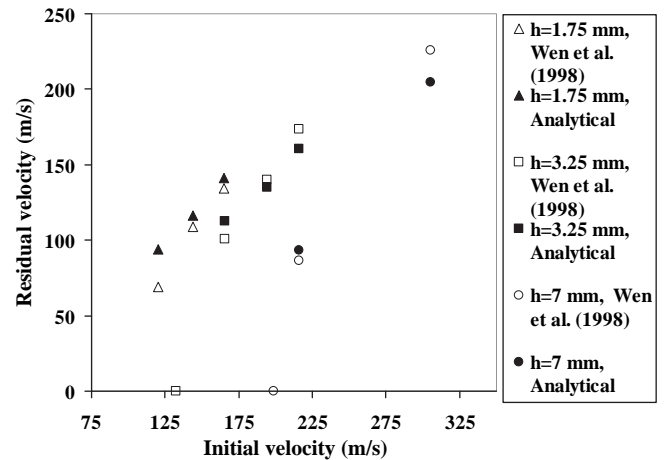


Fig. 11. Comparison of the residual velocity between analytical model and test results from Wen et al. (1998).

performed high strain rate tensile tests on woven roving E-glass epoxy, which would exhibit very similar behavior to woven roving E-glass polyester. From their results on woven roving E-glass epoxy, it was estimated that the woven E-glass polyester would experience a two-fold increase in both stiffness and strength. High strain rate material test on PVC H130 foams by Mahfuz et al. [32] indicated that the core crushing resistance would also be higher at 6400 s^{-1} than values published from quasi-static tests. It is believed that high strain rate behavior of the core, however, is related to the hydrodynamic inertial resistance of the foam. Since this has already been taken into account in the analytical model, adjustment of core properties due to high strain rate was unnecessary. The analytical solution for perforation of the composite sandwich panel was re-derived using a 200% increase in the facesheet stiffness and strength, regardless of property direction. After re-analysis, it was found that the projectile would leave with a residual velocity of 141.2 m/s. Since this was only 1.2% less than the residual velocity found without any adjustment for high strain rate, the contribution by the facesheets must have been very small. Finally, delaminations and other accumulated damage in the facesheets, although important for energy absorption, appear to have little affect on the load resistance functions assumed for local indentation and back facesheet deflections in this test.

The high velocity wave propagation model was used to calculate the residual velocities in several other high velocity impact tests with the hemispherical-nose projectile from Ref. [7]. Two other woven roving E-glass polyester-H130 foam core sandwich panels with facesheet thicknesses 3.25 mm and 7 mm and core thickness 25 mm were also considered. The 1.75 mm, 3.25 mm, and 7 mm facesheets each had 3, 6 and 12 layers of 0/90 degrees woven E-glass polyester, respectively. A factor of two increase in the stiffness and strength of the facesheet was assumed in all cases. The analytical solution and the test results from Wen et al. [7] are compared to each other in Fig. 11. The ballistic limit (defined by zero residual velocity) is not considered a case of high velocity impact but rather low velocity impact, whereby all the kinetic energy of the projectile is consumed in panel deformation and damage. Above the ballistic limit, the analytical predictions of the residual velocities were in relatively good agreement with the test results. The model tends to under-predict the test results at very high impact velocities because both incident and back facesheet deformations become more localized. With very high impact velocity, the situation

approaches the ballistic impact scenario shown in Fig. 1(c), whereby there is hardly any facesheet deformation, and core crushing, delamination, debonding and fracture become dominant mechanisms for failure. Hence, the analytical model for high velocity impact of the composite sandwich panel may be improved by accounting for accumulated damage in the facesheets by introducing a progressive reduction in the facesheet stiffness or load resistance.

7. Concluding remarks

A wave propagation model was developed to obtain residual velocities of a sandwich panel made with E-glass polyester facesheets and Divinycell H130 foam core and subjected to high velocity impact by a hemispherical-nose, cylindrical projectile. Unlike most high velocity impact solution, the solution is fully deterministic and involves the use of no empirical equations. Lagrange’s equations of motion were written for the projectile and effective mass of the facesheets and core as the shock waves travel through sandwich panel. Simple facesheet and core failure criteria were used to determine when to impose changes in the load-bearing resistance of the sandwich during penetration. The transient deflection and velocity of the projectile and sandwich panel compared fairly well with results from finite element analysis. Analytical predictions of the projectile residual velocities were also found to be in good agreement with published experimental data. The analytical model for high velocity impact of the composite sandwich panel may be improved by accounting for accumulated damage in the facesheets and introducing a progressive reduction in the facesheet stiffness or load resistance. These localized damage mechanisms are particularly important at very high projectile velocities where the load resistance functions are primarily controlled by them.

Acknowledgments

This work was supported by Dr. Yapa Rajapakse at the Office of Naval Research under grant N00014-07-1-0423.

Appendix A. Momentum and kinetic energy of incident facesheet during Phase I

The momentum and kinetic energy of the facesheet are found by assuming that the projectile induces the following linear velocity field in the facesheet:

$$\dot{w} = V_1 \left[1 - \frac{r}{\xi_1} \right] \tag{A1}$$

where V_1 is the velocity under the projectile and ξ_1 is the extent of the deformation zone. Since the deformation zone increases with time, the velocity field has a moving boundary and the effective facesheet mass grows as the velocity field spreads away from the impact site. The accumulated linear momentum of the facesheet is

$$L_f = 2\pi \int_0^{\xi_1} \rho_f h V_1 \left(1 - \frac{r}{\xi_1} \right) r dr \tag{A2}$$

$$= \frac{\pi \rho_f h \xi_1^2}{3} V_1$$

The kinetic energy of the facesheet is

$$T_f = \frac{1}{2} (2\pi) \int_0^{\xi_1} \rho_f h V_1^2 \left[1 - \frac{r}{\xi_1} \right]^2 r dr \tag{A3}$$

$$= \frac{\pi \rho_f h \xi_1^2}{12} V_1^2$$

Appendix B. Momentum and kinetic energy of core during Phase I

Both elastic and plastic compressive stress waves propagate in the core with speeds C_d and C_p . Given that $C_d > C_p$, the plastic zone in the foam is confined to a boundary layer just beneath the incident facesheet. The particle velocity in the foam under the projectile is specified by the projectile velocity V_1 , while the particle velocity in the foam away from the projectile is given by the assumed velocity field of the incident facesheet given by Eq. (5). The plastic zone extends to a depth $h_p = L_{pl} \left(1 - \frac{r}{\xi_1} \right)$ as shown in Fig. 7. The depth of the plastic core under the projectile is $L_{pl} = \delta / \epsilon_D$. Ahead of the plastic zone is the elastic zone with depth $h_e = (C_d t - L_{pl}) \left(1 - \frac{r}{\xi_1} \right)$. The distribution of the particle velocities under the projectile at $r = 0$ and at $r = \xi_1 / 2$ are indicated in Fig. 7.

The momentum of the plastically deformed portion of the core is

$$L_c = 2\pi \rho_D \int_0^{\xi_1} \left[\int_0^{h_p} V_1 \left(1 - \frac{r}{\xi_1} \right) dz \right] r dr \tag{B1}$$

where densification of the core has caused the density to become $\rho_D = \rho_c / (1 - \epsilon_D)$. The momentum in the plastic part of the core is

$$L_c = \frac{\pi \rho_c L_{pl}}{6(1 - \epsilon_D)} \xi_1^2 V_1 \tag{B2}$$

The kinetic energy of the plastically deformed portion of the core is

$$T_c = \pi \rho_D \int_0^{\xi_1} \left[\int_0^{h_p} V_1^2 \left(1 - \frac{r}{\xi_1} \right)^2 dz \right] r dr \tag{B3}$$

$$= \frac{\pi \rho_c L_{pl}}{20(1 - \epsilon_D)} \xi_1^2 V_1^2$$

References

- [1] Edgren F, Soutis C, Asp LE. Damage tolerance analysis of NCF composite sandwich panels. *Comp Sci Tech* 2008;68(13):2635–45.
- [2] Karger L, Baaran J, Tessmer J. Rapid simulation of impacts on composite sandwich panels inducing barely visible damage. *Composite Structures* 2007;79(4):527–34.
- [3] Meo M, Vignjevic R, Marengo G. The response of honeycomb sandwich panels under low-velocity impact loading. *Int J Mech Sci* 2005;47(9):1301–25.
- [4] Hampson PR, Moatamedi M. A review of composite structures subjected to dynamic loading. *Int J Crashworthiness* 2007;12(4):411–28.
- [5] Ben-Dor G, Dubinsky A, Elperin T. Ballistic impact: recent advances in analytical modeling of plate penetration dynamics – a review. *Appl Mech Rev* 2005;58:355–71.
- [6] Olsson R. Mass criterion for wave controlled impact response of composite plates. *Composites Part A* 2000;31(8):879–87.
- [7] Wen HM, Reddy TY, Reid SR, Soden SR. Indentation, penetration and perforation of composite laminates and sandwich panels under quasi-static and projectile loading. *Key Eng Mat* 1998;141-143(Part 2):501–52.
- [8] Skvortsov V, Kepler J, Bozhevolnaya E. Energy partition for ballistic penetration of sandwich panels. *Int J Impact Engng* 2003;28(7):697–716.
- [9] Velmurugan R, Babu MG, Gupta NK. Projectile impact on sandwich panels. *Int J Crashworthiness* 2006;11(2):153–64.
- [10] Hoo Fatt MS, Sirivolu D. High velocity impact of a composite sandwich panel. In: Jones N, Brebbia CA, editors. *Proceedings of the 10th International Conference on Structures under Shock and Impact*, The Algarve, Portugal: WIT press; May 14–16, 2008. p. 3–13.

- [11] Kashtalyan M, Soutis C. Analysis of composite laminates with intra- and interlaminar damage. *Progress in Aerospace Sciences* 2005;41:152–73.
- [12] Hashin Z. Failure criteria for unidirectional fiber composites. *J Appl Mech* 1980;47:329–34.
- [13] Matzenmiller A, Lubliner J, Taylor RL. A constitutive model for anisotropic damage in fiber-Composites. *Mechanics of Materials* 1995;20:125–52.
- [14] Tay TE, Liu G, Tan VBC, Sun XS, Pham DC. Progressive failure analysis of composites. *J Comp Mat* 2008;42(18):1921–66.
- [15] McGregor C, Zobeiry N, Vaziri R, Poursartip A. A constitutive model for progressive compressive failure of composites. *J Comp Mat* 2008;42(25):2687–716.
- [16] Olsson R, Donadon MV, Falzon BG. Delamination threshold load for dynamic impact on plates. *Int J Solids Struct* 2006;43(10):3124–41.
- [17] Lin C, Hoo Fatt MS. Perforation of sandwich panels with honeycomb cores by hemispherical nose projectiles. *J Sand Struct Mat* 2005;7(2):133–72.
- [18] Mines RAW, Worrall CM, Gibson AG. Low velocity perforation behaviour of polymer composite sandwich panels. *Int J Impact Engng* 1998;21(10):855–79.
- [19] Lee JW, Kong CD, Soutis C. Modelling of low velocity impact damage in laminated composites. *J Mech Sci Tech* 2005;19(4):947–57.
- [20] Sierakowski RL, Chaturvedi SK. *Dynamic Loading and Characterization of Fiber-Reinforced Composites*. New York: John Wiley and Sons, Inc.; 1997.
- [21] Gibson LJ, Ashby MF. *Cellular Solids Structures and Properties*. Cambridge: Cambridge University Press; 1999.
- [22] Ashby MF, Evans AG, Fleck NA, Gibson LJ, Hutchinson JW, Wadley HNG. *Metal Foams: A Design Guide*. London: Butterworth Heinemann; 2000.
- [23] Timoshenko S, Wionowsky-Krieger S. *Theory of Plates and Shells*. New York: Mc-Graw Hill Inc.; 1959.
- [24] Sirivolu, D. An analytical model for high velocity impact of composite sandwich panels. 2008, MS thesis. The University of Akron, Ohio, Available at http://www.ohiolink.edu/etd/sendpdf.cgi/Sirivolu%20Dushyanth.pdf?acc_num=akron1227548412.
- [25] Daniel IM. Failure of composite materials. *Strain* 2007;43(1):4–12.
- [26] Mines RAW, Roach AM, Jones N. High velocity perforation behaviour of polymer composite laminates. *Int J Impact Engng* 1999;22(6):561–88.
- [27] Scida D, Aboura Z, Benzeggagh ML, Bocherens E. A micromechanics model for 3D elasticity and failure of woven-fibre composite materials. *Comp Sci Tech* 1999;59(4):505–17.
- [28] Hoo Fatt MS, Lin C. Perforation of clamped, woven E-glass/polyester panels. *Composites Part B* 2004;35(5):359–78.
- [29] Boh JW, Louca LA, Choo YS, Mouring SE. Damage modelling of SCRIMP woven roving laminated beams subjected to through-thickness shear. *Composites Part B* 2005;36(5):427–38.
- [30] Toftegaard H. Initial fixture design for direct shear testing of sandwich core materials. In: Lilholt H, Madsen B, Anderson TL, Mikkelsen LP, Thygesen A, editors. *Proceedings of the 27th Riso International Symposium on Material Science*. Roskilde (Denmark): Riso National Laboratory, Roskilde; 2006. p. 337–47.
- [31] Harding J, Welsh LM. A tensile testing technique for fibre-reinforced composites at impact rates of strain. *J Mat Sci* 1983;18(6):1810–26.
- [32] Mahfuz H, Thomas T, Rangari V, Jeelani S. On the dynamic response of sandwich composites and their core materials. *Comp Sci Tech* 2006;66(14):2465–72.

Analytical Modeling of Composite Sandwich Panels under Blast Loads

MICHELLE S. HOO FATT* AND LEELAPRASAD PALLA

*Department of Mechanical Engineering
University of Akron, Akron, OH 44325-3903, USA*

ABSTRACT: Analytical solutions were derived for the transient response and damage initiation of a foam-core composite sandwich panel subjected to blast loading. The panel response was modeled in two consecutive phases: (1) a through-thickness wave propagation phase leading to permanent core crushing deformations and (2) a transverse shear wave propagation phase resulting in global panel deflections. The predicted transient deformation of a sandwich panel consisting of E-glass vinyl ester facesheets and H100 PVC foam core compared well with ABAQUS predictions. Analytical predictions of the critical impulse for damage initiation in several foam sandwich panels also compared well with ABAQUS predictions.

KEY WORDS: composite sandwich panel, blast response, critical impulse to failure, analytical model.

INTRODUCTION

THERE HAS BEEN growing interest in using lightweight composite sandwich panels for the construction of military land and sea vessels, which can be exposed to blast and impact during combat. Composite sandwich panels used in these applications offer significant weight savings leading to increased payload and greater range of travel, reduced electromagnetic and acoustic signatures, better corrosion resistance, and lower maintenance cost when compared to traditional metallic panels. Already a great deal of work has been accomplished in the study of projectile impact of composite sandwich panels. A recent review of dynamic loading of composite panels can be found in Hampson and Moayamedi [1]. Tagarielli et al. [2] have recently demonstrated that glass fiber vinyl sandwich beams with PVC foam cores and balsa wood have higher ballistic resistance than monolithic glass fiber vinyl beams of equal weight. While there has been much research concerning localized

*Author to whom the correspondence should be addressed. E-mail: hoofatt@uakron.edu
Figures 7–11 appear in color online: <http://jasm.sagepub.com>

projectile impact damage of composite sandwich panels, very little work has been done to address damage of composite sandwich panels under distributed pressure pulse loading, such as that caused by an underwater or air blast.

Several recent articles have dealt with the blast resistance of metal sandwich panels with metallic foam, honeycomb, truss, and other types of metal sandwich core topologies [3–6], but none of these can be directly applied to a composite sandwich panel made of anisotropic elastic facesheets and polymeric foam or balsa wood cores. The facesheets of the composite sandwich panels usually consist of fiber-reinforced laminates that are anisotropic, inhomogeneous, and elastic, while the metallic sandwich panel consists of isotropic, homogeneous, and elastic–plastic materials. This article presents an analytical model that can be used to determine the blast performance of a composite sandwich panel. It specifically provides an analytical model for predicting the transient response and failure of a composite sandwich panel subjected to pressure pulse or impulsive loading, i.e., load durations that are of the order of the through-thickness wave travel time and are short compared to the time associated with overall bending/shear panel deformation. Finite element analysis with ABAQUS Explicit is used as a tool for comparing with the results of the analytical model.

PROBLEM FORMULATION

Consider a fully clamped, composite sandwich panel of radius a , as shown in Figure 1. The facesheets consist of orthotropic composite plates of thickness h , and the core is crushable polymeric foam of thickness H . Assume for simplicity that the panel is subjected to a uniformly distributed pressure pulse

$$p(t) = \begin{cases} p_o \left(1 - \frac{t}{\tau}\right), & 0 \leq t \leq \tau \\ 0, & t \geq \tau \end{cases} \quad (1)$$

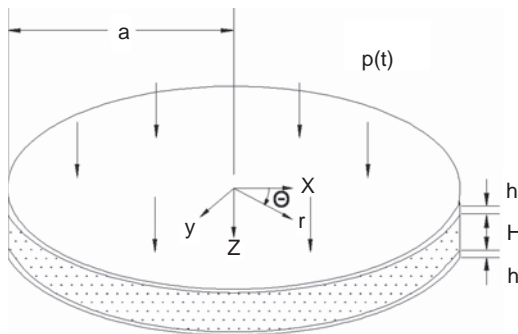


Figure 1. Composite sandwich panel subjected to uniformly distributed pressure pulse.

where p_o is the peak pressure and τ is the load duration. Other more complicated pressure transients can be used to more accurately simulate underwater and air explosions [7,8], but as seen later in this study, that it is not the actual function used to describe the pressure transient; rather, it is used to measure the impulse (integrated area under the pressure pulse diagram) that governs the blast response and ultimate failure of the panel.

Provided no failure has occurred to the panel from the blast, the response of the composite sandwich panel may be described by the three phases of motion depicted in Figure 2(a)–(c). In Phase I, a through-thickness, compressive stress wave propagates from the incident facesheet to the rear facesheet. In this phase the sandwich panel primarily experiences core crushing, while impulsive transverse shear reaction forces are induced around the clamped boundaries. Figure 2(a) shows that there is no global deflection in Phase I. At the end of Phase I, momentum and kinetic energy are transferred globally to the panel and the now-established impulsive transverse shear reaction force just begins to propagate from the clamped boundaries toward the center of the panel. The pressure pulse resulting from the blast would have either ended or decayed to almost negligible amplitude by the start of

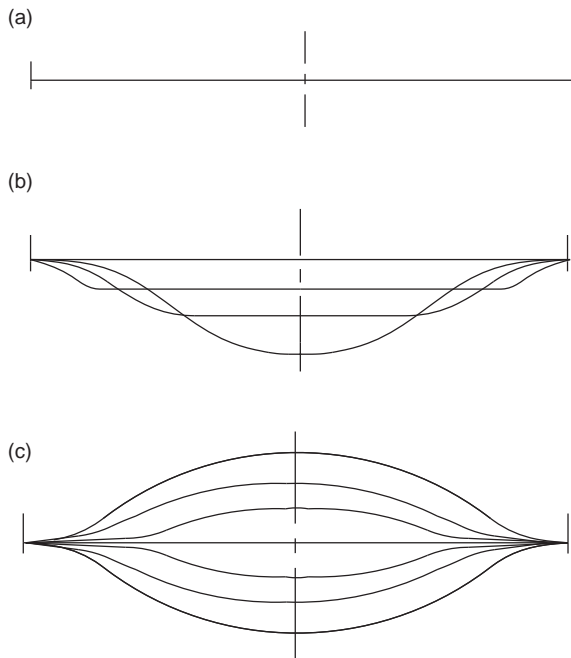


Figure 2. Three phases of blast response: (a) Phase I: through-thickness wave propagation, (b) Phase II: transverse wave propagation, and (c) Phase III: elastic vibration.

Phase II. Momentum, equivalent to the impulse from the blast, would be transferred to the sandwich panel with a reduced core thickness from Phase I. In Phase II, the transverse shear stress wave due to the reaction forces at the clamped boundary propagates from the clamped boundary toward the center of the panel. This transverse stress wave is an unloading wave, causing bending and shear deformations to develop behind its front, as shown in Figure 2(b). The elastic unloading transverse shear wave brings the panel to maximum deflection when it reaches the center of the panel. At the end of Phase II, the unloading transverse shear wave reverses sign and direction of travel thereby causing the panel to rebound. The transverse shear wave reflects back and forth from the boundary to the center of the panel in Phase III. As depicted in Figure 2(c), elastic vibrations take place in Phase III.

During Phase I, high-intensity transverse shear stresses are developed at the clamped boundary and these may cause transverse shear fracture at the clamped boundaries of the panel. Transverse shear fracture can be avoided by using reinforcements at the boundaries. The second mode of failure that can occur during blasts is tensile fracture at the center of the panel where there is maximum bending strain at the end of Phase II. These two failure modes in addition to permanent deformation were first observed on impulsively loaded aluminum beams by Menkes and Opat [9] and later, on aluminum plates by Teeling-Smith and Nurick [10]. They have also been experimentally observed on composite plates by Franz et al. [11].

This article focuses on the first two phases of blast response described in Figure 2(a) and (b) because they are relevant to the failure of the composite sandwich panel subjected to blast loading. The analytical solutions presented for the panel response is to be distinguished from previous models in which Phase II was treated as the forced modal response of sandwich panels [12]. Wave propagation effects are taken into consideration in both phases. The wave propagation models presented here should be distinguished from solutions in the field of ultrasonics which involves the transmission, dispersion, and reflection of very small, amplitude stress-wave propagation in order to evaluate the microstructure of a composite panel. Here we are concerned with the propagation of stress waves in a panel subject to high-intensity loading and the subsequent deformation and damage initiation that results from the loading. Phase II is treated as an initial-value problem because the load duration is short compared to the transverse wave propagation time and the natural period of vibration in Phase III.

PHASE I – THROUGH-THICKNESS WAVE PROPAGATION

The wave speed in polymeric foam is low and a thick composite sandwich panel with a polymeric foam core is likely to undergo transient local facesheet

indentation and core crushing while the pressure pulse is still acting. Take for example, H100 PVC foam core with a density of 100 kg/m^3 and a compressive elastic modulus of 35 MPa. Elastic uniaxial stress waves propagate through a 25 mm-thick core made of H100 PVC foam in $\sim 0.04 \text{ ms}$. An initial pressure pulse duration of this magnitude is not uncommon for naval composite sandwich ships subjected to underwater and air blast explosions [7,8]. Thus one can assume that permanent plastic deformations of the core take place from a transient event, that is, during the load application. Phase I response is described by stress waves propagating through the thickness of the facesheets and core.

Transmission and Reflection at Interfaces

The transmission and reflection of stress waves through the multi-layered composite sandwich panel is shown in Figure 3. Stress waves are transmitted from the incident facesheet to the foam at Interface 1 and from the foam to the distal facesheet at Interface 2. When the incident stress σ_I first reaches Interface 1, the transmitted stress σ_{T_1} and the reflected stress σ_{R_1} are given as follows [13]:

$$\sigma_{T_1} = -k_{T_1}p(t - t_1)u(t - t_1), \quad k_{T_1} = \frac{2\rho_c C_c}{(\rho_f C_f + \rho_c C_c)} \tag{2}$$

and

$$\sigma_{R_1} = -k_{R_1}p(t - t_1)u(t - t_1), \quad k_{R_1} = \frac{(\rho_c C_c - \rho_f C_f)}{(\rho_f C_f + \rho_c C_c)} \tag{3}$$

where $t_1 = h/C_f$ is the wave transit time through the facesheet; C_f and C_c are the wave speeds in the facesheet and core, respectively; ρ_f and ρ_c are the density of the facesheet and core, respectively; and $u(\cdot)$ is the unit step function.

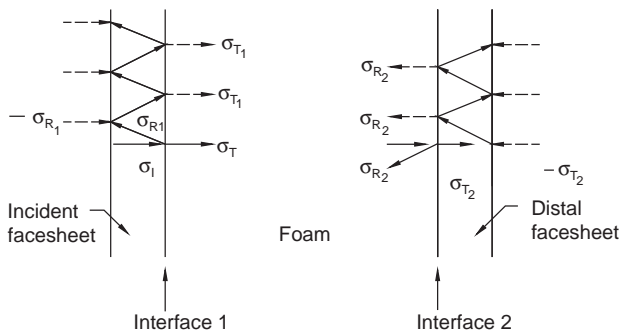


Figure 3. Transmission of stress waves through facesheets and foam in sandwich panel.

The wave speed in an orthotropic plate in uniaxial strain is derived in Appendix A as

$$C_f = \sqrt{\frac{(1 - \nu_{12})E_{33}}{[1 - \nu_{12} - \nu_{32}(\nu_{13} + \nu_{23})]\rho_f}} \tag{4}$$

where E_{ij} and ν_{ij} are elastic modulus and Poisson’s ratio of the orthotropic facesheet. This wave speed is usually higher than the more commonly used uniaxial stress wave speed, which is equal to $\sqrt{E_{33}/\rho_f}$. The wave speed in the foam is discussed in the following section.

The reflected wave in the incident facesheet is tensile because $\rho_f C_f \gg \rho_c C_c$. This reflected wave is again reflected, but as a compressive stress wave when it reaches the outer surface of the incident facesheet. The process of reflection and transmission of waves at Interface 1 repeats itself over and over again at intervals of $2t_1$. Thus the transmitted stress in the foam at Interface 1 is given as

$$\begin{aligned} \sigma_{T_1} = & -k_{T_1} p(t - t_1)u(t - t_1) + k_{T_1} k_{R_1} p(t - 3t_1)u(t - 3t_1) \\ & - k_{T_1} k_{R_1}^2 p(t - 5t_1)u(t - 5t_1) \dots \\ & + (-1)^{n+1} k_{T_1} k_{R_1}^n p(t - (2n + 1)t_1)u(t - (2n + 1)t_1) \end{aligned} \tag{5}$$

where n is the number of reflections up to that time.

The transmitted stress wave in the foam σ_{T_1} reflects back as a compressive wave into the foam and is transmitted as a compressive stress wave in the distal facesheet when it first reaches Interface 2. The transmitted stress in the distal facesheet σ_{T_2} is further reflected as a tensile stress wave from the outer surface of the distal facesheet. This reflected stress waves is then transmitted as a tensile stress wave in the foam and reflected back as a compressive stress wave into the facesheet. The part that is transmitted to the foam adds to the reflected stress waves in the foam σ_{R_2} . This process repeats itself indefinitely so that the reflected stress wave at any time is given by

$$\begin{aligned} \sigma_{R_2} = & -k_{R_2} \sigma_{T_1}(t - t_2)u(t - t_2) + k_{T_2} k_{T_1} \sigma_{T_1}(t - 2t_1 - t_2)u(t - 2t_1 - t_2) + \\ & - k_{T_2} k_{T_1} k_{R_1} \sigma_{T_1}(t - 4t_1 - t_2)u(t - 4t_1 - t_2) \\ & + k_{T_2} k_{T_1} k_{R_1}^2 \sigma_{T_1}(t - 6t_1 - t_2)u(t - 6t_1 - t_2) \dots \\ & + (-1)^{n+1} k_{T_2} k_{T_1} k_{R_1}^n \sigma_{T_1}(t - 2nt_1 - t_2)u(t - 2nt_1 - t_2) \end{aligned} \tag{6}$$

where $t_2 = H/C_c$, $k_{T_2} = 2\rho_f C_f / (\rho_f C_f + \rho_c C_c)$ and $k_{R_2} = (\rho_f C_f - \rho_c C_c) / (\rho_f C_f + \rho_c C_c)$. The reflected stress is a tensile unloading elastic stress wave. Permanent plastic strains or local indentation of the foam results after elastic unloading.

Elastic and Plastic Waves in Foam

The facesheets are very stiff and remain elastic during wave transmissions, but the polymeric foam core is elastic-plastic with a compressive stress-strain characteristic as shown in Figure 4 [14]. The foam is linear elastic with a compressive modulus of E_c until it yields at a flow stress, q . Rapid compaction of cells causes the density to change in the plateau region until full densification has occurred at ϵ_D . The stress rises to a maximum plastic stress σ_p at the densification strain. The maximum plastic stress at the densification strain depends on the load intensity.

If the pressure pulse amplitude is high enough to yield the core, elastic and plastic waves would be generated in the foam during Phase I. In Ashby et al. [15], the elastic uniaxial stress wave speed in the foam is given by $\sqrt{E_c/\rho_c}$ and the plastic wave speed is given by $C_p = \sqrt{(\sigma_p - q)/\rho_c \epsilon_D}$, where σ_p is the stress in the densification region (Figure 4). Elastic waves propagate first in the core and are later followed by plastic waves, as shown in Figure 5. By substituting isotropic properties for foam in Equation (4), one can derive the following expression for elastic wave speed in the foam in a

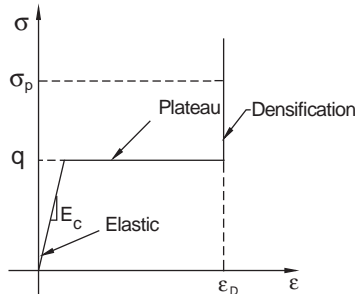


Figure 4. Compressive stress-strain curve of polymeric foam.

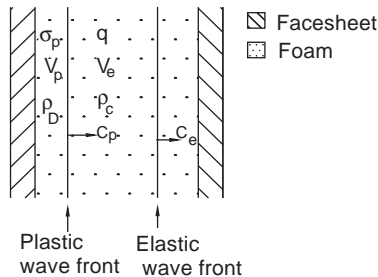


Figure 5. Elastic and plastic wave fronts in foam.

state of uniaxial strain:

$$C_e = \sqrt{\frac{(1 - \nu_c)E_c}{[1 - \nu_c - 2\nu_c^2]\rho_c}} \quad (7)$$

The densification strain is related to particle velocities in the elastic and plastic regions, V_e and V_p , respectively. After time t , the plastic zone gage length is $C_p t$ and the compression in the plastic zone is $V_p t - V_e t$. Therefore, the densification strain is

$$\varepsilon_D = \frac{V_p - V_e}{C_p} \quad (8)$$

The particle velocity in the plastic region is in turn related to the plastic stress σ_p and density of foam after densification ρ_D [13]:

$$V_p = \frac{\sigma_p}{\rho_D C_p} \quad (9)$$

where $\rho_D = \rho_c / (1 - \varepsilon_D)$. Similarly, $V_e = q / \rho_c C_e$. Combining Equations (8) and (9) to eliminate V_p and expressing C_p in terms of σ_p gives the following quadratic equation that can be solved for σ_p :

$$\left(\frac{\rho_c - \rho_D}{\rho_c}\right)^2 \sigma_p^2 + \left[\frac{2\rho_D q}{\rho_c} \left(\frac{\rho_c - \rho_D}{\rho_c}\right) - \frac{V_e^2 \rho_D^2}{\rho_c \varepsilon_D}\right] \sigma_p + \frac{\rho_D^2 q^2}{\rho_c^2} + \frac{V_e^2 \rho_D^2 q}{\rho_c \varepsilon_D} = 0 \quad (10)$$

Local Indentation

Permanent plastic strains arise when the elastic unloading wave reaches the plastic wave front. The local indentation is confined to the plastic zone and may be calculated from the densification strain and the characteristic gage length of the plastic zone. This characteristic gage length is $C_p \Delta T$, where ΔT is the time from the start of transmission of σ_p to the time when the elastic unloading wave reaches the plastic wave front. Thus the local indentation is

$$\delta = \varepsilon_D C_p \Delta T \quad (11)$$

Let t_p be the start time of plastic wave transmission of σ_p at Interface 1. Then,

$$\Delta T = 3t_1 + \frac{H}{C_e} + \frac{(H - C_p \Delta T)}{C_e} - t_p \quad (12)$$

Solving for ΔT , one gets

$$\Delta T = \frac{(2H/C_e + 3t_1 - t_p)}{(1 + C_p/C_e)} \quad (13)$$

The start time of plastic wave transmission t_p is determined by the transmitted core stress defined in Equation (5).

PHASE II – GLOBAL SHEAR/BENDING

Subsequent to Phase I, the load has been removed and the core has been crushed permanently to a height of $H' = H - \delta$. Momentum is transferred to the sandwich panel, which has become impulsively loaded with a uniformly distributed velocity field (Figure 6(a) and (b)). Conservation of momentum gives the initial velocity of the panel as

$$v_i = \frac{p_o \tau}{2(\rho_c H + 2\rho_f h)} \tag{14}$$

Let us denote the distance from the center of the panel to the wave front of the transverse shear wave as ξ . A transverse shear elastic unloading wave propagates from the clamped boundaries with velocity ξ . This unloading wave instantaneously brings the plate to rest behind the wave front. As the plate is brought to rest, it undergoes shear and bending deformations as shown in Figure 6(a).

System Lagrangian

Dynamic equilibrium of the complete sandwich can be expressed in terms of the maximum deflection at the center, Δ , and an equivalent shear angle, α_o . These two degrees of freedom have associated velocities, v_i and Ω , respectively. The kinetic energy for the sandwich is thus $T = (1/2)m_{eff}v_i^2 + (1/2)I_{eff}\Omega^2$, where $m_{eff} = \pi\xi^2[2\rho_f h + \rho_c H]$ is the effective sandwich mass and I_{eff} is the effective

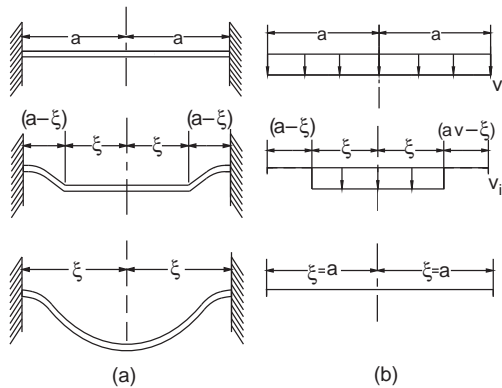


Figure 6. Global panel bending/shear response: (a) deformation profiles and (b) velocity fields.

sandwich rotary inertia. Assuming that the rate of angular rotation is maximum at the wave front and decreases linearly to zero at the boundary,

$$\dot{\alpha}(r) = \begin{cases} 0, & 0 \leq r \leq \xi \\ \Omega \frac{(a-r)}{(a-\xi)}, & \xi \leq r \leq a \end{cases} \tag{15}$$

Then, the effective rotary inertia for the sandwich is $I_{eff} = (\pi/6)\tilde{I}(a - \xi)(a + 3\xi)$, where

$$\tilde{I} = \sum_{k=1}^3 \rho_k(z_k^3 - z_{k-1}^3) = \frac{\rho_f}{12}(3hH^2 + 3h^2H + h^3) + \frac{\rho_c}{12}H^3.$$

The elastic potential energy of the system is equivalent to the bending/shear strain energy of the sandwich, $\Pi = U$. The Lagrangian for the whole model is $L = T - \Pi$. For dynamic equilibrium,

$$\frac{\partial}{\partial t} \left(\frac{\partial L}{\partial v_i} \right) - \frac{\partial L}{\partial \Delta} = 2\pi\xi\dot{\xi}[2\rho_f h + \rho_c H]v_i + \frac{\partial U}{\partial \Delta} = 0 \tag{16}$$

and

$$\frac{\partial}{\partial t} \left(\frac{\partial L}{\partial \Omega} \right) - \frac{\partial L}{\partial \alpha_o} = \Omega \frac{\partial I_{eff}}{\partial t} + I_{eff} \frac{\partial \Omega}{\partial t} + \frac{\partial U}{\partial \alpha_o} = 0 \tag{17}$$

Bending/Shear Strain Energy Potential

Assume that in-plane deformations are negligible compared to the transverse deformation. The elastic strain energy of the symmetric sandwich panel with the orthotropic facesheet is then given as

$$\begin{aligned} U = \int_S & \left\{ \frac{D_{11}^s}{2} \left(\frac{\partial \bar{\alpha}}{\partial x} \right)^2 + D_{12}^s \left(\frac{\partial \bar{\beta}}{\partial y} \right) \left(\frac{\partial \bar{\alpha}}{\partial x} \right) \right. \\ & + \frac{D_{22}^s}{2} \left(\frac{\partial \bar{\beta}}{\partial y} \right)^2 + A_{55}^s \left[\frac{\bar{\alpha}^2}{2} + \bar{\alpha} \frac{\partial w}{\partial x} + \frac{1}{2} \left(\frac{\partial w}{\partial x} \right)^2 \right] \\ & \left. + A_{44}^s \left[\frac{\bar{\beta}^2}{2} + \bar{\beta} \frac{\partial w}{\partial y} + \frac{1}{2} \left(\frac{\partial w}{\partial y} \right)^2 \right] + D_{66}^s \left[\frac{1}{2} \left(\frac{\partial \bar{\alpha}}{\partial y} \right)^2 + \frac{\partial \bar{\alpha}}{\partial y} \frac{\partial \bar{\beta}}{\partial x} + \frac{1}{2} \left(\frac{\partial \bar{\beta}}{\partial x} \right)^2 \right] \right\} dS \end{aligned} \tag{18}$$

where w is the transverse deflections, $\bar{\alpha}$ and $\bar{\beta}$ are shear angles associated with the x and y directions, respectively, D_{ij}^s is the sandwich bending stiffness matrix, A_{44}^s and A_{55}^s are the transverse shear stiffnesses, and S is the panel surface area. The superscript ‘s’ is used to denote the sandwich properties.

Equation (18) is a special case of a more general expression for the elastic strain energy of a symmetric sandwich panel with orthotropic facesheet [16].

Finite element analysis using ABAQUS Explicit indicates that the transverse deformation, w , and the shear rotations with respect to the radial direction, $\bar{\alpha}$, are of the following forms:

$$w(r) = \begin{cases} \Delta, & 0 \leq r \leq \xi \\ \Delta \left(1 - \left(\frac{r - \xi}{a - \xi} \right)^2 \right)^2, & \xi \leq r \leq a \end{cases} \quad (19)$$

and

$$\bar{\alpha}(r) = \begin{cases} 0, & 0 \leq r \leq \xi \\ 4\alpha_o \frac{(r - \xi)(a - r)}{(a - \xi)^2}, & \xi \leq r \leq a \end{cases} \quad (20)$$

where Δ is the global deflection and α_o is the rotation at $r = (a + \xi)/2$. The deflection profile described by Equation (19) was found by fitting functions to the transient deflection profiles in the region. The transverse shear angle function was derived from the transverse shear strain, γ_{rz} , and slope of the deflection profile: $\bar{\alpha} = \gamma_{rz} - \partial w / \partial r$.

To evaluate the integral expression in Equation (18) to polar coordinates, set $dS = r dr d\theta$ and derivatives with respect to x and y as $\partial/\partial x = \cos \theta \partial/\partial r - \sin \theta/r \partial/\partial \theta$ and $\partial/\partial y = \sin \theta \partial/\partial r + \cos \theta/r \partial/\partial \theta$, respectively. Furthermore, for the special case of $D_{22}^s = D_{11}^s$ and $A_{44}^s = A_{55}^s$, Equation (18) becomes

$$\begin{aligned} U = & \frac{8(a + \xi)}{3(a - \xi)} [\pi D_{11}^s + 2D_{12}^s + (2 + \pi)D_{66}^s] \alpha_o^2 \\ & + \frac{2}{105} \frac{A_{55}^s}{(a - \xi)} [28\pi(a^3 - a\xi^2 - a^2\xi + \xi^3) \alpha_o^2 \\ & + (-176a^2 + 16\xi a + 160\xi^2) \alpha_o \Delta + (29\pi\xi + 35\pi a) \Delta^2] \end{aligned} \quad (21)$$

EQUATIONS OF MOTION

The propagation speed of the unloading elastic wave $\dot{\xi}$ is assumed constant and defined as a negative quantity in Figure 6(a) and (b). Denoting $\dot{\xi} = -(a - \xi)/t$ and $\Delta = v_i t$, one gets the following coupled equations of motion from Equations (16) and (17):

$$\begin{aligned} -2\pi[2\rho_f h + \rho_c H] \xi \frac{(a - \xi)}{t} v_i + \frac{2}{105} \frac{A_{55}^s}{(a - \xi)} [-16(a - \xi)(11a + 10\xi) \alpha_o \\ + 2\pi(29\xi + 35a) v_i t] = 0 \end{aligned} \quad (22)$$

and

$$\begin{aligned} & \frac{\pi}{6} \tilde{I}(a - \xi)(a + 3\xi) \frac{d^2 \alpha_o}{dt^2} - \frac{\pi}{3} \tilde{I} \frac{(a - \xi)(a - 3\xi)}{t} \frac{d\alpha_o}{dt} \\ & + \frac{16(a + \xi)}{3(a - \xi)} [\pi D_{11}^s + 2D_{12}^s + (2 + \pi)D_{66}^s] \alpha_o \\ & + \frac{2}{105} A_{55}^s [56\pi(a^2 - \xi^2)\alpha_o - 16(11a + 10\xi)v_{it}] = 0 \end{aligned} \quad (23)$$

where $\alpha_o(0) = 0$ and $\dot{\alpha}_o(0) = 0$.

TRANSIENT DEFORMATIONS

As an example, consider a fully clamped, sandwich panel made of E-glass vinyl ester facesheets and Divinycell H100 foam core, with a radius 250 mm, facesheet thickness 2 mm, and core thickness 25 mm. Material properties for the E-glass vinyl ester and Divinycell H100 foam are given in Table 1. The material properties for the Divinycell H100 and H200 foams in Table 1 were taken from Mines et al. [17]. As noted in the footnotes of Table 1, additional material properties for the Divinycell H100 and H200 foams as well as the Klegecell R300 foam were taken from the data in these references [18–23]. Let the sandwich panel be subject to a uniformly distributed pressure pulse of the form given in Equation (1), where $p_o = 10$ MPa and $\tau = 0.05$ ms.

This problem was modeled in 2D form assuming axi-symmetric conditions for the Phase I response and in full 3D form for both Phase I and Phase II responses using ABAQUS Explicit Version 6.7. In the 2D model, continuum axi-symmetric, four-node reduced integration, CPX4R, was chosen for both facesheets and foam. In the 3D model, four-node reduced integration shell elements, S4R and continuum 3D, and eight-node reduced integration element, C3D8R, were chosen for the facesheets and core, respectively. The E-glass vinyl ester was considered as orthotropic elastic material, and the Divinycell H100 foam was modeled as crushable foam with isotropic hardening. The plastic hardening curves were taken from Ashby et al. [15] for the Divinycell H100 and H200 foams, and Rizov and Mladensky [20] for the Klegecell R300 foam. Although full integration elements could have been used for the FEA analysis, it was found that there would be very minor differences in the solution with full and reduced integration elements. Use of full integration elements simply did not warrant the very long computational run time and huge data files associated with them.

Table 1. Facesheet and foam material properties.

	E-glass/vinyl ester	Divinycell H100	Divinycell H200	Klegecell R300 ⁵
Density (kg/m ³)	1391.3	100	200	300
Thickness (mm)	2	25	25	25
E_{11} (+) (GPa)	17	0.126	0.170	–
E_{22} (+) (GPa)	17	0.126	0.170	–
E_{33} (+) (GPa)	7.48 ¹	0.126	0.170	–
E_{11} (–) (GPa)	19	0.035	0.105	0.263
E_{22} (–) (GPa)	19	0.035	0.105	0.263
E_{33} (–) (GPa)	–	0.035	0.105	0.263
$\nu_{12} = \nu_{21}$	0.13	0.31 ³	0.3 ⁴	0.234 ⁶
$\nu_{13} = \nu_{31}$	0.28 ²	0.31 ³	0.3 ⁴	0.234 ⁶
$\nu_{31} = \nu_{32}$	0.12	0.31 ³	0.3 ⁴	0.234 ⁶
$G_{12} = G_{21}$ (GPa)	4.0	0.01335 ³	0.0403 ⁴	0.106 ⁶
$G_{23} = G_{32}$ (GPa)	1.73 ¹	0.01335 ³	0.0403 ⁴	0.106 ⁶
$G_{13} = G_{31}$ (GPa)	1.73 ¹	0.01335 ³	0.0403 ⁴	0.106 ⁶
q (MPa)	–	1.4	4.35	7.8
ε_D	–	0.76	0.7	0.285
σ_{1f} (+) (MPa)	270	3.2	6.4	–
σ_{1f} (–) (MPa)	200	1.53	4.36	–
σ_{2f} (+) (MPa)	270	3.5	6.4	–
σ_{2f} (–) (MPa)	200	1.53	4.36	–
$\tau_{12f}(+) = \tau_{21f}(+)$ (MPa)	40	1.47	3.86	–
$\tau_{13f}(+) = \tau_{31f}(+)$ (MPa)	31.6 ¹	1.47	3.86	–
$\tau_{23f}(+) = \tau_{32f}(+)$ (MPa)	31.6 ¹	1.47	3.86	–
$\varepsilon_{1f}(+)$	0.021	–	–	–
E_a (MJ/m ³)	2.7	–	–	–

¹Obtained from Reference [18].²Obtained from Reference [19].³Obtained from Reference [20].⁴Obtained from Reference [21].⁵Obtained from Reference [22].⁶Estimated from Reference [23].

Local Core Crushing: Phase I Response

The FEA predicted distributions of the through-thickness particle velocity and compressive stress at various times during Phase I are shown in Figure 7(a) and (b). It is clear that elastic waves propagate at a faster speed than the plastic waves. The elastic wave front is marked by a jump in the stress amplitude of $q = 1.4$ MPa. Particles behind the elastic wave front would have a particle velocity of $V_e = q/\rho_c C_e = 20.1$ m/s. The analytically predicted particle velocity in the elastic region compares very well with the FEA values shown in Figure 7(a) and (b). According to Equations (4) and (7), the elastic wave speed in the E-glass vinyl ester facesheets and the Divinycell H100 foam

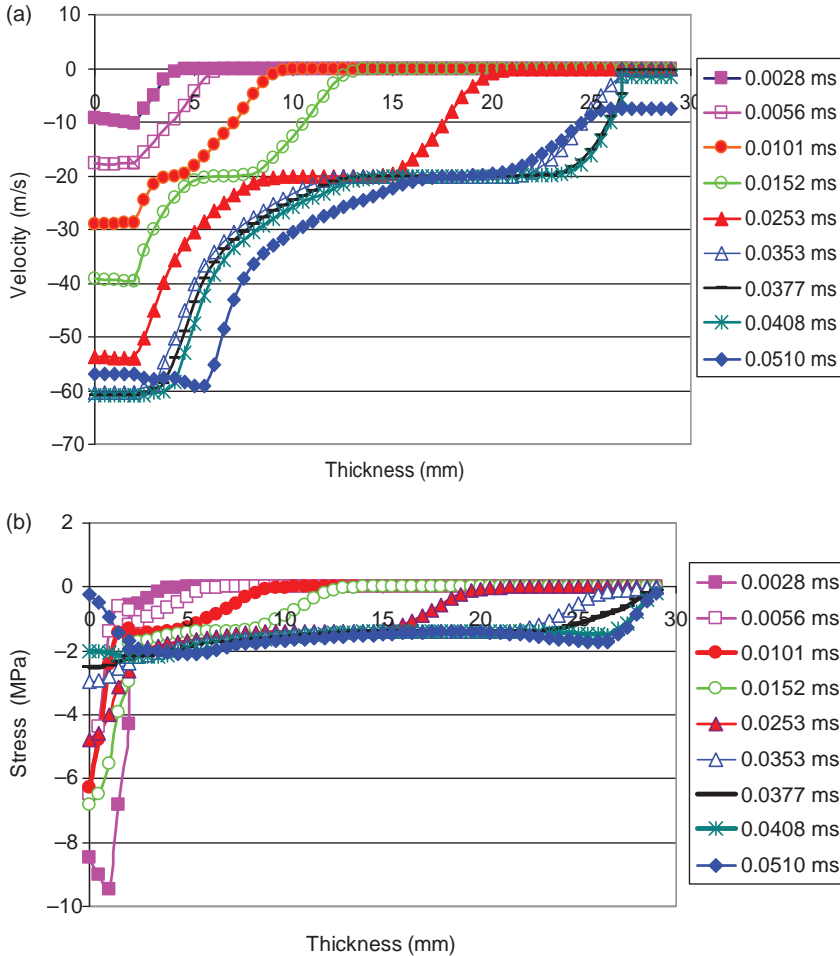


Figure 7. Distribution of through-thickness particle velocity and stress at the center of the panel during and just after Phase I: (a) velocity and (b) stress.

would be 2414 m/s and 696.5 m/s, respectively. For the 2 mm-thick facesheets and the 25 mm-core, the elastic compressive stress wave reaches the distal facesheet at about 0.0375 ms, which corroborates with the FEA results of 0.0377 ms shown in Figure 7(a) and (b).

Behind the elastic stress waves are the plastic stress waves. The amplitude of the plastic stress wave exceeds the flow stress of 1.4 MPa and increases up to a peak value, which can be determined from Equation (10). The highest transmitted stress was calculated from Equation (10) as $\sigma_p = 2.1$ MPa. At this plastic stress value, the plastic wave speed was calculated as $C_p = 95.97$ m/s.

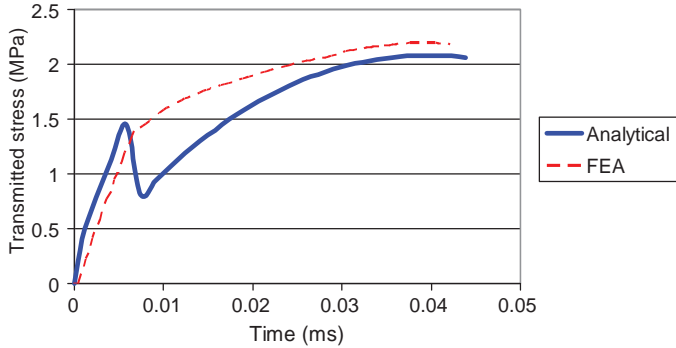


Figure 8. Transmitted stress at Interface 1 up to peak stress.

The transmitted stress at Interface 1, which is described in Equation (5), must be calculated separately for elastic and plastic responses because the transmission and reflection factors, k_{T1} and k_{R1} , respectively, depend on the density and wave speed in the foam. A FORTRAN program was written to evaluate the time variation of the transmitted stress at Interface 1 in two parts: an initial elastic response whereby $\sigma_{T1} < q$ and $\rho_c C_c = \rho_c C_e$ followed by a plastic response whereby $\sigma_{T1} > q$ and $\rho_c C_c = \rho_D C_p$. The FORTRAN results are shown by the solid line in Figure 8. There is a jump in the transmitted stress when the core changes from linear elastic response to plastic response at the densification strain. This follows from the approximate compressive stress-strain relation for foams [14,15]. The peak plastic stress $\sigma_p = 2.1$ MPa occurs at $t_p = 0.039$ ms. The transmitted stress at Interface 1 from FEA is also shown in Figure 8 for comparison. The predicted peak plastic stress was about 4.5% lower than the maximum compressive stress of 2.2 MPa found at 0.0396 ms from FEA. The transmitted stress from FEA is smooth and shows no jump discontinuity when the core begins to plastically flow because the plastic hardening curve is more gradual and only approximates the ideal case of a plateau and an infinite gradient at the densification strain shown in Figure 4. From the calculated values of C_p and t_p , local core crushing was estimated as 2.3 mm from Equations (11) and (13).

Global Bending/Shear: Phase II Response

The initial global panel velocity was determined from Equation (14) as $v_i = 31$ m/s. The sandwich bending and shear stiffness were evaluated with a reduced core thickness $H' = 22.7$ mm. Note that a 2.3 mm indentation changes the core height from 25 mm to 22.7 mm. Since the bending stiffness is proportional to the cube of core height, this reduces the bending stiffness

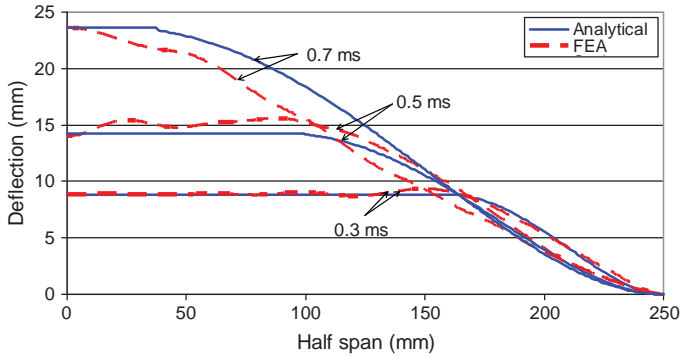


Figure 9. Transient deflection profiles of composite sandwich.

by 25%. A MATLAB program was written to solve Equations (22) and (23) for ξ and α_o . First, an expression for ξ in terms of α_o was derived from Equation (22) and then substituted into Equation (23) to eliminate ξ . Then, the resulting second-order nonlinear differential equation in α_o was solved using a Runge–Kutta ordinary differential equation solver (ode45) in MATLAB. Equation (22) is cubic in ξ , but only one of the three roots for ξ gives physically realistic solutions for α_o .

The transient deflection profile is fully determined from Equation (19), knowledge of $\xi(t)$, and the fact that $\Delta = v_i t$. As shown in Figure 9, the predicted transient deformation profiles compared very well with the FEA results; the predicted value for ξ was within 7% of FEA. The solution for $\alpha_o(t)$ is used to predict strains and damage initiation in the panel in the following section.

DAMAGE INITIATION

One important reason for developing analytical models is to provide simple design tools for determining the survivability of the panel when it is subject to an intense pressure pulse load. There are critical impulses, combinations of peak pressures and pulse durations, which would just cause damage at initiation in the panel. Recall from the transient deformation analysis in the previous section that the maximum bending strains occur either at the center or at the clamped edges of the sandwich panel. It is assumed that the clamped edges would be protected from damage and therefore the center of the panel is the most critical area for damage initiation.

To compare the analytical predictions to the results of ABAQUS Explicit, Hashin's failure criteria [24] was chosen to predict damage initiation. In Hashin's theory, the following four damage-initiation mechanisms are considered for a unidirectional laminate: fiber tension, matrix tension, fiber

compression, and matrix compression. These are expressed in terms of principal stress σ_{ij} , material strengths, and the following failure parameters,

Fiber tension

$$F_f^t = \left(\frac{\sigma_{11}}{X^T}\right)^2 + \left(\frac{\tau_{12}}{S^L}\right)^2 \quad (24)$$

Matrix tension

$$F_m^t = \left(\frac{\sigma_{22}}{Y^T}\right)^2 + \left(\frac{\tau_{12}}{S^L}\right)^2 \quad (25)$$

Fiber compression

$$F_f^c = \left(\frac{\sigma_{11}}{X^C}\right)^2 \quad (26)$$

Matrix compression

$$F_m^c = \left(\frac{\sigma_{22}}{2S^T}\right)^2 + \left(\frac{\tau_{12}}{S^L}\right)^2 + \left[\left(\frac{Y^C}{2S^T}\right)^2 - 1\right] \frac{\sigma_{22}}{Y^C} \quad (27)$$

where X^T and Y^T are the longitudinal and transverse tensile strengths, X^C and Y^C are the longitudinal and transverse compressive strengths, S^L is the longitudinal shear strength, and S^T is the transverse shear strength. When $F_f^t = 1$, $F_m^t = 1$, $F_f^c = 1$, or $F_m^c = 1$, the corresponding damage mode initiates. For the $0^\circ/90^\circ$ orthotropic laminate facesheets, $\sigma_{11} = \sigma_{22}$ and $X^T = Y^T$, so that fiber tension and matrix tension failure conditions in Equations (24) and (25) are identical. The fiber and matrix compression criteria, Equations (26) and (27), also apply to both principal directions.

For the orthotropic facesheet with fibers in 0° and 90° parallel to the x and y axes, one arrives at the following relationship between principal stresses and strains

$$\begin{Bmatrix} \sigma_{11} \\ \sigma_{22} \\ \tau_{12} \end{Bmatrix} = \begin{bmatrix} \bar{Q}_{11} & \bar{Q}_{12} & 0 \\ \bar{Q}_{12} & \bar{Q}_{11} & 0 \\ 0 & 0 & \bar{Q}_{66} \end{bmatrix} \begin{Bmatrix} \varepsilon_x \\ \varepsilon_y \\ \gamma_{xy} \end{Bmatrix} \quad (28)$$

where \bar{Q}_{ij} is the transformed stiffness matrix. The strains in the rectangular coordinates are evaluated using transformed polar coordinates as follows:

$$\varepsilon_x = z \frac{\partial \bar{\alpha}}{\partial x} = z \cos \theta \frac{\partial \bar{\alpha}}{\partial r} \quad (29)$$

$$\varepsilon_y = z \frac{\partial \bar{\beta}}{\partial y} = z \sin \theta \frac{\partial \bar{\alpha}}{\partial r} \quad (30)$$

$$\gamma_{xy} = z \left(\frac{\partial \bar{\alpha}}{\partial x} + \frac{\partial \bar{\alpha}}{\partial y} \right) = z (\cos \theta + \sin \theta) \frac{\partial \bar{\alpha}}{\partial r} \quad (31)$$

Thus, the principal stresses are expressed in polar coordinates as

$$\sigma_{11} = z \frac{4\alpha_o(a + \xi - 2r)}{(a - \xi)^2} (\bar{Q}_{11}\cos\theta + \bar{Q}_{12}\sin\theta) \quad (32)$$

$$\sigma_{12} = z \frac{4\alpha_o(a + \xi - 2r)}{(a - \xi)^2} (\bar{Q}_{12}\cos\theta + \bar{Q}_{22}\sin\theta) \quad (33)$$

$$\tau_{12} = z \frac{4\alpha_o(a + \xi - 2r)}{(a - \xi)^2} \bar{Q}_{66}(\cos\theta + \sin\theta) \quad (34)$$

The principal stress components are greatest at the top or bottom of the outer facesheets, $z = \pm(H'/2 + h)$, and for $\bar{Q}_{11} = \bar{Q}_{22}$, each stress component is maximum at $\theta = 45^\circ$. Furthermore, the impulse that causes damage is related to either the tensile fiber or matrix conditions (Equations (24) or (25)) and first occurs at $r=0$ and when $\xi=0$. A criterion for damage initiation following tensile fiber or matrix failure is given by:

$$1 = \frac{2\alpha_o^2(H' + 2h)^2}{a^2} \left[\left(\frac{(\bar{Q}_{11} + \bar{Q}_{12})}{X^T} \right)^2 + \left(\frac{2\bar{Q}_{66}}{S^L} \right)^2 \right] \quad (35)$$

The above failure criterion gives a combination of permanent core height H' and shear angle α_o for damage initiation. A critical impulse would be responsible for this combination of H' and shear angle α_o .

For the sandwich panel with H100 PVC foam core in the example, it was predicted that a critical impulse $I_{cr} = 54.84$ MPa-s ($p_o = 2.2$ MPa and $\tau = 0.05$ ms) would cause damage initiation at the center of the panel. At this value of the pressure pulse, the core had almost negligible permanent deformation at the end of Phase I, $H' = 24$ mm. The ABAQUS Explicit finite element program was run using Hashin's failure criteria for damage initiation. Figure 10(a) shows that damage was initiated near center of the panel when the pressure pulse was adjusted to $p_o = 3$ MPa and $\tau = 0.05$ ms, or an impulse of 75 MPa-s was applied. Below this peak load and duration, no damage occurred in the FEA. Thus the critical impulse to failure is $I_{cr} = 75$ MPa-s as predicted by FEA. The analytical critical impulse to failure is $\sim 27\%$ less than FEA predictions. The discrepancy between analytical and FEA predictions was attributed to the fact that in the FEA, tensile fiber, and/or matrix damage did not take place at the center of the panel as was assumed in the analytical model.

Damage initiation of sandwich panels with the same 2 mm-thick, E-glass vinyl ester facesheets and two other cores, namely Divinycell H200 and Klegecell R300 foams, were also considered. Material properties for the

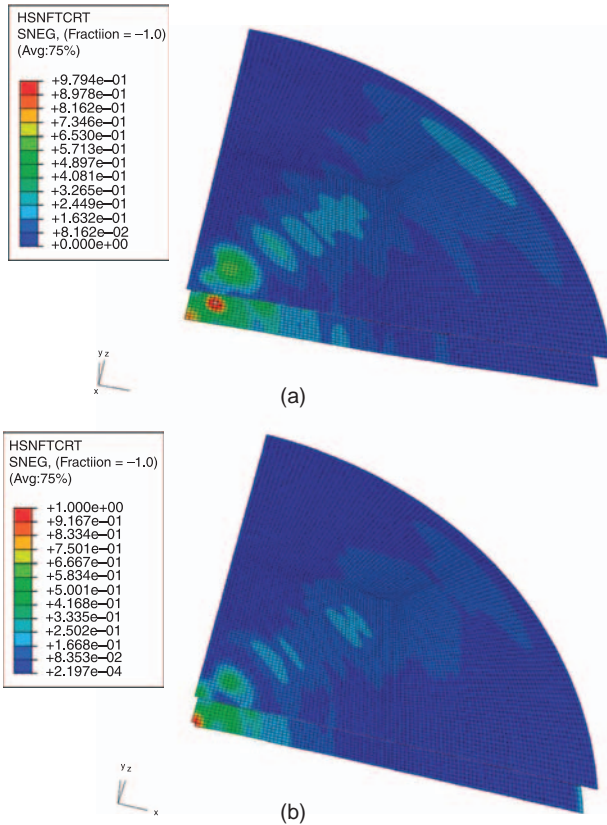


Figure 10. Damage initiation at bottom facesheet using Hashin's failure criteria: (a) Divinycell H100 core sandwich and (b) Divinycell H200 core sandwich.

Divinycell H200 and Klegecell R300 foams are listed in Table 1. The analytical predictions for the critical impulse to failure using the wave propagation model and Hashin's tensile fiber and/or matrix failure criteria compared better with the FEA predictions than with the Divinycell H100 foam core, as indicated in Figure 11. The analytical predictions for the Divinycell H200 and Klegecell R300 foams were about 13% higher than FEA results. The actual failure site for damage initiation in the sandwich panels with the Divinycell H200 and Klegecell R300 foams was exactly at the center of the distal facesheet, as assumed in the analytical model. The damage-initiation site in the Divinycell H200 foam core sandwich panel is shown in Figure 10(b) and should be contrasted with the damage-initiation site in the Divinycell H100 foam core sandwich panel, which is shown in Figure 10(a).

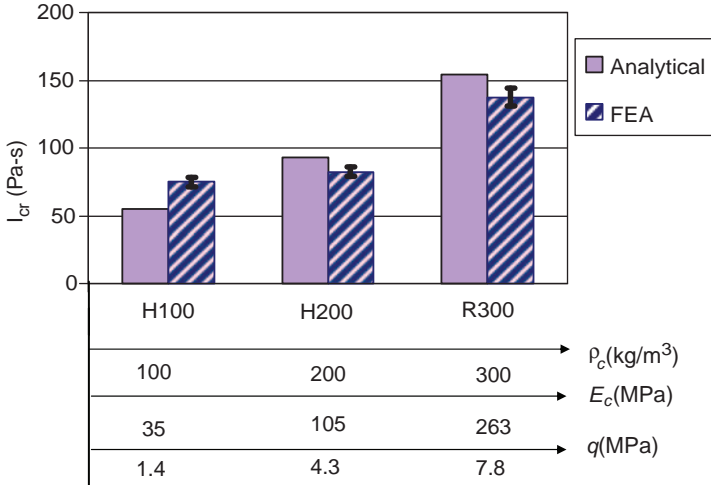


Figure 11. Variation of critical impulse of failure with core material properties.

CONCLUDING REMARKS

Analytical solutions for the blast response of a foam-core composite sandwich panel were derived considering two phases of deformation: (a) core crushing during through-thickness wave propagation and (b) global panel bending/shear during transverse shear wave propagation. Global equilibrium equations of motion were formulated from the system Lagrangian and used to obtain transverse deflection and shear rotations. The predicted transient deformation of the sandwich panel was within 7% of FEA results using ABAQUS Explicit.

The proposed wave propagation model was used in conjunction with Hashin's failure criteria to determine critical impulses that would cause damage to initiate at the center of the panel. Analytical predictions of the critical impulse for damage initiation compared fairly well with ABAQUS predictions, thereby rendering the analytical model a useful design tool for manufacturing blast-resistant composite sandwich panels. In the case of the sandwich panel with the H100 PVC foam core, damage initiated close to, but not at the center of, the distal facesheet in the ABAQUS Explicit solution. This event could have taken place if the small-amplitude, high-frequency waves ahead of the unloading shock front led to a re-distribution of the tensile stresses around the panel center.

These small-amplitude, high-frequency waves were neglected in the analytical model, but they occur in real-life applications. The analytical models proposed in this paper should only be used for providing rough estimates and for comparison purposes.

ACKNOWLEDGMENT

This work was supported by Dr Yapa Rajapakse at the Office of Naval Research under ONR Grant N00014-07-1-0423.

NOMENCLATURE

	a	= Panel radius
	A_{ij}	= Membrane stiffness matrix
A_{44}^s, A_{55}^s		= Shear rigidity of core
	C_c	= Wave speed in core
	C_e	= Elastic wave speed in core
	C_f	= Wave speed in facesheet
	C_p	= Plastic wave speed in core
	D_{ij}^s	= Bending stiffness of the sandwich
	E_{ij}	= Young's modulus
$F_f^T, F_m^T, F_f^C, F_m^C$		= Hashin's failure index
	G_{ij}	= Shear modulus
	h	= Facesheet thickness
	H	= Original core thickness
	H'	= Core thickness after compression
	\tilde{I}	= Sandwich rotary inertia per unit area
	I_{eff}	= Effective rotary inertia of sandwich
	I_{cr}	= Critical impulse to failure
	k_R	= Reflection factor
	k_T	= Transmission factor
	L	= Lagrangian
	m_{eff}	= Effective mass of sandwich
	p	= Pressure pulse
	p_o	= Pressure pulse amplitude
	q	= Core crushing strength
	\bar{Q}_{ij}	= Transformed stiffness matrix
	r	= In-plane radial coordinate
S^L, S^T		= Longitudinal and transverse shear strength

- t = Time
 T = Kinetic energy
 t_p = Start time of transmission
 t_1 = Wave travel time through facesheet
 t_2 = Wave travel time through core
 $u(\cdot)$ = Unit step function
 v_i = Initial sandwich panel velocity
 V_e = Particle velocity in core elastic region
 V_p = Particle velocity in core plastic region
 w = Sandwich panel transverse deflection
 x, y = In-plane rectangular coordinates of panel
 X^C, Y^C = Longitudinal and transverse compressive strength
 X^T, Y^T = Longitudinal and transverse tensile strength
 z = Through-thickness coordinate
 $\bar{\alpha}$ = Shear angle along x -axis
 α_o = Amplitude of shear angle along x -axis
 $\bar{\beta}$ = Shear angle along y -axis
 β_o = Amplitude of shear angle along y -axis
 δ = Local indentation
 Δ = Amplitude of global panel deformation
 ΔT = Time from the start of transmission
 ε_D = Foam densification strain
 ε_x = Strain in the x -direction
 ε_y = Strain in the y -direction
 γ_{xy} = Shear strain
 ν_{ij} = Poisson's ratio
 Π = Potential energy
 θ = In-plane circumferential coordinate
 ρ_c = Density of core
 ρ_D = Core density after densification
 ρ_f = Density of facesheet
 σ_x = Stress in the x -direction
 σ_y = Stress in the y -direction
 σ_I = Incident stress
 σ_p = Maximum foam stress at the densification
 σ_R = Reflected stress
 σ_T = Transmitted stress
 τ = Pressure pulse duration
 τ_{xy} = Shear stress
 ξ = Extent of local indentation
 Ω = Angular velocity amplitude
 $\dot{(\)} = d(\)/dt$ = Time derivative

APPENDIX

Uniaxial Strain Wave Speed in an Orthotropic Plate

Stress waves propagating through the thickness of the orthotropic face-sheets shown in Figure 1 travel in material that is constrained laterally in the x - and y -directions. To evaluate this wave speed, set $\varepsilon_x = \varepsilon_y = 0$. In the special case of a $0^\circ/90^\circ$ laminate, $\sigma_x = \sigma_y$, $E_{11} = E_{22}$, $\nu_{12} = \nu_{21}$, and $\nu_{31} = \nu_{32}$, two of the 3D stress-strain relations become

$$\varepsilon_y = \frac{(1 - \nu_{12})}{E_{11}} \sigma_x - \frac{\nu_{32}}{E_{33}} \sigma_z = 0 \quad (\text{A1})$$

$$\varepsilon_z = \frac{-(\nu_{13} + \nu_{23})}{E_{11}} \sigma_x - \frac{1}{E_{33}} \sigma_z \quad (\text{A2})$$

Solving for σ_x in Equation (A1), we get

$$\sigma_x = \frac{\nu_{32}}{E_{33}} \frac{E_{11}}{(1 - \nu_{12})} \sigma_z \quad (\text{A3})$$

Substituting the above expression for σ_x in Equation (A2) gives

$$\sigma_z = \frac{(1 - \nu_{12})E_{33}}{[1 - \nu_{12} - \nu_{32}(\nu_{13} + \nu_{23})]} \varepsilon_z \quad (\text{A4})$$

Equation (A4) represents a stress-strain relation for an orthotropic material in 1D or uniaxial strain. The wave speed for the material in this state is given by

$$C_f = \sqrt{\frac{(1 - \nu_{12})E_{33}}{[1 - \nu_{12} - \nu_{32}(\nu_{13} + \nu_{23})] \rho_f}} \quad (\text{A5})$$

where ρ_f is the mass density.

REFERENCES

1. Hampson, P.R. and Moayamedi, M. (2007). A Review of Composite Structures Subjected to Dynamic Loading, *Int. J. Crashworthiness*, **12**(4): 411–428.
2. Tagarielli, V.L., Deshpande, V.S. and Fleck, N.A. (2007). The Dynamic Response of Composite Sandwich Beams to Transverse Impact, *Int. J. Solids Struct.*, **44**(7–8): 2442–2457.

3. Vaziri, A. and Hutchinson, J.W. (2007). Metal Sandwich Plates Subject to Intense Air Shocks, *Int. J. Solids Struct.*, **44**(6): 2021–2035.
4. Deshpande, V.S. and Fleck, N.A. (2005). One-Dimensional Response of Sandwich Plates to Underwater Shock Loading, *J. Mech. Phys. Solids*, **53**(11): 2347–2383.
5. Hutchinson, J.W. and Xue, Z. (2005). Metal Sandwich Plates Optimized for Pressure Impulses, *Int. J. Mech. Sci.*, **47**(4–5): 545–569.
6. Xue, Z. and Hutchinson, J.W. (2004). A Comparative Study of Impulse-Resistant Metal Sandwich Plates, *Int. J. Impact Engg.*, **30**(10): 1238–1305.
7. Cole, R.H. (1984). *Underwater Explosions*, Princeton University Press, New Jersey.
8. Smith, P.D. and Hetherington, J.G. (1994). *Blast and Ballistic Loading of Structures*, Butterworth Heinemann, Oxford.
9. Menkes, S.B. and Opat, H.J. (1974). Broken Beams, *Exp. Mech.*, **13**: 480–486.
10. Teeling-Smith, R.G. and Nurick, G.N. (1991). The Deformation and Tearing of Thin Circular Plates Subjected to Impulsive Loads, *Int. J. Impact Engg.*, **11**(1): 77–91.
11. Franz, T., Nurick, G.N. and Perry, M.J. (2002). Experimental Investigation into the Response of Chopped-Strand Mat Glass Fibre Laminates to Blast Loading, *Int. J. Impact Engg.*, **27**(6): 639–667.
12. Librescu, L., Oh, S-Y. and Hohe, J. (2006). Dynamic Response of Anisotropic Sandwich Flat Panels to Underwater and In-Air Explosions, *Int. J. Solids Struct.*, **43**(13): 3794–3816.
13. Graff, K.F. (1975). *Wave Motion in Elastic Solids*, Oxford University Press, London.
14. Gibson, L.J. and Ashby, M.F. (1999) *Cellular Solid: Structures and Properties*, Cambridge University Press, Cambridge.
15. Ashby, M.F., Evans, A.G., Fleck, N.A., Gibson, L.J., Hutchinson, J.W. and Wadley, H.N.G. (2000). *Metal Foams: A Design Guide*, Butterworth Heinemann, London.
16. Vinson, J.R. (1999). *The Behavior of Sandwich Structures of Isotropic and Composite Materials*, Technomic Publishing Co., Lancaster.
17. Mines, R.A.W. and Alias, A. (2002). Numerical Simulation of the Progressive Collapse of Polymer Composite Sandwich Beams under Static Loading, *Composites: Part A*, **33**(1): 11–26.
18. Boh, J.W., Louca, L.A., Choo, Y.S. and Mouring, S.E. (2005). Damage Modelling of SCRIMP Woven Rovings Laminated Beams Subjected to Transverse Shear, *Composites: Part B*, **36**(5): 427–438.
19. Scida, D., Aboura, Z., Benzeggagh, M.L. and Bocherens, E. (1999). A Micromechanics Model for 3D Elasticity and Failure of Woven-Fibre Composite Materials, *Compos. Sci. and Technol.*, **59**(4): 505–517.
20. Rizov, V. and Mladensky, A. (2007). Influence of the Foam Core Material on the Indentation Behaviour of Sandwich Composite Panels, *Cell. Polym.*, **26**(2): 117–131.
21. Steeves, C.A. and Fleck, N.A. (2004). Collapse Mechanisms of Sandwich Beams with Composite Faces and a Foam Core, Loaded in Three-point Bending. Part II: Experimental Investigation and Numerical Modelling, *Int. J. Mech. Sci.*, **46**(4): 585–608.
22. Mahfuz, H., Thomas, T., Rangari, V. and Jeelani, S. (2006). On the Dynamic Response of the Sandwich Composites and their Core Materials, *Compos. Sci. Technol.*, **66**(14): 2465–2472.
23. Diab Klegecell R Grade Technical data, Available at: http://www.compass.cern.ch/compass/tech-board/materials/Klegecell_R.pdf (accessed December 15, 2007).
24. Hashin, Z. (1980). Failure Criteria for Unidirectional Fiber Composites, *J. Appl. Mech.*, **47**: 329–334.

Impact perforation of sandwich panels with Coremat®

Michelle S. Hoo Fatt* and Dushyanth Sirivolu

Department of Mechanical Engineering, The University of Akron, Akron, Ohio, USA

(Received 8 August 2007; final version received 23 January 2008)

Analytical solutions for the quasi-static and low-velocity perforation of sandwich panels with woven roving E-glass/vinyl ester facesheets and Coremat were derived. A multi-stage perforation process involving delamination, debonding, core shear fracture and facesheet fracture was used to predict the quasi-static failure load and ballistic resistance of the panel. The high core-crushing resistance and damping of the Coremat resulted in rupture of the distal facesheet before the incident facesheet during panel perforation because they limited the amount of local indentation compared with global panel deformation. Analytical predictions of the quasi-static load-deflection response and the dynamic contact force history were within 10% of the test results.

Keywords: impact; Coremat; sandwich structures; analytical model

1. Introduction

Composite sandwich panels are used extensively in the aerospace, marine, transportation and recreational industries because of their high-specific stiffness and strength, corrosion resistance, tailorability and high-fatigue life. In many of these applications, the composite panel may be subjected to localized projectile impact. Therefore, much work has been done in an effort to determine the failure load, ballistic limit, perforation energy and damage induced into composite sandwich panels subjected to quasi-static indentation and projectile impact [1,8,15]. Although most of this research has been experimental, few analytical solutions have been proposed because of the complicated interaction between the composite facesheet and core during deformation and failure. Analytical models provide physical insights to a problem, offer simple design tools and can be used to benchmark more refined finite element analysis (FEA).

The objective of this article is to present analytical solutions for the quasi-static and impact perforation of an E-glass/vinyl ester and Coremat sandwich panel. The analytical models are derived using experimental results from Mines *et al.* [8]. Coremat is a high-density/high-energy absorption resin impregnated non-woven polyester with 50% microsphere and is commonly used in the marine industry because of its high-impact resistance [6]. Impregnated Coremat has a density of around 610 kgm^{-3} , whereas the standard foam density for marine craft is 100 kgm^{-3} . It is primarily used in decks and hulls that are susceptible to high-impulsive loads. In earlier work, Lin and Hoo Fatt [7] developed an analytical model to describe the quasi-static and impact perforation of the E-glass/epoxy with the alu-

minium honeycomb core. This article is an extension of earlier work and addresses the impact perforation of composite sandwich panels made with impact resistant core materials.

2. Problem formulation

Consider the composite sandwich panel and rigid indenter/projectile, with hemispherical nose of radius R and a mass M_0 , as shown in Figure 1. The facesheets are thin orthotropic membranes of dimension $2a \times 2a \times h$, and the core is a crushable polymeric foam of dimension $2a \times 2a \times H$. This particular core is made of a Coremat, which has a core-crushing resistance that can be described as rigid, linear strain hardening [8].

Upon loading, the panel experiences simultaneous local indentation and global deformation. Experiments [1, 8, 15] indicate the fracture mechanisms as well as the load-displacement characteristics of sandwich panels subjected to impact velocities near or at the ballistic limit that are similar to those observed in quasi-static cases. Three stages must occur for total perforation of the sandwich panel: (i) initial failure during which one of the skins of the panel fractures; (ii) penetration of the indenter through the core and surviving facesheet and (iii) complete panel perforation including frictional resistance between the indenter/projectile and sandwich panel. Delamination, debonding, core shear fracture and tensile fracture of incident and distal facesheets occur during the perforation process.

*Corresponding author. Email: hoofatt@uakron.edu

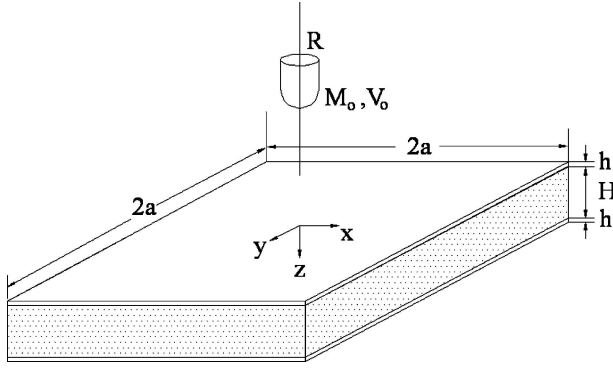


Figure 1. Geometry of composite sandwich panel.

3. Static indentation

Local indentation consists of front facesheet indentation and core crushing, whereas global deformation consists of bending and shearing of the entire panel. Local indentation and global deformation are considered independently because it is assumed that facesheet indentation is localized and has marginal effect on the overall thickness of the sandwich panel.

3.1. Local indentation

Top facesheet indentation is modelled by considering a rigid indenter pressing into an orthotropic plate resting on a rigid, linear strain-hardening foundation. The total potential energy of the system is

$$\Pi = U + D - W \quad (1)$$

where U is the elastic strain energy of the facesheet, D the work dissipated in crushing the core and W the work done by external forces.

When a fully clamped isotropic plate undergoes transverse deflection greater than one half of the thickness of the plate, in-plane membrane forces are no longer insignificant compared with the bending moment resistance of the plate [13]. Membrane plate theory is often used to determine the deflection of plates when deflections are greater than the thickness of the plate.

Hoo Fatt and Lin [3] showed that the same membrane stiffening characteristics of isotropic plates occur in orthotropic laminates. As the top facesheet of most sandwich configurations is thin and local indentation are usually several times greater than the top facesheet thickness, the top facesheet responds like an orthotropic membrane on a foundation (core resistance). In addition, in-plane deformations, u and v , are negligibly small compared to transverse deflections, w . The elastic strain energy therefore becomes

$$U = \frac{1}{8} \int_S \left[A_{11} \left(\frac{\partial w}{\partial x} \right)^4 + A_{22} \left(\frac{\partial w}{\partial y} \right)^4 \right. \\ \left. + (2A_{12} + 4A_{66}) \left(\frac{\partial w}{\partial x} \right)^2 \left(\frac{\partial w}{\partial y} \right)^2 \right] dS \quad (2)$$

where A_{ij} is the membrane stiffness of the orthotropic facesheet and S is the surface area.

The work dissipated in crushing the Coremat is given by

$$D = \int_S \left(a_1 + \frac{k}{2H} w \right) w dS \quad (3)$$

where a_1 and k are the core's crushing flow strength and strain hardening modulus, respectively. Both of these can be obtained from the uniaxial compressive stress-strain curve of the core (see Mines *et al.* [8] for example).

The exact solution for the transverse deflection of an axisymmetrical isotropic plate under centre point loading is used to describe the local indentation of the sandwich panel, w :

$$w(r) = \delta \left[1 - \frac{r}{\xi} \right]^2 \quad (4)$$

where δ is the local indentation under the indenter, ξ is the length of the deformation zone, and $r^2 = x^2 + y^2$. The total potential energy then becomes

$$\Pi = C_1 \frac{\delta^4}{\xi^2} + \frac{\pi a_1}{6} \delta \xi^2 + \frac{k\pi}{30H} \delta^2 \xi^2 - P\delta \quad (5)$$

where $C_1 = \frac{\pi}{60} (3A_{11} + 3A_{22} + 2A_{12} + 4A_{66})$. The total potential energy Π is a function of two unknown parameters, ξ and δ . An equilibrium condition occurs when $\frac{\partial \Pi(\delta, \xi)}{\partial \delta} = 0$. Minimizing the potential energy yields the following load-indentation response:

$$P = \frac{4C_1 \delta^3}{\xi^2} + \frac{\pi a_1 \xi^2}{6} + \frac{\pi k \delta \xi^2}{15H} \quad (6)$$

The load-deformation response is dependent on ξ and is minimum when $\frac{\partial P}{\partial \xi} = 0$. Therefore,

$$P = 4C_1 \delta \sqrt{\frac{(5\pi a_1 H \delta + 2\pi k \delta^2)}{120C_1 H}} + \left(\frac{5\pi a_1 H \delta^2 + 2\pi k \delta^3}{30H} \right) \\ \times \sqrt{\frac{120C_1 H}{(5\pi a_1 H \delta + 2\pi k \delta^2)}} \quad (7)$$

3.2. Global panel deformation

Again assuming in-plane deformations are negligible compared with the transverse deformation, one can express the

elastic strain energy of the symmetric sandwich panel with orthotropic facesheet as

$$\begin{aligned}
 U = 4 \int_0^a \int_0^a & \left\{ \frac{D_{11}^s}{2} \left(\frac{\partial \bar{\alpha}}{\partial x} \right)^2 \right. \\
 & + D_{12}^s \left(\frac{\partial \bar{\beta}}{\partial y} \right) \left(\frac{\partial \bar{\alpha}}{\partial x} \right) + \frac{D_{22}^s}{2} \left(\frac{\partial \bar{\beta}}{\partial y} \right)^2 \\
 & + A_{55}^s \left[\frac{\bar{\alpha}^2}{2} + \bar{\alpha} \frac{\partial w}{\partial x} + \frac{1}{2} \left(\frac{\partial w}{\partial x} \right)^2 \right] \\
 & + A_{44}^s \left[\frac{\bar{\beta}^2}{2} + \bar{\beta} \frac{\partial w}{\partial y} + \frac{1}{2} \left(\frac{\partial w}{\partial y} \right)^2 \right] \\
 & \left. + D_{66}^s \left[\frac{1}{2} \left(\frac{\partial \bar{\alpha}}{\partial y} \right)^2 + \frac{\partial \bar{\alpha}}{\partial y} \frac{\partial \bar{\beta}}{\partial x} + \frac{1}{2} \left(\frac{\partial \bar{\beta}}{\partial x} \right)^2 \right] \right\} dx dy
 \end{aligned} \quad (8)$$

where w is again used to express transverse deflections of the panel, $\bar{\alpha}$ and $\bar{\beta}$ are shear angles associated with the x - and y -directions, respectively, D_{ij}^s is the sandwich bending stiffness matrix, and A_{44}^s and A_{55}^s are the transverse shear stiffness. The superscript 's' is used to denote the sandwich. Equation (8) is a special case of a more general expression for the elastic strain energy potential of a sandwich panel found in Chapter 5 of Vinson [14].

The following functions were used to describe the transverse deformation, w , and the shear rotations with respect to the x - and y -axis, $\bar{\alpha}$ and $\bar{\beta}$:

$$w(x, y) = \Delta \left(1 - \left(\frac{x}{a} \right)^2 \right)^2 \left(1 - \left(\frac{y}{a} \right)^2 \right)^2 \quad (9)$$

and

$$\bar{\alpha}(x, y) = \alpha_o \sin \left(\frac{\pi x}{a} \right) \left(1 - \left(\frac{y}{a} \right)^2 \right)^2 \quad (10)$$

$$\bar{\beta}(x, y) = \beta_o \sin \left(\frac{\pi y}{a} \right) \left(1 - \left(\frac{x}{a} \right)^2 \right)^2 \quad (11)$$

where Δ is the global deflection under the indenter and α_o and β_o are rotations at the centre of the panel. The above functions satisfy the boundary conditions that $w = 0$ and $\bar{\alpha} = \bar{\beta} = 0$ at the edges and were found by fitting functions from static indentation analysis of the sandwich panel using ABAQUS Standard. The transverse deformation of the panel was described by the midline deflection profile of the sandwich panel (midline of the core) in the FEA model. The shear angles were calculated from the relations $\bar{\alpha} = \gamma_{xz} - \frac{\partial w}{\partial x}$ and $\bar{\beta} = \gamma_{yz} - \frac{\partial w}{\partial y}$, where the slopes with respect to the x - and y -axis were calculated from the fitted deflection profile in the FEA model.

Substituting derivatives of the expressions in Equations (9–11) into Equation (8) gives the following expression for the strain energy:

$$U = F_1 \Delta^2 + F_2 \alpha_o^2 + F_3 \beta_o^2 + F_4 \Delta \alpha_o + F_5 \Delta \beta_o + F_6 \alpha_o \beta_o \quad (12)$$

where

$$\begin{aligned}
 F_1 &= \frac{32768}{33075} (A_{44}^s + A_{55}^s), \\
 F_2 &= \frac{128}{315} a^2 A_{55}^s + \frac{128\pi^2}{315} D_{11}^s + \frac{128}{105} D_{66}^s, \\
 F_3 &= \frac{128}{315} a^2 A_{44}^s + \frac{128\pi^2}{315} D_{22}^s + \frac{128}{105} D_{66}^s, \\
 F_4 &= \frac{-4096}{105\pi^3} a A_{55}^s, \quad F_5 = \frac{-4096}{105\pi^3} a A_{44}^s \quad \text{and} \\
 F_6 &= \frac{2304}{\pi^6} (D_{12}^s + D_{66}^s).
 \end{aligned}$$

The total potential energy then becomes

$$\begin{aligned}
 \Pi &= F_1 \Delta^2 + F_2 \alpha_o^2 + F_3 \beta_o^2 + F_4 \Delta \alpha_o \\
 &+ F_5 \Delta \beta_o + F_6 \alpha_o \beta_o - P \Delta
 \end{aligned} \quad (13)$$

Minimizing Π with respect to Δ , α_o and β_o gives a closed-form expression for the global load-deflection response,

$$P = K_g \Delta \quad (14)$$

where $K_g = \frac{[4F_1(F_2+F_3+F_6)-(F_4+F_5)^2]}{2(F_2+F_3+F_6)}$.

Table 1 gives the facesheet and core material properties for the sandwich panels considered in this research. The lateral dimensions of the sandwich panel are $2a \times 2a = 500 \times 500 \text{ mm}^2$. Most of these material properties are taken from Mines *et al.* [8], except for the Mode II fracture toughness (G_{IIc}) of E-glass/vinyl ester and Coremat, which are estimated from similar materials in Stevanovic *et al.* [12] and Kolat *et al.* [5], respectively. The material properties in Table 1 are used to calculate the local indentation and global deformation under static indentation with a 50-mm-diameter tup and a comparison of the predicted load-deflection characteristics under the indenter with test data is shown from points A to C in Figure 2. The total deflection X_1 in Figure 2 is the displacement of the indenter, that is, $X_1 = \delta + \Delta$. The analytical solution for the load deflection is within 5% of the test data except near the failure point.

4. Failure mechanisms

Failure of the composite sandwich panel involves the interaction of several complicated mechanisms including

Table 1. Material properties of woven roving E-glass/vinyl ester and Coremat.

	E-Glass/Vinyl Ester	Coremat
Density (kg/m ³)	1391.3	640
Thickness (mm)	0.48	9.34
E ₁₁ (+) (GPa)	17	0.8
E ₂₂ (+) (GPa)	17	0.8
E ₃₃ (GPa)	–	0.35
ν ₁₂	0.13	0.36
ν ₁₃	–	0.6
ν ₂₃	–	0.6
ν ₂₁	0.13	0.36
ν ₃₁	–	0.45
ν ₃₂	–	0.45
G ₁₂ = G ₂₁ (GPa)	4.0	0.29
G ₂₃ = G ₃₂ (GPa)	–	0.068
G ₁₃ = G ₃₁ (GPa)	–	0.068
σ _{3f} (–) (MPa)	–	22
a ₁ (MPa)	–	10
k (MPa)	–	100
G _{IIc} (J/m ²)	2757	1400
σ _{1f} (+) (MPa)	270	–
σ _{1f} (–) (MPa)	200	–
σ _{2f} (+) (MPa)	270	–
σ _{2f} (MPa)	200	–
τ _{12f} (+) = τ _{21f} (+) (MPa)	40	–
τ _{13f} (+) = τ _{31f} (+) (MPa)	–	5
τ _{23f} (+) = τ _{32f} (+) (MPa)	–	5
ε _{1f} (+)	0.021	–
ε _{3f} (–)	–	0.025
E _a (MJ/m ³)	2.7	–

delaminations in the ply, debonding between the facesheet and core, core shear fracture and fracture of the facesheets. Although some of these mechanisms may be the result of progressive or accumulated damage, failure associated with a sudden loss in panel stiffness is considered due to brittle or unstable fracture. Fracture mechanics is used to calculate the critical contact loads associated delamination and debonding. Core shear fracture and facesheet failure are predicted from the material parameters such as the core

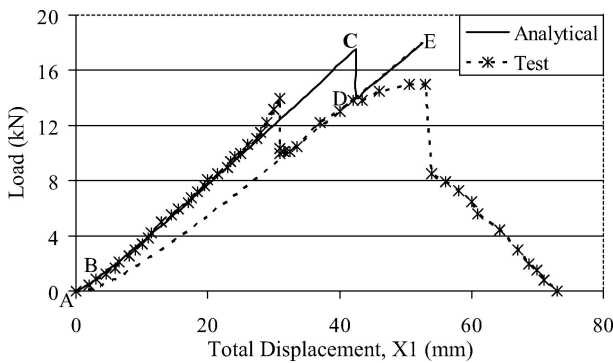


Figure 2. Variation of quasi-static load with indenter displacement.

shear strength and the specific energy absorption of the facesheet laminate.

4.1. Delamination/debonding

An approximate solution for the delamination threshold load in a quasi-isotropic orthotropic plate under static indentation is given by Olsson *et al.* [10] as

$$P_{\text{del}}^{\text{st}} = \pi \sqrt{\frac{32G_{IIc}D}{3}} \quad (15)$$

where G_{IIc} is the Mode II interlaminar fracture toughness and $D = \sqrt{D_{11}D_{22}(\eta + 1)/2}$, $\eta = (D_{12} + 2D_{66})/\sqrt{D_{11}D_{22}}$. Under impact loads, Olsson *et al.* [10] also determined that the threshold delamination load is $P_{\text{del}}^{\text{dyn}} = 1.213P_{\text{del}}^{\text{st}}$. This formula can be used to approximate the threshold load for delamination/debonding in the E-glass/vinyl ester and Coremat sandwich panel by assuming $D_{ij} = D_{ij}^s$. Separate loads should be calculated for delamination and debonding because values for the Mode II interlaminar shear fracture toughness are generally not the same.

4.2. Core shear failure

Consider local indentation of the isolated Coremat (no facesheet) by the hemispherical-nose indenter. The crushing load under the indenter is given by

$$P = 2\pi \int_0^\rho \left(a_1 + \frac{kw}{H} \right) r dr \quad (16)$$

where $w = \sqrt{R^2 - r^2} + \delta - R$ is the local deflection under the indenter and ρ is the contact radius of the indenter with the top facesheet. A simple relation between the local indentation δ and the contact radius ρ is given by

$$\delta = R - \sqrt{R^2 - \rho^2} \quad (17)$$

Isolated core shear failure takes place when $P = P_c = 2\pi\rho_{cr}H\tau_{cr}$, where ρ_{cr} is the critical contact radius at core shear failure and $\tau_{cr} = \tau_{13}$ is the transverse shear strength of the Coremat. Integrating Equation (16), using Equation (17) to eliminate δ , and setting $P = P_c$ give the following implicit solution for ρ_{cr} :

$$\frac{a_1\rho_{cr}}{2H} + \frac{k}{3\rho_{cr}H^2} \left[R^3 - (R^2 - \rho_{cr}^2)^{\frac{3}{2}} \right] - \frac{k\rho_{cr}}{2H^2} \sqrt{R^2 - \rho_{cr}^2} = \tau_{cr} \quad (18)$$

The corresponding load for isolated core shear fracture can be calculated once ρ_{cr} is known. The load at which the

Coremat sandwich panel undergoes core shear failure is higher than the core shear fracture load of isolated Coremat because the sandwich also has to resist the front facesheet membrane resistance. This load is calculated by using Equation (17) to find the local deflection at core shear fracture δ_{cr} and Equation (7) for the corresponding load.

4.3. Facesheet failure

When the strain energy density in the facesheets is greater than the material toughness, that is, the specific energy absorbed in a uniaxial tension test E_a , failure can occur. The strain energy density in an orthotropic facesheet is

$$U_o = \frac{1}{2} (\bar{Q}_{11}\varepsilon_x^2 + \bar{Q}_{22}\varepsilon_y^2 + 2\bar{Q}_{12}\varepsilon_x\varepsilon_y + \bar{Q}_{66}\gamma_{xy}^2) \quad (19)$$

where $\varepsilon_x, \varepsilon_y$ and γ_{xy} are in-plane strains and \bar{Q}_{ij} are components of the transformed stiffness matrix. In the back facesheet, the strain varies through the sandwich panel thickness and is given by $\varepsilon_x = z \frac{\partial \bar{\alpha}}{\partial x}$, $\varepsilon_y = z \frac{\partial \bar{\beta}}{\partial y}$, and $\gamma_{xy} = z(\frac{\partial \bar{\alpha}}{\partial x} + \frac{\partial \bar{\beta}}{\partial y})$, where Equations (10) and (11) are used to evaluate strains. According to these expressions, the maximum compressive and tensile strains due to global deformation occur in the front and back facesheets, respectively. The front facesheet strains are tensile and estimated by the average strain method presented in Lin and Hoo Fatt [7].

4.4. Multi-stage perforation model

Each failure mechanism is considered independently, and the loads for delamination, debonding, core shear fracture and back and front facesheet fractures are calculated. The lowest failure load corresponds to core shear fracture at 0.45 kN, thereby signifying that this takes place before fracture of either the top or bottom facesheets. Debonding and delamination then takes place at 9.92 and 13.92 kN, respectively. Core shear fracture, delamination and debonding have no effect on the load-deflection response. A catastrophic load drop is caused when the back facesheet fractures at 17.5 kN. As shown in Figure 2, this is about 25% higher than the experimental failure load at 14 kN because displacement-based energy methods are generally less accurate in predicting stresses and strains than they are in predicting deflections.

The sandwich panel can still resist loads after the back facesheet fails because the front facesheet is still intact. A multi-stage perforation model illustrated in Figures 3 (a)–(c) are proposed to explain what happens after back facesheet failure:

Stage I – Local indentation and global deformation up to core shear fracture, as depicted in Figure 3 (a). Core shear fracture occurs at roughly 45° with respect to the plane of the panel because this corresponds to a plane of

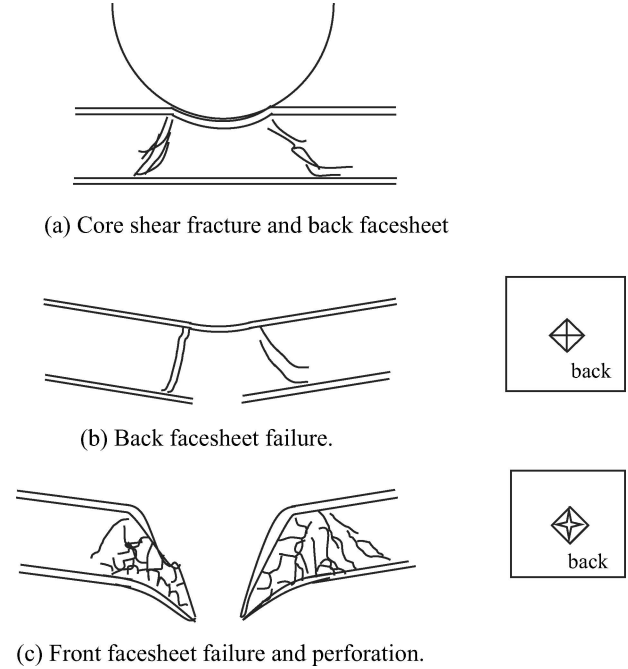


Figure 3. Multi-stage perforation process: (a) core shear failure and back facesheet debonding, (b) back facesheet fracture (c) front facesheet failure and perforation.

maximum shear stress. Back facesheet debonding is triggered by core shear fracture at a 45° angle.

Stage II – Deformation beyond core shear fracture and ending with back facesheet fracture, as indicated in Figure 3 (b). The core-crushing resistance used to calculate the local load-indentation response remains unchanged since the facesheets are intact.

Stage III – Deformation up to front facesheet fracture (Figure 3 (c)). Local petaling occurs immediately following a cross-hair fracture in the back facesheet. Four petals bend from the backside within the debond region. As shown in Figure 4, the load is resisted by membrane stretching of the front facesheet, transverse shearing of the Coremat within an annular region surrounding the projectile and bending resistance of the petals. The size (radius) of the back facesheet debond λ is estimated from the contact force P is transmitted to back facesheet via the truncated cylindrical core that has been sheared.

The strain energy associated with membrane stretching of the front facesheet and is found from the first term of Equation (5) and setting $\xi = \lambda$:

$$U_f = C_1 \frac{\delta^4}{\lambda^2} \quad (20)$$

The elastic strain energy associated with transverse shear deformations γ_{rz} surrounding the projectile is

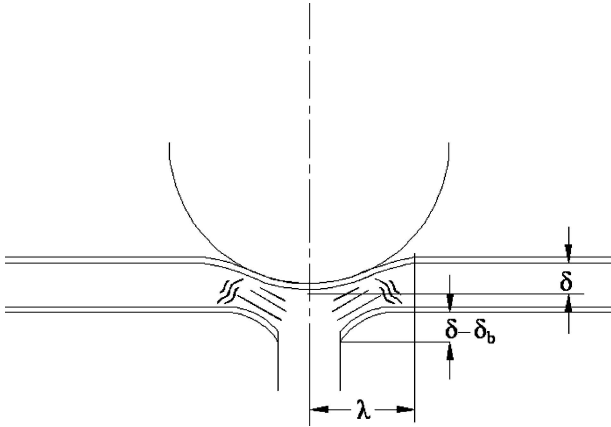


Figure 4. Local deformation in Stage III.

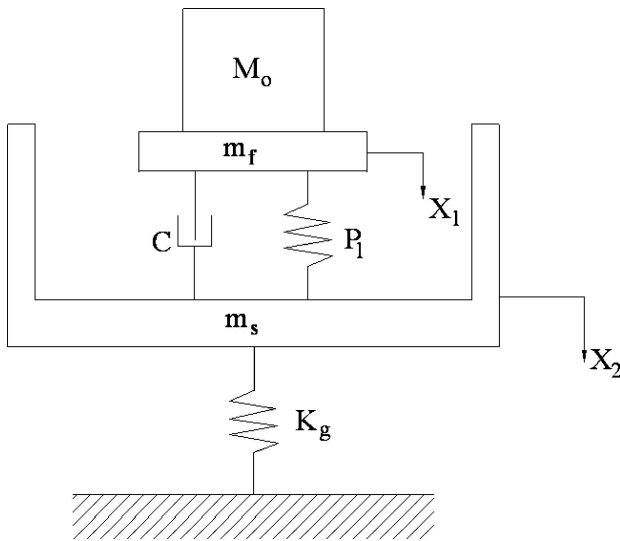


Figure 5. Two-df model for impact of composite sandwich panel.

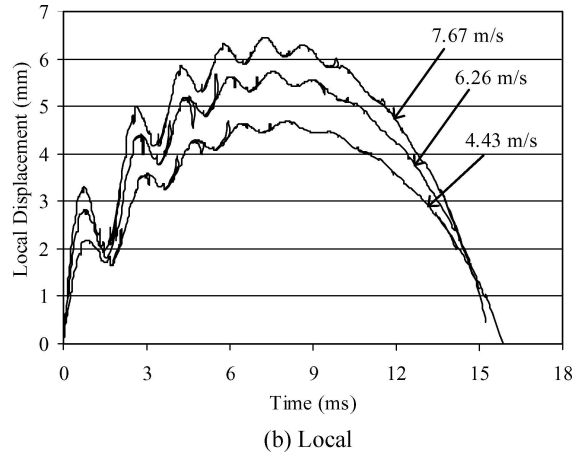
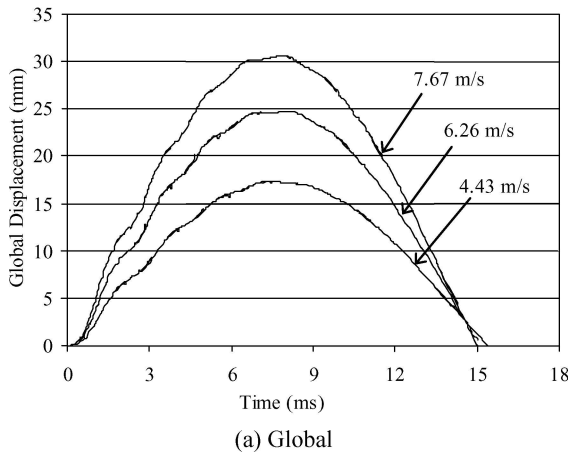


Figure 6. Transient deflection at panel centre with 10-kg projectile travelling at 4.43, 6.26, and 7.67 m/s: (a) Global and (b) Local.

given by

$$U_{sh} = \int_V \frac{1}{2} G_{13}^c \gamma_{rz}^2 dV \quad (21)$$

where G_{13}^c is the core transverse shear stiffness, $dV = 2\pi H r dr$ and r varies from 0 to λ . Assume the following linear distribution for transverse shear strains:

$$\gamma_{rz} = \frac{\delta}{\lambda} \left(1 - \frac{r}{\lambda}\right) \quad (22)$$

Substituting Equation (22) with Equation (21) and integrating give

$$U_{sh} = \frac{G_{13}^c \pi H}{12} \delta^2 \quad (23)$$

The bending energy due to petaling is derived in Appendix A by considering each petal as a cantilever beam with varying width. Since there are four petals associated with the facesheet perforation, the total energy due to petaling is

$$U_p = \frac{8\tilde{D}_{11}}{3\lambda^2} (\delta - \delta_b)^2 \quad (24)$$

where $\tilde{D}_{11} = \sum_{j=1}^N E_{rj} (z_j^3 - z_{j-1}^3)$ is an equivalent bending stiffness, $E_{rj} = \frac{1}{\left[\frac{1}{E_{11}} + \left(\frac{1}{G_{12}} - \frac{2\nu_{12}}{E_{11}}\right) + \frac{1}{E_{22}}\right]}$ is an equivalent modulus along the centre axis of the petal (45° to principal or fibre directions), N is the number of plies in the facesheet and δ_b is the local deflection at back facesheet failure.

The total potential energy during Stage III local indentation is given by

$$\Pi = C_1 \frac{\delta^4}{\lambda^2} + \frac{G_{13}^c \pi H}{12} \delta^2 + \frac{8\tilde{D}_{11}}{3\lambda^2} (\delta - \delta_b)^2 - P\delta \quad (25)$$

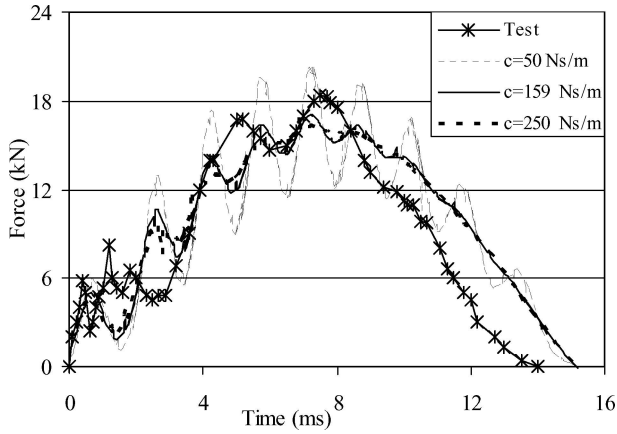


Figure 7. Contact force history with 10-kg mass projectile travelling at 7.67 m/s assuming different damping constants of the Coremat.

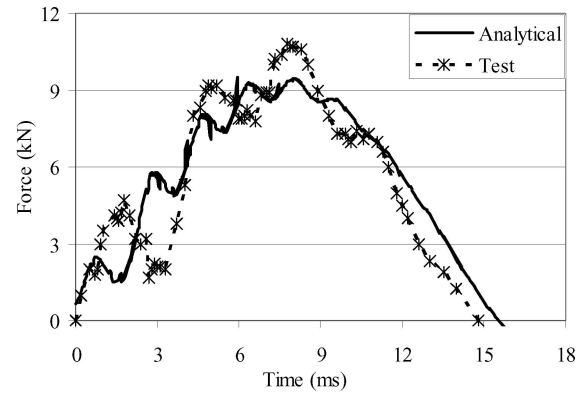
Minimizing the potential energy yields the following load-indentation response:

$$P = \frac{4C_1}{\lambda^2} \delta^3 + \frac{G_{13}\pi H}{6} \delta + \frac{16\tilde{D}_{11}}{3\lambda^2} (\delta - \delta_b) \quad (26)$$

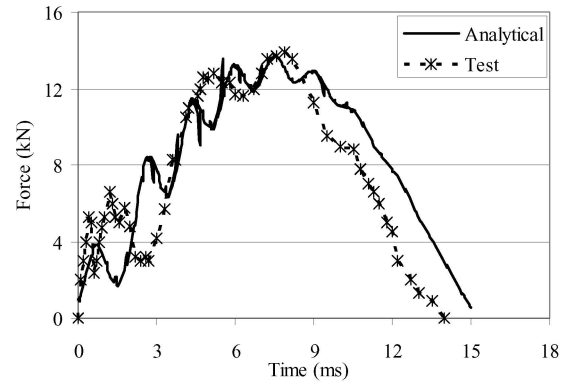
To approximate reduced global panel stiffness, we assume an average value between the global stiffness with fully intact facesheets and the global stiffness with only the top facesheet in the sandwich, that is, the back facesheet does not contribute to the bending stiffness when calculating the D_{ij}^s stiffness matrix. The predicted load-deflection response in Stage III is shown from points D to E in Figure 2. The load drop at E corresponds to tensile failure of the front facesheet.

5. Impact response

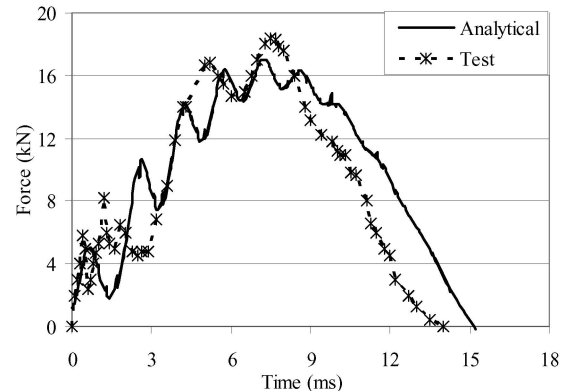
The impact response of the panel is found from the 2-df mass-spring-dashpot system shown in Figure 5. The projectile mass is denoted M_o , and the effective mass of the top facesheet and sandwich are represented by m_f and m_s , respectively. Expressions for the effective facesheet and sandwich masses are derived in Appendices B and C, respectively, by assuming that the local and global velocities are distributed in the same manner as their deformations. The local deformation and global deformation are given by $\delta = X_1 - X_2$ and $\Delta = X_2$, respectively. The local indentation resistance P_l , which is a non-linear function of δ , and the global spring stiffness K_g are found from quasi-static results and adjusted with the strain rate-dependent material properties of the facesheet and core. High-strain material tests show that the stiffness and strength of the E-glass fibre-reinforced composites are very sensitive with strain rate [4, 9, 11, 16]. Although dynamic material properties of Coremat are not readily available, we expect



(a) $V_0 = 4.43$ m/s



(b) $V_0 = 6.26$ m/s



(c) $V_0 = 7.67$ m/s

Figure 8. Contact force history with 10-kg mass projectile travelling at (a) $V_0 = 4.43$ m/s, (b) $V_0 = 6.26$ m/s and (c) $V_0 = 7.67$ m/s.

that it would also be very rate-sensitive. Rate sensitivity of the Coremat is considered by introducing the linear dashpot with damping constant c in Figure 5. This damping constant may be estimated from the impact test data.

The equations of motion for the 2-df system are

$$(M_o + m_f)\ddot{X}_1 + P_l + c(\dot{X}_1 - \dot{X}_2) = 0 \quad (27)$$

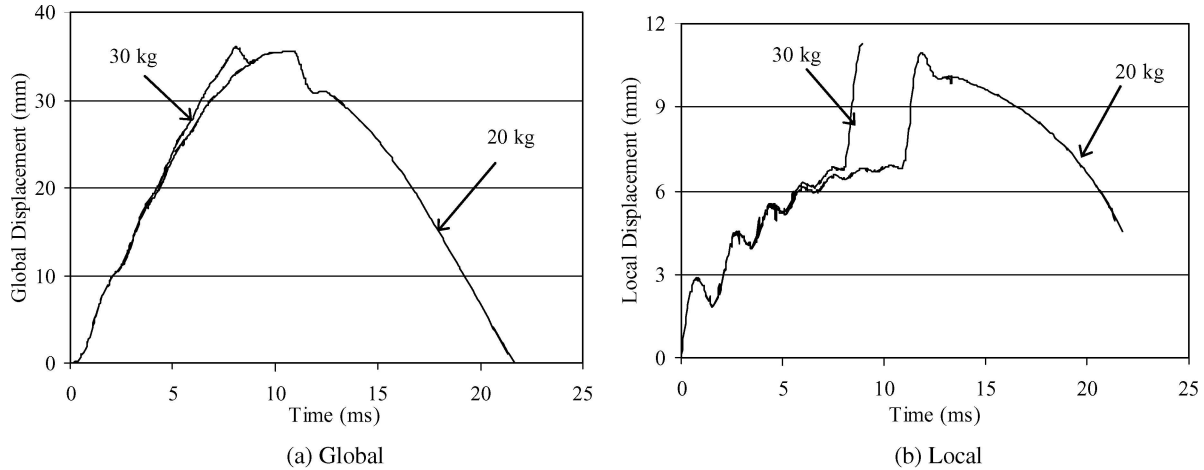


Figure 9. Transient deflection at panel centre with 20-kg and 30-kg projectiles travelling at 6.26 m/s: (a) Global and (b) Local.

and

$$m_s \ddot{X}_2 - P_l - c(\dot{X}_1 - \dot{X}_2) + K_g X_2 = 0 \quad (28)$$

The initial conditions for the 2-df system are as follows: $X_1(0) = 0$, $X_2(0) = 0$, $\dot{X}_1(0) = V_o$ and $\dot{X}_2(0) = 0$, where V_o is the initial velocity of the projectile. Equations (27) and (28) represent a non-linear, coupled initial-value problem. An explicit, Runge-Kutta differential equation solver was used in MATLAB (ode45) to solve for X_1 and X_2 . It should be mentioned that other ode solvers in MATLAB, whether explicit or implicit, gave approximately the same results as ode45. The default error tolerance (10^{-3} to 10^{-4}) in MATLAB was also found to give adequate accuracy in the problem.

Figures 6(a) and (b) show the predicted global and local deflections under the indenter for the composite panel impacted by a 10-kg projectile with various impact velocities, respectively. The average strain rate in the top and bottom facesheets ranged between 2 and 5 s^{-1} . Although these strain rates are low, they are not considered quasi-static and E-glass fibre-reinforced composites exhibit strain rate sensitivity even at low strain rates [2]. A 10% increase in the facesheet stiffness and strength was assumed based on the experimental data for woven E-glass fibre-reinforced polyester in Shah Kahn *et al.* [11] as well as high-strain rate data for unidirectional E-glass/vinyl ester laminates in Oguni and Ravichandran [9].

The damping constant for the Coremat was first assumed and adjusted to match the impact test results. As indicated in Figure 7, for the case of the sandwich panel

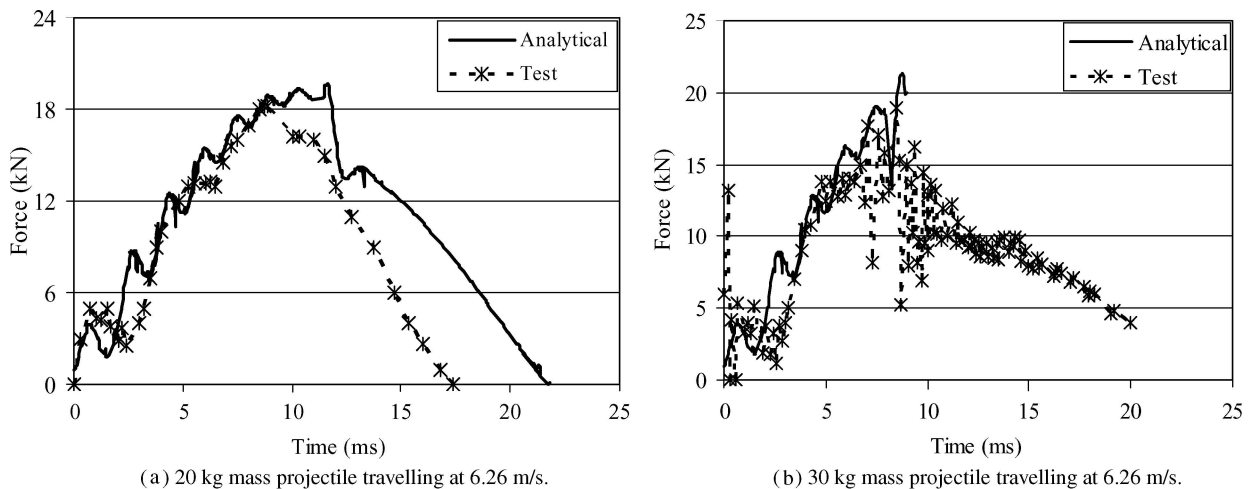


Figure 10. Contact force history with: (a) 20-kg mass projectile travelling at 6.26 m/s and (b) 30-kg mass projectile travelling at 6.26 m/s.

impacted with the 10-kg mass travelling at 7.6 m/s, the amplitude of the high-frequency vibrations would decay to a negligible amount at about 9 ms due to the Coremat damping. With a damping constant set at 50 Ns/m, the predicted contact force would be underdamped when compared to the test results (see dotted line in Figure 7). On the other hand with the damping constant set at 250 Ns/m, the predicted contact force would decay to a negligible amount at about 8 ms (see dashed line in Figure 7), thereby indicating that the assumed damping constant is too high. A damping constant equal to 159 Ns/m was found to agree the best with the contact force test data for the 10-kg mass travelling at 7.6 m/s. It will be shown later that this value appeared to be the best value for the Coremat damping constant in all of the impact tests.

Core shear fracture, delamination and debonding energies, although very small, were subtracted from the kinetic energy of the system at the instant they occurred. The tearing energy in the back facesheets was estimated from the fracture surface associated with petaling. These fracture events were considered instantaneous compared to the sandwich response time because these fractures constituted brittle or unstable crack propagation.

The contact force between the projectile and the impacted facesheet is given by $F = -M_o \ddot{X}_1$ and the predicted contact force is compared to measured test data in Figures 8 (a)–(c). Damping from the Coremat attenuates the high-frequency vibrations associated with local indentation and core crushing. The analytical model is able to predict an average contact force to within 10% of the experimental data. In all of these tests, the maximum global deformations were less than 35.8 mm, which is about the deflection at which the back facesheet would have failed assuming the stiffness and strength of the facesheet increase with increasing strain rate by the same amount. Thus, the analytical model is consistent with the test results.

With increasing mass or projectile velocity, damage would occur. Figures 9(a) and (b) show predicted global and local deflections under the indenter for the composite panel impacted by a 20-kg and 30-kg projectiles travelling at 6.26 m/s, respectively. The corresponding contact force history is shown and compared to test data in Figures 10 (a) and (b). At a global panel deflection of about 35.79 mm, the back facesheet just begins to tear. Impact with the 20-kg mass just causes fracture of the back facesheet when the contact force is at a maximum value, whereas impact with the 30-kg mass just causes back facesheet failure at 7.9 ms, about 5.1 ms before the time peak contact force would have occurred. Stage III deformation in 20-kg mass impact ends without front facesheet failure. In contrast to this, the front facesheet in Stage III of the 30-kg mass impact reaches an amount to cause fracture, roughly 11.3 mm. The projectile thus penetrates the panel in the 30-kg mass impact. The load drops more smoothly in the 30-kg mass experiment because of friction between the projectile and sandwich.

These results are consistent with the experimental results from Mines *et al.* [8], which gave the ballistic limit of the panel for the 30-kg mass projectile at 7.67 m/s.

6. Conclusions

Analytical solutions were derived for the quasi-static and impact perforation of an E-glass/vinyl ester and Coremat sandwich panel. The panel deformation was decomposed into local indentation and global deformation. An equivalent 2-df mass-spring-dashpot system was used to find the dynamic response of the composite sandwich panel subjected to a drop-weight impact by a rigid hemispherical-nose projectile. Several failure modes were considered, including delamination, debonding, core shear fracture and top and bottom facesheet failures. Analytical predictions of the quasi-static load-deflection response were within 5% of the test data, and the calculated failure load was about 25% higher than the test data. The predicted contact force histories from the equivalent 2-df model were within 10% of test data.

The analytical model presented in the article specifically shows how local core properties can influence the deformation and ultimate failure of a composite sandwich panel. It also provides a simple way to approximately describe the material response of non-traditional, high density and damping foams such as Coremat. Our analytical results indicated that the high core-crushing resistance and damping of the Coremat limited the amount of local indentation compared to global panel deformation. As a result the Coremat sandwich panel first ruptured in the distal facesheet rather than the impacted facesheet. Such a failure mode may be desirable from a practical standpoint because the outer surface of a composite sandwich vessel undergoing impact from external sources would remain intact if damage were to just initiate.

Acknowledgements

The authors thank Dr. Yapa Rajapakse at the Office of Naval Research for financial support under grant no. N00014-07-1-0423. The authors also thank Dr. R.A.W. Mines for providing experimental results on the static and low-velocity perforation of the E-glass/vinyl ester and Coremat sandwich panel.

References

- [1] G. Belingardi, M.P. Cavatorta, and R. Duella, *Material characterization of a composite-foam sandwich for front structure of a high speed train*, Comp. Struct. 61(1) (2003), pp. 13–25.
- [2] F. Fereshteh-Saniee, G.H. Majzoobi, and M. Bahrami, *An experimental study on the behaviour of glass-epoxy composite at low strain rates*, J. Mater. Process. Technol. 162–163 (2005), pp. 39–45.

- [3] M.S. Hoo Fatt and C. Lin, *Perforation of clamped, woven E-glass/polyester panels*, Comp. Pt. B. 35 (2004), pp. 359–378.
- [4] H.E. Johnson, L.A. Louca, and S.E. Mouring, *Current research into modelling of shock damage to large scale composite panels*, J. Mater. Sci. 41(20) (2006), pp. 6655–6672.
- [5] K. Kolat, G. Nesar, and C. Ozes, *The effect of sea water exposure on the interfacial fracture of some sandwich systems in marine use*, Comp. Struct. 78(1) (2007), pp. 11–17.
- [6] Lantor Coremat® [Internet], c1993. Veenendaal, The Netherlands: Lantor BV; Available at www.lantor.nl/index.php/id_structuur/10598/coremat.html (accessed 10 March 2008).
- [7] C. Lin and M.S. Hoo Fatt, *Perforation of sandwich panels with honeycomb cores by hemispherical nose projectiles*, J. Sand. Struct. Mat. 7(2) (2005), pp. 113–172.
- [8] R.A.W. Mines, C.M. Worrall, and A.G. Gibson, *Low velocity perforation behaviour of polymer composite sandwich panels*, Int. J. Impact. Eng. 21(10) (1998), pp. 855–879.
- [9] K. Oguni and G. Ravichandran, *Delamination threshold load for dynamic impact on plates*, J. Mater. Sci. 36(4) (2001), pp. 831–838.
- [10] R. Olsson, M.V. Donadon, and B.G. Falzon, *Delamination threshold load for dynamic impact on plates*, Int. J. Solids. Struct. 43(2) (2006), pp. 3124–3141.
- [11] M.Z. Shah Kahn, G. Simpson, and E.P. Gellert, *Resistance of glass-fibre reinforced polymer composites to increasing compressive strain rates and loading rates*, Comp. Pt. A. 31(1) (2000), pp. 57–67.
- [12] D. Stevanovic, P.-Y.B. Jar, S. Kalynasundaram, and A. Lowe, *On crack-initiation conditions for mode I and mode II delamination testing of composite materials*, Comp. Sci. Technol. 60(9) (2000), pp. 1879–1887.
- [13] S. Timoshenko and S. Woinowsky-Krieger, *Theory of Plates and Shells*, 2nd ed., McGraw Hill, Inc., New York, 1959.
- [14] J.R. Vinson, *The Behavior of Sandwich Structures of Isotropic and Composite Materials*, Technomic Publishing Co, Lancaster, PA, 1999.
- [15] H.M. Wen, T.Y. Reddy, S.R. Reid, and P.D. Soden, *Indentation, penetration and perforation of composite laminates and sandwich panels under quasi-static and projectile loading*, Key. Eng. Mat. 141–143 (1998), pp. 501–552.
- [16] G. Zhou and G.A.O. Davies, *Impact response of thick glass fibre reinforced polyester laminates*, Int. J. Impact Eng. 16(3) (1995), pp. 357–374.

Appendix A

Bending energy due to petaling

Petals arise from the cross-hair cracks running along $0/90^\circ$ fibre directions in the back facesheet plies. Consider each petal to be a beam of varying width, $b(r) = 2r$, where r is an axis, 45° to the edge of the petals or principal ply directions and running along in the centre of the petal. The bending moment resistance M_r is given by

$$M_r = \int_{-h/2}^{h/2} \sigma_r z b dz \quad (\text{A-1})$$

where $\sigma_r = \sigma_{rj} = E_{rj} \kappa z$ for the j^{th} ply, E_{rj} is an effective modulus in radial direction and κ is the curvature of the petal. For an

orthotropic ply, the effective modulus in the radial direction is

$$E_{rj} = \frac{4}{\left[\frac{1}{E_{11}} + \left(\frac{1}{G_{12}} - \frac{2\nu_{12}}{E_{11}} \right) + \frac{1}{E_{22}} \right]}. \quad (\text{A-2})$$

The bending moment resistance in an orthotropic petal is therefore given by

$$M_r = \frac{2r\kappa}{3} \sum_{j=1}^N E_{rj} (z_j^3 - z_{j-1}^3) \quad (\text{A-3})$$

The strain energy due to the bending of a petal of length λ is

$$U = \int_0^\lambda \frac{1}{2} M_r \kappa dr = \frac{\tilde{D}_{11}}{6} \int_0^\lambda b \left(\frac{d^2 v}{dr^2} \right)^2 dr \quad (\text{A-4})$$

where $\tilde{D}_{11} = \sum_{j=1}^N E_{rj} (z_j^3 - z_{j-1}^3)$, $\kappa = \frac{d^2 v}{dr^2}$ and v is the deflection of the petal relative to the plane of the back facesheet. Assume $v = \delta_p \left(1 - \frac{r}{\lambda}\right)^2$, where δ_p is the maximum deflection of the petal. Then,

$$U = \frac{2\tilde{D}_{11}}{3} \frac{\delta_p^2}{\lambda^2} \quad (\text{A-5})$$

The maximum petal deflection can be expressed in terms of the current local indentation by considering a shift in coordinates: $\delta_p = \delta - \delta_b$, where δ_b is the local indentation depth at the point of back facesheet failure. In terms of the current local indentation depth,

$$U = \frac{2\tilde{D}_{11}}{3} \frac{(\delta - \delta_b)^2}{\lambda^2} \quad (\text{A-6})$$

Appendix B

Effective mass of facesheet

The effective mass of the facesheet can be approximated by the following velocity profile, which is the derivative of the deformation profile for the facesheet indentation:

$$\dot{w}(r) = \dot{\delta} \left[1 - \frac{r}{\xi} \right]^2 \quad (\text{B-1})$$

where $\dot{\delta}$ is the amplitude of the velocity profile.

The kinetic energy (KE) is then approximately

$$KE = \pi \rho h \dot{\delta}^2 \int_0^\xi \left[1 - \frac{r}{\xi} \right]^4 r dr = \frac{\pi}{30} \rho h \xi^2 \dot{\delta}^2 \quad (\text{B-2})$$

The KE using an effective mass m_f for the facesheet is

$$KE = \frac{1}{2} m_f \dot{\delta}^2 \quad (\text{B-3})$$

Setting equations (2-2) and (2-3) equal to each other, one finds that the effective facesheet mass is

$$m_f = \frac{\pi}{15} \rho h \xi^2 \quad (\text{B-4})$$

Appendix C

Effective mass of sandwich panel

Assume the velocity distribution in the sandwich is the time derivative of the sandwich deformation

$$\dot{w}(x, y) = \dot{\Delta} \left(1 - \left(\frac{x}{a}\right)^2\right)^2 \left(1 - \left(\frac{y}{a}\right)^2\right)^2 \quad (\text{C-1})$$

The total KE is

$$KE = 2 \int_0^a \int_0^a (\rho_c H + 2\rho h) \dot{\Delta}^2 \left[1 - \frac{x^2}{a^2}\right]^4 \times \left[1 - \frac{y^2}{a^2}\right]^4 dx dy \quad (\text{C-2})$$

After integration of Equation (C2), one gets

$$KE = 0.33(\rho_c H + 2\rho h) a^2 \dot{\Delta}^2 \quad (\text{C-3})$$

The KE using a lumped effective sandwich mass m_s is given as

$$KE = \frac{1}{2} m_s \dot{\Delta}^2 \quad (\text{C-4})$$

Therefore, the effective sandwich mass is

$$m_s = 0.66(\rho_c H + 2\rho h) a^2 \quad (\text{C-5})$$

Book Chapter

Modeling Blast and High-Velocity Impact of Composite Sandwich Panels

Michelle S. Hoo Fatt, Leelaprasad Palla, and Dushyanth Sirivolu

Abstract Analytical models for predicting the deformation and failure of composite sandwich panels subjected to blast and projectile impact loading are presented in this paper. The analytical predictions of the transient deformations and damage initiation in the composite sandwich panels were compared with finite element solutions using ABAQUS Explicit. For the blast model, the predicted transient deformation of the sandwich panel was within 7% of FEA results, while the predicted damage initiation using Hashin's composite failure criteria was about 15% higher than FEA results in most cases. For the high velocity impact model, the predicted transient deformations were within 20% of FEA results.

1 Introduction

Lightweight polymer composite sandwich panels are becoming more widely used in military and civilian transport vehicles because they offer greater load-bearing capabilities per unit weight and easier maintenance. In some instances, these composite sandwich panels may be subjected to blast and/or high velocity impact from flying debris of a nearby explosion. During blast and high velocity impact loading of the composite sandwich panel, loads are characterized by a very short time duration compared to panel structural response time. The sharply applied loads initially involve the transmission or propagation of stress waves, which after multiple reflections from the panel boundaries result in structural vibration. If the transient loads are of high intensity, however, they may cause fracture or perforation of the structure during the initial transient phase. This paper provides analytical techniques that can be used to obtain the transient response and determine the damage initiation of composite sandwich panels subjected to blast and high velocity impact.

M.S. Hoo Fatt (✉), L. Palla, and D. Sirivolu
Department of Mechanical Engineering, The University of Akron, Akron, OH 44325-3903, USA
e-mail: {hoofoatt;lp21;ds64}@uakron.edu

There is a paucity of research articles addressing analytical methods for determining the behavior and survivability of composite sandwich panels under dynamic loading [1]. Analytical models are essential for elucidating physical mechanisms that control the deformation and survivability of composite panels under blast and impact. Analytical solutions are used by many researchers as a starting point for setting up test and parametric studies. Analytical solutions are also useful in numerical studies because they can be used to benchmark more refined finite element analysis. Analytical models are developed separately for a composite sandwich panel under blast and high velocity projectile impact in the following sections.

2 Impulsively-Loaded Sandwich Panels

Consider the fully clamped, composite sandwich panel of radius a , as shown in Fig. 1. The facesheets consist of orthotropic composite plates of thickness h , and the core is crushable polymeric foam of thickness H . Assume for simplicity that the panel is subjected to a uniformly distributed pressure pulse

$$p(t) = \begin{cases} p_0 \left(1 - \frac{t}{\tau}\right), & 0 \leq t \leq \tau \\ 0, & t > \tau \end{cases} \quad (1)$$

where p_0 is the peak pressure and τ is the load duration. Other more complicated pressure transients can be used to more accurately simulate underwater and air explosions [2, 3], and it will be found later in this study that it is not the actual function used to describe the pressure transient but rather the impulse (integrated area under the pressure pulse diagram) that governs the blast response and ultimate failure of the panel.

Provided no failure has occurred to the panel during the blast, the response of the composite sandwich panel may be described by the three phases of motion depicted in Fig. 2a-c. In Phase I, a through-thickness, compressive stress wave propagates from the incident facesheet to the distal facesheet. In this phase the sandwich panel experiences primarily core crushing, while impulsive transverse shear reaction forces are induced around the clamped boundaries. As indicated in Fig. 2a, there is no global deflection in Phase I.

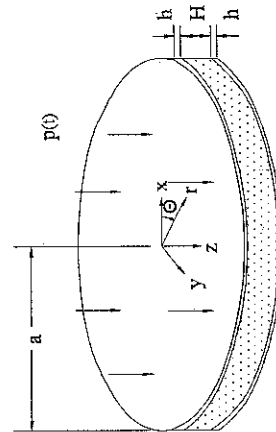


Fig. 1 Composite sandwich panel subjected to uniformly distributed, pressure pulse

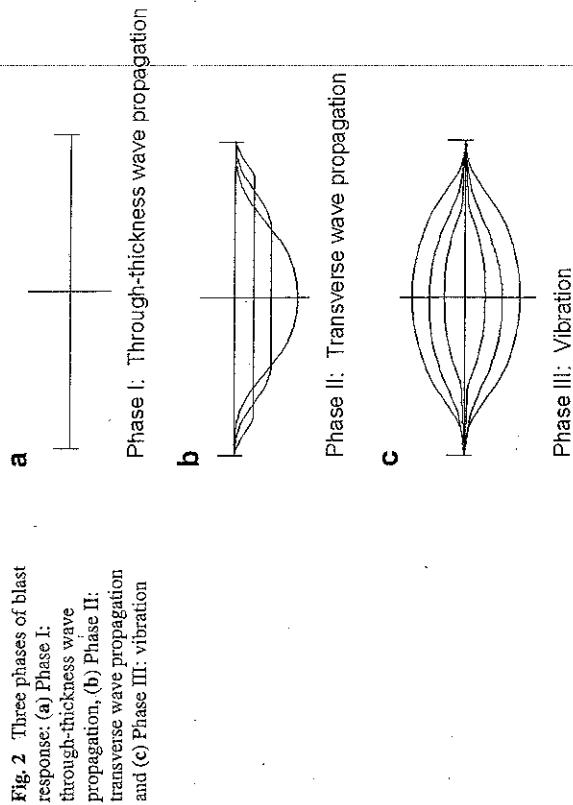


Fig. 2 Three phases of blast response: (a) Phase I: through-thickness wave propagation, (b) Phase II: transverse wave propagation and (c) Phase III: vibration

At the end of Phase I, momentum and kinetic energy are transferred globally to the panel and the now established impulsive transverse shear reaction force just begins to propagate from the clamped boundaries towards the panel center. The pressure pulse resulting from the blast would have either ended or decayed to almost negligible amplitude by the start of Phase II. Momentum, equivalent to the impulse from the blast, would be transferred to the sandwich panel with a reduced core thickness from Phase I. In Phase II, the transverse shear stress wave due to the reaction forces at the clamped boundary propagates from the clamped boundary towards the center of the panel. This transverse stress wave is an unloading wave, causing bending and shear deformations to develop behind its front, as shown in Fig. 2b.

The elastic unloading transverse shear wave brings the panel to maximum deflection when it reaches the panel center. At the end of Phase II, the unloading transverse shear wave reverses sign and direction of travel thereby causing the panel to rebound. The transverse shear wave reflects back and forth from the boundary to the panel center in Phase III. As depicted in Fig. 2c, elastic vibrations take place in Phase III.

During Phase I, high intensity transverse shear stresses are developed at the clamped boundary and these may cause transverse shear fracture at the clamped boundaries of the panel. Transverse shear fracture can be avoided by using reinforcements at boundaries. The second mode of failure that can occur during blasts is tensile fracture in the center of the panel where the bending strains are at a maximum at the end of Phase II. These two failure modes in addition to permanent

deformation were first observed on impulsively-loaded aluminum beams by Menkes and Opat [4] and later on aluminum plates by Teeling-Smith and Nurick [5]. They have also been experimentally observed on composite plates by Franz et al. [6].

Analytical methods for predicting the panel response in Phases I and II are given in the following sections. These analytical solutions will then be used to establish damage initiation criteria for the sandwich panel.

2.1 Phase I – Through-Thickness Wave Propagation

The wave speed in polymeric foam is low compared to the wave speed in fiber-reinforced laminates or metals. A thick composite sandwich panel with a polymeric foam core is likely to undergo transient local facesheet indentation and core crushing while the pressure pulse is still acting. Take for example, H100 PVC foam core with a density of 100 kg/m^3 and a compressive elastic modulus of 35 MPa. Elastic uniaxial stress waves propagate through a 25 mm thick core made of H100 PVC foam in about 0.04 ms. An initial pressure pulse duration of this magnitude is common for naval composite sandwich ships subjected to underwater and air blast explosions [2]. Thus one can assume that permanent plastic deformations of the core will take place from a transient event, i.e., during the load application. Phase I response is described by stress waves propagating through the thickness of the facesheets and core.

2.1.1 Transmission and Reflection at Interfaces

The transmission and reflection of a stress wave through the multi-layered composite sandwich panel is shown in Fig. 3. Stress waves are transmitted from the incident facesheet to the foam at Interface 1 and from the foam to the distal facesheet at Interface 2. When the incident stress σ_I first reaches Interface 1, the transmitted stress σ_{T1} and the reflected stress σ_{R1} are given as follows (see Ref. [7]):

$$\sigma_{T1} = -k_{T1} p(t - t_1) u(t - t_1), \quad k_{T1} = \frac{2\rho_c C_c}{(\rho_f C_f + \rho_c C_c)} \quad (2)$$

and

$$\sigma_{R1} = -k_{R1} p(t - t_1) u(t - t_1), \quad k_{R1} = \frac{(\rho_c C_c - \rho_f C_f)}{(\rho_f C_f + \rho_c C_c)} \quad (3)$$

where $t_1 = h/C_f$ is the wave travel time through the facesheet, C_f and C_c are the wave speeds in the facesheet and core, respectively; ρ_f and ρ_c are the density of the facesheet and core, respectively; and $u(\cdot)$ is the unit step function.

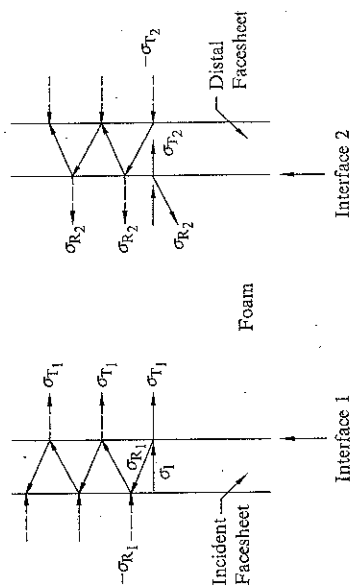


Fig. 3 Transmission of stress waves through facesheets and foam in sandwich panel

The wave speed in an orthotropic plate in uniaxial strain is derived in Appendix A as

$$C_f = \sqrt{\frac{(1 - \nu_{12}) E_{33}}{[1 - \nu_{12} - \nu_{32}(\nu_{13} + \nu_{23})] \rho_f}} \quad (4)$$

where E_{ij} and ν_{ij} are elastic modulus and Poisson's ratio of the orthotropic facesheet. This wave speed is usually higher than the more commonly used uniaxial stress wave speed, which is equal to $\sqrt{E_{33}/\rho_f}$. The wave speed in the foam will be discussed in the following section.

The reflected wave in the incident facesheet is tensile because $\rho_f C_f \gg \rho_c C_c$. This reflected wave is again reflected, but as a compressive stress wave, when it reaches the outer surface of the incident facesheet. The process of reflection and transmission of waves at Interface 1 repeats itself over and over again at intervals $2t_1$. Thus the transmitted stress in the foam at Interface 1 is given as

$$\begin{aligned} \sigma_{T1} = & -k_{T1} p(t - t_1) u(t - t_1) + k_{T1} k_{R1} p(t - 3t_1) u(t - 3t_1) \\ & - k_{T1} k_{R1}^2 p(t - 5t_1) u(t - 5t_1) \\ & \dots + (-1)^{n+1} k_{T1} k_{R1}^n p(t - (2n + 1)t_1) u(t - (2n + 1)t_1) \end{aligned} \quad (5)$$

where n is the number of reflections up to that time.

The transmitted stress wave in the foam σ_{T1} will reflect back as a compressive wave into the foam and be transmitted as a compressive stress wave in the distal facesheet when it first reaches Interface 2. The transmitted stress in the distal facesheet σ_{T2} is further reflected as a tensile stress wave from the outer surface of the distal facesheet. This reflected stress waves will then be transmitted as tensile stress wave in the foam and reflected back as compressive stress wave into the facesheet. The part that is transmitted to the foam will add to the reflected stress waves in the foam σ_{R2} . This process repeats itself indefinitely so that the reflected stress wave at any time is given by

$$\begin{aligned} \sigma_{R_2} = & -k_{R_2}\sigma_{T_1}(t-t_2)u(t-t_2) + k_{T_2}k_{T_1}\sigma_{T_1}(t-2t_1-t_2)u(t-2t_1-t_2) + \\ & -k_{T_2}k_{T_1}k_{R_1}\sigma_{T_1}(t-4t_1-t_2)u(t-4t_1-t_2) \\ & + k_{T_2}k_{T_1}k_{R_1}^2\sigma_{T_1}(t-6t_1-t_2)u(t-6t_1-t_2) \\ & \dots + (-1)^{n+1}k_{T_2}k_{T_1}k_{R_1}^n\sigma_{T_1}(t-2nt_1-t_2)u(t-2nt_1-t_2) \end{aligned} \quad (6)$$

where $t_2 = H/C_c$, $k_{T_2} = \frac{2\rho_f C_f}{(\rho_f C_f + \rho_c C_c)}$ and $k_{R_2} = \frac{(\rho_f C_f - \rho_c C_c)}{(\rho_f C_f + \rho_c C_c)}$. The reflected stress is a tensile unloading elastic stress wave. Permanent plastic strains or local indentation of the foam results after elastic unloading.

2.1.2 Elastic and Plastic Waves in Foam

The facesheets are very stiff and remain elastic during wave transmissions, but the polymeric foam core is elastic-plastic with a compressive stress-strain characteristic as shown in Fig. 4 [8]. The foam is linear elastic with a compressive modulus of E_c until yielding at a flow stress q . Rapid compaction of cells causes the density to change during the plateau region until full densification has occurred at ϵ_D . The stress rises to a maximum plastic stress σ_p at the densification strain. The maximum plastic stress at the densification strain depends on the load intensity.

If the pressure pulse amplitude is high enough to yield the core, elastic and plastic waves will be generated in the foam during Phase I. In Ashby et al. [9], the elastic uniaxial stress wave speed in the foam is given by $\sqrt{E_c/\rho_c}$ and the plastic wave speed is given by $C_p = \sqrt{\frac{\sigma_p - q}{\rho_c \epsilon_D}}$, where σ_p is the stress in the densification region (see Fig. 4). Elastic waves propagated first in the core and are later followed by plastic waves, as shown in Fig. 5. By substituting isotropic properties for foam in Eq. 4, one can derive the following expression for elastic wave speed in the foam in a state of uniaxial strain:

$$C_e = \sqrt{\frac{(1-\nu_c)E_c}{[1-\nu_c-2\nu_c^2]\rho_c}} \quad (7)$$

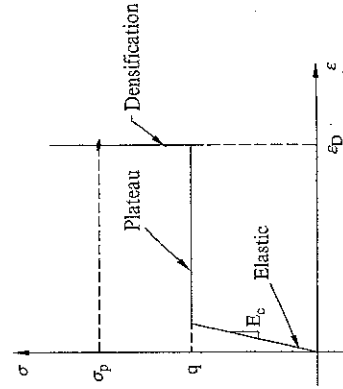


Fig. 4 Compressive stress-strain curve of polymeric foam

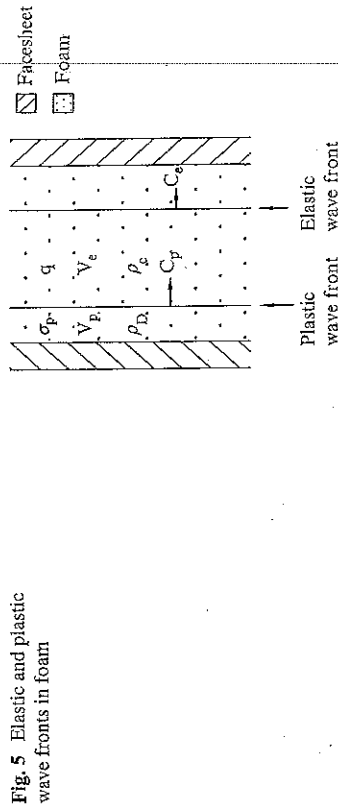


Fig. 5 Elastic and plastic wave fronts in foam

The densification strain is related to particle velocities in the elastic and plastic regions, V_e and V_p , respectively. After time t , the plastic zone gage length is $C_p t$ and the compression in the plastic zone is $(V_p - V_e)t$. Therefore, the densification strain is

$$\epsilon_D = \frac{V_p - V_e}{C_p} \quad (8)$$

The particle velocity in the plastic region is in turn related to the plastic stress σ_p and density of foam after densification ρ_D [7]:

$$V_p = \frac{\sigma_p}{\rho_D C_p} \quad (9)$$

where $\rho_D = \frac{\rho_c}{(1-\epsilon_D)}$. Similarly, $V_e = \frac{q}{\rho_c C_e}$. Combining Eqs. 8 and 9 to eliminate V_p and expressing C_p in terms of σ_p give the following quadratic equation that can be solved for σ_p :

$$\left(\frac{\rho_c - \rho_D}{\rho_c}\right)^2 \sigma_p^2 + \left[\frac{2\rho_D q}{\rho_c} + \left(\frac{\rho_c - \rho_D}{\rho_c}\right) - \frac{V_e^2 \rho_D^2}{\rho_c \epsilon_D}\right] \sigma_p + \frac{\rho_D^2 q^2}{\rho_c^2} + \frac{V_e^2 \rho_D^2 q}{\rho_c \epsilon_D} = 0 \quad (10)$$

2.1.3 Local Indentation

Permanent plastic strains arise when the elastic unloading wave reaches the plastic wave front. The local indentation is confined in the plastic zone and may be calculated from the densification strain and the characteristic gage length of the plastic zone. This characteristic gage length is $C_p \Delta T$, where ΔT is the time from the start of transmission of σ_p to the time when the elastic unloading wave reaches the plastic wave front. Thus the local indentation is

$$\delta = \epsilon_D C_p \Delta T \quad (11)$$

Let t_p be the start time of plastic wave transmission of σ_p at Interface 1. Then,

$$\Delta T = 3t_1 + \frac{H}{C_e} + \frac{(H - C_p \Delta T)}{C_e} - t_p \tag{12}$$

Solving for ΔT , one gets

$$\Delta T = \frac{(2H/C_e + 3t_1 - t_p)}{(1 + C_p/C_e)} \tag{13}$$

The start time of plastic wave transmission t_p is determined from the transmitted core stress given in Eq. 5.

2.2 Phase II – Global Bending/Shear

The global sandwich deformation and velocity fields in Phase II are shown in Fig. 6a, b. Subsequent to Phase I, the load has ended and the core has crushed permanently to a height of $H' = H - \delta$. Momentum is transferred to the sandwich panel, which has become impulsively loaded with a uniformly distributed velocity field (see top diagram in Fig. 6b). Conservation of momentum gives the initial velocity of the panel as

$$v_i = \frac{p_o \tau}{2(\rho_c H + 2\rho_f h)} \tag{14}$$

Denote the distance from the center of the panel to the wave front of the transverse shear wave as ξ . A transverse shear elastic unloading wave propagates from the clamped boundaries with velocity ξ . This unloading wave instantaneously brings the plate to rest behind the wave front. As the plate is brought to rest, it undergoes shear and bending deformations as exemplified in Fig. 6a, b.

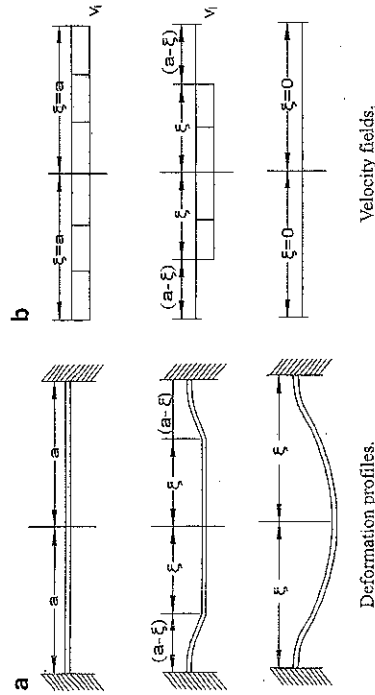


Fig. 6 Global panel bending/shear response: (a) deformation profiles and (b) velocity fields

2.2.1 System Lagrangian

Dynamic equilibrium of the complete sandwich can be expressed in terms of the maximum deflection at the center, Δ , and an equivalent shear angle, α_o . These two degrees of freedom have associated velocities, v_i and $\dot{\Omega}$, respectively. The kinetic energy for the sandwich is thus $T = \frac{1}{2} m_{eff} v_i^2 + \frac{1}{2} I_{eff} \dot{\Omega}^2$, where $m_{eff} = \pi \xi^2 [2\rho_f h + \rho_c H]$ is the effective sandwich mass and I_{eff} is the effective sandwich rotary inertia. Assume the rate of angular rotation is a maximum at the wave front and decreases linearly to zero at the boundary:

$$\dot{\alpha}(r) = \begin{cases} 0, & 0 \leq r \leq \xi \\ \Omega \frac{(a-r)}{(a-\xi)}, & \xi < r \leq a \end{cases} \tag{15}$$

Then, the effective rotary inertia for the sandwich is $I_{eff} = \frac{\pi}{6} \bar{I} (a - \xi) (a + 3\xi)$, where $\bar{I} = \sum_{k=1}^3 \rho_k (z_k^3 - z_{k-1}^3) = \frac{\rho_f}{12} (3hH^2 + 3h^2H + h^3) + \frac{\rho_c}{12} H^3$.

The elastic potential energy of the system is equivalent to the bending/shear strain energy of the sandwich, $\Pi = U$. The Lagrangian for the whole model is $L = T - \Pi$. For dynamic equilibrium,

$$\frac{\partial}{\partial t} \left(\frac{\partial L}{\partial v_i} \right) - \frac{\partial L}{\partial \Delta} = 2\pi \xi \dot{\xi} [2\rho_f h + \rho_c H] v_i + \frac{\partial U}{\partial \Delta} = 0 \tag{16}$$

and

$$\frac{\partial}{\partial t} \left(\frac{\partial L}{\partial \dot{\Omega}} \right) - \frac{\partial L}{\partial \alpha_o} = \Omega \frac{\partial I_{eff}}{\partial t} + I_{eff} \frac{\partial \Omega}{\partial t} + \frac{\partial U}{\partial \alpha_o} = 0 \tag{17}$$

2.2.2 Bending/Shear Strain Energy Potential

Assume in-plane deformations are negligible compared to the transverse deformation. The elastic strain energy of the symmetric sandwich panel with orthotropic facesheet is then given as

$$U = \int_S \left\{ \frac{D_{11}^i}{2} \left(\frac{\partial \bar{\alpha}}{\partial x} \right)^2 + D_{12}^i \left(\frac{\partial \bar{\beta}}{\partial y} \right) \left(\frac{\partial \bar{\alpha}}{\partial x} \right) + \frac{D_{22}^i}{2} \left(\frac{\partial \bar{\beta}}{\partial y} \right)^2 \left[\frac{\partial^2}{\partial x^2} + \alpha \frac{\partial w}{\partial x} + \frac{1}{2} \left(\frac{\partial v}{\partial x} \right)^2 \right] + A_{44}^s \left[\frac{\bar{\beta}^2}{2} + \bar{\beta} \frac{\partial w}{\partial y} + \frac{1}{2} \left(\frac{\partial w}{\partial y} \right)^2 \right] + D_{66}^i \left[\frac{1}{2} \left(\frac{\partial \bar{\alpha}}{\partial y} \right)^2 + \frac{\partial \bar{\alpha}}{\partial y} \frac{\partial \bar{\beta}}{\partial x} + \frac{1}{2} \left(\frac{\partial \bar{\beta}}{\partial x} \right)^2 \right] \right\} dS \tag{18}$$

where w is the transverse deflections, $\bar{\alpha}$ and $\bar{\beta}$ are shear angles associated with the x- and y-directions, respectively, D_{ij}^i is the sandwich bending stiffness matrix, A_{44}^s and A_{55}^s are the transverse shear stiffnesses, and S is the panel surface area. The

superscript "s" is used to denote the sandwich properties. Equation 18 is a special case of a more general expression for the elastic strain energy of a symmetric sandwich panel with orthotropic facesheet [10].

Finite element analysis using ABAQUS Explicit indicates that the transverse deformation w and the shear rotations with respect to the radial direction $\bar{\alpha}$ are of the following forms:

$$w(r) = \begin{cases} \Delta, & 0 \leq r \leq \xi \\ \Delta \left(1 - \left(\frac{r-\xi}{a-\xi}\right)^2\right), & \xi < r \leq a \end{cases} \quad (19)$$

and

$$\bar{\alpha}(r) = \begin{cases} 0, & 0 \leq r \leq \xi \\ 4\alpha_0 \frac{(r-\xi)(a-r)}{(a-\xi)^2}, & \xi < r \leq a \end{cases} \quad (20)$$

where Δ is the global deflection and α_0 is the rotation at $r = (a + \xi)/2$. The deflection profile described by Eq. 19 was found by fitting functions to the transient deflection profiles in the region. The transverse shear angle function was derived from the transverse shear strain, γ_{rz} , and slope of the deflection profile: $\bar{\alpha} = \gamma_{rz} - \partial w/\partial r$.

To evaluate the integral expression in Eq. 18 to polar coordinates, set $dS = r dr d\theta$ and derivatives with respect to x and y as $\frac{\partial}{\partial x} = \cos\theta \frac{\partial}{\partial r} - \frac{\sin\theta}{r} \frac{\partial}{\partial \theta}$ and $\frac{\partial}{\partial y} = \sin\theta \frac{\partial}{\partial r} + \frac{\cos\theta}{r} \frac{\partial}{\partial \theta}$, respectively. Furthermore, for the special case of $D_{22}^s = D_{11}^s$ and $A_{44}^s = A_{55}^s$, Eq. 18 becomes

$$U = \frac{8(a+\xi)}{3(a-\xi)} [\pi D_{11}^s + 2D_{12}^s + (2+\pi)D_{66}^s] \alpha_0^2 + \frac{2}{105} \frac{A_{55}^s}{(a-\xi)} [28\pi(a^3 - a\xi^2 - a^2\xi + \xi^3) \alpha_0^2 + (-176a^2 + 16\xi a + 160\xi^2) \alpha_0 \Delta + (29\pi\xi + 35\pi a) \Delta^2] \quad (21)$$

2.2.3 Equations of Motion

The propagation speed of the unloading elastic wave ξ is assumed constant and defined as a negative quantity in Figs. 6a and b. Denoting $\dot{\xi} = \frac{-(a-\xi)}{t}$ and $\Delta = v_1 t$, one gets the following coupled equations of motion from Eqs. (16) and (17):

$$-2\pi [2\rho_f h + \rho_c H] \xi \frac{(a-\xi)}{t} v_1 + \frac{2}{105} \frac{A_{55}^s}{(a-\xi)} [-16(a-\xi)(11a+10\xi)\alpha_0 + 2+2\pi(29\xi+35a)v_1 t] = 0 \quad (22)$$

and

$$\frac{\pi}{6} \dot{I}(a-\xi)(a+3\xi) \frac{d^2\alpha_0}{dt^2} - \frac{\pi}{3} \dot{I} \frac{(a-\xi)(a-3\xi)}{t} \frac{d\alpha_0}{dt} + \frac{16(a+\xi)}{3(a-\xi)} [\pi D_{11}^s + 2D_{12}^s + (2+\pi)D_{66}^s] \alpha_0 + \frac{2}{105} A_{55}^s [56\pi(a^2 - \xi^2) \alpha_0 - 16(11a + 10\xi)v_1 t] = 0 \quad (23)$$

where $\alpha_0(0) = 0$ and $\dot{\alpha}_0(0) = 0$.

2.3 Transient Deformations

As an example consider a fully clamped, sandwich panel made of E-glass vinyl ester facesheets and Divinycell H100 foam core, with a radius 250 mm, facesheet thickness 2 mm, and core thickness 25 mm. Material properties for the E-glass vinyl ester and Divinycell H100 foam are given in Table 1. The material properties for the

Table 1 Facesheet and foam material properties

	E-Glass/Vinyl Ester	Divinycell H100	Divinycell H200	Klegecell R300
Density (kg/m ³)	1391.3	100	200	300
Thickness (mm)	2	25	25	25
E ₁₁ (+) (GPa)	17	0.126	0.170	-
E ₂₂ (+) (GPa)	17	0.126	0.170	-
E ₃₃ (+) (GPa)	7.48	0.126	0.170	-
E ₁₁ (-) (GPa)	19	0.035	0.105	0.263
E ₂₂ (-) (GPa)	19	0.035	0.105	0.263
E ₃₃ (-) (GPa)	-	0.035	0.105	0.263
$\nu_{12} = \nu_{21}$	0.13	0.31	0.3	0.234
$\nu_{13} = \nu_{31}$	0.28	0.31	0.3	0.234
$\nu_{31} = \nu_{32}$	0.12	0.31	0.3	0.234
G _{12} = G₂₁ (GPa)}	4.0	0.01335	0.0403	0.106
G _{13} = G₃₁ (GPa)}	1.73	0.01335	0.0403	0.106
G _{13} = G₃₁ (GPa)}	1.73	0.01335	0.0403	0.106
q (MPa)	-	1.4	4.35	7.8
ϵ_D	-	0.76	0.7	0.285
$\sigma_{1r}(+)$ (MPa)	270	3.2	6.4	-
$\sigma_{1r}(-)$ (MPa)	200	1.53	4.36	-
$\sigma_{2r}(+)$ (MPa)	270	3.5	6.4	-
$\sigma_{2r}(-)$ (MPa)	200	1.53	4.36	-
$\tau_{12r}(+) = \tau_{21r}(+)$ (MPa)	40	1.47	3.86	-
$\tau_{13r}(+) = \tau_{31r}(+)$ (MPa)	31.6	1.47	3.86	-
$\tau_{23r}(+) = \tau_{32r}(+)$ (MPa)	31.6	1.47	3.86	-

Divinycell H100 and H200 foams in Table 1 were taken from Mines and Alias [11]. Let the sandwich panel be subject to a uniformly distributed pressure pulse of the form given in Eq. 1, where $P_0 = 10$ MPa and $\tau = 0.05$ ms.

This problem was modeled in 2D assuming axi-symmetric conditions for the Phase I response and in full 3D for both Phase I and Phase II responses using ABAQUS Explicit Version 6.7. In the 2D model, continuum axi-symmetric, 4 node reduced integration, CAX4R, were chosen for both facesheets and foam. In the 3D model, four node, reduced integration shell elements S4R and continuum 3D, eight node reduced integration elements C3D8R were chosen for the facesheets and core, respectively. The E-glass vinyl ester was considered as orthotropic elastic material, and the Divinycell H100 foam was modeled as crushable foam with isotropic hardening. The plastic hardening curves were taken from Ref. [11] for the Divinycell H100 and H200 foams and Ref. [12] for the Klegecell R300 foam. Although full integration elements could have been used for the FEA analysis, it was found that there would be very minor differences in the solution with full and reduced integration elements. Use of full integration elements simply did not warrant the very long computational run time and huge data files associated with them.

2.3.1 Local Core Crushing: Phase I Response

The FEA predicted distributions of the through-thickness particle velocity and transverse compressive stress at various times during Phase I are shown in Fig. 7a, b. It is clear to see that elastic waves propagated at a faster speed than the plastic waves. The elastic wave front is marked by a jump in the stress amplitude of $q = 1.4$ MPa. Particles behind the elastic wave front would have a particle velocity of $V_e = \frac{q}{\rho_e C_e} = 20.1$ m/s. The analytically predicted particle velocity in the elastic region compares very well to the FEA values shown in Fig. 7a, b. According to Eqs. 4 and 7, the elastic wave speed in the E-glass vinyl ester facesheets and the Divinycell H100 foam would be 2,414 m/s and 696.5 m/s, respectively. For the 2 mm thick facesheets and the 25 mm core, the elastic compressive stress wave reaches the distal facesheet at about 0.0375 ms, which corroborates with the FEA results at 0.0377 ms shown in Fig. 7a, b.

Behind the elastic stress waves are the plastic stress waves. The amplitude of the plastic stress wave exceeds the flow stress of 1.4 MPa and increases up to a peak value, which can be determined from Eq. 10. The highest transmitted stress was calculated from Eq. 10 as $\sigma_p = 2.1$ MPa. At this plastic stress value the plastic wave speed was calculated as $C_p = 95.97$ m/s.

The transmitted stress at Interface 1, which is described in Eq. 5, must be calculated separately for elastic and plastic responses because the transmission and reflection factors, k_T and k_{R1} , respectively, depend on the density and wave speed in the foam. A FORTRAN program was written to evaluate the time variation of the transmitted stress at Interface 1 in two parts: an initial elastic response

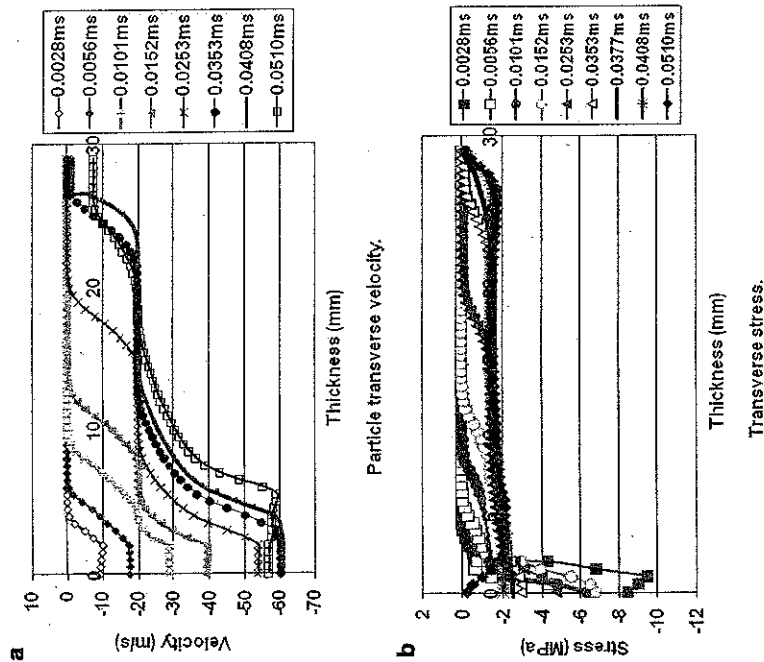


Fig. 7 Distribution of through-thickness particle velocity and stress at the panel center during and just after Phase I: (a) particle transverse velocity and (b) transverse stress

whereby $\sigma_{T1} < q$ and $\rho_e C_e = \rho_c C_c$ followed by a plastic response whereby $\sigma_{T1} > q$ and $\rho_e C_e = \rho_D C_p$. The FORTRAN results are shown by the solid line in Fig. 8. There is a jump in the transmitted stress when the core changes from linear elastic response to plastic response at the densification strain. This follows from the approximate compressive stress-strain relation for foams [8, 9]. The peak plastic stress $\sigma_p = 2.1$ MPa occurs at $t_p = 0.039$ ms. The transmitted stress at Interface 1 from FEA is also shown in Fig. 8 for comparison. The predicted peak plastic stress was about 4.5% lower than the maximum compressive stress of 2.2 MPa found at 0.0396 ms from FEA. The transmitted stress from FEA is smooth and shows no jump discontinuity when the core begins to plastically flow because the plastic hardening curve is more gradual and only approximates the ideal case of a plateau and an infinite gradient at the densification strain shown in Fig. 4. From the calculated values of C_p and t_p , local core crushing was estimated at 2.3 mm from Eqs. 11 and 13.

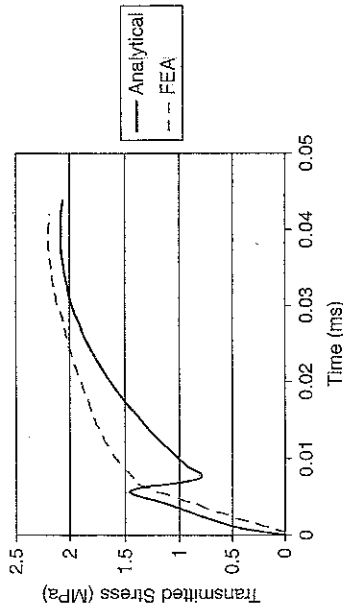


Fig. 8 Transmitted stress at Interface 1 up to peak stress

2.3.2 Global Bending/Shear: Phase II Response

The initial global panel velocity was determined from Eq. 14 as $v_i = 31$ m/s. The sandwich bending and shear stiffness were evaluated with a reduced core thickness $H' = 22.7$ mm. Note that a 2.3 mm indentation changes the core height from 25 to 22.7 mm. Since the bending stiffness is proportional to the cube of core height, this reduces the bending stiffness by 25%. A MATLAB program was written to solve Eqs. 22 and 23 for ξ and α_o . First, an expression for ξ in terms of α_o was derived from Eq. 22 and then substituted into Eq. 23 to eliminate ξ . Then, the resulting second order non-linear differential equation in α_o was solved using a Runge Kutta ordinary differential equation solver (ode45) in MATLAB. Eq. 22 is cubic in ξ , but only one of the three roots for ξ gives physically realistic solutions for α_o .

The transient deflection profile is fully determined from Eq. 19, knowledge of $\xi(t)$ and the fact that $\Delta = v_i t$. As shown in Fig. 9, the predicted transient deformation profiles compared very well to FEA results; the predicted value for ξ was within 7% of FEA. The solution for $\alpha_o(t)$ will be used to predict strains and damage initiation in the panel in the following section.

2.4 Damage Initiation

An important reason for developing analytical models is to provide simple design tools for determining the survivability of the panel when it is subjected to an intense pressure pulse load. There are critical impulses, combinations of peak pressures and pulse durations, which would just cause damage to initiate in the panel. Recall from the transient deformation analysis in the previous section that the maximum bending strains occur either in the center or clamped edges of the sandwich panel. It is assumed that the clamped edges would be protected from damage so that the panel center is the most critical area for damage initiation.

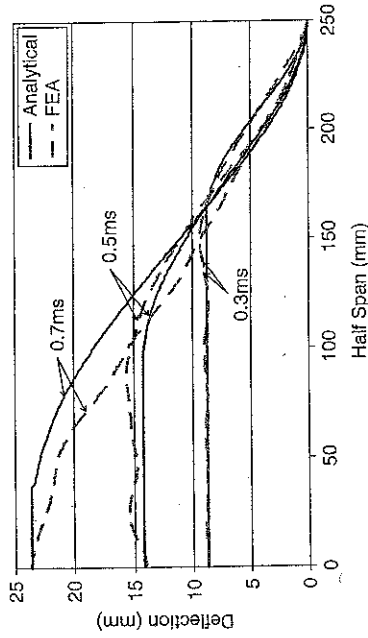


Fig. 9 Transient deflection profiles of composite sandwich

So that the analytical predictions could be compared to ABAQUS Explicit results, Hashin's failure criteria [13] was chosen to predict damage initiation. In Hashin's theory, the following four damage initiation mechanisms are considered for a unidirectional laminate: fiber tension, matrix tension, fiber compression, and matrix compression. These are expressed in terms of principal stresses σ_{ij} , material strengths, and the following failure parameters,

$$F_f^t = \left(\frac{\sigma_{11}}{X^T} \right)^2 + \left(\frac{\tau_{12}}{S^L} \right)^2 \quad (24)$$

$$F_m^t = \left(\frac{\sigma_{22}}{Y^T} \right)^2 + \left(\frac{\tau_{12}}{S^L} \right)^2 \quad (25)$$

$$F_f^c = \left(\frac{\sigma_{11}}{X^C} \right)^2 \quad (26)$$

$$F_m^c = \left(\frac{\sigma_{22}}{2S^T} \right)^2 + \left(\frac{\tau_{12}}{S^L} \right)^2 + \left[\left(\frac{Y^C}{2S^T} \right)^2 - 1 \right] \frac{\sigma_{22}}{Y^C} \quad (27)$$

Matrix compression

where X^T and Y^T are the longitudinal and transverse tensile strengths, X^C and Y^C are the longitudinal and transverse compressive strengths, S^L is the longitudinal shear strength and S^T is the transverse shear strength. When $F_f^t = 1$, $F_m^t = 1$, $F_f^c = 1$, or $F_m^c = 1$, the corresponding damage mode initiates. For the 0/90 degree orthotropic laminate facesheets, $\sigma_{11} = \sigma_{22}$ and $X^T = Y^T$, so that fiber tension and matrix tension failure conditions in Eqs. 24 and 25 would be identical. The fiber and matrix compression criteria, Eqs. 26 and 27, would also apply in both principal directions.

For the orthotropic facesheet with fibers in 0 and 90 degrees parallel to the x- and y-axes, one gets that the following relationship between principal stresses and strains

$$\begin{Bmatrix} \sigma_{11} \\ \sigma_{22} \\ \tau_{12} \end{Bmatrix} = \begin{bmatrix} \bar{Q}_{11} & \bar{Q}_{12} & 0 \\ \bar{Q}_{12} & \bar{Q}_{11} & 0 \\ 0 & 0 & \bar{Q}_{66} \end{bmatrix} \begin{Bmatrix} \epsilon_x \\ \epsilon_y \\ \gamma_{xy} \end{Bmatrix} \quad (28)$$

where \bar{Q}_{ij} is the transformed stiffness matrix. The strains in rectangular coordinates are evaluated in transformed polar coordinates as follows:

$$\epsilon_x = z \frac{\partial \bar{\alpha}}{\partial x} = z \cos \theta \frac{\partial \bar{\alpha}}{\partial r} \quad (29)$$

$$\epsilon_y = z \frac{\partial \bar{\beta}}{\partial y} = z \sin \theta \frac{\partial \bar{\alpha}}{\partial r} \quad (30)$$

$$\gamma_{xy} = z \left(\frac{\partial \bar{\alpha}}{\partial x} + \frac{\partial \bar{\alpha}}{\partial y} \right) = z (\cos \theta + \sin \theta) \frac{\partial \bar{\alpha}}{\partial r} \quad (31)$$

Thus, the principal stresses are expressed in polar coordinates as

$$\sigma_{11} = z \frac{4\alpha_o (a + \xi - 2r)}{(a - \xi)^2} (\bar{Q}_{11} \cos \theta + \bar{Q}_{12} \sin \theta) \quad (32)$$

$$\sigma_{12} = z \frac{4\alpha_o (a + \xi - 2r)}{(a - \xi)^2} (\bar{Q}_{12} \cos \theta + \bar{Q}_{22} \sin \theta) \quad (33)$$

$$\tau_{12} = z \frac{4\alpha_o (a + \xi - 2r)}{(a - \xi)^2} \bar{Q}_{66} (\cos \theta + \sin \theta) \quad (34)$$

The principal stress components are greatest at the top or bottom of the outer facesheets, $z = \pm (H'/2 + h)$, and for $\bar{Q}_{11} = \bar{Q}_{22}$, each stress components will be maximum at $\theta = 45$ degrees. Furthermore, the impulse that would just cause damage relate to either tensile fiber or matrix conditions (Eqs. 24 or 25) and first occurs at $r = 0$ and when $\xi = 0$. A criterion for damage initiation following tensile fiber or matrix failure is given by

$$1 = \frac{2\alpha_o^2 (H' + 2h)^2}{a^2} \left[\left(\frac{\bar{Q}_{11} + \bar{Q}_{12}}{X_T} \right)^2 + \left(\frac{2\bar{Q}_{66}}{S^L} \right)^2 \right] \quad (35)$$

The above failure criterion gives a combination of permanent core height H' and shear angle α_o for damage initiation. A critical impulse would be responsible for this combination of H' and shear angle α_o .

For the sandwich panel with H100 PVC foam core in the example problem, it was predicted that a critical impulse $I_{cr} = 54.83$ Pa-s ($p_o = 2.2$ MPa and $\tau = 0.05$ ms) would just cause damage initiation in the panel center. At this value of the pressure pulse the core had almost negligible permanent deformation at the end of

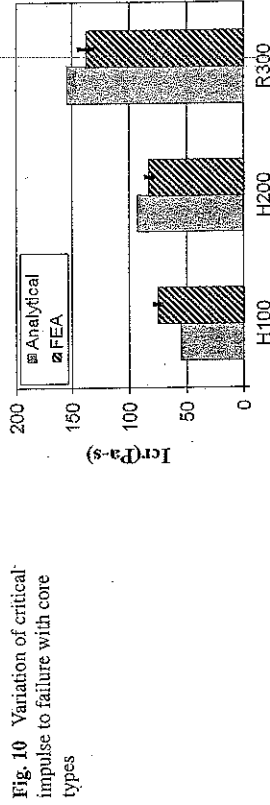


Fig. 10 Variation of critical impulse to failure with core types

Phase I, $H' = 24$ mm. The ABAQUS Explicit finite element program was run using Hashin's failure criteria for damage initiation. It was found that damage initiated near the panel center when the pressure pulse was adjusted to $p_o = 3$ MPa and $\tau = 0.05$ ms or an impulse of 75 Pa-s. Below this peak load and duration, no damage occurred in the FEA. Thus the critical impulse to failure is $I_{cr} = 75$ Pa-s as predicted by FEA. The analytical critical impulse to failure is about 27% less than FEA predictions. The discrepancy between analytical and FEA predictions was attributed to the fact that in the FEA, tensile fiber and/or matrix damage took place near but not exactly in the panel center as was assumed in the analytical model.

Damage initiation of sandwich panels with the same 2 mm-thick, E-glass vinyl ester facesheets and two other cores, namely Divinycell H200 and Klegecell R300 foams, were also considered. Material properties for the Divinycell H200 and Klegecell R300 foams are listed in Table 1. The analytical predictions for the critical impulse to failure using the wave propagation model and Hashin's tensile fiber and/or matrix failure criteria compared better to FEA predictions than with the Divinycell H100 foam core, as indicated in Fig. 10. The analytical predictions for the Divinycell H200 and Klegecell R300 foams were only about 13% higher than FEA results. The actual failure site for damage initiation in the sandwich panels with the Divinycell H200 and Klegecell R300 foams were exactly in the center of the distal facesheet, as assumed in the analytical model.

3 High-Velocity Impact of Sandwich Panels

Consider the composite sandwich panel, as shown in Fig. 11. The facesheets are orthotropic plates of thickness h , and the core is crushable polymeric foam of thickness H . The blunt cylindrical projectile has a radius r_p , a mass M_o , and a velocity V_o . The projectile is assumed rigid compared to the sandwich panel.

Upon impact, the panel experiences local indentation as well as global bending/shear deformation. At the early stages of impact, compressive stress waves are generated under the projectile. These stress waves must travel through the incident facesheet, core and distal facesheet before global transverse shear and bending waves can be transmitted laterally in the sandwich panel. During this phase, the

Fig. 11 Projectile impact of composite sandwich panel

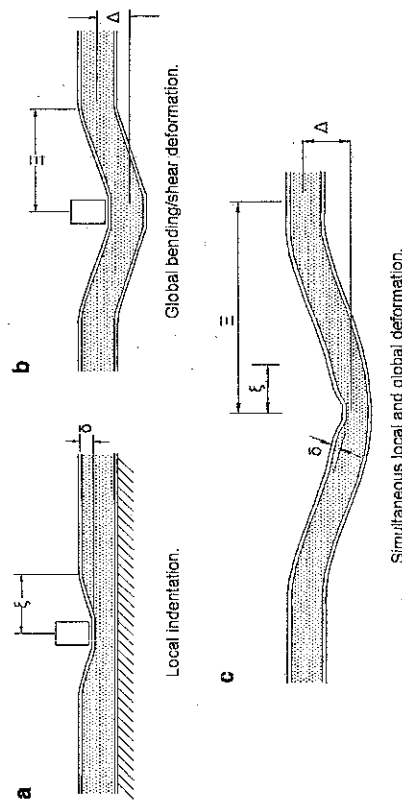
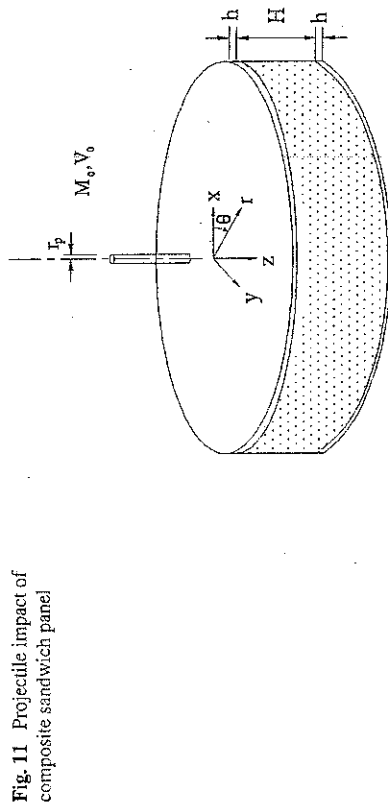


Fig. 12 Local and global sandwich deformations: (a) local indentation, (b) global bending/shear and (c) simultaneous local and global deformations

problem becomes one of local indentation only, i.e., the incident facesheet deflects under the projectile and the core crushes as if the distal facesheet of the sandwich panel were rigidly-supported. In Fig. 12a, the local indentation under the projectile is denoted δ and the lateral extent of deformation is denoted ξ . Once the through-thickness compressive stress waves have reached the distal side of the sandwich panel, global panel bending/shear deformation can initiate. These global bending/shear deformations are also shown Fig. 12b, where the maximum global deflection under the projectile is denoted Δ and the lateral extent of global deformation is denoted E . Simultaneous local indentation and global deformation actually occurs until the core can no longer crush because of material densification or failure has occurred (see Fig. 12c). Analytical solutions for the local and local/global transient response of the panel will be given in the following section.

3.1 Phase I: Local Indentation

The local indentation is found by considering projectile impact of a facesheet resting on a foam foundation. The duration of Phase I is determined from the wave travel time through the thickness of the panel.

3.1.1 Through-Thickness Wave Propagation

Compressive stress waves must pass through the full thickness of the sandwich, i.e., two facesheets and core, before any response can be characterized as global bending/shear deformation. The through-thickness wave travel time is given by

$$t_I = \frac{2h}{C_f} + \frac{H}{C_d} \quad (36)$$

where C_f is the wave speed in the transverse direction of the facesheet and C_d is the elastic dilatational wave speed in the core. The transverse wave speed in an orthotropic plate is given by

$$C_f = \sqrt{\rho_f (1 - \nu_{12}\nu_{21} - \nu_{23}\nu_{32} - \nu_{13}\nu_{31} - 2\nu_{21}\nu_{32}\nu_{13})} \quad (37)$$

where E_{ij} , ν_{ij} and ρ_f are the elastic modulus, Poisson's ratio and density of the orthotropic facesheet, respectively [14]. The dilatational wave speed in the core is given in terms of Lamé's constant, λ and μ , as follows:

$$C_d = \sqrt{\frac{\lambda + 2\mu}{\rho_c}} \quad (38)$$

where $\lambda = \frac{E_c \nu_c}{(1+\nu_c)(1-2\nu_c)}$, $\mu = \frac{E_c}{2(1+\nu_c)}$ and ν_c is Poisson's ratio of the foam.

3.1.2 Local Indentation

Local indentation is found by considering the projectile presses onto the incident facesheet resting on a foam foundation. A single degree-of-freedom equation of motion governing the dynamics of the projectile and effective facesheet mass can be written considering the system Lagrangian. The Lagrangian L for a system is defined as $L = T - \Pi$, where T and Π are the kinetic energy and potential energy of the system, respectively.

Kinetic Energy

The kinetic energy of the system is given by

$$T = \frac{1}{2} M_o V_1^2 + \frac{1}{2} m_f V_1^2 + \frac{1}{2} m_a V_1^2 \tag{39}$$

where V_1 is the velocity under the projectile, m_f is the effective mass of the facesheet and m_a is the added mass of core. The last two terms in Eq. 39 increase over time as waves propagate laterally across the panel and through the thickness of the panel. The effective mass of the facesheet is found by assuming that the projectile induces the following linear velocity field in the facesheet:

$$\dot{w} = V_1 \left[1 - \frac{r}{\xi} \right] \tag{40}$$

The spread of the deformation zone ξ in the above equation varies with time, i.e., the velocity field has a moving boundary and the effective facesheet mass grows as the velocity field spreads away from the impact site. The total kinetic energy of the facesheet is thus given by

$$T_f = \frac{1}{2} (2\pi) \int_0^\xi \rho_f h V_1^2 \left[1 - \frac{r}{\xi} \right]^2 r dr \tag{41}$$

Integrating the kinetic energy of the facesheet and setting it equal to the equivalent kinetic energy produced by an effective facesheet mass m_f give

$$m_f = \frac{\pi \rho_f h}{6} \xi^2 \tag{42}$$

The added mass of core is more complicated to evaluate because core particle velocities are governed by elastic and plastic response. Elastic and plastic regions in the foam are shown in Fig. 13a. Under the projectile, the elastic wave front has advanced a distance $C_d t$, while the plastic wave front has advanced a distance $C_p t$. As the deformation spreads laterally, the distances from the incident facesheet to the elastic and plastic wave fronts decrease in an approximately linear fashion. The volume of plastic and elastic foam is described by a cone and a truncated cone, respectively. The particle velocity in the plastic zone is controlled by the projectile impact speed and the velocity field of incident facesheet, which is described in Eq. 40. The particle velocity in the elastic zone depends on the magnitude of the elastic stress $V = \frac{q}{\rho_c C_d}$. Thus the maximum particle velocity in the elastic zone is $V_e = \frac{q}{\rho_c C_d}$. It is assumed that the elastic particle velocity decreases linearly through the thickness of the foam. The variation of the particle velocities through the foam thickness under the projectile and half-way across the local deformation zone is shown in Fig. 13b. Following

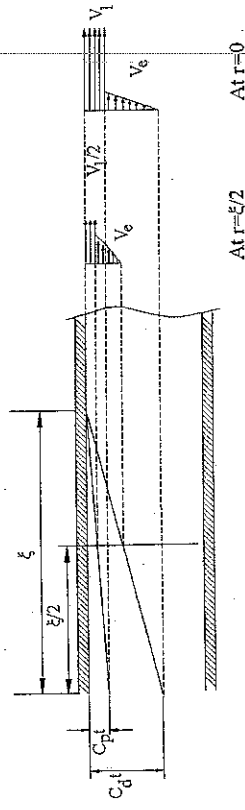


Fig. 13 Propagation of elastic and plastic waves in the core during Phase I (particle velocity fields shown right)

these velocity distributions, the kinetic energy of the elastic and plastic parts of the foam is derived in Appendix B and is taken as

$$T_a = \frac{\pi \rho_c \delta}{20 (1 - \epsilon_D) \epsilon_D} \xi^2 V_1^2 + \frac{\pi \rho_c}{18} \left(C_d t - \frac{\delta}{\epsilon_D} \right) \xi^2 V_e^2 \tag{43}$$

The first and second terms on the right-hand side of Eq. 43 are the kinetic energy of the plastically and elastically deformed core, respectively. The added mass of the core is therefore

$$m_a = \frac{\pi \rho_c \delta}{10 (1 - \epsilon_D) \epsilon_D} \xi^2 + \frac{\pi \rho_c}{9} \left(C_d t - \frac{\delta}{\epsilon_D} \right) \xi^2 \frac{V_e^2}{V_1^2} \tag{44}$$

Potential Energy

The total potential energy of the system, Π , consists of the elastic strain energy of the facesheet, U_i , and the work dissipated in crushing the core, D :

$$\Pi = U_i + D \tag{45}$$

Assuming in-plane deformations are negligibly small compared to transverse deflections, w , the elastic strain energy due to bending and membrane stretching in an orthotropic facesheet is

$$U_i = \frac{1}{2} \int \int_S \left[D_{11} \left(\frac{\partial^2 w}{\partial x^2} \right)^2 + 2D_{12} \frac{\partial^2 w}{\partial x^2} \frac{\partial^2 w}{\partial y^2} + D_{22} \left(\frac{\partial^2 w}{\partial y^2} \right)^2 + 4D_{66} \left(\frac{\partial^2 w}{\partial x \partial y} \right)^2 \right] dS + \frac{1}{8} \int \int_S \left[A_{11} \left(\frac{\partial w}{\partial x} \right)^4 + A_{22} \left(\frac{\partial w}{\partial y} \right)^4 + (2A_{12} + 4A_{66}) \left(\frac{\partial w}{\partial x} \right)^2 \left(\frac{\partial w}{\partial y} \right)^2 \right] dS \tag{46}$$

where it is assumed that $\dot{\xi} = \xi/t$. Conservation of linear momentum relates the projectile and effective facesheet mass velocity, V_1 , with $\dot{\xi}$:

$$M_o V_o = M_o V_1 + 2\pi \int_0^{\xi} \rho_f h V_1 \left(1 - \frac{r}{\xi}\right) r dr + L_p + L_e \tag{52}$$

where L_p and L_e are the momentum associated with the plastic and elastic regions of the foam, respectively. The following expressions were derived for them in Appendix B: $L_p = \frac{\pi \rho_c \delta V_1 \xi^2}{6\epsilon_D(1-\epsilon_D)}$ and $L_e = \frac{\pi \rho_c V_e \xi^2}{6} \left(C_d t - \frac{\delta}{\epsilon_D}\right)$. Momentum balance thus gives

$$M_o V_o = M_o V_1 + \frac{\pi \rho_f h V_1 \xi^2}{6} + \frac{\pi \rho_c \delta V_1 \xi^2}{6\epsilon_D(1-\epsilon_D)} + \frac{\pi \rho_c V_e \xi^2}{6} \left(C_d t - \frac{\delta}{\epsilon_D}\right) \tag{53}$$

Note that the momentum of the facesheet and core has been integrated using the velocity and mass field described earlier. Equation 51 becomes a nonlinear second order differential equation in δ when Equation 53 is used to eliminate ξ . The initial conditions for Eq. 51 are $\delta(t_o) = 0$ and $\frac{d\delta}{dt}(t_o) = \frac{M_o V_o}{(M_o + \pi r_o^2 \rho_f h)}$, where $t_o = \frac{h}{C_d}$.

3.2 Phase II: Global Bending/Shear

At the end of Phase I, transverse shear waves propagate from the point of impact across the sandwich panel. The global panel deflection is denoted Δ and the lateral extent of global deformation is denoted \bar{S} , as shown in Fig. 12c. A two degree-of-freedom model shown in Fig. 14 is considered for combined local indentation and global panel bending/shear deformations. Degrees of freedom, X_1 and X_2 , are related to the position of the projectile and incident facesheet, and the deflection of the sandwich panel under the projectile if there were no local indentation of core crushing, respectively. Therefore, $\delta = X_1 - X_2$ and $\Delta = X_2$. Applying Lagrange's equations of motion results in two equations of motion:

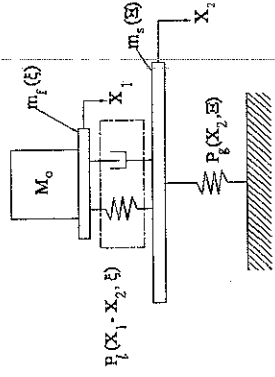


Fig. 14 Two degree-of-freedom model for coupled local and global deformation

where D_{ij} and A_{ij} are the bending and membrane stiffness of the facesheet and S is the surface area associated with indentation. When deflections are less than 0.5 h, the bending energy, which is calculated from the first integral in Eq. 46, dominates in the expression for U_1 . The membrane energy, which is represented by the second integral in Eq. 46, becomes greater than the bending energy when deflections are greater than h.

Finite element analysis has shown that the transverse deflection of the facesheet may be assumed as follows:

$$w(r) = \delta \left[1 - \left(\frac{r}{\xi} \right)^2 \right]^3 \tag{47}$$

where $r^2 = x^2 + y^2$. To evaluate the integral expression in Eq. 46 in polar coordinates, set $dS = r dr d\theta$ and derivatives with respect to x and y as $\frac{\partial}{\partial x} = \text{Cos}\theta \frac{\partial}{\partial r} - \frac{\text{Sin}\theta}{r} \frac{\partial}{\partial \theta}$ and $\frac{\partial}{\partial y} = \text{Sin}\theta \frac{\partial}{\partial r} + \frac{\text{Cos}\theta}{r} \frac{\partial}{\partial \theta}$, respectively. The strain energy due to facesheet bending and membrane stretching is

$$U_1 = \bar{D} \frac{\delta^2}{\xi^2} + \bar{A} \frac{\delta^4}{\xi^2} \tag{48}$$

where $\bar{D} = \frac{6\pi}{5} [3(D_{11} + D_{22}) + 2D_{12} + 4D_{66}]$ and $\bar{A} = \frac{\pi}{250} [27(A_{11} + A_{22}) + 18A_{12} + 36A_{66}]$.

The elastic strain energy and plastic work in the foam are derived separately in Appendix C, giving a total energy consumed in the foam as

$$D = \frac{\pi q \delta \xi^2}{3} + \frac{\pi q^2}{18 E_c} \left(C_d t - \frac{\delta}{\epsilon_D} \right) \xi^2 \tag{49}$$

The first and second terms on the right-hand side of Eq. 49 are the plastic work and elastic strain energy, respectively.

Equation of Motion

Lagrange's equation of motion for the projectile and effective facesheet mass is

$$\frac{\partial}{\partial t} \left(\frac{\partial L}{\partial \dot{V}_1} \right) - \frac{\partial L}{\partial \delta} = 0 \tag{50}$$

where $L = T - \Pi$ and $V_1 = \frac{d\delta}{dt}$. Substituting T and Π into Eq. 50 gives

$$\left(M_o + m_f + \frac{\pi \rho_c \delta \xi^2}{10(1-\epsilon_D)\epsilon_D} \right) \frac{d^2 \delta}{dt^2} + \left(\frac{\pi \rho_f h \xi^2}{3t} + \frac{\pi \rho_c \delta \xi^2}{5(1-\epsilon_D)\epsilon_D t} \right) \frac{d\delta}{dt} + \frac{\pi \rho_c \xi^2 V_1^2}{20(1-\epsilon_D)\epsilon_D} + \frac{\pi \rho_c V_e \xi^2}{18\epsilon_D} + \frac{2\bar{D}\delta}{\xi^2} + \frac{\pi q \xi^2}{\xi^2} + \frac{\pi q^2 \xi^2}{3} - 18E_c \epsilon_D = 0 \tag{51}$$

$$\frac{\partial}{\partial t} \left(\frac{\partial L}{\partial \dot{V}_1} \right) - \frac{\partial L}{\partial X_1} = 0 \quad (54)$$

$$\frac{\partial}{\partial t} \left(\frac{\partial L}{\partial \dot{V}_2} \right) - \frac{\partial L}{\partial X_2} = 0 \quad (55)$$

where $V_1 = \frac{dX_1}{dt}$ and $V_2 = \frac{dX_2}{dt}$.

3.2.1 Kinetic Energy

Assume the mass of the core is small compared to the mass of the facesheet and neglect rotary inertia of the sandwich panel. Then the kinetic energy of the system is given by

$$T = \frac{1}{2} M_o V_1^2 + \frac{1}{2} m_f V_1^2 + \frac{1}{2} m_s V_2^2 \quad (56)$$

where m_s is the effective mass of the sandwich and V_2 is the velocity of the sandwich under the projectile. The added mass of the core is taken into account in the effective mass of the sandwich. The effective mass of the sandwich is calculated by again assuming a linear velocity field for the sandwich:

$$\dot{w} = V_2 \left(1 - \frac{r}{\bar{E}} \right) \quad (57)$$

From the above velocity field, one finds that the effective sandwich mass is

$$m_s = \frac{\pi}{6} (2\rho_f h + \rho_c H) \bar{E}^2 \quad (58)$$

3.2.2 Global Bending/Shear Energy

The elastic strain energy due to bending and shear of a symmetric sandwich panel with orthotropic facesheet is

$$U_\xi = \int_S \left\{ \frac{D_{11}^s}{2} \left(\frac{\partial \bar{\alpha}}{\partial x} \right)^2 + D_{12}^s \left(\frac{\partial \bar{\beta}}{\partial y} \right) \left(\frac{\partial \bar{\alpha}}{\partial x} \right) + \frac{D_{22}^s}{2} \left(\frac{\partial \bar{\beta}}{\partial y} \right)^2 + D_{66}^s \left[\frac{1}{2} \left(\frac{\partial \bar{\alpha}}{\partial y} \right)^2 + \frac{\partial \bar{\alpha}}{\partial y} \frac{\partial \bar{\beta}}{\partial x} + \frac{1}{2} \left(\frac{\partial \bar{\beta}}{\partial x} \right)^2 \right] + A_{44}^s \left[\frac{\bar{\beta}^2}{2} + \bar{\beta} \frac{\partial w}{\partial y} + \frac{1}{2} \left(\frac{\partial w}{\partial y} \right)^2 \right] + A_{55}^s \left[\frac{\bar{\alpha}^2}{2} + \bar{\alpha} \frac{\partial w}{\partial x} + \frac{1}{2} \left(\frac{\partial w}{\partial x} \right)^2 \right] \right\} dS \quad (59)$$

where w is again used to express transverse deflections, $\bar{\alpha}$ and $\bar{\beta}$ are shear angles associated with the x- and y-directions, respectively, D_{ij}^s is the sandwich bending

stiffness matrix, and A_{44}^s and A_{55}^s are the transverse shear stiffnesses. The superscript "s" is used to denote sandwich properties.

Assume the following global transverse deflection and shear rotations:

$$w(r) = \begin{cases} \Delta \left(1 - \left(\frac{r}{\bar{E}} \right)^2 \right)^3, & 0 \leq r \leq \bar{E} \\ 0, & r > \bar{E} \end{cases} \quad (60)$$

and

$$\bar{\alpha}(r) = \bar{\beta}(r) = \begin{cases} \frac{27\alpha_o}{4} \frac{r}{\bar{E}} \left(1 - \frac{r}{\bar{E}} \right)^2, & 0 \leq r \leq \bar{E} \\ 0, & r > \bar{E} \end{cases} \quad (61)$$

where Δ is the global deflection under the projectile and α_o is the shear rotation at the center of the panel.

Substituting derivatives of the expressions in Eqs. 60 and 61 into Eq. 59 gives the following expression for the strain energy:

$$U_\xi = \bar{D}_s \alpha_o^2 + \frac{1}{4480} (A_{44}^s + A_{55}^s) (-5472\bar{E}\alpha_o\Delta + 729\pi\bar{E}^2\alpha_o^2 + 1344\pi\Delta^2) \quad (62)$$

where $\bar{D}_s = \frac{243}{320} [\pi (D_{11}^s + D_{22}^s) + 4D_{12}^s + 2(\pi + 2)D_{66}^s]$.

3.2.3 Equations of Motion

Satisfying Lagrange's equations of motion stated in Eqs. 54 and 55 one gets

$$(M_o + m_f) \frac{d^2 X_1}{dt^2} + \frac{\pi \rho_f h \xi^2 V_1}{3t} + \frac{2\bar{D} (X_1 - X_2)}{\xi^2} + \frac{4\bar{A} (X_1 - X_2)^3}{\xi^2} + \frac{\pi q \xi^2}{3} = 0 \quad (63)$$

and

$$\begin{aligned} m_s \frac{d^2 X_2}{dt^2} + \frac{\pi (2\rho_f h + \rho_c H) \bar{E}^2 dX_2}{3t} + \frac{(A_{44}^s + A_{55}^s)}{140} (-171\bar{E}\alpha_o + 84\pi X_2) \\ - \frac{2\bar{D} (X_1 - X_2)}{\xi^2} - \frac{4\bar{A} (X_1 - X_2)^3}{\xi^2} - \frac{\pi q \xi^2}{3} = 0 \end{aligned} \quad (64)$$

where it is assumed that $\dot{\bar{E}} = \bar{E}/t$. Rotary inertia is neglected so that $\frac{\partial H}{\partial \alpha_o} = 0$ gives

$$\alpha_o = \frac{2736 (A_{44}^s + A_{55}^s) \bar{E} X_2}{4480 \bar{D}_s + 729\pi (A_{44}^s + A_{55}^s) \bar{E}^2} \quad (65)$$

The extent of local indentation and global deflections, ξ and \bar{E} , are evaluated from conservation of momentum and energy. Conservation of linear momentum is given as

$$M_o V_o = M_o V_1 + \frac{\pi (\rho_f h + \rho_c H)}{3} \mathcal{E}^2 \left(\frac{V_1 + V_2}{2} \right) \quad (66)$$

Conservation of energy stipulates that

$$\begin{aligned} \frac{1}{2} M_o V_o^2 &= \frac{1}{2} M_o V_1^2 + \frac{1}{2} m_s \left(\frac{V_1 + V_2}{2} \right)^2 + \bar{D} \frac{\delta^2}{\xi^2} + \bar{A} \frac{\delta^4}{\xi^2} + \frac{\pi q \delta \xi^2}{3} + \bar{D} s \alpha_o^2 \\ &+ \frac{1}{4480} (A_{44}^S + A_{55}^S) (-5472 \alpha_o \Delta \mathcal{E} + 1344 \pi \Delta^2 + 729 \pi \alpha_o^2 \mathcal{E}^2) \end{aligned} \quad (67)$$

The momentum and kinetic energy of the panel in Eqs. 66 and 67 are given in average forms in order to simplify the solution for ξ and \mathcal{E} . Equations 63 and 64 are solved with the following initial conditions: $\dot{X}_1(t_I) = X_{10}$, $\dot{X}_1(t_I) = \dot{X}_{10}$, $X_2(t_I) = 0$, and $\dot{X}_2(t_I) = 0$, where t_I is defined in Eq. 36 and X_{10} and \dot{X}_{10} are taken at the end of Phase I.

3.3 Comparison with Finite Element Analysis

As an example, consider a fully clamped sandwich panel made of E-glass vinyl ester facesheets and PVC H200 foam core, with a panel radius of 250 mm, facesheet thickness of 2 mm, and core thickness of 25 mm. Material properties for the E-glass vinyl ester and the PVC H200 foam are given in Table 1. Let the sandwich panel undergo impact by a rigid cylindrical rod of radius 2.5 mm, mass 0.5 kg, and velocity 40 m/s.

This impact problem was modeled using ABAQUS Explicit using continuum C3D8R elements for both the facesheets and the foam. The PVC H200 foam was modeled as crushable foam with isotropic hardening. Additional foam properties, such as the plastic hardening curve were taken from Reference [11]. The analytical solution for the incident facesheet under the projectile and global panel deflections are compared to FEA results in Fig. 15. The deflection of the distal facesheet

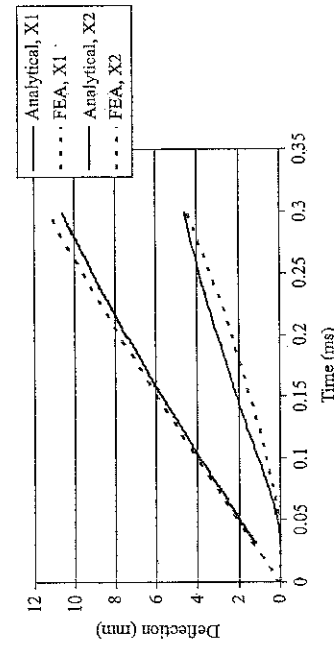


Fig. 15 Transient deflections of incident and distal facesheets under the projectile

under the projectile was taken as the global panel deflection in FEA. The analytical deflections are about 15% lower than FEA predictions.

4 Conclusions

Wave propagation models were developed to examine the damage resistance of composite sandwich panels subjected to blast and high velocity projectile impact. Analytical solutions were derived for the transient response and damage initiation of a foam-core composite sandwich panel subjected to uniformly-distributed, pressure pulse loading. The panel response was modeled in two consecutive phases: (1) a through-thickness wave propagation phase leading to permanent core crushing deformations and (2) a transverse shear wave propagation phase resulting in global panel deflections. The predicted transient deformation of a sandwich panel consisting of E-glass vinyl ester facesheets and PVC foam core was found to be within 7% of ABAQUS predictions. Analytical predictions of the critical impulse for damage initiation also compared fairly well with ABAQUS predictions.

The second wave propagation model was developed for the deformation response of a composite sandwich panel subjected to high velocity impact by a rigid blunt, cylindrical projectile. Waves travelling through the sandwich core thickness and laterally across the panel were incorporated in a previously developed two degrees-of-freedom model for the sandwich panel. Modelling the sandwich with two degrees of freedom allowed local indentation and core crushing to be coupled with global bending/shear deformations of the sandwich. An example was given for a composite sandwich panel consisting of orthotropic E-glass vinyl ester facesheets and PVC foam core and subjected to high velocity impact of a blunt cylindrical projectile. The analytical solution for the local indentation and global deflection under the projectile was found to be within 20% of FEA results.

Acknowledgement This work was supported by Dr. Yapa Rajapakse at the Office of Naval Research under grant N00014-07-1-0423.

Appendix A Uniaxial Strain Wave Speed in an Orthotropic Plate

Stress waves propagating through the thickness of the orthotropic facesheets travel in material that is constrained laterally in the x- and y-directions. To evaluate this wave speed, set $\epsilon_x = \epsilon_y = 0$. For the special case of a 0°/90° laminate, $\sigma_x = \sigma_y$, $E_{11} = E_{22}$, $\nu_{12} = \nu_{21}$, and $\nu_{31} = \nu_{32}$, two of the three-dimensional stress-strain relations become

$$\epsilon_y = \frac{(1 - \nu_{12})}{E_{11}} \sigma_x - \frac{\nu_{32}}{E_{33}} \sigma_z = 0 \quad (A.1)$$

$$\epsilon_z = -\frac{(v_{13} + v_{23})}{E_{11}}\sigma_x - \frac{1}{E_{33}}\sigma_z \quad (\text{A2})$$

and

$$\sigma_x = \frac{v_{32}}{E_{33}} \frac{E_{11}}{(1 - \nu_{12})} \sigma_z \quad (\text{A3})$$

Substituting the above expression for σ_x in Eq. A2 gives

$$\sigma_z = \frac{(1 - \nu_{12}) E_{33}}{[1 - \nu_{12} - \nu_{32}(v_{13} + v_{23})] \epsilon_z} \quad (\text{A4})$$

Equation A4 represents a stress-strain relation for an orthotropic material in one-dimensional or uniaxial strain. The wave speed for the material in this state is given by

$$C_f = \sqrt{\frac{(1 - \nu_{12}) E_{33}}{[1 - \nu_{12} - \nu_{32}(v_{13} + v_{23})] \rho_f}} \quad (\text{A5})$$

where ρ_f is the mass density.

Appendix B Momentum and Kinetic Energy of Core During Phase I

Both elastic and plastic compressive stress waves propagate in the core with speeds C_e and C_p . Given that $C_e > C_p$, the plastic zone in the foam is confined to a boundary layer just beneath the incident facesheet. The particle velocity in the foam under the projectile is specified by the projectile velocity V_1 , while the particle velocity in the foam away from the projectile is specified by the assumed velocity field of the incident facesheet given by Eq. 40. The plastic zone extends a distance $h_p = \frac{\delta}{\epsilon_D} \left(1 - \frac{r}{\xi}\right)$ as shown in Fig. 13. Ahead of the plastic zone is the elastic zone $h_e = \left(C_d t - \frac{\delta}{\epsilon_D}\right) \left(1 - \frac{r}{\xi}\right)$. The distribution of the particle velocities under the projectile, at $r = 0$, and at $r = \xi/2$ are indicated in Fig. 13.

The momentum of the plastically deformed portion of the core is

$$L_p = 2\pi\rho_D \int_0^{\xi} \int_0^{h_p} V_1 \left(1 - \frac{r}{\xi}\right) dz \quad r dr \quad (\text{B1})$$

where densification of the core has caused the density to become $\rho_D = \frac{\rho_c}{(1 - \epsilon_D)}$. The momentum in the plastic part of the core is

$$L_p = \frac{\pi\rho_c\delta}{6\epsilon_D(1 - \epsilon_D)} \xi^2 V_1 \quad (\text{B2})$$

The kinetic energy of the plastically deformed portion of the core is

$$\begin{aligned} T_p &= \pi\rho_D \int_0^{\xi} \int_0^{h_p} V_1^2 \left(1 - \frac{r}{\xi}\right)^2 dz \quad r dr \\ &= \frac{2\pi\rho_c\delta}{20\epsilon_D(1 - \epsilon_D)} \xi^2 V_1^2 \end{aligned} \quad (\text{B3})$$

The momentum of the elastic portion of the core is

$$\begin{aligned} L_e &= 2\pi\rho_c \int_0^{\xi} \int_0^{h_e} V_e \left(1 - \frac{z}{h_e}\right) dz \quad r dr \\ &= \frac{\pi\rho_c}{6} \left(C_d t - \frac{\delta}{\epsilon_D}\right) \xi^2 V_e \end{aligned} \quad (\text{B4})$$

where $V_e = \frac{q}{\rho C_d}$. The kinetic energy of the elastic portion of the core is

$$\begin{aligned} T_e &= \pi\rho_c \int_0^{\xi} \int_0^{h_e} V_e^2 \left(1 - \frac{z}{h_e}\right)^2 dz \quad r dr \\ &= \frac{\pi\rho_c}{18} \left(C_d t - \frac{\delta}{\epsilon_D}\right) \xi^2 V_e^2 \end{aligned} \quad (\text{B5})$$

Appendix C Elastic Strain Energy and Plastic Work in Core

The core absorbs both elastic strain energy and plastic work in Phase I. The plastic work dissipated in the core plastic region shown in Fig. 13 is

$$D_p = 2\pi \int_0^{\xi} q\delta \left(1 - \frac{r}{\xi}\right) r dr = \frac{\pi q\delta^2 \xi^2}{3} \quad (\text{C1})$$

The elastic strain energy in the core is

$$D_e = 2\pi \int_0^{\xi} \int_0^{h_e} \frac{1}{2} E_c \epsilon^2 dz r dr \quad (\text{C2})$$

where E_c is the core compressive modulus, $h_e = \left(C_d t - \frac{\delta}{\epsilon_D}\right) \left(1 - \frac{f}{\xi}\right)$ and the elastic strain vary through the thickness as $\epsilon = \frac{q}{E_c} \left(1 - \frac{z}{h_e}\right)$. After integration, the elastic strain energy in the core becomes

$$D_e = \frac{\pi q^2}{18E_c} \left(C_d t - \frac{\delta}{\epsilon_D}\right)^2 \xi^2 \quad (C3)$$

References

1. Hampson PR, Moayamed M (2007) A review of composite structures subjected to dynamic loading. *Int J Crashworthiness* 12: 411–428.
2. Cole RH (1984) Underwater explosions. Princeton University Press, New Jersey.
3. Smith PD and Hetherington JG (1994) Blast and ballistic loading of structures. Butterworth Heinemann, Oxford.
4. Menkes SB, Opat HJ (1974) Broken beams. *Exp Mech* 13: 480–486.
5. Teeling-Smith, RG, Nurick GN (1991) The deformation and tearing of thin circular plates subjected to impulsive loads. *Int J Impact Eng* 11: 77–91.
6. Franz T, Nurick GN, Perry MJ (2002) Experimental investigation into the response of chopped-strand mat glass fibre laminates to blast loading. *Int J Impact Eng* 27: 639–667.
7. Graff KF (1975) Wave motion in elastic solids. Oxford University Press, London.
8. Gibson LJ, Ashby MF (1999) Cellular solids structures and properties. Cambridge University Press, Cambridge.
9. Ashby, MF, Evans AG, Fleck NA, Gibson LJ, Hutchinson JW, Wadley HNG (2000) Metal foams: a design guide. Butterworth Heinemann, London.
10. Vinson JR (1999) The behavior of sandwich structures of isotropic and composite materials. Technomic Publishing Company, Lancaster.
11. Mines RAW, Alias A (2002) Numerical simulation of the progressive collapse of polymer composite sandwich beams under static loading. *Composites Part A* 33: 11–26.
12. Rizov V, Mladensky A (2007) Influence of the foam core material on the indentation behaviour of sandwich composite panels. *Cellular Polymers* 26: 117–131.
13. Hashin Z (1980) Failure criteria for unidirectional fiber composites. *J Appl Mech* 47: 329–334.
14. Sierakowski RL, Chaturvedi SK (1997) Dynamic loading and characterization of fiber-reinforced composites. John Wiley and Sons, New York.

Conference Papers

IMPLOSION OF COMPOSITE SHELLS UNDER BLAST

M. S. Hoo Fatt and S. G. Pothula
Department of Mechanical Engineering
The University of Akron
hoofatt@uakron.edu

SUMMARY

Analytical and finite element solutions are presented in this paper for the impulsive response of laminated composite cylindrical shells subjected to uniform and asymmetric pressure pulse loading (side-on explosion). Unstable buckling modes arise depending on shell geometry, material properties and load intensity.

Keywords: blast, composite shell, dynamic pulse buckling.

INTRODUCTION

Laminated composite cylindrical shells are finding widespread applications in aerospace, transportation and marine industries. In some of these applications, the strength and stability of the composite cylindrical shell may be compromised external pressure pulse loading, such as one caused by a nearby explosion. There are numerous solutions for the collapse and failure of isotropic, cylindrical shells subjected to external blast loading, but only a few papers can be found concerning that of the laminated cylindrical shells in recent years [1-3]. Many of these solutions describe the shell response under periodic loading (vibration) or when the pressure pulse is applied while the shell is deforming. This paper examines dynamic pulse buckling of a laminated composite shell subjected to impulsive pressure loads. It follows from the principles governing pulse buckling of metallic shells in Ref. [4].

PROBLEM FORMULATION

Consider a long and thin, laminated composite cylinder of radius a and thickness h , and subjected to impulsive pressure loading as shown in Figs. 1(a)-(c). The composite shell may be subjected to uniformly-distributed impulsive pressure loads

$$p(t) = p_o \left[1 - \frac{t}{\Delta T} \right] \quad (1)$$

or non-axisymmetric impulsive pressure loads, such as one caused by a side-on explosions

$$p(\theta, t) = \begin{cases} p_o \cos^2 \theta \left[1 - \frac{t}{\Delta T} \right], & |\theta| \leq \pi/2 \\ 0, & |\theta| > \pi/2 \end{cases} \quad (2)$$

where p_o is the peak pressure, ΔT is the pulse duration, and t is time.

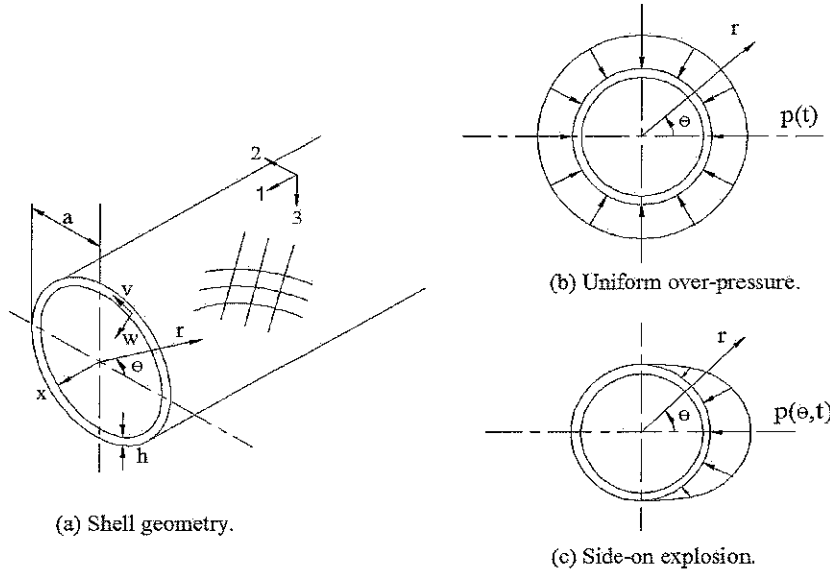


Figure 1 Composite cylinder under external pressure pulse loading: (a) Shell geometry, (b) Uniform over-pressure, and (c) Side-on explosion.

We limit our discussion to shells that are thin, $a/h > 10$, and long, $L/a > 20$, where L is the length of the shell. The later assumption combined with the fact that the pressure load do not vary along the shell longitudinal axis allows us to consider the cylinder as a ring deforming under plane strain conditions. Following the plane strain assumptions, $\epsilon_x = 0$, $\epsilon_{x\theta} = 0$, $\kappa_x = 0$, and $\kappa_{x\theta} = 0$. The hoop strain ϵ_θ in the shell is

$$\epsilon_\theta = \epsilon_{\theta m} + z\kappa_\theta \quad (3)$$

where $\epsilon_{\theta m}$ is the mid-surface strain, κ_θ is the change in curvature of the shell and z the radial coordinate in shell measured from the mid surface of the shell. As shown in

Fig. 1 (a), the cylindrical shell has radial displacement $w(\theta, t)$ and angular displacement $v(\theta, t)$. Points on the mid-surface of the cylindrical shell have polar coordinates a, θ before deformation and r, ϕ after deformation. The radial displacement is given by

$$w = a - r \quad (4)$$

and the angular displacement is given by

$$\frac{v}{a} = \phi - \theta \quad (5)$$

The mid-surface strain is

$$\varepsilon_{\theta n} = \frac{1}{a} \left[\left(\frac{\partial w}{\partial \theta} \right)^2 + (a-w)^2 \left(1 + \left(\frac{1}{a} \frac{\partial v}{\partial \theta} \right)^2 \right) \right]^{\frac{1}{2}} - 1 \quad (6)$$

The change in shell curvature is

$$\kappa_{\theta} = \frac{1}{a^2} \left(\frac{\partial^2 w}{\partial \theta^2} + w \right) \quad (7)$$

EQUATIONS OF MOTION

It is convenient to derive the equations of motion for the shell using the Lagrangian method. In this method, the Lagrangian is $L = T - \Pi$, where T is the kinetic energy and Π is the total potential energy of the shell. The kinetic energy of the shell is given by

$$T = \frac{1}{2} \rho h \int_0^{2\pi} \left[\left(\frac{\partial w}{\partial t} \right)^2 + \left(\frac{\partial v}{\partial t} \right)^2 \right] a d\theta \quad (8)$$

In general, the total potential energy of the shell is the sum of the strain energy U and potential of the applied loads. For an impulsively-loaded shell, the total potential energy of the shell consists only of strain energy because energy is transferred from the pressure pulse as an initial velocity or impulse. There are no loads acting on the shell during deformation and $\Pi = U$.

Strain Energy of a Laminated Composite Shell

Following plane strain assumptions, the elastic strain energy of a long, composite shell is

$$U = \frac{1}{2} \int (A_{22} \varepsilon_{\theta n}^2 + B_{12} \varepsilon_{\theta n} \kappa_{\theta} + B_{22} \varepsilon_{\theta n} \kappa_{\theta} + D_{22} \kappa_{\theta}^2) a d\theta \quad (9)$$

where $A_{ij} = \sum_{k=1}^n (\bar{Q}_{ij})_k (z_k - z_{k-1})$ is the membrane stiffness, $B_{ij} = \frac{1}{2} \sum_{k=1}^n (\bar{Q}_{ij})_k (z_k^2 - z_{k-1}^2)$

is the coupling stiffness, $D_{ij} = \frac{1}{3} \sum_{k=1}^n (\bar{Q}_{ij})_k (z_k^3 - z_{k-1}^3)$ is the bending stiffness, \bar{Q}_{ij} is the reduced stiffness matrix, and n is the total number of plies. We examine a special class of laminated composite shells that are orthotropic, mid-surface symmetric and quasi-isotropic. In shells that are orthotropic and mid-surface symmetric, $B_{ij} = 0$. For quasi-isotropic shells, $B_{12} = 0$ and $B_{22} = 0$. In these types of laminated composite shells, the elastic strain energy reduces to

$$U = \frac{1}{2} \int (A_{22} \varepsilon_{\theta n}^2 + D_{22} \kappa_{\theta}^2) a d\theta \quad (10)$$

Initial Velocity

The initial velocity imparted to the shell from the impulsive pressure is found from conservation of momentum

$$\rho h \frac{dw}{dt}(\theta, 0) = \int_0^{\Delta T} p(\theta, t) dt \quad (11)$$

Substituting the pressure pulse defined in Eqs. (1) and (2) into Eq. (11) gives

$$\frac{dw}{dt}(\theta, 0) = v_o \quad (12)$$

for the uniformly distributed load and

$$\frac{dw}{dt}(\theta, 0) = v_o \cos^2 \theta \quad (13)$$

for the side-on pressure pulse, where $v_o = \frac{P_o \Delta T}{2 \rho h}$ is the amplitude of the distributed velocity field.

Normalized Variables

Define a normalized radial deflection $\zeta = \frac{w}{a}$, tangential deflection, $\psi = \frac{v}{a}$, and

time $\tau = \frac{ct}{a}$, where $c = \sqrt{\frac{A_{22}}{\rho h}}$ is the wave speed in the circumferential direction.

The kinetic and potential energy in terms of the above normalized variables are

$$T = \frac{1}{2} A_{22} a \int_0^{2\pi} (\dot{\zeta}^2 + \dot{\psi}^2) d\theta \quad (14)$$

where $\dot{[\]} = \partial[\] / \partial \tau$ and

$$U = \frac{1}{2} A_{22} a \int_0^{2\pi} [(\psi' - \zeta)^2 + (\psi' - \zeta)(\zeta'' - 2\zeta\psi') + \alpha^2(\zeta'' + \zeta)^2] d\theta \quad (15)$$

where $\alpha^2 = D_{22} / (a^2 A_{22})$ and $[\]' = \partial[\] / \partial \theta$.

The normalized initial velocity are

$$\dot{\zeta}(\theta, 0) = \frac{v_o}{c} \quad (16)$$

for the uniformly loaded shell and

$$\zeta(\theta,0) = \frac{v_o}{c} \text{Cos}^2 \theta \quad (17)$$

for the shell with side-on pressure loading.

FOURIER SERIES SOLUTION

Assume a Fourier series representation of the normalized radial and tangential displacement

$$\zeta = a_0 + \sum_{n=1}^{\infty} [a_n \text{Cos}(n\theta) + b_n \text{Sin}(n\theta)] \quad (18)$$

and

$$\psi = \sum_{n=1}^{\infty} [c_n \text{Cos}(n\theta) + d_n \text{Sin}(n\theta)] \quad (19)$$

Following the inextensionality condition [5,6], $\psi' = \zeta - a_0$ and one gets that $c_n = -b_n/n$ and $d_n = a_n/n$. Substituting Eqs. (18) and (19) into Eqs. (14) and (15) and using inextensionality condition give

$$T = \pi A_{22} a \left[\dot{a}_0^2 + \frac{1}{2} \sum_{n=1}^{\infty} \left(\frac{n^2 + 1}{n^2} \right) (\dot{a}_n^2 + \dot{b}_n^2) \right] \quad (20)$$

for the kinetic energy

$$U = \pi A_{22} a \left\{ a_0^2 (1 + \alpha^2) + \frac{1}{2} \sum_{n=1}^{\infty} \left[a_0 (2 - n^2) + \alpha^2 (n^2 - 1)^2 \right] (a_n^2 + b_n^2) \right\} \quad (21)$$

for the strain energy. Since we will limit our analysis to small deflections, terms of order higher than a_n^2 and b_n^2 have been neglected. Lagrange's equations of motion for the shell is given by

$$\frac{d}{d\tau} \left(\frac{\partial T}{\partial \dot{a}_i} \right) + \frac{\partial U}{\partial a_i} = 0 \quad (22)$$

Substituting Eqs. (20) and (21) into Eq. (22) gives the solution for the breathing mode ($n = 0$)

$$\ddot{a}_0 + a_0 (1 + \alpha^2) - \frac{1}{4} \sum_{n=1}^{\infty} (n^2 - 2) (a_n^2 + b_n^2) = 0 \quad (23)$$

and for modes of $n \geq 1$

$$\ddot{a}_n + \frac{n^2}{n^2 + 1} \left[(n^2 - 1)^2 \alpha^2 - (n^2 - 2) a_0 \right] a_n = 0, \quad (24)$$

and

$$\ddot{b}_n + \frac{n^2}{n^2 + 1} \left[(n^2 - 1)^2 \alpha^2 - (n^2 - 2) a_0 \right] b_n = 0, \quad (25)$$

The breathing mode is in general coupled with the bending modes. The above equations of motion are solved from initial conditions: $\zeta(\theta, 0) = 0$ and

$$\dot{\zeta}(\theta, 0) = \dot{a}_{00} + \sum_{n=1}^{\infty} [\dot{a}_{n0} \cos(n\theta) + \dot{b}_{n0} \sin(n\theta)] \quad (26)$$

where $\dot{a}_0(0) = \dot{a}_{00}$, $\dot{a}_n(0) = \dot{a}_{n0}$, $\dot{b}_n(0) = \dot{b}_{n0}$, $a_n(0) = 0$, and $b_n(0) = 0$. When deflections are small, a_n^2 and b_n^2 are negligible compared to a_n and b_n . Equations (23)-(25) reduce to

$$\ddot{a}_0 + a_0(1 + \alpha^2) = 0 \quad (27)$$

$$\ddot{a}_n + (\Omega_n - \mu_n \sin \tau) a_n = 0, \quad n \geq 1 \quad (28)$$

$$\ddot{b}_n + (\Omega_n - \mu_n \sin \tau) b_n = 0, \quad n \geq 1 \quad (29)$$

where $\Omega_n = \frac{\alpha^2 n^2 (n^2 - 1)^2}{(n^2 + 1)}$ and $\mu_n = \frac{n^2 (n^2 - 2)}{(n^2 + 1) \sqrt{1 + \alpha^2}} \dot{a}_{00}$. The differential equations

described in Eqs. (28) and (29) are Mathieu's equation [7]. They yield unstable solutions for values of μ_n and Ω_n that are not in the cross-hatched zones shown in

Fig. 2 (a). We examine specific solutions for the uniform and side-on pressure loads.

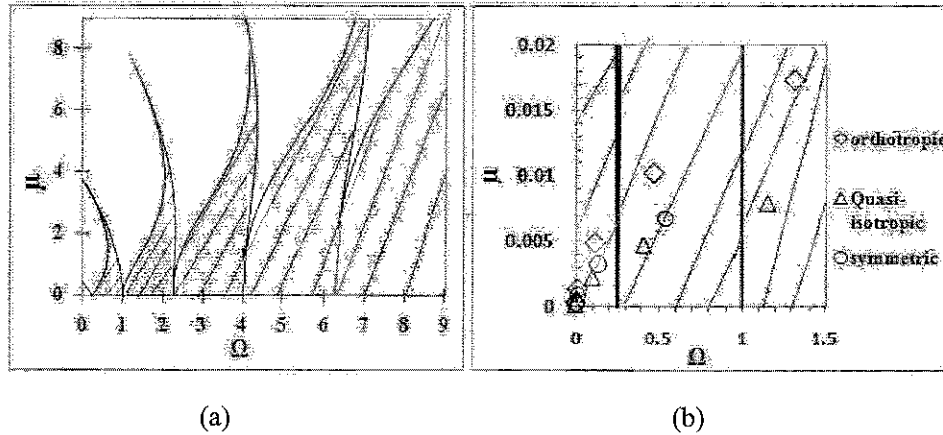


Figure 2 Mathieu's stability diagrams: (a) expanded and (b) reduced scales.

Uniform Over-Pressure

Under uniform pressure load, there can be no rigid body motion of the shell. Hence, the terms involving $n = 1$ do not exist and the solution for the shell is given in terms of its Fourier series

$$\zeta = a_0 + \sum_{n=2}^{\infty} [a_n \cos(n\theta) + b_n \sin(n\theta)] \quad (30)$$

The initial velocity condition becomes

$$\dot{\zeta}(\theta, 0) = \dot{a}_{00} + \sum_{n=2}^{\infty} [\dot{a}_{n0} \cos(n\theta) + \dot{b}_{n0} \sin(n\theta)] \quad (31)$$

For the uniform velocity, $\dot{a}_{00} = \frac{v_o}{c}$, $\dot{a}_{n0} = 0$ and $\dot{b}_{n0} = 0$. Thus, the solution for

Eq. (27) is

$$a_0(\tau) = \frac{v_o}{c} \sin \tau \quad (32)$$

This is simply the breathing mode. The stability of laminated composite cylindrical shells follows exactly the same trends as for an isotropic, elastic shell under uniformly distributed impulsive pressure as discussed in Refs. [4] and [6], and will not be repeated here.

Side-On Explosion

For the side-on pressure pulse described by Eq. (2), the shell deforms and moves with rigid-body motion ($n = 1$ term is not neglected) and only the Cosine terms of the Fourier series are retained because of load symmetry, i.e., $b_n = 0$. The normalized solution becomes

$$\zeta = a_0 + \sum_{n=1}^{\infty} a_n \cos(n\theta) \quad (33)$$

The centroid of the shell will have a non-zero velocity in a fixed plane, and we will refer to motion in a plane travelling with it. The initial velocity of the shell is then written as

$$\dot{\zeta}(\theta, 0) = \dot{a}_{00} + \frac{1}{2} \dot{a}_{10} \cos(\theta) + \sum_{n=2}^{\infty} \dot{a}_{n0} \cos(n\theta) \quad (34)$$

where $\dot{a}_{00} = \frac{1}{4} \frac{v_o}{c}$ and

$$\dot{a}_{n0} = \frac{1}{2\pi} \left\{ \frac{2}{n} \sin\left(\frac{n\pi}{2}\right) + \frac{1}{(n+2)} \sin\left(\frac{\pi(n+2)}{2}\right) + \frac{1}{(n-2)} \sin\left(\frac{\pi(n-2)}{2}\right) \right\} \frac{v_o}{c}, \quad n \geq 1$$

Once again the stability of the solution depends on the values of μ_n and Ω_n . If these lie in the stable regions of Mathieu's diagram, the shell undergoes deformation with each mode shape. We examine stable shell deformations and the stability of the composite shell when it is subjected to a side-on explosion in the next sections.

SHELL DEFORMATIONS

Three laminated shell geometries are chosen: an orthotropic shell made of woven roving E-Glass/Vinyl Ester, and a mid-surface symmetric, laminated shell ($[60^0/-45^0]_s$) and a quasi-isotropic, laminated shell ($60^0/0^0/-60^0$) made of unidirectional E-Glass/Epoxy plies. Each of the cylinders has a total shell thickness of $h = 4$ mm and a shell radius of $a = 80$ mm. The impulse is chosen so that μ_n and Ω_n occur in the stable region of Mathieu's diagram. These points are plotted on a reduced scale of the Mathieu's diagram in Fig. 2 (b). Figures 3 and 4 (a) and (b) show the transient deflections of the shells as well as finite element analysis predictions using ABAQUS Explicit. There is very good agreement between analytical and FEA results.

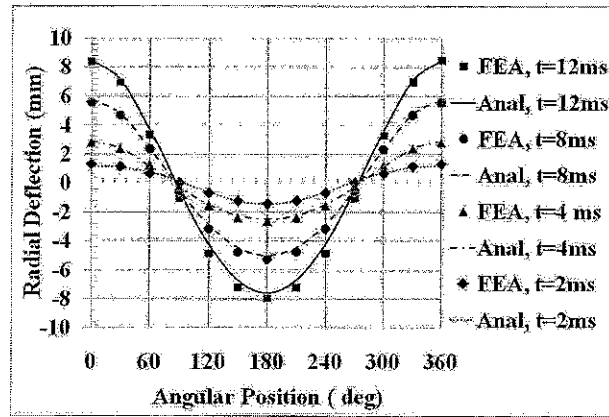


Figure 3 Transient deflections of the orthotropic, woven roving E-Glass/Vinyl Ester shell; $p_o = 10$ MPa, $\Delta T = 3.5 \mu s$.

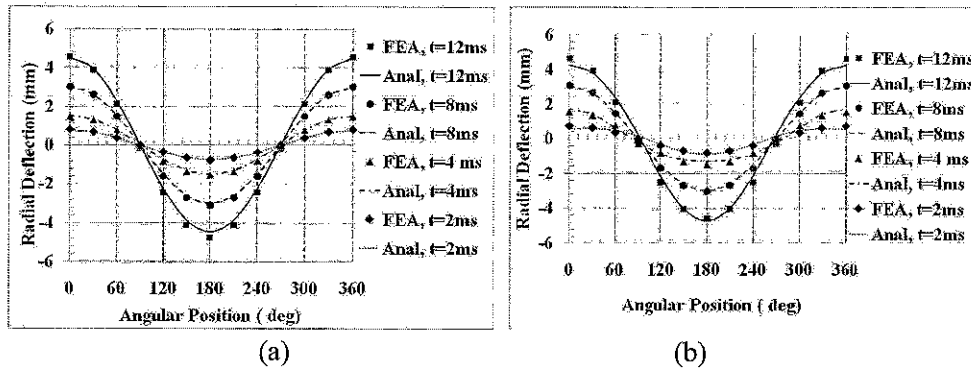


Figure 4 Transient deflections of the E-Glass/Epoxy shells; $p_o = 10$ MPa, $\Delta T = 2.9 \mu s$: (a) mid-surface symmetric ($[60^0/-45^0]_s$) and (b) quasi-isotropic ($60^0/0^0/-60^0$).

SHELL INSTABILITY

Instability may occur at higher impulse loads or initial shell velocities. Figure 5(a) shows the values of μ_n and Ω_n plotted on Mathieu's stability graph for various normalized velocity v_o/c in the woven E-Glass/Vinyl Ester, orthotropic shell. Points on the Mathieu's stability diagram shift upwards as the normalized velocity v_o/c increases. The fifth and seventh mode both just becomes unstable when $v_o/c = 0.0448$ and the critical impulse for buckling instability for this shell is 882 Pa-s ($p_o = 504 \text{ MPa}, \Delta T = 3.5 \mu\text{s}$). The Mathieu's stability diagram is also used to determine the stability of the mid-surface symmetric and quasi-isotropic E-Glass/Epoxy shells in Fig. 5(b). The buckling pressures and the unstable modes are listed in Table 1.

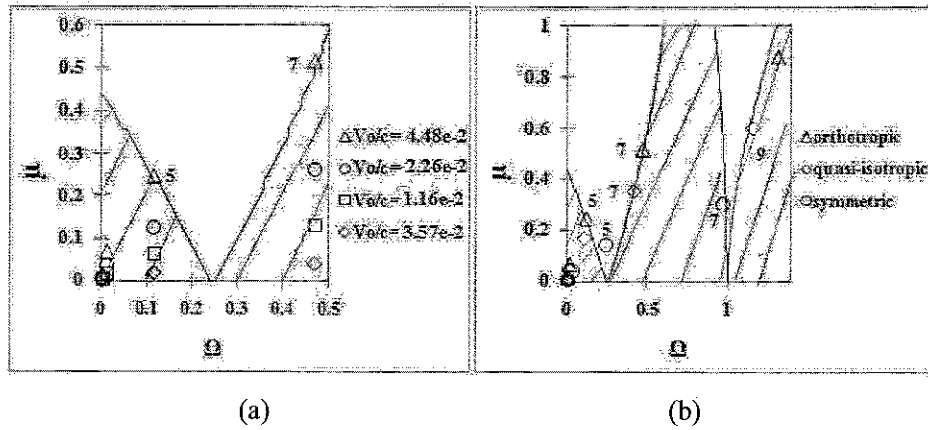


Figure 5 Mathieu's stability diagrams: (a) effect of increasing v_o/c in orthotropic, E-Glass/Vinyl Ester shell and (b) critical buckling modes for three laminates.

Table 1 Critical buckling pressure for composite shells.

	$c(m/s)$	α^2	$(p_o)_{crit}$ (MPa)	$\Delta t(\mu s)$	Unstable Modes
Orthotropic E-Glass/Vinyl Ester	3,525	$2.08e^{-4}$	504	3.5	5,7
Mid-surface symmetric E-Glass/Epoxy ($[60^0/-45^0]_s$)	3,723	$2.39e^{-4}$	860	2.9	5
Quasi-isotropic E-Glass/Epoxy ($60^0/0^0/-60^0$)	4,321	$1.82e^{-4}$	752	2.9	7,9

The critical buckling pressures depend on the circumferential wave speed $c = \sqrt{\frac{A_{22}}{\rho h}}$ and bending to extension ratio $\alpha^2 = D_{22} / (a^2 A_{22})$, which are listed for each shell in Table 1. In general, the critical buckling pressure increases with increasing values of α^2 . For the orthotropic, woven roving E-Glass/Vinyl Ester shell, $\alpha^2 = h^2 / (12a^2)$ and a shell made of this material becomes thicker with increasing values of α^2 . For the laminated E-Glass/Epoxy shell, α^2 is controlled not only by shell thickness but also by the layup.

CONCLUDING REMARKS

Analytical solutions for the transient response of orthotropic, mid-surface symmetric and quasi-isotropic, laminated composite shell subjected to subjected to uniform and asymmetric pressure pulse loading (side-on explosion) have been presented. The equations of motion governing shell deformations are of a type belonging to Mathieu's differential equations, which sometimes yield unstable results. Unstable buckling modes arise depending on shell geometry, material properties and load intensity. The stable transient deformations of an orthotropic E-Glass/Vinyl Ester shell and a mid-surface symmetric and a quasi-isotropic E-Glass/Epoxy shell with a side-on explosion compared very well with finite element predictions using ABAQUS Explicit.

ACKNOWLEDGEMENTS

The authors would like to acknowledge financial support from Dr. Yapa Rajapakse at the Office of Naval Research under Grant N00014-07-1-0423.

References

1. Turkmen HS. Structural response of laminated composite shells subjected to blast loading: comparison of experimental and theoretical methods. *Journal of Sound and Vibration* 2002; 249(4): 663-678.
2. Prusty BG, Satsangi SK. Finite element transient dynamic analysis of laminated stiffened shells. *Journal of Sound and Vibration* 2001; 248(2): 215-233.
3. Lee Y-S, Lee K-D. On the dynamic response of laminated circular cylindrical shells under impulse loads. *Computers & Structures* 1997; 63(1): 149-157.
4. Lindberg HE, Florence AL, *Dynamic Pulse Buckling*, Martinus Nijhoff Publishers, Dordrecht, 1987.
5. Lord Rayleigh. *Theory of Sound*, Dover Publications, New York, NY, 1945.
6. Goodier JN, McIvor IK. The elastic cylindrical shell under nearly uniform radial impulse, *Journal of Applied Mechanics* 1964; 31: 259-266.
7. McLachlan NW. *Theory and Application of Mathieu Functions*, Oxford University Press, Oxford, 1941.

High velocity impact of a composite sandwich panel

M. S. Hoo Fatt & D. Sirivolu
*Department of Mechanical Engineering,
The University of Akron, Ohio, USA*

Abstract

Analytical solutions for the deformation response of a composite sandwich panel subjected to high velocity impact by a rigid blunt, cylindrical projectile are presented. The solution is derived from a two degrees-of-freedom model for the sandwich panel involving local indentation, core crushing and global bending/shear deformations. An example is given for a composite sandwich panel consisting of orthotropic E-glass vinyl ester facesheets and PVC H100 foam core and subjected to the high velocity impact of a blunt cylindrical projectile. The analytical solution for the local indentation and global deflection under the projectile was found to be within 15% of FEA results.

Keywords: high velocity impact, composite sandwich panels, analytical model.

1 Introduction

Light weight composite sandwich panels are becoming more widely used in military transport vehicles because they offer greater load bearing capabilities per unit weight and easier maintenance. In some instances, these composite sandwich panels may be subjected to high velocity impact from flying debris from a nearby explosion. While there has been much research on the low velocity impact of composite sandwich panels, very few papers deal with the issue of the high velocity impact of composite sandwich panels [1,2]. The objective of this paper is to develop an analytical model for the deformation response of a composite sandwich panel subjected to high velocity impact by a rigid blunt, cylindrical projectile. Only the mechanical constitutive equations for the facesheet and core are considered in this paper because the thermo-mechanical equations of state for them are presently unknown.

2 Problem formulation

Consider the composite sandwich panel, as shown in Fig. 1. The facesheets are orthotropic plates of thickness h , and the core is crushable polymeric foam of thickness H . The blunt cylindrical projectile has a radius r_p , a mass M_0 and a velocity V_0 . The projectile is assumed rigid compared to the sandwich panel. During impact, the panel experiences local indentation as well as global bending/shear deformation.

Upon impact, compressive stress waves are generated under the projectile. These stress waves must travel through the incident facesheet, core and distal facesheet before global transverse shear and bending waves can be transmitted laterally in the sandwich panel. During this phase, the problem becomes one of local indentation, i.e., the incident facesheet deflects under the projectile and the core crushes. Once the through-thickness compressive stress waves have reached the distal side of the sandwich panel, a global panel bending/shear deformation will initiate. Analytical solutions for the local and local/global transient response of the panel will be given in the following section.

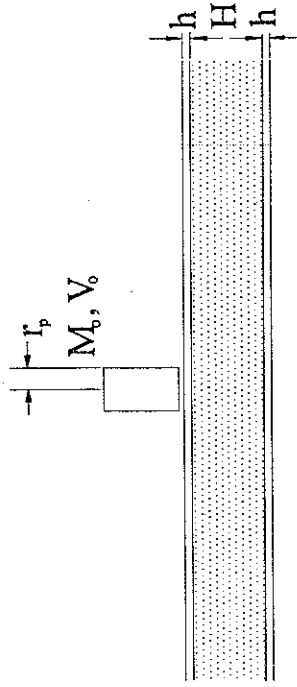


Figure 1: Projectile impact of the composite sandwich panel.

3 Phase I: local indentation

The sandwich undergoes only local indentation during Phase I. As depicted in Fig. 2, the problem is reduced to one involving projectile impact of a facesheet

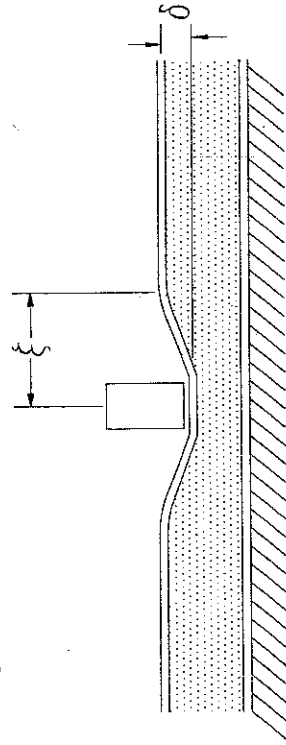


Figure 2: Local indentation and extent of the damage.

resting on a foam foundation. Local indentation under the projectile is denoted δ and the lateral extent of deformation is denoted ξ . The duration of Phase I is determined from the wave travel time through the thickness of the panel.

3.1 Through-thickness wave propagation

Compressive stress waves must pass through the full thickness of the sandwich, i.e., two facesheets and core, before any response can be characterized as global bending/shear deformation. The through-thickness wave travel time is given by

$$t_1 = \frac{2h}{C_f} + \frac{H}{C_c} \quad (1)$$

where C_f and C_c are the wave speeds in the facesheet and core, respectively. The wave speed in an orthotropic plate in plane strain is given by

$$C_f = \sqrt{\frac{E_{33}(1-\nu_{12})}{[1-\nu_{12}-\nu_{32}(\nu_{13}+\nu_{23})]\rho_f}} \quad (2)$$

where E_{ij} , ν_{ij} and ρ_f are the elastic modulus, Poisson's ratio and density of the orthotropic facesheet, respectively. The wave speed in the foam is determined by the amount of core crushing.

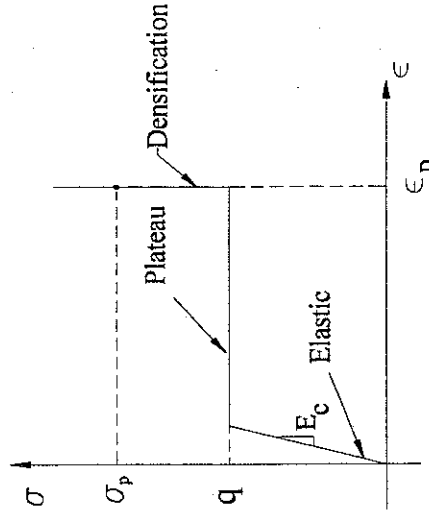


Figure 3: Compressive stress-strain curve of the polymeric foam.

A polymeric foam core is elastic-plastic with a compressive stress-strain characteristic as shown in Fig. 3 [3]. The foam is linear elastic with a compressive modulus of E_c until yielding at a flow stress, q . Rapid compaction of cells causes the density to change during the plateau region until full densification has occurred at ϵ_D . The stress rises to a maximum plastic stress, σ_p , at the densification strain. Both elastic and plastic waves could therefore be generated in the foam. The elastic wave speed in the foam is given

by $C_e = \sqrt{E_c/\rho_c}$ and the plastic wave speed is given by $C_p = \sqrt{\frac{\sigma_p - q}{\rho_c \epsilon_D}}$ [4],

where σ_p is the stress in the densification region. The elastic wave speed is generally faster than the plastic wave speed so that $C_c = C_e$ for the through-thickness wave travel time in Eq. (1).

3.2 Local indentation

Local indentation is found by considering the projectile presses onto the incident facesheet resting on a rigid-plastic foundation. A single degree-of-freedom equation of motion governing the dynamics of the projectile and effective facesheet mass can be written considering the system Lagrangian. The Lagrangian L for a system is defined as $L = T - \Pi$, where T and Π are the kinetic energy and potential energy of the system, respectively.

3.2.1 Kinetic energy

Assume the mass of the core is small compared to the mass of the facesheet. Then the kinetic energy of the system is given by

$$T = \frac{1}{2} M_o V_1^2 + \frac{1}{2} m_f V_1^2 \quad (3)$$

where V_1 is the velocity under the projectile at any time and m_f is the effective mass of the facesheet. The effective mass of the facesheet is found by assuming that the projectile induces the following linear velocity field in the facesheet:

$$\dot{w} = \begin{cases} V_1, & 0 \leq r \leq r_p \\ V_1 \left[1 - \frac{(r - r_p)}{(\xi - r_p)} \right], & r_p \leq r \leq \xi \end{cases} \quad (4)$$

Note that ξ in the above equation varies with time, i.e., the velocity field has a moving boundary and the effective facesheet mass grows as the velocity field spreads away from the impact site. Integrating the distributed kinetic energy of the facesheet and setting it equal to the equivalent kinetic energy produced by an effective facesheet mass, m_f , gives:

$$m_f = \pi r_p^2 \rho_f h + \frac{\pi \rho_f h}{6} (\xi + 3r_p)(\xi - r_p) \quad (5)$$

3.2.2 Potential energy

The total potential energy of the system, Π , consists of the elastic strain energy of the facesheet, U_1 , and the work dissipated in crushing the core, D :

$$\Pi = U_1 + D \quad (6)$$

Assuming in-plane deformations are negligibly small compared to transverse deflections, w , the elastic strain energy due to bending in an orthotropic facesheet is

$$U_1 = \frac{1}{2} \int_S \left[D_{11} \left(\frac{\partial^2 w}{\partial x^2} \right)^2 + 2D_{12} \frac{\partial^2 w}{\partial x^2} \frac{\partial^2 w}{\partial y^2} + D_{22} \left(\frac{\partial^2 w}{\partial y^2} \right)^2 + 4D_{66} \left(\frac{\partial^2 w}{\partial x \partial y} \right)^2 \right] dS \quad (7)$$

where D_{ij} is the bending stiffness of the facesheet and S is the area associated with indentation.

The work dissipated in foam core crushing is given by

$$D = \int_S q w dS \quad (8)$$

where q is the constant, compressive flow stress in the foam.

Finite element analysis has shown that the transverse deflection of the facesheet may be assumed as follows:

$$\delta, \quad w(r) = \begin{cases} \delta, & 0 \leq r \leq r_p \\ \delta \left[1 - \frac{(r - r_p)}{(\xi - r_p)} \right]^2, & r_p \leq r \leq \xi \end{cases} \quad (9)$$

where $r^2 = x^2 + y^2$. Transforming derivatives from rectangular to polar coordinates, allows one to calculate the strain energy due to facesheet bending as

$$U_1 = \frac{C_1 \pi \delta^2}{4} \frac{(\xi + r_p)}{(\xi - r_p)^3} - \frac{C_2 \pi \delta^2}{2} \frac{(\xi + r_p)}{(\xi - r_p)^2} + \frac{C_1 \pi \delta^2}{4(\xi - r_p)^4} \left[-3\xi^2 + 4\xi r_p - r_p^2 - 2\xi^2 \ln \left(\frac{\xi}{r_p} \right) \right] \quad (10)$$

where $C_1 = 3(D_{11} + D_{22}) + 2D_{12} + 4D_{66}$ and $C_2 = D_{11} + D_{22} + 6D_{12} - 4D_{66}$.

The work dissipated in foam core crushing is also given by

$$D = 2\pi q \delta \left[\frac{(\xi^2 - r_p^2)}{2} + \frac{(\xi^4 - r_p^4)}{4\xi^2} + \frac{2(\xi^3 - r_p^3)}{3\xi} \right] \quad (11)$$

3.2.3 Equation of motion

Lagrange's equation of motion for the projectile and effective facesheet mass is

$$\frac{\partial}{\partial t} \left(\frac{\partial L}{\partial V_1} \right) - \frac{\partial L}{\partial \delta} = (M_o + m_f) \frac{dV_1}{dt} + V_1 \frac{dm_f}{dt} + \frac{\partial \Pi}{\partial \delta} = 0 \quad (12)$$

where $V_1 = \frac{d\delta}{dt}$. Substituting m_f and Π into Eq. (12) gives

$$\begin{aligned} (M_o + m_f) \frac{d^2 \delta}{dt^2} + \frac{\pi \rho_f h}{3r} \xi (\xi + r_p) \frac{d\delta}{dt} + \frac{C_1 \pi \delta}{2} \frac{(\xi + r_p)}{(\xi - r_p)^3} - \frac{C_2 \pi \delta}{(\xi - r_p)^2} \\ + \frac{C_1 \pi \delta}{2(\xi - r_p)^4} \left[-3\xi^2 + 4\xi r_p - r_p^2 - 2\xi^2 \ln \left(\frac{\xi}{r_p} \right) \right] + 2\pi q \left[\frac{(\xi^2 - r_p^2)}{2} + \frac{(\xi^4 - r_p^4)}{4\xi^2} + \frac{2(\xi^3 - r_p^3)}{3\xi} \right] = 0 \end{aligned} \quad (13)$$

where it is assumed that $\dot{\xi} = \xi/t$. Conservation of linear momentum relates the projectile and effective facesheet mass velocity, V_1 , with ξ :

$$M_o V_o = M_o V_1 + \left[\pi r_p^2 \rho_f h + \frac{\pi \rho_f h}{3} (\xi + 2r_p)(\xi - r_p) \right] V_1 \quad (14)$$

Equation (13) becomes a nonlinear second order differential equation in δ when Eq. (14) is used to eliminate ξ . The initial conditions for Eq. (13)

$$\text{are } \delta(0) = 0 \text{ and } V_1(0) = \dot{\delta}(0) = \frac{M_o V_o}{(M_o + \pi r_p^2 \rho_f h)}$$

4 Phase I: global bending/shear

At the end of Phase I, transverse shear waves propagate from the point of impact across the sandwich panel. The global panel deflection is denoted Δ and the lateral extent of global deformation is denoted Ξ as shown in Fig. 4.

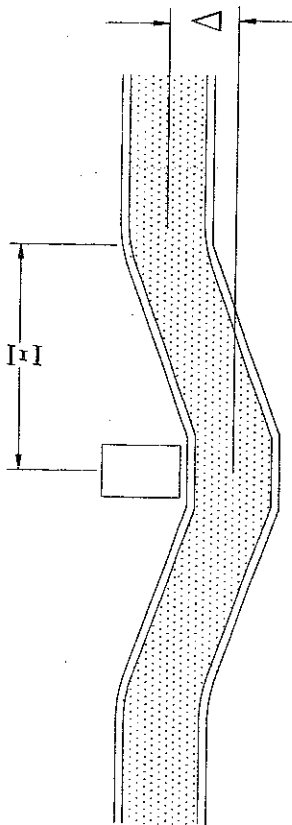


Figure 4: Global deformation and extent of the damage.

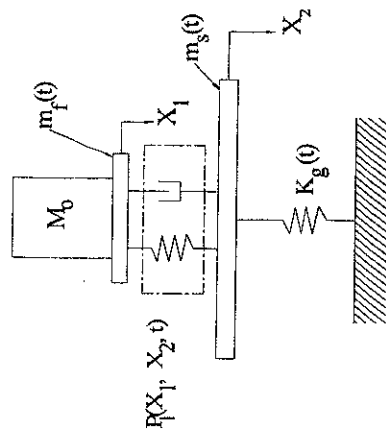


Figure 5: Coupled local and global deformation model.

The two degree-of-freedom model shown in Fig. 5 is considered for combined local indentation and global panel bending/shear deformations. Degrees of freedom, X_1 and X_2 , are related to the position of the projectile and incident facesheet, and the deflection of the sandwich panel under the projectile if there were no local indentation or core crushing, respectively. Therefore, $\delta = X_1 - X_2$ and $\Delta = X_2$. Applying Lagrange's equations of motion results in two equations of motion:

$$\frac{\partial}{\partial t} \left(\frac{\partial L}{\partial V_1} \right) - \frac{\partial L}{\partial X_1} = 0 \quad (15)$$

$$\frac{\partial}{\partial t} \left(\frac{\partial L}{\partial V_2} \right) - \frac{\partial L}{\partial X_2} = 0 \quad (16)$$

$$\text{where } V_2 = \frac{dX_2}{dt}$$

4.1 Kinetic energy

Assume the mass of the core is small compared to the mass of the facesheet and neglect rotary inertia of the sandwich panel. Then the kinetic energy of the system is given by

$$T = \frac{1}{2} M_o V_1^2 + \frac{1}{2} m_f V_1^2 + \frac{1}{2} m_s V_2^2 \quad (17)$$

where m_s is the effective mass of the sandwich and V_2 is the velocity of the sandwich under the projectile. The effective mass of the sandwich is calculated by again assuming a linear velocity field for the sandwich:

$$\dot{w} = V_2 \left(1 - \frac{r}{\Xi} \right) \quad (18)$$

From the above velocity field, one finds that the effective sandwich mass is

$$m_s = \frac{\pi}{6} (\rho_f h + \rho_c H) \Xi^2 \quad (19)$$

Note that only one facesheet mass is in Eq. (19) because an effective mass of the incident facesheet has already been considered.

4.2 Global bending/shear energy

The elastic strain energy due to bending and shear of a symmetric sandwich panel with orthotropic facesheet is

$$U_g = \int \int \left\{ \frac{D_{11}^i}{2} \left(\frac{\partial \bar{\alpha}}{\partial x} \right)^2 + D_{12}^i \left(\frac{\partial \bar{\beta}}{\partial y} \right) \left(\frac{\partial \bar{\beta}}{\partial x} \right) + \frac{D_{22}^i}{2} \left(\frac{\partial \bar{\beta}}{\partial y} \right)^2 + A_{55}^i \left[\frac{\bar{\alpha}^2}{2} + \bar{\alpha} \frac{\partial w}{\partial x} + \frac{1}{2} \left(\frac{\partial w}{\partial x} \right)^2 \right] + A_{44}^i \left[\frac{\bar{\beta}^2}{2} + \bar{\beta} \frac{\partial w}{\partial y} + \frac{1}{2} \left(\frac{\partial w}{\partial y} \right)^2 \right] + D_{66}^i \left[\frac{1}{2} \left(\frac{\partial \bar{\alpha}}{\partial y} \right)^2 + D_{66}^i \left[\frac{\partial \bar{\alpha}}{\partial y} \frac{\partial w}{\partial y} + \frac{1}{2} \left(\frac{\partial w}{\partial y} \right)^2 \right] \right] \right\} dS \quad (20)$$

where w is again used to express transverse deflections, $\bar{\alpha}$ and $\bar{\beta}$ are shear angles associated with the x- and y-directions, respectively, D_{ij}^s is the sandwich bending stiffness matrix, and A_{44} and A_{55} are the transverse shear stiffnesses. The superscript "s" is used to denote the sandwich.

Assume the following global transverse deflection and shear rotations:

$$w(r) = \begin{cases} \Delta \left(1 - \left(\frac{r}{\Xi} \right)^2 \right), & 0 \leq r \leq \Xi \\ 0, & r \geq \Xi \end{cases} \quad (21)$$

and

$$\bar{\alpha}(r) = \bar{\beta}(r) = \begin{cases} \frac{4\alpha_o r}{\Xi^2} (\Xi - r), & 0 \leq r \leq \Xi \\ 0, & r \geq \Xi \end{cases} \quad (22)$$

where Δ is the global deflection under the projectile and α_o is the shear rotation at the center of the panel.

Substituting derivatives of the expressions in Eqs. (21) and (22) into Eq. (20) gives the following expression for the strain energy:

$$U_g = \frac{4}{3} \left[\pi(D_{11}^s + D_{22}^s) + 4D_{12}^s + 2(\pi + 2)D_{66}^s \right] \rho_o^2 + \frac{1}{105} (A_{44}^s + A_{55}^s) \left(-176\Xi\alpha_o\Delta + 28\pi\Xi^2\alpha_o^2 + 35\pi\Xi\Delta^2 \right) \quad (23)$$

4.3 Equations of motion

Satisfying Lagrange's equations stated in Eqs. (15) and (16) one gets

$$\begin{aligned} (M_o + m_f) \frac{d^2 X_1}{dt^2} + \frac{\pi \rho_f h}{3t} \xi (\xi + r_p) \frac{dX_1}{dt} + C_1 \pi (X_1 - X_2) \left(\frac{\xi + r_p}{\xi - r_p} \right) - C_2 \pi (X_1 - X_2) \left(\frac{\xi - r_p}{\xi + r_p} \right) \\ + \frac{C_1 \pi (X_1 - X_2)}{2(\xi - r_p)^2} \left[-3\xi^2 + 4\xi r_p - r_p^2 - 2\xi^2 \ln \left(\frac{\xi}{r_p} \right) \right] + 2m_f \left[\frac{(\xi^2 - r_p^2)}{2} + \frac{(\xi^4 - r_p^4)}{4\xi^2} - \frac{2(\xi^3 - r_p^3)}{3\xi} \right] = 0 \end{aligned} \quad (24)$$

and

$$\begin{aligned} m_s \frac{d^2 X_2}{dt^2} + \frac{\pi(\rho_f h + \rho_c H)}{3t} \Xi^2 \frac{dX_2}{dt} - C_1 \pi (X_1 - X_2) \left(\frac{\xi + r_p}{\xi - r_p} \right) + C_2 \pi (X_1 - X_2) \left(\frac{\xi - r_p}{\xi + r_p} \right) \\ - \frac{C_1 \pi (X_1 - X_2)}{2(\xi - r_p)^2} \left[-3\xi^2 + 4\xi r_p - r_p^2 - 2\xi^2 \ln \left(\frac{\xi}{r_p} \right) \right] \\ - 2m_f \left[\frac{(\xi^2 - r_p^2)}{2} + \frac{(\xi^4 - r_p^4)}{4\xi^2} - \frac{2(\xi^3 - r_p^3)}{3\xi} \right] + \frac{1}{105} (A_{44}^s + A_{55}^s) \left(-176\Xi\alpha_o + 70\pi\Xi X_2 \right) = 0 \end{aligned} \quad (25)$$

where it is assumed that $\dot{\Xi} = \Xi / t$. Requiring that $\frac{\partial \Pi}{\partial \alpha_o} = 0$ gives

$$\alpha_o = \frac{22(A_{44}^s + A_{55}^s)\Xi X_2}{35[\pi(D_{11}^s + D_{22}^s) + 4D_{12}^s + 2(\pi + 2)D_{66}^s] + 7\pi(A_{44}^s + A_{55}^s)\Xi^2} \quad (26)$$

Conservation of linear momentum also gives

$$M_o V_o = M_o V_1 + \left[\pi^2 \rho_f h + \frac{\pi \rho_f h}{3} (\xi + 2r_p) (\xi - r_p) \right] V_1 + \frac{\pi(\rho_f h + \rho_c H)}{3} \Xi^2 V_2 \quad (27)$$

Finally, the kinetic energy of the sandwich with both facesheets is compared to the sum of the kinetic energy of the facesheet and the sandwich with only the distal facesheet:

$$\frac{1}{2} \left[\frac{\pi(2\rho_f h + \rho_c H)}{6} \Xi^2 V_1^2 = \frac{1}{2} \left[\frac{\pi(\rho_f h + \rho_c H)}{6} \Xi^2 V_2^2 \right. \right. \\ \left. \left. + \frac{1}{2} \left[\pi^2 \rho_f h + \frac{\pi \rho_f h}{6} (\xi + 3r_p) (\xi - r_p) \right] V_1^2 \right] \quad (28)$$

Equations (24) - (28) are solved with the following initial conditions: $X_1(t_f) = X_{10}$, $\dot{X}_1(t_f) = \dot{X}_{10}$, $X_2(t_f) = 0$, and $\dot{X}_2(t_f) = 0$, where t_f is defined in Eq. (1) and X_{10} and \dot{X}_{10} are taken at the end of Phase I.

5 An example

As an example, consider a fully clamped sandwich panel made of E-glass vinyl ester facesheets and PVC H100 foam core, with a panel radius of 250 mm, facesheet thickness of 2 mm, and core thickness of 25 mm. Material properties for the E-glass vinyl ester and the PVC H100 foam are given in Table 1.

Let the sandwich panel undergo impact by a rigid cylindrical rod of radius 2.5 mm, mass 0.5 kg, and velocity 40 m/s. This impact problem was modeled using ABAQUS Explicit using continuum C3D8R elements for both the facesheets and the foam. The PVC H100 foam was modeled as crushable foam with volumetric hardening. Additional foam properties, such as the plastic hardening curve were taken from [5].

The analytical solution for the incident facesheet under the projectile and global panel deflections is compared to FEA results in Fig. 6. The deflection of the distal facesheet under the projectile was taken as the global panel deflection in FEA. The analytical deflections are about 15% lower than FEA predictions.

Table 1: Facesheet and foam material properties.

	E-Glass/Vinyl Ester	Divinycell H100
Density (kg/m^3)	1391.3	100
Thickness (mm)	2	25
E_{11} (+) (GPa)	17	0.126
E_{22} (+) (GPa)	17	0.126
E_{33} (+) (GPa)	8.5	0.126
E_{11} (-) (GPa)	17	0.035
E_{22} (-) (GPa)	17	0.035
E_{33} (-) (GPa)	8.5	0.035
ν_{12}	0.13	0
ν_{13}	0.28	0
ν_{23}	0.28	0
$G_{12}=G_{21}$ (GPa)	4.0	0.0175
$G_{23}=G_{32}$ (GPa)	4.2	0.0175
$G_{13}=G_{31}$ (GPa)	4.2	0.0175
q (MPa)	--	1.66
ϵ_D	--	0.8

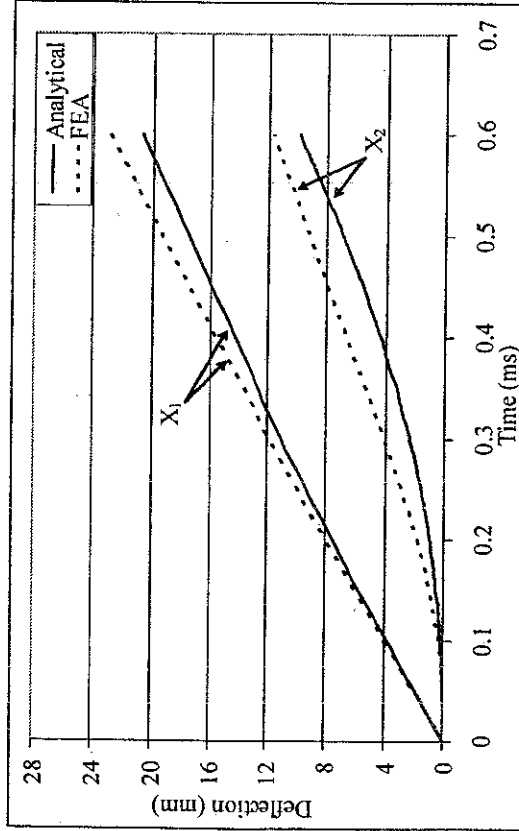


Figure 6: Transient deflections of incident and distal facesheets under the projectile.

6 Conclusions

A two degree-of-freedom model was developed and used to obtain the local indentation and global deformation response of a sandwich panel made with E-glass vinyl ester facesheets and PVC H100 foam core and subjected to high

velocity impact by a rigid blunt, cylindrical projectile. The analytical solution for the local indentation and global deflection under the projectile was found to be 15% lower than FEA results.

Acknowledgement

This work was supported by Dr. Yapa Rajapakse at the Office of Naval Research under grant N00014-07-1-0423.

References

- [1] Skvortsov, V., Kepler, J. & Bozhevolnaya, E. Energy Partition for Ballistic Penetration of Sandwich Panels, *Int. J. Impact Engng.*, Vol. 28, pp. 697-716, 2003.
- [2] Tagarielli, V.L., Deshpande, V.S. & Fleck, N.A. The dynamic response of composite sandwich beams to transverse impact, *Int. J. Solids Struct.*, Vol. 44, pp. 2442-2457, 2007.
- [3] Gibson, L.J. & Ashby, M.F. *Cellular Solids Structures and Properties*, Cambridge University Press, Cambridge, 1999.
- [4] Ashby, M.F., Evans, A.G., Fleck, N.A., Gibson, L.J., Hutchinson, J.W. & Wadley, H.N.G. *Metal Foams: A Design Guide*, Butterworth Heinemann, London, 2000.
- [5] Mines, R.A.W. & Alias, A. Numerical simulation of the progressive collapse of polymer composite sandwich beams under static loading, *Composites Part A*, Vol. 33, pp. 11-26, 2002.

BLAST RESPONSE OF COMPOSITE SANDWICH PANELS

Michelle S. Hoo Fatt and Leelaprasad Palla

Department of Mechanical Engineering
The University of Akron
Akron, OH 44325-3903
e-mail: hoofatt@uakron.edu, web page: <http://www.uakron.edu>

Key words: Composite sandwich, Blast, Analytical model.

Summary. *Analytical solutions were derived for the transient response of a foam-core composite sandwich panel subjected to blast loading. The panel response consisted of two consecutive phases: (1) a through-thickness wave propagation phase leading to permanent core crushing deformations and (2) a transverse shear wave propagation phase resulting in global panel deflections. The predicted transient deformation of the sandwich panel was within 7% of FEA results using ABAQUS Explicit.*

1 INTRODUCTION

There is growing interest in using lightweight composite sandwich panels for construction of naval ships, which can be exposed to blast and impact during combat. Tagarielli et al. [1] have recently demonstrated that glass fiber vinyl sandwich beams with PVC foam cores and balsa wood have higher ballistic resistance than monolithic beams of equal weight. While there has been much research concerning localized projectile impact damage of composite sandwich panels, very little work has been done to address damage of composite sandwich panels under distributed pressure pulse loading, such as that caused by an underwater or air blast. Several recent articles have dealt with the blast resistance of metal sandwich panels with metallic foam, honeycomb, truss and wide variety of metal sandwich core topologies [2-5] but none of these can be directly applied to a composite sandwich panel made of anisotropic elastic facesheets and polymeric foam or balsa wood cores. The purpose of this paper is to present an analytical model that can be used to determine the blast performance of a composite sandwich panel. The paper specifically provides an analytical model for predicting the transient response and failure of a composite sandwich panel subjected to pressure pulse or impulsive loading, i.e., load durations are on the order of the through-thickness wave travel time and are short compared to the time associated with overall bending/shear panel deformation.

2 PROBLEM FORMULATION

Consider a fully clamped, composite sandwich panel of radius a , as shown in Fig. 1. The facesheets consist of orthotropic composite plates of thickness h , and the core is crushable polymeric foam of thickness H . Assume for simplicity that the panel is subjected to a uniformly distributed pressure pulse

$$p(t) = \begin{cases} p_o \left(1 - \frac{t}{\tau}\right), & 0 \leq t \leq \tau \\ 0, & t \geq \tau \end{cases} \quad (1)$$

where p_o is the peak pressure and τ is the load duration. Other pressure transients can be used to more accurately simulate underwater and air explosions [6,7]; they will produce similar impulsive sandwich response as the triangular pressure pulse in Eq. (1).

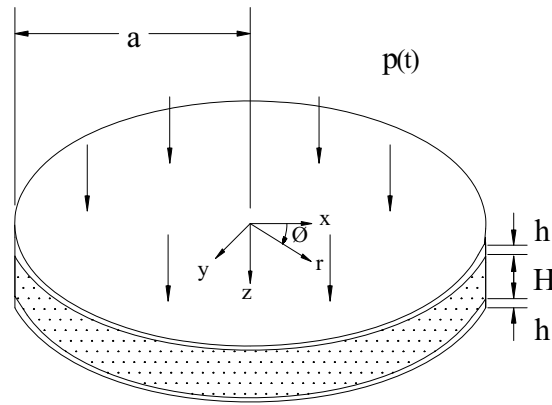


Figure 1: Composite sandwich panel subjected to uniformly distributed, pressure pulse.

Provided no failure has occurred to the panel during the blast, the response of the composite sandwich panel may be described by the three phases of motion shown in Fig. 2. In Phase I, a through-thickness stress wave propagates from the incident facesheet to the rear facesheet. In this phase the sandwich panel experiences local core crushing and local facesheet deformation, while an impulsive transverse shear reaction force is induced at the clamped boundaries. At the end of Phase I, kinetic energy is transferred globally to the panel and the impulsive transverse shear reaction force propagates from the clamped boundaries towards the panel center. Phase II consists of the propagation of an elastic unloading transverse shear wave. The pressure pulse has already ended and momentum is transferred to the sandwich panel, with reduced core thickness from Phase I. The transverse shear stress wave due to the reaction forces at the clamped boundary propagates from the clamped boundary towards the center of the panel. This transverse stress wave is an unloading wave, causing bending and shear deformations to develop behind the wave front. The elastic unloading transverse shear wave brings the panel to maximum deflection. At the end of Phase II, the panel rebounds and vibrates. Elastic vibrations take place in Phase III.

During Phase I, high intensity transverse shear stresses are developed at the clamped

boundary and these may cause transverse shear fracture at the clamped boundaries of the panel. Transverse shear fracture is usually avoided by using reinforcements at boundaries. The second mode of failure that can occur during blasts is tensile fracture in the center of the panel when bending strains are at a maximum at the end of Phase II. These two failure modes in addition to permanent deformation were first observed on impulsively loaded aluminum beams by Menkes and Opat [8] and later on aluminum plates by Teeling-Smith and Nurick [9]. They have also been experimentally observed on composite plates by Franz et al. [10].

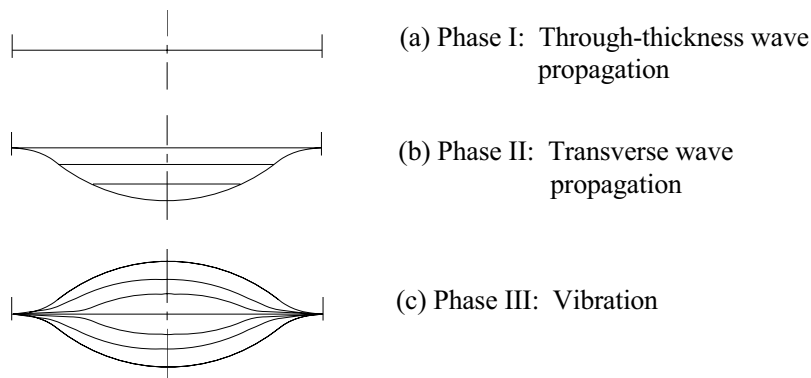


Figure 2: Three phases of blast response: (a) Phase I: Through-thickness wave propagation, (b) Phase II: Transverse wave propagation and (c) Phase III: Vibration.

This paper focuses on the first two phases of blast response described in Fig. 2 because they are relevant to the failure of the composite sandwich panel subjected to blast effects. The analytical solutions presented for the panel response is to be distinguished from previous models in which the Phase II was treated as the forced modal response of sandwich panels [11]. In this paper, Phase II is taken as an initial-value problem since the load duration is short compared to the transverse wave propagation time and the natural period of vibration in Phase III.

3 PHASE I – THROUGH-THICKNESS WAVE PROPAGATION

In most blast situations the load duration is short compared to the natural period of the global sandwich response and the pressure pulse can be realized as an impulsive loading to the sandwich. However, the wave speed in polymeric foam is low and a thick composite sandwich panel with a polymeric foam core is likely to undergo transient local facesheet indentation and core crushing while the pressure pulse is still acting. Take for example, H100 PVC foam core with a density of 100 kg/m^3 and a compressive elastic modulus of 35 MPa. Elastic waves propagate through a 25 mm thick core made of H100 PVC foam in 0.04 ms. Blast pressure pulse durations of this magnitude are not uncommon for naval composite sandwich ships subjected to underwater and air blast explosions [6,7]. Thus one can assume that permanent plastic deformations of the core will take place from a transient event, i.e., during the load application.

3.1 Transmission and reflection at interfaces

The transmission and reflection of plane strain stress waves through the multi-layered composite sandwich panel is shown in Fig. 3. Stress waves are transmitted from the incident facesheet to the foam at Interface 1 and from the foam to the distal facesheet at Interface 2. When the incident stress σ_I first reaches Interface 1, the transmitted stress σ_{T_1} and the reflected stress σ_{R_1} are given as follows:

$$\sigma_{T_1} = -k_{T_1} p(t-t_1)u\langle t-t_1 \rangle, \quad k_{T_1} = \frac{2\rho_c C_c}{(\rho_f C_f + \rho_c C_c)} \quad (2)$$

and

$$\sigma_{R_1} = -k_{R_1} p(t-t_1)u\langle t-t_1 \rangle, \quad k_{R_1} = \frac{(\rho_c C_c - \rho_f C_f)}{(\rho_f C_f + \rho_c C_c)} \quad (3)$$

where $t_1 = h/C_f$ is the wave transit time through the facesheet, C_f and C_c are the wave speeds in the facesheet and core, respectively; ρ_f and ρ_c are the density of the facesheet and core, respectively; and $u\langle \cdot \rangle$ is the unit step function. The wave speed in an orthotropic plate in plane strain is given by

$$C_f = \sqrt{\frac{E_{33}(1-\nu_{12})}{[1-\nu_{12} - \nu_{32}(\nu_{13} + \nu_{23})]\rho_f}} \quad (4)$$

where E_{ij} and ν_{ij} are elastic modulus and Poisson's ratio of the orthotropic facesheet. The wave speed in the foam will be discussed in the following section.

The reflected wave in the incident facesheet is tensile because $\rho_f C_f \gg \rho_c C_c$. This reflected wave is again reflected, but as a compressive stress wave, when it reaches the outer surface of the incident facesheet. The process of reflection and transmission of waves at Interface 1 repeats itself over and over again at intervals $2t_1$. Thus the transmitted stress in the foam at Interface 1 is given as

$$\begin{aligned} \sigma_{T_1} = & -k_{T_1} p(t-t_1)u\langle t-t_1 \rangle + k_{T_1} k_{R_1} p(t-3t_1)u\langle t-3t_1 \rangle - k_{T_1} k_{R_1}^2 p(t-5t_1)u\langle t-5t_1 \rangle \\ & \dots + (-1)^{n+1} k_{T_1} k_{R_1}^n p(t-(2n+1)t_1)u\langle t-(2n+1)t_1 \rangle \end{aligned} \quad (5)$$

where n is the number of reflections up to that time.

The transmitted stress wave in the foam σ_{T_1} will reflect back as a compressive wave into the foam and be transmitted as a compressive stress wave in the distal facesheet when it first reaches Interface 2. The transmitted stress in the distal facesheet σ_{T_2} is further reflected as a tensile stress wave from the outer surface of the distal facesheet. This reflected stress waves will then be transmitted as tensile stress wave in the foam and reflected back as compressive

stress wave into the facesheet. The part that is transmitted to the foam will add to the reflected stress waves in the foam σ_{R_2} . This process repeats itself indefinitely so that the reflected stress wave at any time is given by

$$\begin{aligned} \sigma_{R_2} = & -k_{R_2} p(t - t_1 - t_2) u \langle t - t_1 - t_2 \rangle + k_{T_2} k_{T_1} p(t - 3t_1 - t_2) u \langle t - 3t_1 - t_2 \rangle + \\ & -k_{T_2} k_{T_1} k_{R_1} p(t - 5t_1 - t_2) u \langle t - 5t_1 - t_2 \rangle + k_{T_2} k_{T_1} k_{R_1}^2 p(t - 7t_1 - t_2) u \langle t - 7t_1 - t_2 \rangle \quad (6) \\ & \dots + (-1)^{n+1} k_{T_2} k_{T_1} k_{R_1}^n p(t - (2n+1)t_1 - t_2) u \langle t - (2n+1)t_1 - t_2 \rangle \end{aligned}$$

where $t_2 = H / C_c$, $k_{T_2} = \frac{2\rho_f C_f}{(\rho_f C_f + \rho_c C_c)}$ and $k_{R_2} = \frac{(\rho_f C_f - \rho_c C_c)}{(\rho_f C_f + \rho_c C_c)}$. The reflected stress is a tensile unloading elastic stress wave. Permanent plastic strains or local indentation of the foam results after elastic unloading.

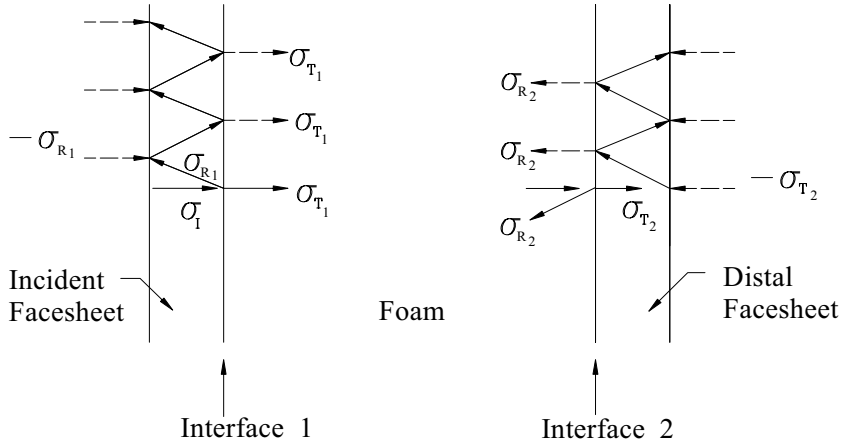


Figure 3: Transmission of stress waves through facesheets and foam of sandwich panel.

3.2 Elastic and plastic stress waves in polymeric foam

The facesheets are very stiff and remain elastic during wave transmissions but the polymeric foam core is elastic-plastic with a compressive stress-strain characteristic as shown in Fig. 4 [12]. The foam is linear elastic with a compressive modulus of E_c until yielding at a flow stress q . Rapid compaction of cells causes the density to change during the plateau region until full densification has occurred at ε_D . The stress rises to a maximum plastic stress σ_p at the densification strain.

Elastic and plastic waves could therefore be generated in the foam during Phase I. The elastic wave speed in the foam is given by $C_e = \sqrt{E_c / \rho_c}$ and the plastic wave speed is given

by $C_p = \sqrt{\frac{\sigma_p - q}{\rho_c \varepsilon_D}}$ [13], where σ_p is the stress in the densification region (see Fig. 4). Elastic

waves propagated first in the core and are later followed by plastic waves, as shown in Fig. 5.

The densification strain is related to particle velocities in the elastic and plastic regions, V_e and V_p , respectively, by

$$\varepsilon_D = \frac{V_p - V_e}{C_p} \quad (7)$$

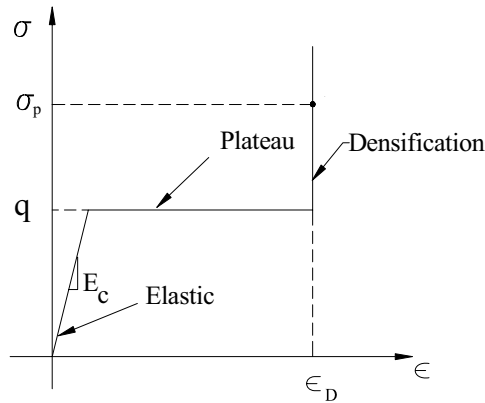


Figure 4: Compressive stress-strain curve of polymeric foam.

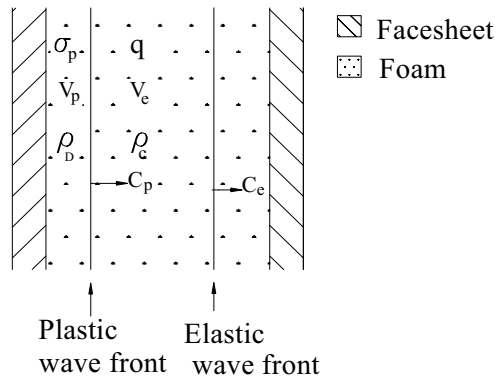


Figure 5: Elastic and plastic wave fronts in foam.

The particle velocity in the plastic region is in turn related to the plastic stress σ_p and density of foam after densification ρ_D :

$$V_p = \frac{\sigma_p}{\rho_D C_p} \quad (8)$$

where $\rho_D = \frac{\rho_c}{(1 - \varepsilon_D)}$. Similarly, $V_e = \frac{q}{\rho_c C_e}$. Expressing C_p in terms of σ_p and combining Eqs. (7) and (8) give the following quadratic equation that can be solved for σ_p :

$$\left(\frac{\rho_c - \rho_D}{\rho_c}\right)^2 \sigma_p^2 + \left[\frac{2\rho_D q}{\rho_c} \left(\frac{\rho_c - \rho_D}{\rho_c}\right) - \frac{V_e^2 \rho_D^2 q}{\rho_c \varepsilon_D}\right] \sigma_p + \frac{\rho_D^2 q^2}{\rho_c^2} + \frac{V_e^2 \rho_D^2 q}{\rho_c \varepsilon_D} = 0 \quad (9)$$

3.3 Local indentation

Permanent plastic strains arise when the elastic unloading wave reaches the plastic wave front. The local indentation is given by

$$\delta = \varepsilon_D C_p \Delta T \quad (10)$$

where ΔT is the time from the start of transmission of σ_p to the time when the elastic unloading wave reaches the plastic wave front. A simple expression for ΔT is

$$\Delta T = \frac{(2H/C_e + 3t_1 - t_p)}{(1 + C_p/C_e)} \quad (11)$$

where t_p is the start time of transmission of σ_p at Interface 1.

4 PHASE II– GLOBAL SHEAR/BENDING

Subsequent to Phase I, the load has ended and the core has crushed permanently to a height $H' = H - \delta$. Momentum is transferred to the sandwich panel, which has become impulsively loaded with a uniformly distributed velocity field (see Figs. 6 (a) and (b)). Conservation of momentum gives the initial velocity of the panel as

$$v_i = \frac{P_o \tau}{2(\rho_c H + 2\rho_f h)} \quad (12)$$

Denote the distance from the center of the panel to the wave front of the transverse shear wave as ξ . A transverse shear elastic unloading wave propagates from the clamped boundaries with velocity $\dot{\xi}$. This unloading wave instantaneously brings the plate to rest behind the wave front. As the plate is brought to rest, it undergoes shear and bending deformations as exemplified in Fig. 6(a).

4.1 System Lagrangian

Dynamic equilibrium of the complete sandwich can be expressed in terms of the maximum deflection at the center, Δ , and an equivalent shear angle, α_o . These two degrees of freedom have associated velocities, v_i and Ω , respectively. The kinetic energy for the sandwich is thus $T = \frac{1}{2} m_{eff} v_i^2 + \frac{1}{2} I_{eff} \Omega^2$, where $m_{eff} = \pi \xi^2 [2\rho_f h + \rho_c H]$ is the effective sandwich mass and I_{eq} is the effective sandwich rotary inertia. The elastic potential energy of the system is equivalent to the bending/shear strain energy of the sandwich, $\Pi = U$. The Lagrangian for the

whole model is $L = T - \Pi$. For dynamic equilibrium,

$$\frac{\partial}{\partial t} \left(\frac{\partial L}{\partial v_i} \right) - \frac{\partial L}{\partial \Delta} = 2\pi \xi \dot{\xi} [2\rho_f h + \rho_c H] v_i + \frac{\partial U}{\partial \Delta} = 0 \quad (13)$$

and

$$\frac{\partial}{\partial t} \left(\frac{\partial L}{\partial \Omega} \right) - \frac{\partial L}{\partial \alpha_o} = \Omega \frac{\partial I_{eff}}{\partial t} + I_{eff} \frac{\partial \Omega}{\partial t} + \frac{\partial U}{\partial \alpha_o} = 0 \quad (14)$$

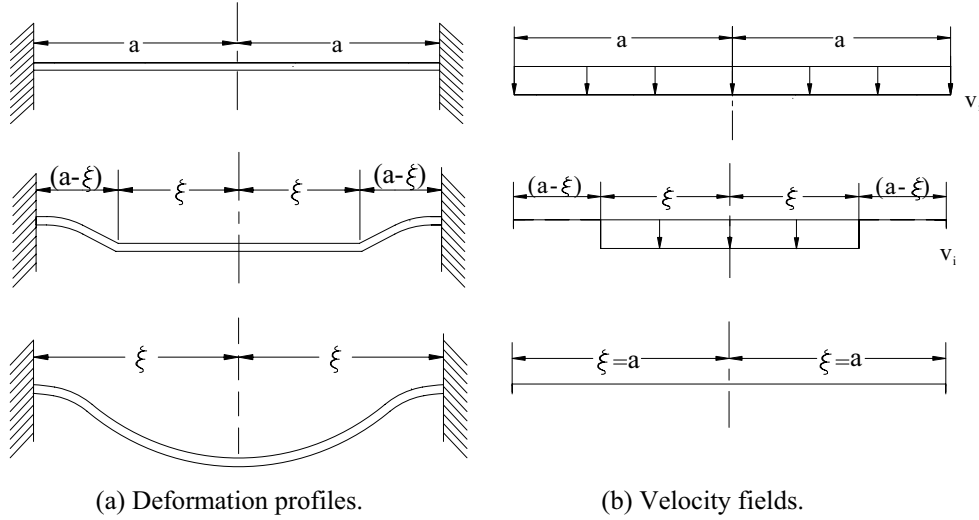


Figure 6: Global panel bending/shear response: (a) Deformation profiles and (b) Velocity fields.

4.2 Bending/shear strain energy

Assume in-plane deformations are negligible compared to the transverse deformation. The elastic strain energy of the symmetric sandwich panel with orthotropic facesheet is then given as

$$U = 4 \int_0^{\pi/2} \int_{-\xi}^{\xi} \left\{ \frac{D_{11}^s}{2} \left(\frac{\partial \bar{\alpha}}{\partial x} \right)^2 + D_{12}^s \left(\frac{\partial \bar{\beta}}{\partial y} \right) \left(\frac{\partial \bar{\alpha}}{\partial x} \right) + \frac{D_{22}^s}{2} \left(\frac{\partial \bar{\beta}}{\partial y} \right)^2 + A_{55}^s \left[\frac{\bar{\alpha}^2}{2} + \bar{\alpha} \frac{\partial w}{\partial x} + \frac{1}{2} \left(\frac{\partial w}{\partial x} \right)^2 \right] \right. \\ \left. + A_{44}^s \left[\frac{\bar{\beta}^2}{2} + \bar{\beta} \frac{\partial w}{\partial y} + \frac{1}{2} \left(\frac{\partial w}{\partial y} \right)^2 \right] + D_{66}^s \left[\frac{1}{2} \left(\frac{\partial \bar{\alpha}}{\partial y} \right)^2 + \frac{\partial \bar{\alpha}}{\partial y} \frac{\partial \bar{\beta}}{\partial x} + \frac{1}{2} \left(\frac{\partial \bar{\beta}}{\partial x} \right)^2 \right] \right\} r dr d\theta \quad (15)$$

where w is the transverse deflections, $\bar{\alpha}$ and $\bar{\beta}$ are shear angles associated with the x - and y -directions, respectively, D_{ij}^s is the sandwich bending stiffness matrix, and A_{44}^s and A_{55}^s are the transverse shear stiffnesses. The superscript “s” is used to denote the sandwich. Derivatives with respect to x and y can be transformed to polar coordinates before evaluating the above-mentioned integral expression.

Finite element analysis using ABAQUS Explicit indicates that the transverse deformation, w , and the shear rotations with respect to the radial direction $\bar{\alpha}$ are of the following forms:

$$w(r) = \begin{cases} 0, & 0 < r < \xi \\ \Delta \left(1 - \left(\frac{r - \xi}{a - \xi} \right)^2 \right)^2, & \xi < r < a \end{cases} \quad (16)$$

and

$$\bar{\alpha}(r) = \begin{cases} 0, & 0 < r < \xi \\ 4\alpha_o \frac{(r - \xi)(a - r)}{(a - \xi)^2}, & \xi < r < a \end{cases} \quad (17)$$

where Δ is the global deflection and α_o is the rotation at $r = (a + \xi)/2$. Substituting derivatives of the expressions in Eqs. (16) and (17) into Eq. (15) gives the following expression for the strain energy:

$$U = \frac{8(a + \xi)}{3(a - \xi)} [\pi D_{11} + 2D_{12} + (2 + \pi)D_{66}] \alpha_o^2 + \frac{2}{105} \frac{A_{55}}{(a - \xi)} [28\pi(a^3 - a\xi^2 - a^2\xi + \xi^3) \alpha_o^2 + (-176a^2 + 16\xi a + 160\xi^2) \alpha_o \Delta + (29\pi\xi + 35\pi a) \Delta^2] \quad (18)$$

4.3 Equations of motion

Assume the rate of angular rotation is similar to the shear rotation field in Eq. (17):

$$\dot{\alpha}(r) = \begin{cases} 0, & 0 < r < \xi \\ 4\Omega \frac{(r - \xi)(a - r)}{(a - \xi)^2}, & \xi < r < a \end{cases} \quad (19)$$

Then, the effective rotary inertia for the sandwich is $I_{eff} = \frac{8\pi}{15} \tilde{I}(a^2 - \xi^2)$, where

$$\tilde{I} = \sum_{k=1}^3 \rho_k (z_k^3 - z_{k-1}^3) = \frac{\rho_f}{12} (3hH^2 + 3h^2H + h^3) + \frac{\rho_c}{12} H^3. \quad \text{Denoting } \dot{\xi} = \frac{-(a - \xi)}{t} \text{ and } \Delta = v_i t,$$

one gets the following coupled equations of motion from Eqs. (13) and (14):

$$-2\pi [2\rho_f h + \rho_c H] \xi \frac{(a - \xi)}{t} v_i + \frac{2}{105} \frac{A_{55}}{(a - \xi)} [(-176a^2 + 16\xi a + 160\xi^2) \alpha_o + 2(29\pi\xi + 35\pi a) v_i t] = 0 \quad (20)$$

and

$$\frac{8\pi}{15} \tilde{I}(a^2 - \xi^2) \frac{d^2 \alpha_o}{dt^2} + \frac{16\pi}{15} \tilde{I} \xi \frac{(a - \xi)}{t} \frac{d\alpha_o}{dt} + \frac{16(a + \xi)}{3(a - \xi)} [\pi D_{11} + 2D_{12} + (2 + \pi)D_{66}] \alpha_o + \frac{2}{105} \frac{A_{55}}{(a - \xi)} [56\pi(a^3 - a\xi^2 - a^2\xi + \xi^3) \alpha_o + (-176a^2 + 16\xi a + 160\xi^2) v_i t] = 0 \quad (21)$$

where $\alpha_o(0) = 0$ and $\dot{\alpha}_o(0) = 0$.

5 AN EXAMPLE

As an example consider a fully clamped, sandwich panel made of E-glass vinyl ester facesheets and H100 foam core, with a radius 250 mm, facesheet thickness 2 mm, and core thickness 25 mm. Material properties for the E-glass vinyl ester and H100 are given in Table 1. Let the sandwich panel be subject to a uniformly distributed pressure pulse of the form given in Eq. (1), where $p_o = 10$ MPa and $\tau = 0.05$ ms.

Table 1 : Facesheet and foam material properties.

	E-Glass/Vinyl Ester	Divinycell H100
Density (kg/m ³)	1391.3	100
Thickness (mm)	2	25
E ₁₁ (+) (GPa)	17	0.126
E ₂₂ (+) (GPa)	17	0.126
E ₃₃ (+) (GPa)	8.5	0.126
E ₁₁ (-) (GPa)	17	0.035
E ₂₂ (-) (GPa)	17	0.035
E ₃₃ (-) (GPa)	8.5	0.035
v ₁₂	0.13	0
v ₁₃	0.28	0
v ₂₃	0.28	0
G ₁₂ =G ₂₁ (GPa)	4.0	0.0175
G ₂₃ =G ₃₂ (GPa)	4.2	0.0175
G ₁₃ =G ₃₁ (GPa)	4.2	0.0175
q (MPa)	--	1.66
ε _D	--	0.8

This problem was modeled in 2D assuming plane strain conditions for Phase I response and in full 3D for both Phase I and II responses using ABAQUS Explicit. The H100 foam was modeled as an elastomeric foam with volumetric hardening. Additional foam properties, such as the plastic hardening curve were taken from Ref. [14].

5.1 Local core crushing: Phase I response

The transmitted stress transient at Interface 1, Eq. (5), and the same stress transient from FEA are shown in Fig. 7. The highest transmitted stress was calculated from Eq. (9) as $\sigma_p = 2.42$ MPa, which occurs at $t_p = 0.037$ ms from Fig. 7. This was about 10% higher than the maximum compressive stress of 2.2 MPa found from FEA. From the calculated values of σ_p and t_p , local core crushing was estimated as 3.2 mm from Eqs. (10) and (11).

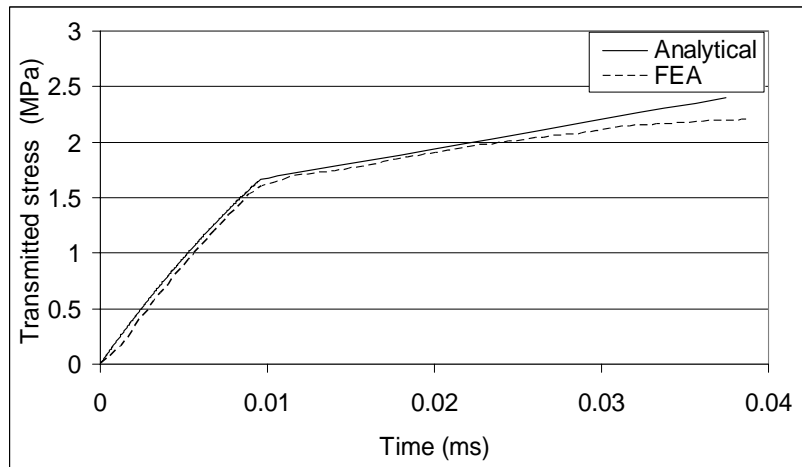


Figure 7: Transmitted stress at Interface 1 up to peak stress.

5.2 Global bending /shear: Phase II response

The initial global panel velocity was determined from Eq. (12) as $v_i = 31\text{m/s}$. The sandwich bending and shear stiffness were evaluated with a reduced core thickness $H' = 21.8\text{mm}$. A MATLAB program was written to solve Eqs. (20) and (21) for ξ and α_o . As shown in Fig. 8, the predicted transient deformation profiles compared very well to FEA results; the predicted value for ξ was within 7% of FEA.

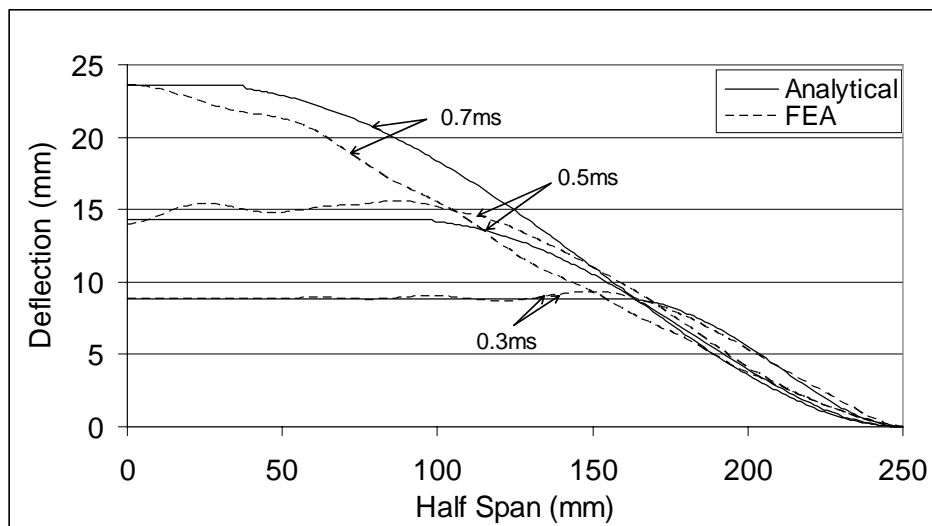


Figure 8: Transient deflection profiles of composite sandwich.

6 CONCLUDING REMARKS

Analytical solutions for the blast response of a foam-core composite sandwich panel were derived considering two phases: (a) core crushing during through-thickness wave propagation and (b) global panel bending/shear during transverse shear wave propagation. Global equilibrium equations of motion were used to obtain transverse deflection and shear rotations. The predicted transient deformation of the sandwich panel was within 7% of FEA results using ABAQUS Explicit.

ACKNOWLEDGEMENT

This work was supported by Dr. Y. Rajapakse under ONR grant N00014-07-1-0423.

REFERENCES

- [1] V.L. Tagarielli, V.S. Deshpande and N.A. Fleck, "The dynamic response of composite sandwich beams to transverse impact", *Int. J. Solids Struct.*, 44, 2442-2457 (2007).
- [2] A. Vaziri and J.W. Hutchinson, "Metal sandwich plates subject to intense air shocks", *Int. J. Solids Struct.*, 44, 2021-2035 (2007).
- [3] V.S. Deshpande and N. Fleck, "One-dimensional response of sandwich plates to underwater shock loading", *J. Mech. Phys. Solids*, 53, 2347-2383 (2005).
- [4] J.W. Hutchinson and Z. Xue, "Metal sandwich plates optimized for pressure impulses", *Int. J. Mech. Sci.*, 47, 545-569 (2005).
- [5] Z. Xue and J.W. Hutchinson, "A comparative study of impulse-resistant metal sandwich plates", *Int. J. Impact Engng.*, 30, 1238-1305 (2004).
- [6] R.H. Cole, *Underwater Explosions*, Princeton University Press, New Jersey (1948).
- [7] P.D. Smith and J.G. Hetherington, *Blast and Ballistic Loading of Structures*, Butterworth Heinemann, Oxford (1994).
- [8] S.B. Menkes and H.J. Opat, "Broken Beams", *Exp. Mech.*, 13, 480-486 (1974).
- [9] R.G. Teeling-Smith and G.N. Nurick, "The deformation and tearing of thin circular plates subjected to impulsive loads", *Int. J. Impact Engng.*, 11, 77-91 (1991).
- [10] T. Franz, G.N. Nurick and M.J. Perry, "Experimental investigation into the response of chopped-strand mat glass fibre laminates to blast loading", *Int. J. Impact Engng.*, 27, 639-667 (2002).
- [11] L. Librescu, S.-Y. Oh and J. Hohe, "Dynamic response of anisotropic sandwich flat panels to underwater and in-air explosions", *Int. J. Solids Struct.*, 43, 3794-3816 (2006).
- [12] L.J. Gibson and M.F. Ashby, *Cellular Solids Structures and Properties*, Cambridge University Press, Cambridge (1999).
- [13] M.F. Ashby, A.G. Evans, N.A. Fleck, L.J. Gibson, J.W. Hutchinson, H.N.G. Wadley, *Metal Foams: A Design Guide*, Butterworth Heinemann, London (2000).
- [14] R.A.W. Mines and A. Alias, "Numerical simulation of the progressive collapse of polymer composite sandwich beams under static loading", *Composites Part A*, 33, 11- 26 (2002).

IMPACT PERFORATION OF COMPOSITE SANDWICH PANELS

Michelle S. Hoo Fatt, Dushyanth Sirivolu

Department of Mechanical Engineering, The University of Akron, Akron OH 44325-3903

Keywords: Composite sandwich; impact perforation, analytical models.

Abstract

Analytical models for the quasi-static and low-velocity perforation of composite sandwich panel with woven roving E-glass/vinyl ester facesheets and CorematTM were developed. A multi-stage perforation process involving delamination, debonding, core shear fracture and facesheet fracture was used to calculate the quasi-static failure load and ballistic limit of the panel. The high core crushing resistance of the CorematTM caused the distal facesheet to fracture before the incident facesheet during panel perforation. This is in contrast to sandwich panel with honeycomb and conventional polymeric foams, whereby damage first occurs on the incident faceheet. Analytical predictions of the quasi-static load-deflection response and the dynamic contact force history were within 10% of the test results.

1 Introduction

Composite sandwich panels are used extensively in the aerospace, marine, transportation, and recreational industries because of their high specific stiffness and strength, corrosion resistance, tailorability, and high fatigue life. In many of these applications, the composite panel may be subjected to localized projectile impact. Therefore, much work has been done in an effort to determine the failure load, ballistic limit, perforation energy and damage induced into composite sandwich panels subjected to quasi-static indentation and projectile impact [1-3]. While most of this research has been experimental, few analytical solutions have been proposed because of the complicated interaction between the composite facesheet and core during deformation and failure.

The objective of this paper is to present analytical models that can be used to describe quasi-static and impact perforation of an E-glass/vinyl

ester and CorematTM sandwich panel. The analytical models are derived using experimental results from Mines et al. [3]. In Ref. [3], quasi-static and low-velocity impact perforation tests with a hemispherical-ended indenter/projectile were done on two types of composite sandwich panels: a woven roving E-glass/vinyl ester skin with CorematTM core and an E-glass/epoxy with an aluminum honeycomb core. CorematTM is a high density/high energy absorption resin impregnated non-woven polyester with 50% microsphere and is commonly used in the marine industry [4]. Although the mechanical properties of the facesheets in both sandwich panels were similar in these tests, the Coremat had a much higher crushing resistance than the aluminum honeycomb. As a result of this, failure in the Coremat sandwich first occurred on the back (distal) facesheet while failure in the aluminum honeycomb sandwich occurred on the front (incident) facesheet. In earlier work, Lin and Hoo Fatt [5] developed an analytical model to describe the quasi-static and impact perforation the E-glass/epoxy with the aluminum honeycomb core. This paper is an extension of earlier work to develop analytical models for the impact perforation of composite sandwich panels.

2 Problem Formulation

Consider the composite sandwich panel, as shown in Fig. 1. The facesheets are thin orthotropic membranes of dimension $a \times a \times h$, and the core is a crushable polymeric foam of dimension $a \times a \times H$. This particular core is made of a Coremat, which has a core crushing resistance that is linear strain-hardening [3]. Typical low-density foam cores have constant core crushing resistance. The indenter/projectile has a hemispherical-nose of radius R and a mass M_0 . The indenter/projectile is assumed rigid compared to the sandwich panel.

Upon loading, the panel experiences simultaneous local indentation and global deformation. Analytical solutions for the local load-deflection as well as the global load-deflection will be derived using the principle of minimum potential energy in the following section. Experiments [1-3] indicate the fracture mechanisms as well as the load-displacement characteristics of sandwich panels subjected to low-velocity impact are similar to those observed in quasi-static cases. Three stages must occur for total perforation of the sandwich panel: (i) initial failure during which one of the skins of the panel fractures; (ii) penetration of the indenter through core and surviving facesheet; and (iii) complete panel perforation including frictional resistance between the indenter/projectile and sandwich panel. Delamination, debonding, core shear fracture, and tensile fracture of incident and distal facesheets occur during the perforation process. The order in which these failure mechanisms occur depends on geometry and material properties. Simple analytical failure criteria have been proposed for composite sandwich beam structures [6], but these cannot be directly applied to the composite sandwich plate.

3 Static Perforation

Approximate solutions for the quasi-static local indentation and global deformation of a composite sandwich panel will be derived using the principle of minimum potential energy. Local indentation consists of front facesheet indentation and core crushing, while global deformation consists of bending and shearing of the entire panel. Local indentation and global deformation will be considered independently, and the total panel deformation is considered as the sum of the local indentation and global deformation. When either the top or bottom facesheet fails, both local and global load-deflection characteristics will change. Complete sandwich panel perforation does not occur until both facesheets and core have failed.

3.1 Local indentation

Top facesheet indentation is modeled by considering a rigid indenter pressing into an orthotropic membrane resting on a rigid-plastic foundation. The total potential energy of the system is

$$\Pi = U + D - W \quad (1)$$

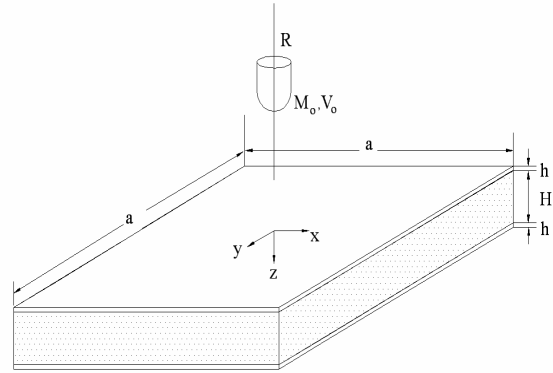


Fig. 1 Geometry of composite sandwich panel.

where U is the elastic strain energy of the facesheet, D the work dissipated in crushing the core, and W the external work done.

Under moderately large deflection, the facesheet responds like an orthotropic membrane. The strain energy associated with bending is negligible compared to the membrane energy associated with in-plane stretching. In addition, in-plane deformations, u and v , are negligibly small compared to transverse deflections, w . With these two assumptions, the elastic strain energy becomes

$$U = \frac{1}{8} \int_S \left[A_{11} \left(\frac{\partial w}{\partial x} \right)^4 + A_{22} \left(\frac{\partial w}{\partial y} \right)^4 + (2A_{12} + 4A_{66}) \left(\frac{\partial w}{\partial x} \right)^2 \left(\frac{\partial w}{\partial y} \right)^2 \right] dS \quad (2)$$

where A_{ij} is the membrane stiffness of the orthotropic facesheet and S is the area.

The work dissipated in crushing the Coremat is given by

$$D = \int_S \left(a_1 + \frac{k}{H} w \right) w dS \quad (3)$$

where a_1 and k are the core's crushing flow strength and strain hardening modulus, respectively.

The exact solution for the transverse deflection of an axi-symmetrical isotropic plate under center point loading is used to describe the local indentation of the sandwich panel, w :

$$w(r) = \delta \left[1 - \frac{r}{\xi} \right]^2 \quad (4)$$

where δ is the local indentation under the indenter, ξ is the length of the deformation zone, and $r^2 = x^2 + y^2$. The total potential energy then becomes

$$\Pi = C_1 \frac{\delta^4}{\xi^2} + \frac{\pi a_1}{6} \delta \xi^2 + \frac{k\pi}{15H} \delta^2 \xi^2 - P\delta \quad (5)$$

where $C_1 = \frac{\pi}{60} (3A_{11} + 3A_{22} + 2A_{12} + 4A_{66})$.

The total potential energy Π is a function of two unknown parameters, ξ and δ . From the principle of minimum potential energy, an equilibrium condition occurs when $\frac{\partial \Pi(\delta, \xi)}{\partial \delta} = 0$. Minimizing the potential energy yields the following load-indentation response:

$$P = \frac{4C_1 \delta^3}{\xi^2} + \frac{\pi a_1 \xi^2}{6} + \frac{2\pi k \delta \xi^2}{15H} \quad (6)$$

The load-deformation response is dependent on ξ

and is minimum when $\frac{\partial P}{\partial \xi} = 0$. Therefore,

$$P = 4C_1 \delta \sqrt{\frac{5\pi a_1 H \delta + 4\pi k \delta^2}{120C_1 H}} + \left(\frac{5\pi a_1 H \delta^2 + 4\pi k \delta^3}{30H} \right) \sqrt{\frac{120C_1 H}{5\pi a_1 H \delta + 4\pi k \delta^2}} \quad (7)$$

The first term in the right-hand side of Eq. (7) represents membrane resistance of the facesheet, while the second term in Eq. (7) is due to the Coremat crushing resistance.

3.2 Global panel deformation

Again assuming in-plane deformations are negligible compared to the transverse deformation, one finds the following expression for the elastic strain energy of the symmetric sandwich panel with orthotropic facesheet:

$$U = 4 \int \int_{00}^{aa} \left\{ \frac{D_{11}^s}{2} \left(\frac{\partial \bar{\alpha}}{\partial x} \right)^2 + D_{12}^s \left(\frac{\partial \bar{\beta}}{\partial y} \right) \left(\frac{\partial \bar{\alpha}}{\partial x} \right) + \frac{D_{22}^s}{2} \left(\frac{\partial \bar{\beta}}{\partial y} \right)^2 + A_{55}^s \left[\frac{\bar{\alpha}^2}{2} + \bar{\alpha} \frac{\partial w}{\partial x} + \frac{1}{2} \left(\frac{\partial w}{\partial x} \right)^2 \right] + A_{44}^s \left[\frac{\bar{\beta}^2}{2} + \bar{\beta} \frac{\partial w}{\partial y} + \frac{1}{2} \left(\frac{\partial w}{\partial y} \right)^2 \right] + D_{66}^s \left[\frac{1}{2} \left(\frac{\partial \bar{\alpha}}{\partial y} \right)^2 + \frac{\partial \bar{\alpha}}{\partial y} \frac{\partial \bar{\beta}}{\partial x} + \frac{1}{2} \left(\frac{\partial \bar{\beta}}{\partial x} \right)^2 \right] \right\} dx dy \quad (8)$$

where w is again used to express transverse deflections, $\bar{\alpha}$ and $\bar{\beta}$ are shear angles associated with the x - and y -directions, respectively, D_{ij}^s is the sandwich bending stiffness matrix, and A_{44}^s and A_{55}^s are the transverse shear stiffnesses. The superscript “s” is used to denote the sandwich.

Finite element analysis using ABAQUS Standard was used to describe the transverse deformation, w , and the shear rotations with respect to the x - and y -axis, $\bar{\alpha}$ and $\bar{\beta}$, as follows:

$$w(x, y) = \Delta \left(1 - \left(\frac{x}{a} \right)^2 \right)^2 \left(1 - \left(\frac{y}{a} \right)^2 \right)^2 \quad (9)$$

and

$$\bar{\alpha}(x, y) = \alpha_o \sin \left(\frac{\pi x}{a} \right) \left(1 - \left(\frac{y}{a} \right)^2 \right)^2 \quad (10)$$

$$\bar{\beta}(x, y) = \beta_o \sin \left(\frac{\pi y}{a} \right) \left(1 - \left(\frac{x}{a} \right)^2 \right)^2 \quad (11)$$

where Δ is the global deflection under the indenter and α_o and β_o are rotations at the center of the panel. The above functions satisfy the boundary conditions that $w = 0$ and $\bar{\alpha} = \bar{\beta} = 0$ at the edges.

Substituting derivatives of the expressions in Eqs. (9)-(11) into Eq. (8) gives the following expression for the strain energy:

$$U = F_1 \Delta^2 + F_2 \alpha_o^2 + F_3 \beta_o^2 + F_4 \Delta \alpha_o + F_5 \Delta \beta_o + F_6 \alpha_o \beta_o \quad (12)$$

where

$$\begin{aligned}
 F_1 &= \frac{32768}{33075} (A_{44}^s + A_{55}^s) \\
 F_2 &= \frac{128}{315} a^2 A_{55}^s + \frac{128\pi^2}{315} D_{11}^s + \frac{128}{105} D_{66}^s \\
 F_3 &= \frac{128}{315} a^2 A_{44}^s + \frac{128\pi^2}{315} D_{22}^s + \frac{128}{105} D_{66}^s \\
 F_4 &= \frac{-4096}{105\pi^3} a A_{55}^s \\
 F_5 &= \frac{-4096}{105\pi^3} a A_{44}^s \\
 F_6 &= \frac{2304}{\pi^6} (D_{12}^s + D_{66}^s)
 \end{aligned}$$

The total potential energy then becomes

$$\begin{aligned}
 \Pi &= F_1 \Delta^2 + F_2 \alpha_o^2 + F_3 \beta_o^2 + F_4 \Delta \alpha_o \\
 &\quad + F_5 \Delta \beta_o + F_6 \alpha_o \beta_o - P \Delta
 \end{aligned} \tag{13}$$

Minimizing Π with respect to Δ , α_o and β_o gives a closed-form expression for the global load-deflection response,

$$P = K_g \Delta \tag{14}$$

$$\text{where } K_g = \frac{[4F_1(F_2 + F_3 + F_6) - (F_4 + F_5)^2]}{2(F_2 + F_3 + F_6)}.$$

Table 1 gives the facesheet and core material properties for the sandwich panels considered in this research. Most of these material properties come from Ref. [3], but some have been estimated from Refs. [7] and [8]. These material properties were used to calculate the local indentation and global deformation under static indentation with a 25 mm diameter tup. A comparison of the predicted load-deflection characteristics under the tup with test data is shown from points A-C in Fig. 2. The total deflection X_1 in Fig. 2 is the displacement of the indenter. It is the sum of local indentation δ and global deformation Δ , i.e., $X_1 = \delta + \Delta$. Neither the front (incident) nor the back (distal) facesheet were perforated during this event, and the analytical solution for the load-deflection is within 5% of the test data.

Table1. Material properties of woven roving E-glass/vinyl ester and Coremat.

	E-Glass/ Vinyl Ester	Firet Coremat
Density (kg/m ³)	1391.3	640
Thickness (mm)	0.48	9.34
E ₁₁ (+) (GPa)	17	0.8
E ₂₂ (+) (GPa)	17	0.8
E ₃₃ (GPa)	--	0.35
v ₁₂	0.13	0.36
v ₁₃	--	0.57
v ₂₃	--	0.57
v ₂₁	0.13	0.36
v ₃₁	--	0.45
v ₃₂	--	0.45
G ₁₂ =G ₂₁ (GPa)	4.0	0.29
G ₂₃ =G ₃₂ (GPa)	--	0.068
G ₁₃ =G ₃₁ (GPa)	--	0.068
σ _{3f} (-) (MPa)	--	22
a ₁ (MPa)	--	10
k (MPa)	--	100
ILSS (MPa)	51.6	51.6*
G _{IIC} (J/m ²)	2757	1400
σ _{1f} (+) (MPa)	270	--
σ _{1f} (-) (MPa)	200	--
σ _{2f} (+) (MPa)	270	--
σ _{2f} (-) (MPa)	200	--
τ _{12f} (+)=τ _{21f} (+) (MPa)	40	--
τ _{13f} (+)=τ _{31f} (+) (MPa)	--	5
τ _{23f} (+)=τ _{32f} (+) (MPa)	--	5
ε _{1f} (+)	0.021	--
ε _{3f} (-)	--	0.025
E _a (MJ/m ³)	2.7	--

* Interlaminar shear strength is assumed equal to E-Glass/vinyl ester.

4 Failure Mechanisms

As mentioned earlier several failure mechanisms may occur during local indentation and global deformation. Simple failure criteria are derived for each of these mechanisms below. A multi-stage damage model to complete perforation will be proposed once the initial failure mechanism is determined.

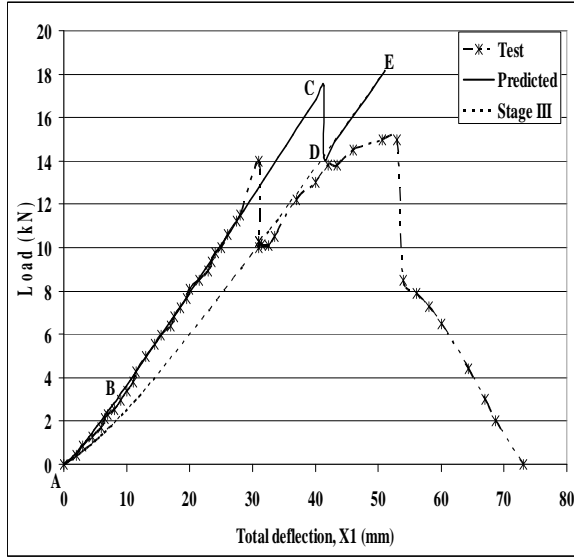


Fig. 2 Variation of quasi-static load with penetrator displacement.

4.1 Delamination/debonding

Although not a catastrophic failure mode, delamination between plies and debonding between facesheets and core will occur when the interlaminar shear strength and bond strength are exceeded. Fracture mechanics can be used to calculate threshold loads for the onset of delamination and debonding. An approximate solution for the delamination threshold load in a quasi-isotropic orthotropic plate under static indentation is given by Olsson et al. [9] as

$$P_{del}^{st} = \pi \sqrt{\frac{32G_{IIc}D}{3}} \quad (15)$$

where G_{IIc} is the Mode II interlaminar fracture toughness and $D = \sqrt{D_{11}D_{22}(\eta + 1)}/2$,

$\eta = (D_{12} + 2D_{66})/\sqrt{D_{11}D_{22}}$. This formula can be used to calculate the threshold load for delamination/debonding in the E-glass/vinyl ester and Coremat sandwich panel by assuming $D_{ij} = D_{ij}^s$. Under impact loads, the threshold

delamination load is $P_{del}^{dyn} = 1.213P_{del}^{st}$. Separate loads should be calculated for delamination and debonding because values for the Mode II

interlaminar shear fracture toughness are generally not the same.

The size of the delamination may found from equilibrium considerations and assuming that the transverse stress is parabolic through the thickness,

$$\tau_{rz} = \frac{3P}{4\pi r(H + 2h)} \left[1 - \left(\frac{2z}{H + 2h} \right)^2 \right] \quad (16)$$

where r and z are the radial and through-thickness coordinates, respectively. The delamination or debonding radius is found by evaluating τ_{rz} at the appropriate interlayer and setting it equal to the interlaminar shear strength of the facesheet or the interlaminar bond strength of between the facesheet and core.

4.2 Core shear failure

Consider local indentation of isolated Coremat (no facesheet) by the hemispherical-nose indenter. The crushing load under the indenter is given by

$$P = 2\pi \int_0^{\rho} \left(a_1 + \frac{kw}{H} \right) r dr \quad (17)$$

where $w = \sqrt{R^2 - r^2} + \delta - R$ is the local deflection under the indenter and ρ is the contact radius of the indenter with the top facesheet. A simple relation between local indentation δ and contact radius ρ is given by

$$\delta = R - \sqrt{R^2 - \rho^2} \quad (18)$$

Isolated core shear failure takes place when

$P = P_c = 2\pi\rho_c H \tau_{cr}$, where ρ_c is the critical contact radius at core shear failure and $\tau_{cr} = \tau_{13}$ is the transverse shear strength of Coremat. Integrating Eq. (17), using Eq. (18) to eliminate δ , and setting $P = P_c$ give the following implicit solution for ρ_c :

$$\frac{a_1\rho_c}{2H} + \frac{k}{3\rho_c H^2} \left[R^3 - \left(R^2 - \rho_c^2 \right)^{\frac{3}{2}} \right] - \frac{k\rho_c}{2H^2} \sqrt{R^2 - \rho_c^2} = \tau_{cr} \quad (19)$$

The corresponding load for isolated core shear fracture can be calculated once ρ_c is known. The load at which the Coremat sandwich panel undergoes core shear failure is higher than the core shear fracture load of isolated Coremat since the sandwich also has to resist the front facesheet membrane resistance. The core shear fracture load for the Coremat sandwich panel is found by requiring the second term of Eq. (7) be equal to P_c .

4.3 Front/back facesheet failure

One can use strain energy density to predict facesheet failure. The strain energy density in an orthotropic facesheet is

$$U_o = \frac{1}{2}(\bar{Q}_{11}\epsilon_x^2 + \bar{Q}_{22}\epsilon_y^2 + 2\bar{Q}_{12}\epsilon_x\epsilon_y + \bar{Q}_{66}\gamma_{xy}^2) \quad (20)$$

where ϵ_x , ϵ_y , and γ_{xy} are in-plane strains and \bar{Q}_{ij} are components of the transformed stiffness matrix. When the strain energy density is larger than the toughness, i.e, the specific energy absorbed in a uniaxial tension test E_a , failure can occur.

In the back facesheet, the strain varies through the sandwich panel thickness and are given by

$$\epsilon_x = z \frac{\partial \bar{\alpha}}{\partial x}, \epsilon_y = z \frac{\partial \bar{\beta}}{\partial y}, \quad \text{and} \quad \gamma_{xy} = z \left(\frac{\partial \bar{\alpha}}{\partial x} + \frac{\partial \bar{\beta}}{\partial y} \right).$$

where Eqs. (10) and (11) are used to evaluate strains. According to these expressions, the maximum compressive and tensile strains due to global deformation occur in the front and back facesheets, respectively. The front facesheet strains may be estimated by the average strain method presented in Ref. [5]. Since the strains due to local indentation in the front facesheet are tensile and opposite in sign to the compressive strains caused by global bending, the magnitude of the strains in the back facesheet is always larger. Failure due to global deformation will therefore first occur in the back facesheet rather than the front facesheet.

Our calculated results show that the strain energy density in both front and back facesheets are maximum under the indenter and along the 0 and 90° directions. This means cracks in the front or back facesheet will emanate in four directions corresponding to the 0 and 90° reinforcement directions of the woven skins.

The failure loads for delamination, debonding, cores shear fracture, and back facesheet fracture are given in Table 2. The lowest load corresponds to core shear fracture, thereby signifying that this takes place before fracture of either top or bottom facesheets. Since the core is still trapped between facesheets, the local indentation and global deformation response remain relatively unchanged. After core shear fracture, the contact radius between indenter and top facesheet still increases with load and the Coremat crushes with almost the same characteristics as when there was no core shear fracture. Debonding and delamination then takes place at 7.6 and 10.7 kN, respectively. The back facesheet finally fractures at 17.4 kN. This is about 25% higher than the experimental failure load at 14 kN. Approximate energy methods are generally less accurate in predicting stresses and strains than they are deflections.

When the back facesheet fails, new load-deflection relations must be derived since the panel becomes weaker and less stiff. A progressive or multi-stage perforation model will be used to derive these new load-deflection relations in the next section.

Table 2. Load and deflection at each failure mode.

Failure Mode	Load (kN)	Local Indentation (mm)	Global Deflection (mm)
Delamination	10.7	4.5	23.8
Debonding	7.6	3.8	17.4
Core Shear	3.8	2.6	8.6
Back Facesheet	17.4	5.9	36.8

4.4 Multi-stage perforation model

The following multi-stage perforation model is proposed as illustrated in Figure 3 (a)-(c):

Stage I – Local indentation and global deformation up to core shear fracture, as depicted in Fig. 3 (a). Core shear fracture occurs at roughly 45 degrees with respect to the plane of the panel since this corresponds to a plane of maximum shear stress. It is easier for the crack to extend horizontally thereby debonding the core from the back facesheet rather than continue at the 45 degree angle into the facesheet. The transverse bond strength is an order of magnitude smaller than the transverse shear strength of the facesheet.

Stage II – Deformation beyond core shear fracture and ending with back facesheet fracture, as indicated in Fig. 3 (b). The core crushing resistance used to calculate the local load-indentation response remains unchanged since the facesheet are intact. Eventually a cross-hair fracture develops on the back facesheet, as is also shown in Fig. 3(b).

Stage II I– Deformation up to front facesheet fracture (see Fig. 3 (c)). Both global and local deformation continues after the back facesheet fails. The back facesheet petals under the indenter and local indentation becomes softer. A new load-deformation response will occur in Stage III and will be discussed in the next section. The global panel stiffness is little affected by the cross-hair fracture and is assumed to be roughly the same prior to back facesheet fracture.

4.4 Back facesheet debonding after core shear fracture

Back facesheet debonding is triggered by core shear fracture at a 45 degree angle. The size (radius) of the back facesheet debond λ can be calculated by assuming the tensile strength at the interface of the E glass/vinylester and Coremat is $\sigma_t = 73$ [10] and the following equilibrium condition:

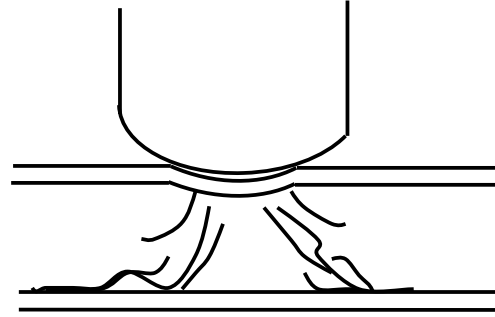
$$\sigma_t \pi (\lambda^2 - d^2) = \pi a_1 \rho^2 + \frac{2\pi k}{3H} \left[R^3 - (R^2 - \rho^2)^{\frac{3}{2}} \right] - \frac{\pi k \rho^2}{H} \sqrt{R^2 - \rho^2} \quad (21)$$

where $d = \rho_c + H$ is the radial distance to the start of the debonding region and ρ_c is the critical contact radius at core shear fracture. The right-hand side of Eq. (21) is the force exerted on the back facesheet by the Coremat in terms of ρ . Since ρ is related to δ by Eq. (18), one can determine the debond radius for any load using the load-indentation relation in Eq. (7). Substituting geometric and materials properties into Eq. (19) gives $\rho_c = 7.8$ mm. Solving Eq. (21) at the back facesheet failure load and deflection gives $\lambda = 32.9$ mm.

4.5 Local indentation response in Stage III

Local petaling occurs immediately following cross-hair fracture in the back facesheet. The global

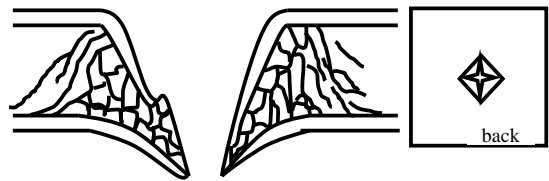
sandwich panel stiffness is little affected by the localized petaling, but the local indentation resistance is much reduced, especially under the indenter. As shown in Fig. 3 (c), transverse shearing rather than compression of the Coremat is occurring beneath the indenter. Once again the minimum potential energy is used to predict the local-indentation response.



(a) Core shear fracture and back facesheet debonding.



(b) Back facesheet failure.



(c) Front facesheet failure and perforation.

Fig. 3 Multi-stage perforation process: (a) core shear failure and back facesheet debonding, (b) back facesheet fracture, (c) front facesheet failure and perforation.

The total potential energy during Stage III local indentation is given by

$$\Pi = C_1 \frac{\delta^4}{\lambda^2} + \frac{G_{13} \pi H}{12} \delta^2 + \frac{8\tilde{D}_{11}}{3\lambda^2} (\delta - \delta_c)^2 - P\delta \quad (22)$$

where G_{13} is the core transverse shear stiffness,

$$\tilde{D}_{11} = \sum_{j=1}^N \sqrt{E_{11j}^2 + E_{22j}^2} (z_j^3 - z_{j-1}^3) \quad \text{is a beam}$$

equivalent bending stiffness, N is the number of plies in the facesheet, and δ_c is the local deflection at back facesheet failure. The first term of the potential energy is the membrane energy of the front facesheet, the second term is the core shearing energy and the last term is the bending energy of four petals (see Fig. 3 (c)). Minimizing the potential energy yields the following load-indentation response:

$$P = \frac{4C_1}{\lambda^2} \delta^3 + \frac{G_{13}\pi H}{6} \delta + \frac{16\tilde{D}_{11}}{3\lambda^2} (\delta - \delta_c) \quad (23)$$

The predicted load-deflection response in Stage III is indicated by the dashed line in Fig. 2. Because the back facesheet failure load was overpredicted only a small portion of this graph is actually used in the predicted response. The load drop at E corresponds to tensile failure of the front facesheet.

5 Low-Velocity Impact Response

The impact response of the panel is found from the two degree-of-freedom mass-spring-dashpot system shown in Fig. 4. The projectile mass is denoted M_o , and the effective mass of the top facesheet and sandwich are represented by m_f and m_s , respectively. Expressions for the effective facesheet and sandwich masses are derived by assuming the local and global velocities are distributed the same as their deformations. The local deformation and global deformation are given by $\delta = X_1 - X_2$ and $\Delta = X_2$, respectively. The local indentation resistance P_l and the global spring stiffness K_g are found from quasi-static results and adjusted with the strain rate-dependent material properties of the facesheet and core. High strain material tests show that the stiffness and strength of the E-glass/vinyl ester increases with increasing strain rate [11]. High strain rate tests on polymeric foams indicate that they are fairly rate insensitive [12]. The Coremat material properties are therefore assumed to be the same as in quasi-static tests. In addition to the local and global stiffness, a linear dashpot is used to represent damping of the

Coremat. The damping constant for the dashpot is calculated from the impact test results since there is no published data on Coremat damping properties.

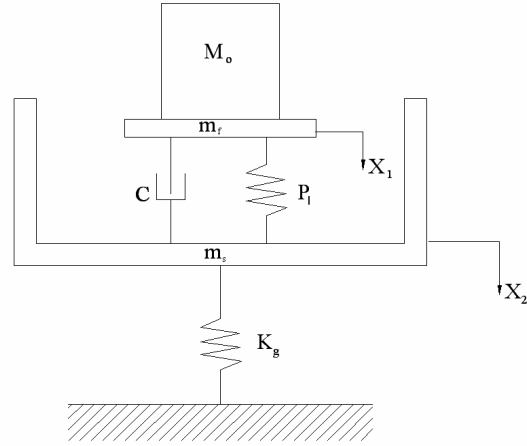


Fig. 4 Two degree-of-freedom model for impact of composite sandwich panel.

The equations of motion for the two-degree-of-freedom system are

$$(M_o + m_f)\ddot{X}_1 + P_l + c(\dot{X}_1 - \dot{X}_2) = 0 \quad (24)$$

and

$$m_s\ddot{X}_2 - P_l - c(\dot{X}_1 - \dot{X}_2) + K_g X_2 = 0 \quad (25)$$

The initial conditions for the two-degree-of-freedom system are as follows: $X_1(0) = 0$, $X_2(0) = 0$, $\dot{X}_1(0) = V_o$, and $\dot{X}_2(0) = 0$, where V_o is the initial velocity of the projectile.

Equations (24) and (25) represent a nonlinear, coupled initial-value problem. An ode solver was used in MATLAB to solve for X_1 and X_2 . The contact force between the projectile and the impacted facesheet is given by

$$F = -M_o\ddot{X}_1 \quad (26)$$

Each failure event occurring during transient deformation would decrease the kinetic energy of the system. The energy absorbed by delamination/debonding is the product of the interlaminar shear fracture toughness and appropriate areas. These areas may be estimated from Eq. (15) and the delamination and debonding

loads. The core shear fracture energy is given also given by the product of the core transverse shear fracture toughness and its associated fracture area. The fracture energy due to petaling of the back and front facesheets are estimated from the tear energy of the E-glass/vinyl ester. Expressions for the tear energy associated with petaling are taken from Lin and Hoo Fatt [5].

Figure 5 compares the calculated contact force with test data for panels impacted by a 10 kg projectile and exhibiting neither top or bottom facesheet fracture. A 10% increase in the facesheet stiffness and strength is assumed and the damping constant is estimated at 159.8 Ns/m. The analytical model is able to predict an average contact force to within 10% of the experimental data. In all of these tests, the maximum global deformations were less than 36.8 mm, which is about the deflection at which the back facesheet would have failed. It is assumed both the stiffness and strength of the facesheet would increase with increasing strain rate by the same amount such that the global deflection at back facesheet failure remains the same in the impact tests.

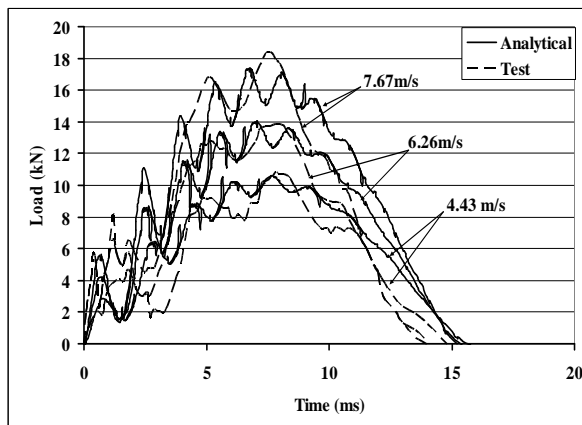


Fig. 5 Contact force history of impact with 10 kg mass projectile at 4.43, 6.26 and 7.67 m/s.

Core shear fracture, delamination and debonding energy should be subtracted from the kinetic energy of the system at the instant they occur. The time duration of these events are instantaneous compared to the sandwich response time since these failures constituted brittle or unstable crack propagation. The energy associated with delamination and debonding is very small and has negligible effect on the solution. The core

transverse shear fracture energy could not be estimated for lack of data on the core transverse fracture toughness. It is assumed to be negligibly small, although it was noticed that there was a load drop in the test data at about the load core shear fracture would occur.

With increasing mass or projectile velocity, damage would occur. Figure 6 compares the calculated and experimental contact forces for the panel with an impact mass of 20 and 30 kg and an impact velocity of 6.26 m/s.

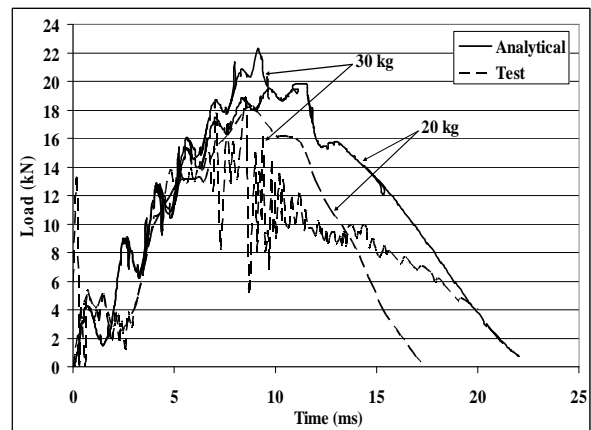


Fig. 6 Contact force history of impact with 20 and 30 kg mass projectile at 6.26 m/s.

Impact with the 20 kg just causes fracture of the back facesheet when the contact force is at a maximum value. At this time, the global panel deflection is almost 36.8 mm. The final deflections and velocities at this time are used as initial conditions in a new simulation of the coupled equations of motion with the Stage III local-indentation response instead of the Stage I/II local-indentation response. The damping constant is assumed to increase to 1000 Ns/m since damping associated with localized core shearing is higher than damping associated with core crushing. The predicted solution is very close to the test data in Stage I/II, but the contact force in Stage III is about 20% higher than the test results. This is because loss of kinetic energy due to tearing of the back facesheet is not accounted for since the velocities at the instant of back facesheet fracture are zero at the peak contact force.

Impact with the 30 kg mass causes complete panel perforation. Unlike the 20 kg mass impact, back facesheet failure takes place at 8.1 ms, about

4.4 ms before the time peak contact force would have occurred. The tear energy is subtracted from the kinetic energy of the back facesheet at this time and a new residual velocity of the back facesheet is calculated. The coupled equations of motion are then solved again using this residual velocity and the corresponding displacements and projectile velocity as initial conditions, the Stage III local indentation response and the damping constant set to 1000 Ns/m. Immediately the local deflection $X_1 - X_2$, exceeds the amount to cause front facesheet failure. Therefore both back and front facesheet take place at the same time. This predicted result is similar to what was found in the test.

6 Conclusions

Analytical models were derived for quasi-static and impact perforation of an E-glass/vinyl ester and Coremat sandwich panel. The panel deformation was decomposed into local indentation and global deformation. An equivalent two degree-of-freedom mass-spring-dashpot system was used to find the dynamic response of the composite sandwich panel subjected to a drop-weight impact by a rigid hemispherical-nose projectile. Equivalent spring resistances were derived from the quasi-static load-displacement response and adjusted dynamic material properties of the facesheet. Several failure modes were considered, including delamination, debonding, core shear fracture, and top and bottom facesheet failures.

Analytical predictions of the quasi-static load-deflection response were within 5% of the test data. However, the calculated failure load was about 25% higher than the test data. This type of accuracy is typical of using the minimum potential energy to approximate the load-deformation response of panels. Analytical predictions of the dynamic response, in particular the contact force history, also compared very well with the test data. The two degree-of-freedom model was able to simulate the correct physics of impact perforation. Without failure of either back or front facesheets, predicted contact force histories were within 10% of test data.

Acknowledgement

The authors acknowledge financial support from Dr. Yapa Rajapakse at the Office of Naval Research under grant N00014-07-1-0423. The authors would like to thank Dr. R. A. W. Mines for

providing experimental results on the static and low-velocity perforation of the E-glass/vinyl ester and Coremat sandwich panel.

References

- [1] Belingardi G., Cavatorta M.P., Duella R. "Material characterization of a composite-foam sandwich for front structure of a high speed train," *Composite Structures*, Vol. 61, No. 1, pp. 13-25, 2003.
- [2] Wen H.W., Reddy T.Y., Reid S.R., Soden P.D. "Indentation, penetration and perforation of composite laminates and sandwich panels under quasi-static and projectile loading," *Key Engineering Materials*, Vols. 141-143, pp. 501-552, 1998.
- [3] Mines R.A.W., Worrall C.M., Gibson A. G. "Low velocity perforation behavior of polymer composite sandwich panels," *International Journal of Impact Engineering*, Vol. 21, No. 10, pp. 855-879, 1998.
- [4] Lantor, B.V. "Fire Coremat data sheet," Veenendaal, The Netherlands, 1993.
- [5] Lin C., Hoo Fatt, M.S. "Perforation of sandwich panels with honeycomb cores by hemispherical-nose projectiles," *Journal of Sandwich Structures and Materials*, Vol. 7, No. 2, pp. 113-172, 2005.
- [6] Mines R.A.W., Jones N. "Approximate elastic-plastic analysis of the static and impact behavior of polymer composite sandwich beams," *Composites*, Vol. 26, No. 12, pp. 803-814, 1995.
- [7] Stevanovic D., Jar P.-Y.B., Kalynasundaram S., Lowe A. "On crack-Initiation conditions for mode I and mode II delamination testing of composite materials," *Composite Science and Technology*, Vol. 60, No. 9, pp. 1879-1887, 2000.
- [8] Kolat K., Naser G., Ozes C. "The effect of sea water exposure on the interfacial fracture of some sandwich systems in marine use," *Composite Structures*, Vol. 78, No. 1, pp. 11-17, 2007.
- [9] Olsson R., Donadon M.V., Falzon B.G. "Delamination threshold load for dynamic impact on plates," *Int J Solids Struct*, Vol. 43, No. 10, pp. 3124-3141, 2006.
- [10] Swaminathan G., Shivakumar K.N., Sharpe M. "Materials property characterization of glass and carbon/vinyl ester composites," *Composite Science and Technology*, Vol. 66, No. 10, pp. 1399-1408, 2006.
- [11] Johnson H.E., Louca L.A., Mouring S.E. "Current research into modelling of shock damage to large scale composite panels," *J. Mater. Sci.*, Vol. 41, No. 20, pp 6655-6672, 2006.
- [12] Ouellet S., Cronin D., Worswick M. "Compressive response of polymeric foams under quasi-static, medium and high strain rate conditions," *Polymer Testing*, Vol. 25, No. 6, pp. 731-741, 2006.